

NASA Contractor Report 3960

(NASA-CR-3960) ANALYSIS OF AIRBORNE DOPPLER
LIDAR, DOPPLER RADAR AND TALL TOWER
MEASUREMENTS OF ATMOSPHERIC FLOWS IN
QUIESCENT AND STORMY WEATHER Contractor
Report, 27 Apr. 1982 - 31 Jul. (Oklahoma

N86-23159

Unclas

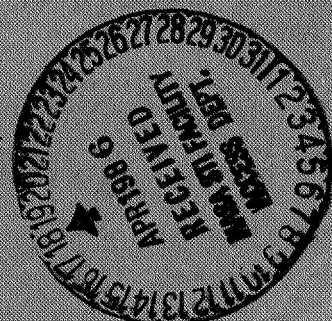
H1/47 04140

Analysis of Airborne Doppler Lidar, Doppler Radar, and Tall Tower Measurements of Atmospheric Flows in Quiescent and Stormy Weather

H. B. Bluestein, R. J. Doviak,
M. D. Eilts, E. W. McCaul,
R. Rabin, A. Sundara-Rajan,
and D. S. Zrnic'

CONTRACT NAS8-34749
FEBRUARY 1986

NASA



Analysis of Airborne Doppler Lidar, Doppler Radar, and Tall Tower Measurements of Atmospheric Flows in Quiescent and Stormy Weather

H. B. Bluestein

*University of Oklahoma
Norman, Oklahoma*

R. Rabin

*National Severe Storms Laboratory
Norman, Oklahoma*

R. J. Doviak and M. D. Eilts

*National Severe Storms Laboratory
Norman, Oklahoma*

A. Sundara-Rajan

*Cooperative Institute for
Mesoscale Meteorological Studies
Norman, Oklahoma*

E. W. McCaul

*University of Oklahoma
Norman, Oklahoma*

D. S. Zrnic'

*National Severe Storms Laboratory
Norman, Oklahoma*

Prepared for
George C. Marshall Space Flight Center
under Contract NAS8-34749



National Aeronautics
and Space Administration

**Scientific and Technical
Information Branch**

1986

PREFACE AND ACKNOWLEDGMENTS

The first experiment to combine airborne Doppler lidar and ground based dual Doppler-radar measurements of wind to detail the lower tropospheric flows in quiescent and stormy weather was conducted in Central Oklahoma during four days of June-July 1981. Data from these unique remote sensing instruments, coupled with those from conventional and novel in-situ facilities such as a 500 m tall meteorologically instrumented tower, rawinsonde, and a dense network of surface based sensors, have been analyzed to enhance the understanding of wind, waves, and turbulence. The data collected for this study and the analyses presented in this report had the multifaceted purposes of (1) comparing winds mapped by ground-based dual Doppler radars, by anemometers on a tall tower, and by NASA's innovative airborne Doppler lidar, (2) comparing measured atmospheric boundary layer flow with flows predicted by theoretical models; (3) investigating the kinematic structure of air mass boundaries that precede the development of severe storms and; (4) studying the kinematic structure of thunderstorm phenomena (e.g. downdrafts, gust fronts, etc.) that produce wind shear and turbulence hazardous to aircraft but are difficult to observe with conventional instrumentation.

The results of experiments reported herein show that it is feasible to have detailed but remotely acquired measurements of the cloudless atmospheric motion in many provocative weather situations, whereas such observations were previously limited to scaled-down laboratory experiments. We have carried out these detailed measurements in nature's own laboratory so we can improve forecasts using data that may become available to operational meteorologists. Meeting the challenge of improving weather forecasts and storm hazard warnings demands an integrated and well-conceived experimental design that builds upon a base of theoretical and experimental results and uses the technological expertise, leadership, and cooperation of several research groups, bound together with strong and enduring commitments. NASA's Marshall Space Flight Center (MSFC), NOAA's National Severe Storms Laboratory (NSSL), and the University of Oklahoma's Department of Meteorology and Cooperative Institute for Mesoscale Meteorological Studies (CIMMS) have this commitment. This report is the first one showing the results of the combined efforts from this group dedicated to improve our understanding of weather.

The report is divided into 3 parts. Part I, "Intercomparison of Wind Data From Airborne Lidar, Ground-Based Radars and Instrumented 444 m Tower," gives results of the first intercomparison of atmospheric boundary layer wind measured by dual Doppler radars and airborne Doppler lidar. The second part, "The Structure of the Convective Atmospheric Boundary Layer as Revealed by Lidar and Doppler Radars" relates remotely sensed properties of homogeneous turbulent flow in the atmospheric boundary layer to those properties predicted by theories. Part III, "Doppler Lidar Observations in Thunderstorm Environments," gives an analysis of the first observations with an airborne Doppler lidar of thunderstorm outflows and flow of environmental air into a complex of cumulus clouds. Appendix A describes the Doppler lidar instrumentation, its operation, and methods used to deduce the Doppler velocity component of horizontal wind.

These first results are due to the dedicated efforts of many and the authors are indebted to NASA for its support, under the management of Drs. James Dodge and William Vaughan, and to both the NSSL and NASA staffs for their fine engineering support for this large data collection effort. Jim Bilbro and Ed Weaver of NASA, Chuck DiMarzio of Raytheon, and Bob Lee of Lassen Research, helped us to better understand the airborne lidar system, its unique features and the errors that it is vulnerable to. Dr. Dan Fitzjarrald, NASA, is to be especially thanked for presenting us with the lidar data in an easily usable form, and for constructive discussions. Drs. Douglas Lilly and Claude E. Duchon of the University of Oklahoma gave beneficial comments and suggestions during the course of this study. Encouragement and support from Dr. E. Kessler and staff at NSSL were critical to the quality of the work. Joan Kimpel of CIMMS and Robert Goldsmith of NSSL provided graphic services, and Michelle Foster of NSSL typed the manuscript.

The work reported herein has already led to the publication of nine papers and to two others in preparation. The article "The structure of the convective atmospheric boundary layer as revealed by lidar and Doppler radars" has appeared in a recent issue of the international journal: Boundary-Layer Meteorology and another article "Estimation of the average surface heat flux over an inhomogeneous terrain" has been accepted for publication in that journal. The paper "Comparison of winds, waves, turbulence as observed by airborne lidar, ground based radars, and instrumented tower" has appeared in the

American Geophysical Union's journal: Radio Science. The research on "An observational study of a mesoscale area of convection under weak synoptic-scale forcing" has been published by the American Meteorological Society's Monthly Weather Review. Papers to Applied Optics and The Journal of Atmospheric and Oceanic Technology are in preparation. This work has also supported two Master's Theses.

Editor. Richard J. Doviak
National Severe Storms Laboratory
1313 Halley Circle
Norman, OK 73069
April 1985

TABLE OF CONTENTS

Part	Page
Preface and Acknowledgments.....	ii
I. Intercomparison of Wind Data From Airborne Lidar, Ground-Based Radars and Instrumented 444 m Tower	1
Abstract	2
1.1 Introduction	3
1.2 The Experiment	3
1.3 Synthesis of Wind Fields ...	6
1.4.1 Mean Wind	7
1.4.2 Wind Profiles	8
1.4.3 Intensity of Turbulence	9
1.4.4 Spectra of Horizontal Velocity Fluctuations	13
1.5 Explanation of Differences Between Lidar and Radar Measured Winds	14
1.6 Comparison of Data Collected on July 2, 1981 ...	18
1.7 Conclusions	25
II. The Structure of the Convective Atmospheric Boundary Layer as Revealed by Lidar and Doppler Radars	27
Abstract	28
2.1 Introduction	29
2.2 Data Collection	29
2.3 Data Analysis	29
2.3.1 Construction of the Wind Profile	30
2.3.2 Calculation of Velocity Spectra ..	31
2.3.3 Determination of Micrometeorological Parameters ...	31
2.3.4 Estimation of Momentum Flux Profiles	35
2.4 Results	36
2.4.1 Vertically Averaged Winds	36
2.4.2 Momentum Flux and Geostrophic Wind Profiles	38
2.4.3 Spectra of Horizontal Wind	41
2.5 Concluding Remarks	41
III. Doppler Lidar Observations in Thunderstorm Environments ..	43
Abstract	44
3.1 Introduction	45
3.2 Meteorological Setting for the Experiment	47
3.3 Data Collection	49
3.4 Data Analysis	55
3.4.1 Navigation Data Review and Editing	56
3.4.2 Doppler Spectral Moment Data Review and Editing	58
3.4.3 Velocity Errors Due to Beam Pointing Errors	59
3.4.4 Preparation of Meteorological Data Fields	61
3.5 Meteorological Interpretation	64
3.5.1 Interpretation of Thunderstorm Outflow Data	64
3.5.2 Interpretation of Data at the Edge of an Isolated Cumulus Congestus	80

TABLE OF CONTENTS (Concluded)

Part	Pag
3.6 Conclusions and Recommendations	90
Appendix	
A. Description of Instrumentation	95
A.1 Doppler Lidar.....	95
A.2 Doppler Radar	106
A.3 Other Instruments on Board the Aircraft	106
B. Estimation of the Average Surface Heat Flux Over an Inhomogeneous Terrain from the Vertical Velocity Variance	111
B.1 Introduction	111
B.2 The Method Used and Results	111
B.3 Concluding Remarks	114
C. Inspection and Verification of CV990 INS Data	115
C.1 Errors in Conversion Factors	116
C.2 Correction to the Recorded INS Derived Position Data	117
C.3 INS Generated Errors in Aircraft Position and Ground Velocity....	125
C.4 Effects of Navigation Errors on Doppler Lidar Derived Wind Fields	132
D. Inspection and Verification of Doppler Spectral Moment Data	136
D.1 Preparation of Reflectivity Fields	138
D.2 Thresholding and Editing of Doppler Moment Data	139
D.3 Diagnosis and Removal of Radial Velocity Biases	147
E. Assessment of Scanner Performance	150
F. Tests Using Model Wind Field	153
Bibliography	161

LIST OF TABLES

Table	Title	Page
1.1	Comparison of Lidar and Radar Estimated Mean Wind	8
1.2	Corrections That Needed to be Added to Forward and Aft Radial Velocities	17
1.3	Difference Between Actual and INS Positions	18
A.1	Doppler Radar and Lidar Parameters	108
B.1	Surface Kinematic Heat Flux Estimates	113
C.1	Sample of Raw Position Data NASA CV 990	119
C.2	Sample of Raw Meteorological Data NASA CV 990	120
C.3	Sample of Corrected Position Data NASA CV 990	121
C.4	Sample of Corrected Meteorological Data NASA CV 990	122
C.5	Sample of Raw and Corrected Time Data	124
D.1	Sample of Raw Lidar Moment Data	137
D.2	Sample of Corrected Lidar Wind, Intensity and Width Data	140
D.3	Summary of Characteristics of Lidar Data Runs	143

LIST OF ILLUSTRATIONS

Figure	Title	Page
1.1	Schematic of Airborne Doppler Lidar System	
1.2	Location of Doppler Radars, Instrumented Tower, Rawinsonde Release Point, Aircraft Track, and Grid Area	
1.3	Comparison of 1400 CST Radar and Lidar Vector Wind Fields	
1.4	Comparison of Wind Profiles	
1.5	Comparison of Adjusted Wind Profiles	1
1.6	Standard Deviation of Horizontal Velocity Fluctuations	1
1.7	Direction Schematic	1
1.8	Comparison of Spectra of the u and v Velocity Component Fluctuations from Lidar and Radar Data	1
1.9	Comparison of Wind Spectra Measured by Tower Instruments and Radar...	1
1.10	Trend Removed Lidar and Radar Wind Profiles	1
1.11	Plot of Aircraft Movement	1
1.12	Map Showing Difference Between Actual Aircraft Location and INS Indicated Location	1
1.13	Flight Path of the ADLS on July 2, 1981	2
1.14	Rawinsonde Wind Profile on July 2, 1981	2
1.15	Example of an Average of 100 Doppler Velocity Spectra	2
1.16	Comparison of Radial Velocities	2
1.17	Photo of NSSL's WSR-57 Radar Display	2
2.1	Observed Wind Profile and Estimated Geostrophic Wind Profile	3
2.2	Spectra of Horizontal Wind Velocity Fluctuations (Radar)	3
2.3	Spectra of Horizontal Wind Velocity Fluctuations (Lidar)	3
2.4	Spectra of Horizontal Wind Velocity Fluctuations (Tower)	3
2.5	Virtual Potential Temperature Profile	3
2.6	Momentum Flux Profiles (Estimated)	3
2.7	Momentum Flux Profiles (Computed)	4

LIST OF ILLUSTRATIONS (Continued)

Figure	Title	Page
2.8	Momentum Flux Profiles with Assumption	40
3.1	Skew T-log p Diagram and Hodograph of Winds	48
3.2	Flight Track of NASA CV 990 on June 30, 1981	50
3.3	Photo at 1419 CST During Run 2	51
3.4	Photo at 141930 CST During Run 2	52
3.5	Photo at 1427 CST During Run 3	53
3.6	Photo at 145030 CST During Run 7	54
3.7	Construction of Wind Vector from Fore and Aft Radial Velocities	63
3.8	Sample Field of Radial Velocity Data and Synthesized Wind Vectors During Run 3	65
3.9	Vector Plot of Lidar-Derived Winds of Storm Outflow During Run 2 ..	66
3.10	Contour Plot of Normalized Reflectivity (Run 2)	67
3.11	Contour Plot of Spectral Widths (Turbulence)	68
3.12	Plot of Meteorological Observations at TTS	74
3.13	Vector Plot of Lidar-Derived Winds During Run 3	76
3.14	Contour Plot of Normalized Reflectivity (Run 3)	78
3.15	Contour Plot of Spectral Widths (Turbulence) During Run 3	79
3.16	Vector Plot of Lidar-Derived Winds During Runs 5-8	81
3.17	Vector Plot of Lidar-Derived Winds During Runs 9-12	82
3.18	Vector Plot of Lidar-Derived Winds During Runs 5-8 Using Pairs of Adjacent Runs	83
3.19	Vector Plot of Perturbation Winds at 1130 m AGL	85
3.20	Vector Plot of Perturbation Winds at 2290 m AGL	86
3.21	Contour Plot of Normalized Reflectivity at 2290 m AGL	88
3.22	Contour Plot of Normalized Reflectivity at 1129 m AGL	89

LIST OF ILLUSTRATIONS (Continued)

Figure	Title	Page
A.1	Block Diagram of NASA's Airborne CO ₂ Doppler Lidar System (ADLS)	96
A.2	Transmitted Pulses, Doppler-Shifted Echo, and Input to PPPP	100
A.3	Velocity Components to Derive Horizontal Wind Vector from Lidar Measurements	104
A.4	Typical Arrangement of Data Samples in Space	107
B.1	Comparison of Surface Heat Flux Estimates	114
C.1	Aircraft Flight Parameters	116
C.2	INS Derived Position Error Vectors for Run 4	127
C.3	The x-position Errors for Run 4	129
C.4	The y-position Errors for Run 4	129
C.5	Fourier-filtered Version of x-position Error	130
C.6	Fourier-filtered Version of y-position Error	130
C.7	The x-component of Ground Velocity Errors	131
C.8	The y-component of Ground Velocity Errors	131
C.9	Wind Field Corresponding to INS Velocity Errors	134
D 1	Typical Raw Intensity Profile	141
D.2	Relative Reflectivity Profile	141
D.3	Raw Lidar Radial Winds from Run 10	144
D.4	Graphical Output for Editing Data (Run 10)	144
D.5	Graphical Output for Editing Velocity Data (Fore Frame).....	145
D.6	Graphical Output for Editing Velocity Data (Aft Frame)	146
D.7	Geometrical Explanation of Ground Velocity Errors....	149
E.1	Ground Strike Ranges and Aircraft Roll Angles	151
F.1	Wind Field Synthesized from Simulated Lidar Observations	154
F 2	Perturbation Wind Field, $U_a = V_a = 2.5 \text{ m s}^{-1}$...	155

LIST OF ILLUSTRATIONS (Concluded)

figure	Title	Page
F.3	Velocity Vector Differences, $U_a = V_a = 2.5 \text{ m s}^{-1}$	156
F.4	Same as Figure F.1 except $U_a = V_a = 10 \text{ m s}^{-1}$	157
F.5	Same as Figure F.2 except $U_a = V_a = 10 \text{ m s}^{-1}$	158
F.6	Same as Figure F.3 except $U_a = V_a = 10 \text{ m s}^{-1}$	159

PART I: INTERCOMPARISON OF WIND DATA FROM
AIRBORNE LIDAR, GROUND-BASED RADARS AND
INSTRUMENTED 444 m TOWER

ABSTRACT

On June 29, 1981 two ground-based Doppler radars, an airborne Doppler lidar, a very tall (444 m) instrumented tower, and a rawinsonde collected wind data in the Planetary Boundary Layer (PBL) in Central Oklahoma. This allowed, for the first time, intercomparison of wind fields synthesized from airborne Doppler lidar data with those from dual Doppler radar data. The vertical profile of wind in the PBL measured by the radars compared favorably with the profiles measured by the tower and rawinsonde while the one obtained from lidar data differed from the other three by as much as $3 \text{ m}\cdot\text{s}^{-1}$ in wind speed and 38° in direction. The time dependence of differences in wind estimates from radar and lidar suggested that these discrepancies could be attributed to a Schuler resonance in the aircraft's inertial navigation system which caused an erroneous component of the aircraft velocity vector to be subtracted from the lidar radial velocities, thus creating errors in the synthesized wind speed and direction. The vertical profile of turbulent fluctuations of the horizontal wind detected by the different sensing systems compared well. Also, spectra from the different sensing systems compared well in both magnitude and shape, suggesting that the lidar and radar detected similar turbulent structure. On July 2, 1981 an experiment was conducted to compare the point-by-point wind measurements made with the lidar, radar, and INS systems. The results of this experiment also suggest that Schuler resonance may account for discrepancies between the lidar and radar measurements.

1.1. INTRODUCTION

During June 29 - July 2, 1981, four research flights totaling 11 hours were made in Oklahoma by the NASA Convair 990, Galileo II aircraft, instrumented with a coherent Doppler lidar. These flights were made within the range (i.e. < 100 km) of the NSSL Doppler radars and most of the time within the area of optimum dual Doppler analysis for the radars (one at Norman and the other Cimarron radar located at Page Airfield 40 km northwest of Norman). The data collected during these flights besides giving information on the structure of the cloud-free boundary layer, the prestorm environment, and the airflow in and around the clouds, afforded an opportunity for the first time intercomparison of wind data from totally different systems -- airborne Doppler lidar, ground-based Doppler radars, rawinsonde, and instrumented tower. For this study, the principal instruments used in the data collection process were the Airborne Doppler Lidar and Ground-Based Doppler Radar whose operation and performance are described in Appendix A. In this part intercomparison data collected on June 29 and July 2 will be discussed.

1.2 THE EXPERIMENT

On June 29, 1981 data were collected between 1150-1410 CST. At this time skies were mostly clear and winds were moderate ($5-8 \text{ m}\cdot\text{s}^{-1}$) out of the south and tended to back (turn counter-clockwise) and increase during the hours of data collection. Real time displays of Doppler velocities measured by radar indicated that the wind field was relatively uniform to ranges of at least 80 km in all directions which was consistent with hourly surface observations during the time of data collection. There was significant daytime heating (maximum temperature of 35°C) and abundant gulf moisture, making the atmosphere convectively unstable; the height of the capping inversion was approximately 1140m. Doppler lidar radial velocity estimates are calculated in resolution volumes spaced 320 m in range from the aircraft out to approximately 15 km in range (see Appendix A for complete description). However, on this day attenuation of the lidar beam by atmospheric water vapor only allowed accurate velocity estimates to 5 km whereas on drier days a range of 10 km was achieved. Velocity vectors are calculated at intersections of fore and aft directed beams (Fig. 1.1) in a similar way in which velocity vectors are synthesized from the two Doppler radars (Doviak and Zrnic', 1984).

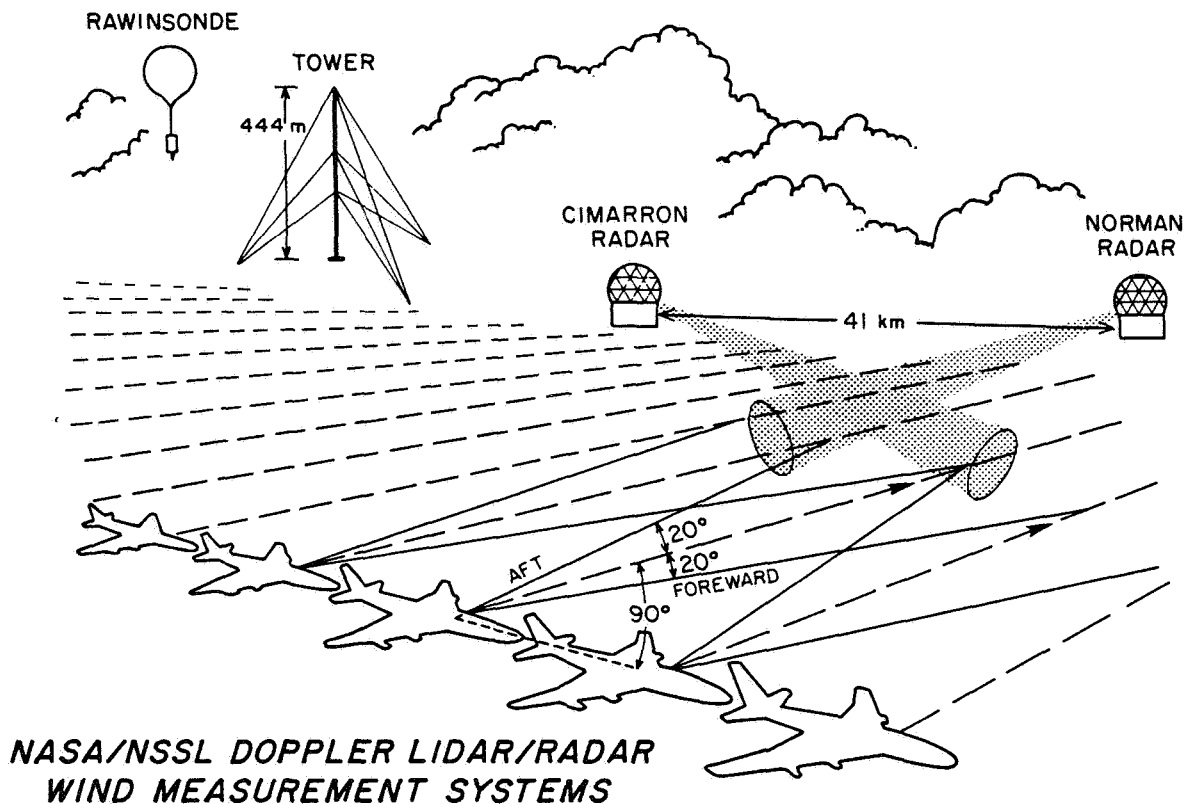


Figure 1.1 Schematic of Airborne Doppler Lidar system showing intersections of forward and aft lidar beams where wind vectors relative to the ground are calculated. Also shown are the other sensing systems that were used for data collections on June 29, 1981.

The lidar instrumented aircraft was flown in oblong "race tracks" approximately 65 km x 15 km, southwest of Norman (Fig. 1.2) where wind observation by the two NSSL Doppler radars are relatively free of ground clutter interference (Doviak and Berger, 1980). Complete circuits were made at four different heights: 900, 750, 600, and 400 meters above ground level. The aircraft was flown in a counter-clockwise direction so that the Doppler lidar, which is located on the left side of the aircraft, would scan the same approximate area when going in opposite directions. However, on this day targets were only detected out to 5 km; so no intercomparison of lidar data collected just minutes apart was possible. All in all, eight data runs were made (each of approximately 5 minutes duration) during the period 1300-1410 CST.

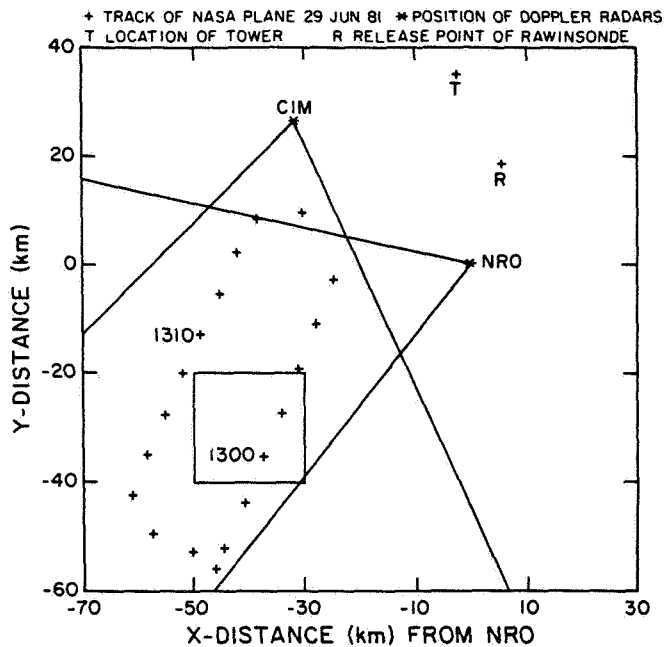


Figure 1.2 Location of two Doppler radars, the instrumented tower T, the rawinsonde release point R, the approximate lidar instrumented aircraft track +, the grid area (square box) to where 1300-1302 CST data were interpolated.

During this period, NSSL's two Doppler radars had their range resolution set at 450 m and were scanning the same volume in which the aircraft was being flown. Their Nyquist velocities were about $11 \text{ m}\cdot\text{s}^{-1}$ and their unambiguous ranges were 345 km (Appendix Table A.1).

Every 5 minutes each radar scanned a volume subtended by 60° azimuth and 3.4° elevation. This was done by scanning the radar 60° azimuthally, starting at 0.4° elevation angle and incrementing the elevation angle 0.5° at the end of each azimuthal sector. The Doppler radars are able to detect returns from refractive index fluctuations (cause by turbulent mixing of gradients of temperature and moisture) in the clear air boundary layer. Doviak and Jobson (1979) were able to observe clear air wind perturbations using these Doppler radars. Doviak and Berger (1980) were able to follow perturbations in the wind field as they were advected downwind by the mean flow. When data from consecutive radar scans (approximately 3.5 minutes apart) were compared, it was noticed that perturbations had moved downwind by a distance that the mean

wind would have advected them during this time. They concluded that velocity estimates synthesized from NSSL's dual Doppler radars are accurate enough (a few tenths of a ms^{-1}) to map the wind field and its kinematic properties in the clear air out to ranges of 60 km. Sixteen volume scans were recorded from each radar (1250-1400 CST).

Data were also collected throughout June 29th by instruments on a tower, operated and maintained by NSSL. This 444 m tall tower is located 39 km north of Norman. On this day wind speed, wind direction, temperature and vertical velocity data were collected at seven different heights between the surface and 444 m.

A rawinsonde was released at 1150 CST from Tinker Air Force Base which is located approximately 30 km north-northeast of Norman. Data from the rawinsonde allowed us to determine the height of the inversion as well as the wind profile throughout the boundary layer.

1.3. SYNTHESIS OF WIND FIELDS

In order to compare data from the airborne Doppler lidar and the Doppler radars, data from both were interpolated to common horizontal Cartesian grids (20 km x 20 km, grid spacing 500 m) using a Cressman weight (Cressman, 1959) with horizontal radius of influence of 1.5 km. A vertical radius of influence of 300 m was used for the radar data but no vertical interpolation was needed for the lidar data because data were collected along beams on nearly horizontal surfaces.

Before interpolation, data from both sensing systems were edited using reflectivity, spectral width, and signal-to-noise ratio thresholds. This removed data that were erroneous due to weak signal or other measurement uncertainties. The Doppler radar data were also edited along each radial to remove erroneous data points caused by point targets (aircraft, birds, etc.). This was done using an algorithm that compared the velocity value in question with the eight nearest points along the radial. If the velocity value was more than $3.5 \text{ m}\cdot\text{s}^{-1}$ from this mean, the velocity value was not used.

Data from each radar (interpolated to common grids) were vectorially combined to arrive at a velocity vector at each grid point. In a similar way, data from the airborne lidar forward and aft directed beams were vectorially combined.

Grid volume locations were determined by plotting the Inertial Navigation System's (INS) derived track of the NASA aircraft. The gridded volumes were placed such that data collection by both Doppler radars and the lidar were acquired together. All in all, nine grid volumes were chosen to compare lidar and radar data. Location of the grid to where the 1300-1302 data were interpolated is shown in Fig. 1.2.

1.4. COMPARISON OF WIND DATA

1.4.1. Mean Wind

Fig. 1.3 is a sample of comparable vector wind fields from both the lidar and radars at about 1400 CST. Mean wind given at the top of the figures is the vector average over the entire grid. Differences in mean wind speed of 2.4 ms^{-1} and direction of 16° can easily be noticed. Comparison of mean wind for all of the nine common grid volumes is shown in Table 1.1. A systematic difference between the lidar and radar mean winds can be noticed. Lidar detected winds at earlier times and higher heights were lighter and had a more westerly component while at later times and lower heights the lidar detected winds were stronger and had a more easterly component than the radar detected winds.

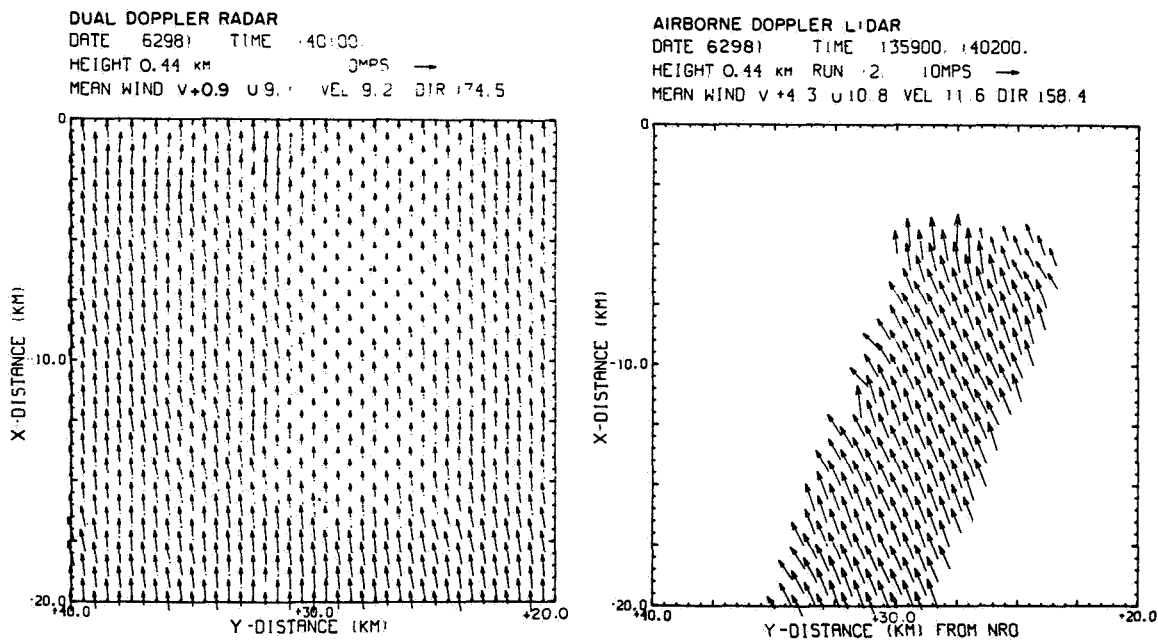


Figure 1.3 Comparison of 1400 CST radar and lidar vector wind fields (the radar wind field is on the left).

TABLE 1.1

Comparison of Lidar and Radar Estimated Mean Wind
(north and west distances from NRO are positive)

TIME (CST)	Grid Origin (from NRO, km)	Height (km)	Lidar		Radar	
			Vel (m/s)	Dir (deg)	Vel (m/s)	Dir (deg)
1300	(-40, +30)	.90	6.8	197.9	6.6	185.7
1310	(-30, +40)	.88	6.8	218.6	7.8	180.6
1320	(-30, +25)	.79	7.4	199.4	8.0	177.7
1325	(-15, +35)	.78	7.0	204.9	8.3	181.1
1330	(-40, +40)	.76	7.1	192.8	8.4	177.0
1335	(-50, +35)	.58	8.7	169.4	8.5	173.6
1340	(-25, +25)	.61	9.5	165.8	8.9	176.1
1355	(-45, +25)	.40	11.4	156.5	9.0	171.3
1400	(-20, +20)	.44	11.6	158.4	9.2	174.5

1.4.2. Wind Profiles

Another way of comparing data from the two sensing systems is to compare the vertical profile of wind that the two systems measure. Wind profiles can be constructed from lidar and radar data using the mean vector winds listed on Table 1.1 because these were computed at different heights throughout the boundary layer. The wind profile in the boundary layer as measured by lidar, radar, rawinsonde, and tower is shown in Fig. 1.4. The radar wind profile is nearly linear and also nearly constant with height, as is the rawinsonde profile. The lidar wind profile shows more vertical wind shear and non-linearity.

Because the profile data were collected over an hour time period (the data near the top nearly an hour before the data at the bottom), changes in the wind speed and direction during this time would cause the wind profiles to be skewed. From the tower data continuously collected at the 444 m height, we detected a trend in both wind speed and direction between 1300-1400 CST. The wind speed increased 1.3 ms^{-1} during this time and the wind direction had a counter-clockwise shift (i.e., backing) of 13° . Using the observation that

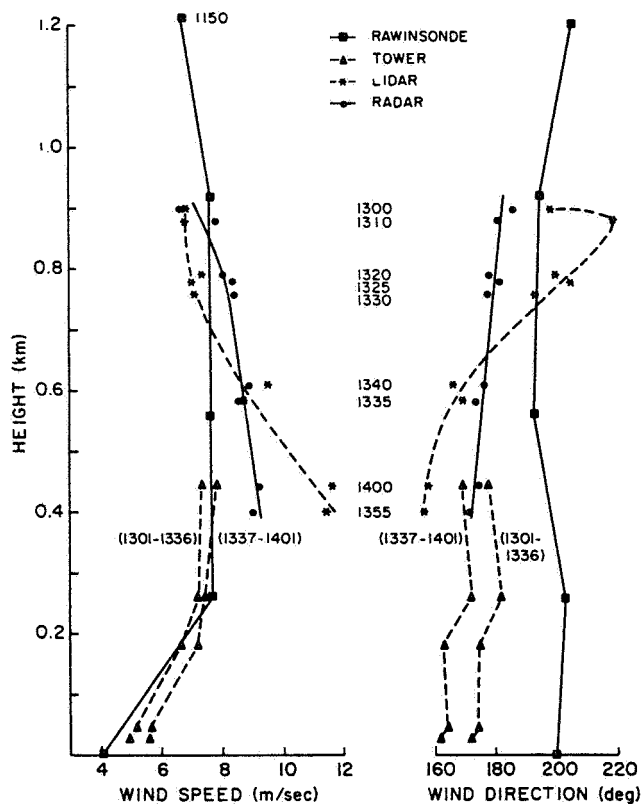


Figure 1.4 Comparison of wind profiles measured by lidar, radar, tower, and rawinsonde.

the wind field was horizontally homogeneous, we assumed that this time trend observed by the tower occurred throughout the lowest kilometer of the atmosphere in the air mass probed by the lidar and radars. We then adjusted the wind profiles relative to 1330 CST to remove this time trend (Fig. 1.5). The tower profile was constructed from a 12-minute average of data from 1321-1333 CST. The rawinsonde profile was adjusted using the two-hour trend from the tower data. These wind profiles are now estimates of the actual vertical profiles as detected by the different sensing systems at the common reference time. The trend removal does not change any of the differences between the lidar and radar profiles, but it shows that the radar profile compares better in wind speed and direction with both rawinsonde and tower profiles than it does with the lidar profile.

1.4.3. Intensity of Turbulence

The variances σ_u^2 and σ_v^2 of the orthogonal wind components (u is in the direction of the mean surface layer wind) were computed for each lidar and radar-estimated vector wind field, and then combined, $\sigma_T = (\sigma_u^2 + \sigma_v^2)^{1/2}$, to get the standard deviation of the horizontal wind velocity fluctuations. The total variance is

$$\sigma_T^2 = \sigma_\epsilon^2 + \sigma_t^2 \quad (1.1)$$

where σ_ϵ is the standard deviation due to errors in the velocity estimates and σ_t is the standard deviation caused solely by turbulence and small scale organized flows such as waves and convective cells (Doviak and Zrnic', 1984). The variances in (1.1) relate to the velocity estimated at grid points and includes errors introduced by interpolation and variance reduction due to the Cressman interpolation scheme (Doviak, *et al.*, 1976).

We estimated the radar error standard deviation, σ_ϵ , by assuming that errors were due only to the radar's electronic noise. From signal-to-noise ratio measurements we calculated radial velocity estimate standard deviation using a technique described by Doviak and Jobson (1979). Following the methods of Doviak *et al.*, (1976), we computed about a $1.1 \text{ m}\cdot\text{s}^{-1}$ standard error for the single radial velocity estimate from each radar. However, about 25

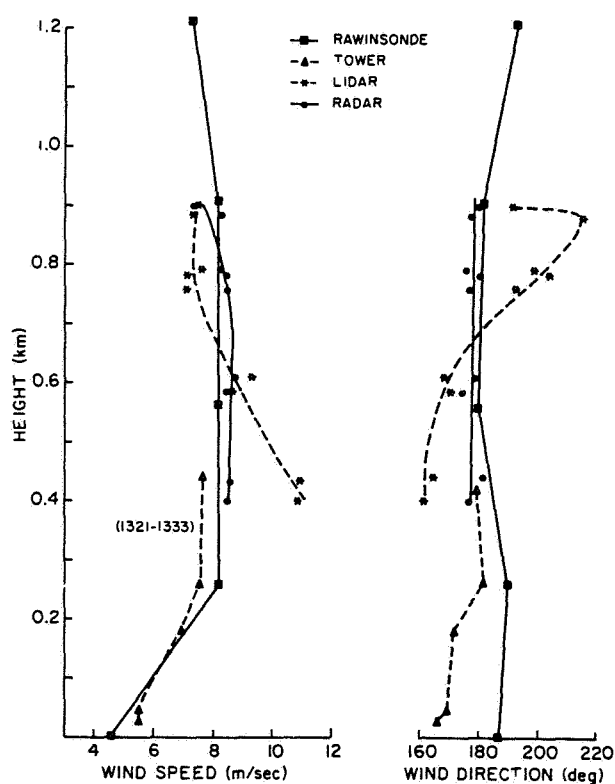


Figure 1.5 Comparison of wind profiles measured by lidar, radar, tower, and rawinsonde. Profiles have been adjusted to remove a time trend relative to 1330 CST.

data from each radar were interpolated to each grid point using a Cressman weighted filter function. Doviak *et al.*, (1976) have shown that a spherically symmetric Cressman influence region reduces the variance of interpolated data by an amount:

$$R^2 = 1 - \frac{1.69}{N} \quad (1.2)$$

where $1 - R^2$ is the ratio of the grid point radial velocity variance σ_1^2 to the variance of each radial velocity estimate used in the Cressman filter. N is the number of velocity estimates interpolated to a grid point and although the influence region used here is ellipsoidal we assume that (1.2) approximates the variance reduction. Thus, the error variance σ_1^2 of the interpolated radial velocity is approximately $7.4 \times 10^{-2} \text{ m}^2 \text{ s}^{-2}$. Now the variance σ_ϵ^2 of horizontal wind speed is a function of wind direction and for the case under consideration here, in which the wind intersects the line connecting the radars by about 45° , σ_ϵ is nearly equal to $\sigma_1 \approx 0.3 \text{ m s}^{-1}$ (Doviak *et al.*, 1976). All standard deviations larger than this value are attributed to actual variations in the windfield.

An estimation of the lidar error standard deviation was made assuming that errors were caused by: (1) electronic noise in the lidar system which was estimated from the signal-to-noise ratio (Lee, 1980); (2) errors in ground speed and ground track angle as given in specifications for the Inertial Navigation System (INS); and (3) errors in the line-of-sight angle of the laser beam. Specified accuracies of the aircraft ground speed and the ground track angle are approximately $\pm 0.5 \text{ m} \cdot \text{s}^{-1}$ and $\pm 0.4^\circ$ respectively. Pointing of the laser beam is accurate to within $\pm 0.3^\circ$ (Raytheon, 1983). Error estimates calculated from the signal-to-noise ratio averaged $0.35 \text{ m} \cdot \text{s}^{-1}$ within 5 km of the aircraft. If we assume independent errors, the SD of the lidar radial velocity estimates due to errors is equal to 1.2 m s^{-1} sec. After the wind vectors are synthesized with approximately 35 radial velocity estimates interpolated to each grid point, the standard deviation caused by errors in the velocity estimates is equal to 0.6 m s^{-1} .

Figure 1.6 shows the comparison of the standard deviation of velocity fluctuations measured by the three sensing systems. Standard deviations for wind measured by the tower instruments were averaged for approximately 10 min. The total standard deviation σ_T detected by the radar is nearly constant with height, although noticeable time trends are evident. From 1300

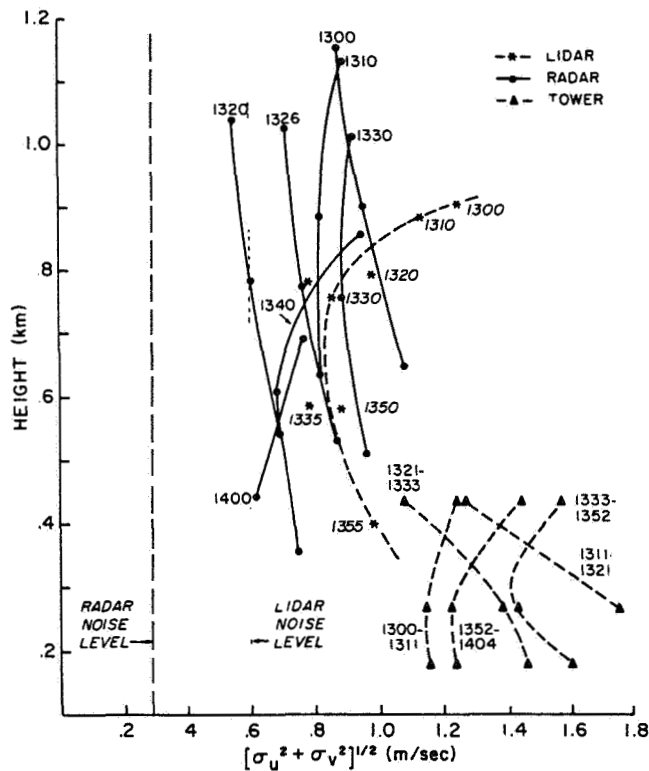


Figure 1.6 Standard deviation of the horizontal velocity fluctuations from lidar, radar, and tower.

to 1320 CST there is a general decrease in standard deviation with time, while from 1320 to 1335 there is a general increase. From 1335 to 1400 CST no apparent trends are noticed.

The total standard deviation measured by the lidar compares well in magnitude with that measured by the radars. Neglecting variations with height, a time trend similar to that of the radar σ_T is noticed from 1300 to 1320 CST (decrease in standard deviation with time), while from 1320 to 1400, little variation is noticed.

The total standard deviation calculated from the tower data shows no apparent trends and tends to be larger than that estimated by either the lidar or radars. Two reasons may be responsible for these larger values. (1) the tower is close to the surface, where velocity fluctuations may be expected to be larger because of surface effects (Mason and Sykes, 1980), and (2) the tower instruments make point measurements while the lidar and radar both average through a resolution volume, thus, in effect, smoothing the data and decreasing the estimate of σ_T .

1.4.4. Spectra of Horizontal Velocity Fluctuations

Spectra of horizontal velocity fluctuations of the u and v wind components were computed from the lidar, radar, and tower data. For comparison of radar and tower data, spectra were calculated in the direction of the mean wind while for comparison of lidar and radar data, spectra were calculated in the direction of the flight path (Fig. 1.7).

Spectra were calculated from radar data by interpolating data to a line of 32 grid points spaced 500 m apart. After the mean and trend were removed, Fourier analysis was done to resolve wavelengths between 1 and 16 km. Twenty spectra were averaged to give the spectra shown in Figs. 1.8 and 1.9 that were used for comparison.

Spectra were calculated in a similar way from the lidar data. Several lines of 32 grid points spaced 500 m apart and parallel to the flight path were selected. Data were interpolated to these grid points and after the mean and trend were removed, Fourier analysis was done to resolve wavelengths between 1 and 16 km. Six spectra were averaged to give the spectra shown in Fig. 1.8. Spectra from lidar and radar data compare well in both magnitude and shape, especially in the v-component where peaks in both spectra occur at about the same wavelength.

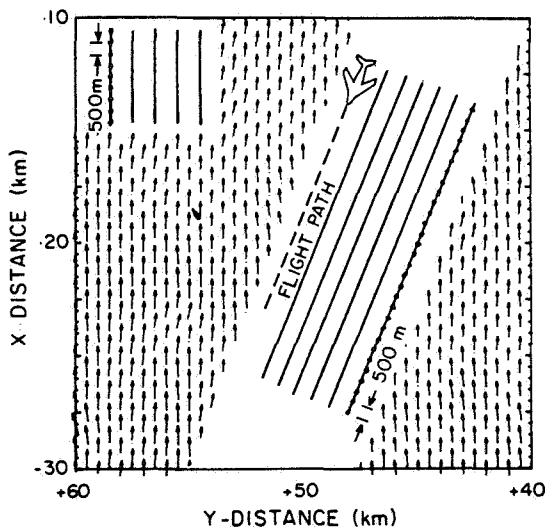


Figure 1.7 Schematic showing the direction along which spectra were calculated to compare data.

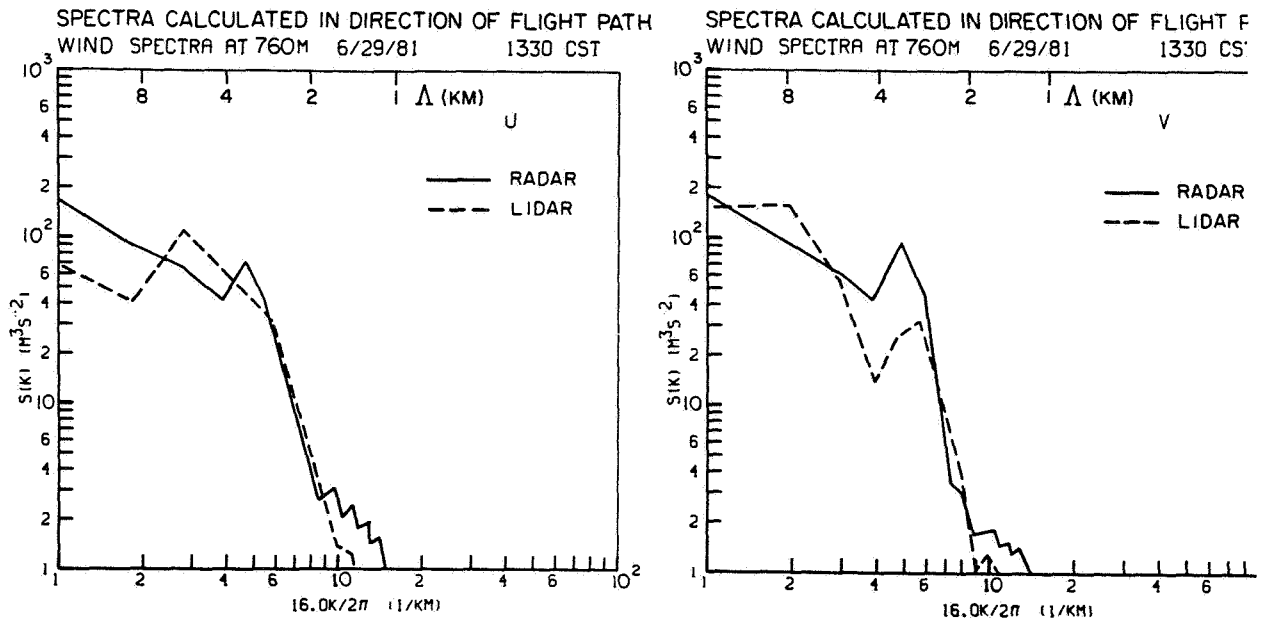


Figure 1.8 Comparison of spectra of the u and v velocity component fluctuations from lidar and radar data. Spectra are for scales (wavelengths Δ) along directions parallel to the flight path.

Figure 1.9 is the comparison of spectra in the direction of the mean wind from tower and radar data. Spectra were calculated from the tower data assuming that all perturbations in the wind field were advected with the mean wind and did not change in the time frame needed to get enough data for spectral analysis (Taylor's hypothesis). Thus, a line of grid points was set up in the direction of the mean wind and radar data were interpolated to them. Likewise, radar data interpolated to lines parallel to the mean wind direction were used in the comparison shown in Fig. 1.9. Radar and tower spectra compare well in both magnitude and shape.

1.5. EXPLANATION OF DIFFERENCES BETWEEN LIDAR AND RADAR MEASURED WINDS

Two factors may be responsible for the differences between the lidar and radar measured mean winds (Table 1.1) and the difference between the lidar wind profile and the other wind profiles (Fig. 1.5). These are: (1) the lidar has a very small vertical resolution (20 cm) which may have allowed it to detect small vertical scale variations in the wind field that were not detected by the radar because of its larger vertical resolution (~700 m) or by the tower or rawinsonde because of time and location differences, or (2) an inherent error in the Doppler lidar system or in the INS of the aircraft

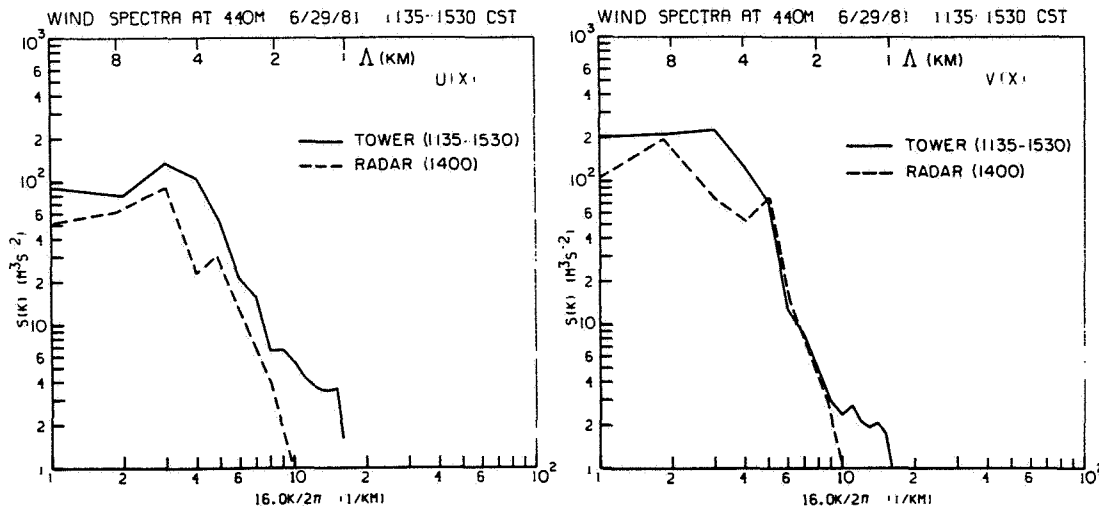


Figure 1.9 Comparison of wind spectra measured by tower instruments and radar. Spectra are for scales Δ along the direction of the mean wind.

(which is used to subtract out the motion of the aircraft from the lidar measured radial velocities) may have caused the lidar measured winds to oscillate about the actual mean winds.

In order to test whether the different vertical resolutions of the sensing systems may have been the cause of differences in the estimated wind profiles, we constructed comparable wind profiles from the lidar and radar data. This was done using radar data as close as possible to the radars to construct a wind profile with the highest vertical resolution possible. Data about a 20 km range were used to construct a wind profile, because ground clutter overwhelmed air velocity data from closer ranges. The vertical resolution of the radars at this range is approximately 280 m. Wind profiles at 20 km range were constructed by finding a representative velocity value for each elevation angle at range 20 km. The representative velocity was calculated by finding the modal velocity (the average was found to be biased towards zero due to ground clutter effects) for the data points in a 4 km x 10° sector. Hence, two radial velocity profiles were constructed (one from each radar) using 1330 tilt sequence data. Assuming horizontal homogeneity, we synthesized these two profiles arriving at mean wind speed and direction profiles.

The lidar profile was altered for better comparison by taking a vertical average of the trend-removed profile (valid at 1330 CST) over a 280 m vertical distance centered at the heights where radar data were available. Even with the same vertical resolution there were still differences as large as $1.8 \text{ m}\cdot\text{s}^{-1}$ in wind speed and 18° in wind direction (Fig. 1.10). Thus, we concluded that the different vertical resolution of the systems cannot explain the large differences between the lidar-detected and the radar-detected wind profiles.

We then turn to the possibility of an error in either the lidar system or in the aircraft's INS. Looking at Fig. 1.4 it is evident that winds measured by the lidar between 1300-1330 CST had a more westerly component and were

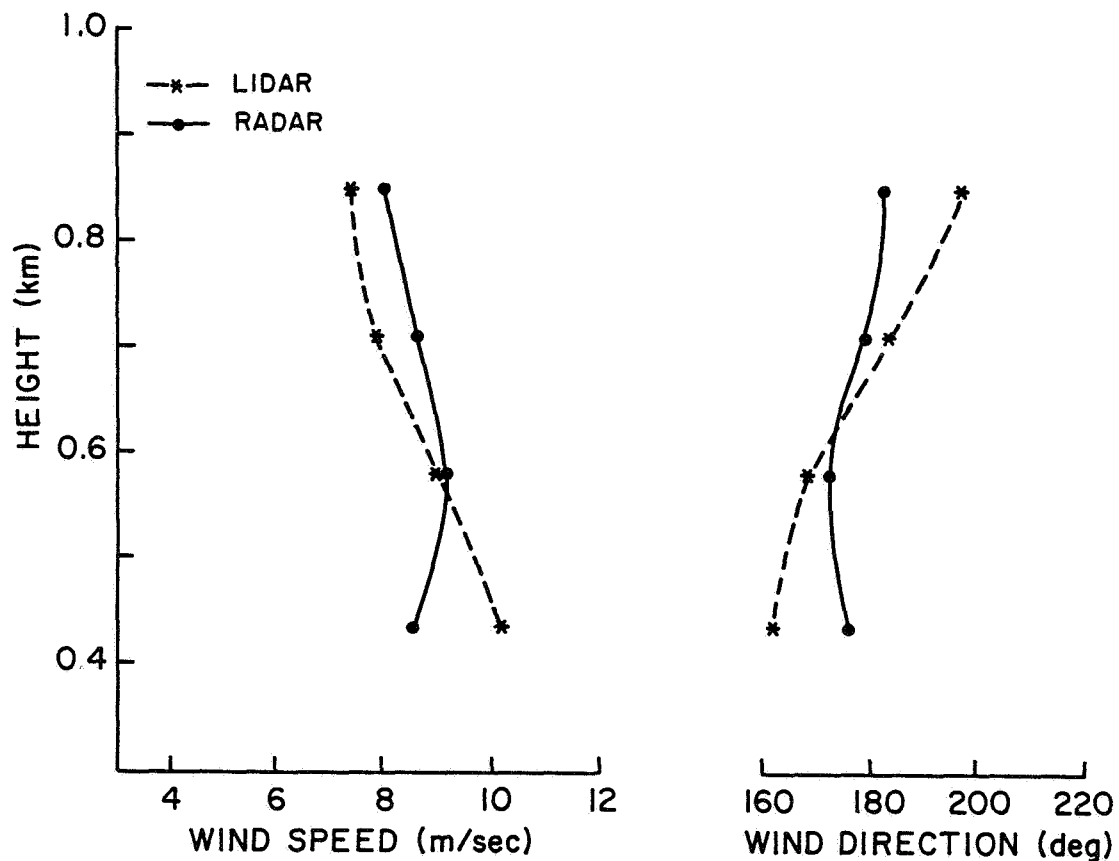


Figure 1.10 Trend removed lidar wind profile valid at 1330 CST (averaged over a 280 m depth) and radar wind profile (vertical resolution 280 m) at 1330 CST.

lighter than winds measured by the radars. Between 1330-1400 CST the lidar measured winds had a more easterly component and were stronger than winds measured by the radar.

To investigate reasons for this apparent bias of the lidar winds, we calculated the correction that had to be added to the forward and aft radial velocities to make the lidar and radar-measured winds consistent. The corrections to the forward and aft radial velocities that were needed at different times throughout the hour of data collection are given in Table 1.2. Unexpectedly, it was found that in all cases the correction needed was nearly the same for both forward and aft radial velocities. The only wind vector that could cause equal addition to both radial velocities is a vector perpendicular to the aircraft path. Hence, we plotted the corrections perpendicular to the aircraft track vs. time, setting corrections to the west negative and to the east positive (Fig. 1.11). Also plotted in Fig. 1.11 is a sinusoidal wave with amplitude $4 \text{ m}\cdot\text{s}^{-1}$ and period 84 minutes, the period associated with the Schuler resonance, which is an inherent source of error in an INS (Frye, 1958; Britting, 1971). The calculated corrections follow this curve remarkably well.

TABLE 1.2

Corrections that needed to be added to forward and aft radial velocities to make the lidar measured mean wind consistent with the radar measured mean wind.

<u>Time</u>	<u>Correction</u>		<u>Aircraft Heading</u>
	<u>Forward</u>	<u>Aft</u>	
1300 CST	-1.45 m/sec	-1.87 m/sec	20°
1310	+4.75	+4.27	205°
1320	-2.75	-2.81	20°
1330	+2.49	+2.09	200°
1340	+1.50	+1.72	25°
1350	-2.67	-2.63	200°
1400	+3.52	+3.48	25°

To support the possibility of a Schuler resonance, we examined photographs that were taken from the aircraft every 10 seconds looking

straight down. We were able to locate certain landmarks found on the ground and compare these locations with that given by the INS. We found that the aircraft location given by the INS was consistently offset by ~15 km to the northeast of its actual location (Fig. 1.12). When this offset was removed, we found that the actual positions of the aircraft oscillated about the INS locations in a way consistent with the position curve (integral of the velocity curve) associated with the Schuler resonance shown in Fig. 1.11. Table 1.3 is a comparison of position errors of the INS (after the offset was removed) vs. the estimated position error due to the Schuler resonance. We zeroed the difference of data in the first of Table 1.3.

The agreement seen in Table 1.3 corroborates the evidence presented earlier, leading us to believe that a Schuler resonance of the aircraft's INS caused the subtraction of erroneous components of the aircraft's ground-relative velocity vector from the lidar measured forward and aft radial velocities resulting in errors in the synthesized mean wind speed and direction. Furthermore, the maximum position error of the Schuler resonance shown in Fig. 1.11 is 3.2 km (disregarding the offset position error which may be due to other sources) after 4 hours of flight from California and is well within the stated accuracy of the INS of 3.2 km per hour of flight (NASA, 1979).

TABLE 1.3

Difference between actual and INS positions compared with estimated difference due to the Schuler resonance from Fig. 1.11.

Time	Actual Position Error Estimated From Photos	Position Error Estimated From Schuler Resonance
1358 CST	+0.7 (km)	+0.7 (km)
1338	-3.1	-3.0
1320	-0.6	-1.6

1.6. COMPARISON OF DATA COLLECTED ON JULY 2, 1981

On July 2, 1981, the CV-990 aircraft circled the Norman Doppler radar at a range of about 50 km, at 1.1 km height (Fig. 1.13) in a counter-clockwise direction. This was done so that the Airborne Doppler Lidar System (ADLS),

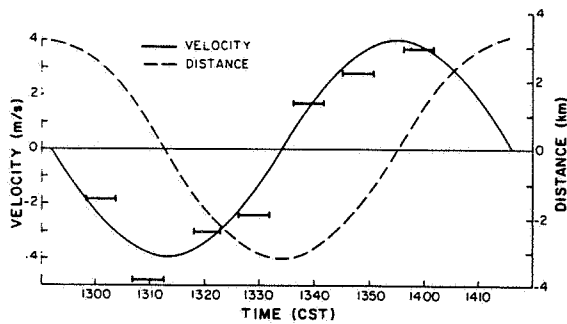


Figure 1.11 Plot of aircraft movement (undetected by the INS) perpendicular to the aircraft heading vs. time. Velocities and distances to the northwest are negative and to the southeast positive.

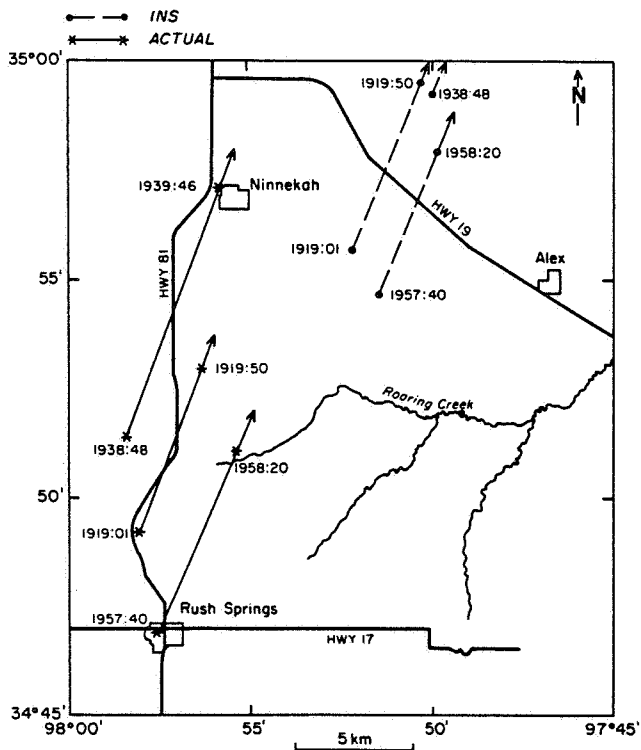


Figure 1.12 Map showing difference between actual aircraft location and INS indicated location.

which was located on the left side of the plane, could collect data on the side of the plane nearest to the radar where Doppler radar velocity estimates were not contaminated by echoes of the plane. The lidar-instrumented aircraft collected data from 1353-1438 CST, while the plane was flown in a one and one half circle around the Norman Doppler radar.

During this time, data were also collected in two different modes by the Doppler radar as it tracked the aircraft. Data were collected in the time series mode from 1350-1439 CST (i.e., in-phase and quadrature-phase echo samples at 16 range gates are recorded) and in the pulse pair mode (i.e., real time estimates of radial velocity are made by the pulse-pair processor and recorded in addition to the echo samples of I and Q) from 1423-1439 CST. However, the pulse pair velocity estimates were found to be in error because of contamination by overlaid echoes and thus were not used for this comparison.

A rawinsonde was released at 1150 CST on this date from Tinker Air Force Base, located 30 km NNE of Norman. The wind profile in the lowest 2 km of the atmosphere as detected by the rawinsonde is shown in Fig. 1.14. Wind measured

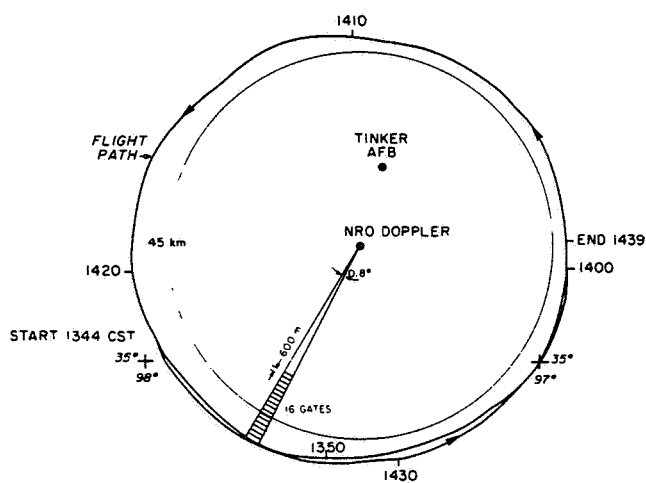


Figure 1.13 Flight path of the ADLS on July 2, 1981. Tinker AFB is the rawinsonde release site.

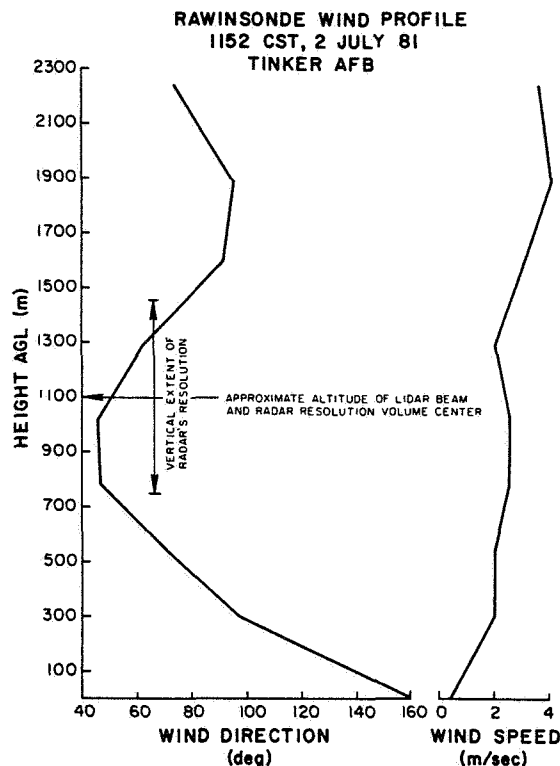


Figure 1.14 Wind profile as detected by rawinsonde at 1152 CST July 2, 1981.

by the rawinsonde at the height at which data collection by the lidar and radar was made, was approximately $2 \text{ m}\cdot\text{s}^{-1}$ from 55° .

In order to compare data from the lidar and radar, lidar data from the forward and aft-pointed beams were interpolated to separate (but commonly located) Cartesian grids using a Cressman weight with radius of influence of 500 m (Cressman, 1959). The radial velocities of the two grids of data were then vectorially combined to determine wind speed and direction, and then the component of this wind towards the radar was computed. All lidar data within a 2° azimuthal sector from the radar were then averaged, and assumed valid at the mid-point, to enable comparison with the radar data.

The radar-measured radial velocity values were determined from averages of 100 Doppler spectra (Fig. 1.15). Spectra at the same range were averaged over an azimuth sector of approximately 10° (~20 seconds of data) and the peak of this average spectra was used as the radial velocity value representative for that azimuthal sector at that range. The width σ (the square root of the second moment) of the Doppler spectra is 2 m s^{-1} . However, this should not be taken to be indicative of the velocity fluctuations within the beam because

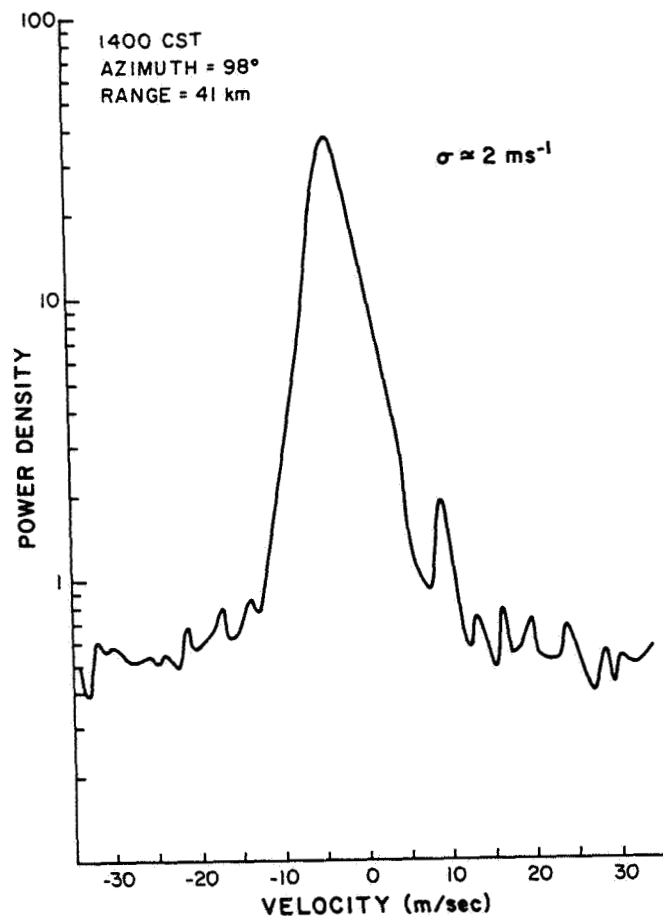


Figure 1.15 Example of an average of 100 Doppler velocity spectra showing approximate 20 dB signal-to-noise ratio in the spectral power densities.

window bias needs to be removed (Waldteufel, 1976). The velocities in sixteen sector volumes (spaced 600 m in range) were then averaged together to arrive at a mean radial velocity for a volume approximately 10° (azimuth) by 10 km (range) by 0.7 km (vertical).

Winds derived from the aircraft's INS were also available every minute during the time the aircraft was flown. The component of the INS-derived winds towards the radar was used for intercomparison.

Fig. 1.16 is a plot of the radial velocities from the three different sensors through a full 360° arc about the Norman Doppler radar. The points are connected for visual clarity and do not represent interpolation. The lidar and INS-derived winds have both been converted to radial velocities towards the radar so that these winds can be compared to the radial velocity estimates made with the Doppler radar. The mean wind detected by the three sensing systems is approximately out of the east at 5 m s^{-1} .

Although we can expect deviations about the sine wave because of non uniformities in the wind field, Fig. 1.16 shows that the deviations found in any one sensor's velocity estimates are not consistent with those found in

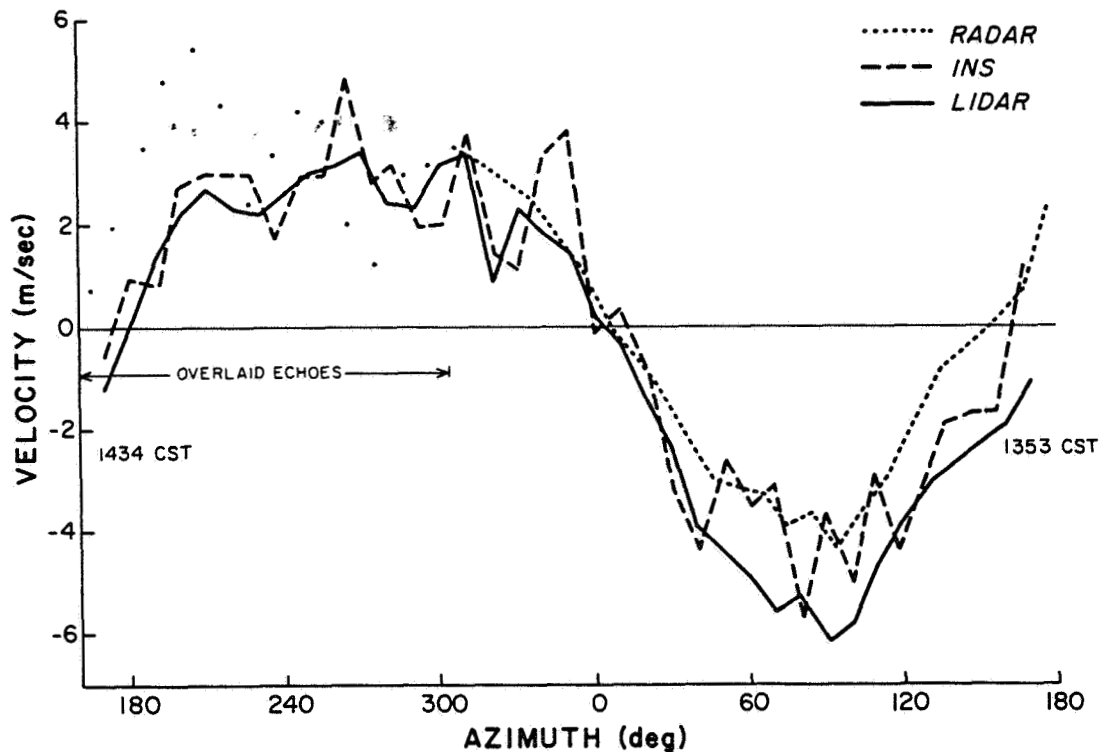


Figure 1.16 Comparison of radial velocities detected by radar, lidar, and the aircraft's INS.

either of the other sensors' estimates over more than a few tens of degrees. Possible reasons for this disparity between sensors are numerous. For one, the Doppler radar velocity estimates are inconsistent and biased between 180° - 300° due to overlaid second trip echoes (Doviak and Zrnic', 1984) of storms that were 100-180 km west of Norman (Fig. 1.17). The apparent departure of the radial velocities from a sine curve expected for uniform wind (e.g., velocities in the azimuthal sector $180 - 0$ deg. reach values about 3 m s^{-1} whereas velocities in the sector $0 - 180$ deg. reach a peak value of about 4 m s^{-1} for the radar and INS data and almost 6 m s^{-1} for the lidar data), measured by all of the sensing systems could be due to perturbations in the wind field caused by storms which were 50 km west of the data collection circle. Furthermore, the resolution volume over which the radial velocities are estimated differs vastly for the lidar and radar measurements. The INS measurements are point values smoothed by the response of the aircraft. And finally, the lidar measures the velocity of air weighted by the reflectivity distribution of aerosols, whereas the radar measures air velocity weighted by the reflectivity distribution of refractive index irregularities or by insects, if they contribute to target reflectivity.

ORIGINAL PAGE IS
OF POOR QUALITY

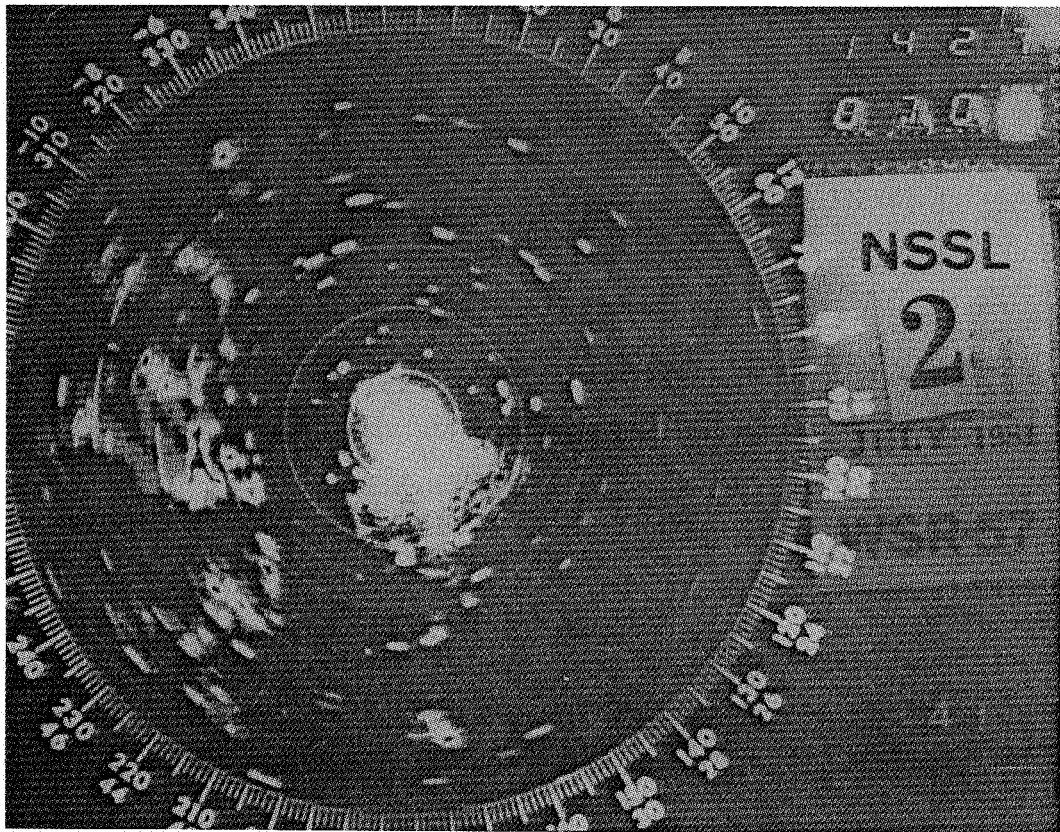


Figure 1.17 Photo of NSSL's WSR-57 radar display (1427 CST, July 2, 1981) depicting storms to the west which caused second trip echoes in the Doppler radar data. Range rings are spaced 40 km.

It can be seen from Fig. 1.16 that the INS-derived radial velocities tend to fluctuate more than either the lidar or radar radial velocities, possibly because the INS velocities are point measurements whereas the lidar and radar velocities are averages (over an azimuth sector of about 2° and 10° respectively). The obvious bias between lidar and radar radial velocities between 0° and 180° could be possibly related to a Schuler resonance of the aircraft's INS, as was found in the lidar data collected on June 29, 1981.

1.7. CONCLUSIONS

A major objective of this experiment was to compare data from NASA's airborne Doppler lidar and NSSL's dual Doppler radar system. Discrepancies in the mean wind and wind profile detected by the different sensing systems were explained as being caused by a Schuler resonance of the aircraft's INS, which caused an erroneous component of the aircraft's ground-relative velocity vector to be subtracted from the lidar-measured velocities. Furthermore, it is believed that these errors were as large as $4.5 \text{ m}\cdot\text{s}^{-1}$ due to the lengthy time that the aircraft was in flight before collecting data.

Standard deviation of velocity fluctuations measured by the lidar and radar compared well, as did spectra of the velocity fluctuations of lidar, radar, and tower data. Thus, it is concluded that the lidar and radars are accurate enough to map velocity perturbations in the clear-air boundary layer.

Finally, it is concluded that NASA's airborne Doppler lidar system is capable of measuring wind fields in the clear air environment on a smaller scale than was previously available. An improved version of the airborne Doppler lidar system will be used to conduct research flights in the future. This improved lidar system will incorporate changes designed to correct all of the major error sources encountered in the flights conducted in 1981. Accelerations of the aircraft, which are not detected by the INS (such as a Schuler resonance), will be accounted for by alternately pointing the lidar beam below the horizon so that ground returns can be observed and their apparent Doppler velocities removed in later analysis. This system will be used to observe regions surrounding convective phenomena which at present is not possible using conventional Doppler radars. The airborne Doppler lidar system will be especially useful when used in conjunction with Doppler radars because radars are capable of mapping the wind field inside a convective storm whereas the lidar maps the wind field just outside the storm. This should give us a better insight into convective phenomena. The airborne Doppler lidar system

will also be useful to examine turbulence and waves in the clear air planetary boundary layer, especially near the capping inversion where few observations have been conducted.

PART II: THE STRUCTURE OF THE CONVECTIVE ATMOSPHERIC
BOUNDARY LAYER AS REVEALED BY LIDAR
AND DOPPLER RADARS

ABSTRACT

The turbulent structure of the convective atmospheric boundary layer, based on the analyses of data from the instrumented NSSL-KTVY tower, airborne Doppler lidar, and ground-based Doppler radars, is presented. The vertically averaged winds over the baroclinic boundary layer agree well with those for a barotropic atmosphere supporting the hypothesis of Arya and Wyngaard (1975) that vertically averaged winds are insensitive to baroclinicity. The computed momentum flux profiles are affected by baroclinicity. The momentum flux profiles deduced from wind measured with radar agree well with those numerically predicted. Application of the assumptions that measured wind equals the geostrophic wind V_g at levels above the inversion and that the V_g profile is linear yields surface pressure gradients consistent with those estimated from a network of pressure sensors. Horizontal wind spectra from lidar, radar, and tower data compare well with each other in shape and magnitude. A consistent peak near 4 km in all the computed spectra might have been caused by horizontally symmetric cells with a horizontal wavelength 4 times the boundary layer height as shown in Kuettner (1971) for the case of weak wind shear.

2.1. INTRODUCTION

Our present knowledge of the structure of the convective atmospheric boundary layer comes mainly from the results of numerical models (Deardoff, 1972, Wyngaard, *et al.*, 1974). Although data from the Wangara expedition (Clarke, *et al.*, 1971) and the Minnesota boundary layer experiment (Izumi and Caughey, 1976; Kaimal, *et al.*, 1976) confirm some of the numerical model predictions, there is still an urgent need for observational studies on the convective atmospheric boundary layer (ABL).

Results on the structure of the convective ABL based on the analyses of data from the instrumented 444 m NSSL-KTVY tower, airborne Doppler lidar, and ground-based Doppler radars will be presented here. A brief description of the NASA airborne Doppler lidar system and the NSSL Doppler radars is given in Appendix A.

The data collected on June 29, 1981 were found to be especially suitable for the study of the convective ABL structure. The skies during this data collection period were mostly clear and void of precipitation targets. Also, there was a well-defined inversion lid for making a reliable estimate of the height of the convective ABL, which is an important scaling length for the generalization of observational results on ABL structure.

2.2. DATA COLLECTION

On June 29, 1981 the lidar-instrumented aircraft was flown in oblong "race tracks" (Fig. 1.2 of Part I) and data collected for the intercomparison experiment described in Sect. 1.2 is used here to deduce the kinematic structure of the ABL. The radar data were collected simultaneously as described in Section 1.2 and data from the instrumented NSSL-KTVY tower, located about 39 km north of Norman, were also collected throughout June 29, 1981. A rawinsonde was also released at 1150 CST on this day from Tinker Air Force Base which is located approximately 30 km north-northeast of Norman.

2.3. DATA ANALYSIS

Data from the radars, lidar, and tower were edited to screen out data that were obviously erroneous. Editing was done using signal-to-noise ratio, spectral width, and reflectivity thresholds, if data at a point exceeded any

of these thresholds, they were discarded. The Doppler radar data were also edited along a radial to remove erroneous data due to anomalous targets such as aircraft and birds. This edit procedure is fully described by Eilts (1983).

2.3.1. Construction of the Wind Profile

An observed wind profile (Fig. 2.1) was constructed using tower data below 444 m and dual Doppler radar data from 500 m up to 2 km. Lidar data were not used in the construction of the wind profile because of the errors in the mean wind detected by the lidar, possibly due to a Schuler resonance of the aircraft's INS which caused erroneous components of the aircraft's ground relative motion to be subtracted from the measured radial velocities (see Part I). The Cartesian coordinate system was rotated such that the x-axis and the u-component of wind were aligned along the direction of surface wind and the y-axis and v-component of wind were 90° counterclockwise to the surface wind. The mean wind data from the tower represent a time average of the data

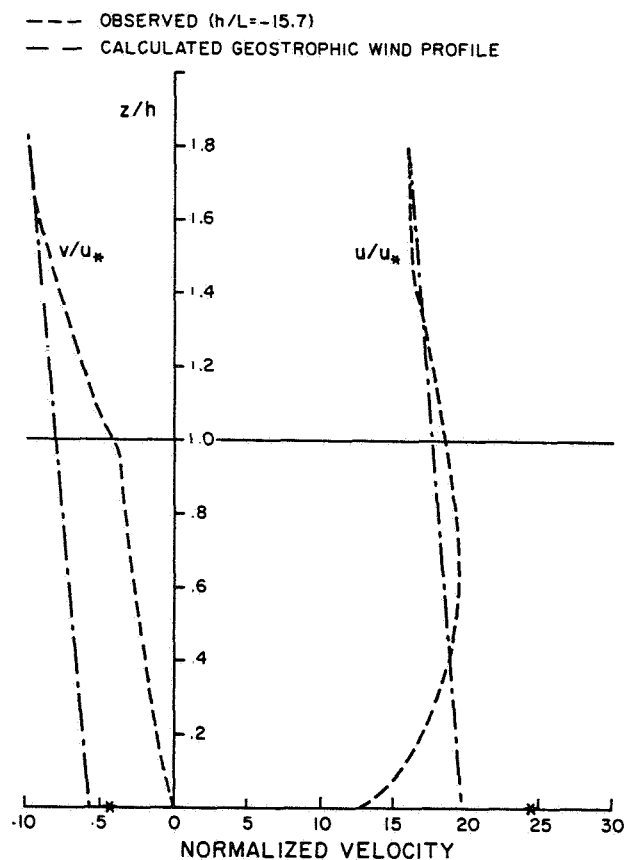


Figure 2.1 Observed wind profile and estimated geostrophic wind profile. The asterisks at the surface denote the surface geostrophic wind components estimated from surface pressure gradients.

collected between 1320-1335 CST, while those from the dual Doppler radars represent a space average of 1330 CST tilt sequence data that had been interpolated to 20 x 20 km grids placed every 250 m from 500 m up to 2 km. The geostrophic wind profile is calculated using the methods described in section 2.4.2 under the assumption that it is linear with height and equals the observed wind above (z=2 km) the inversion.

2.3.2. Calculation of Velocity Spectra

Spectra of the longitudinal and transverse components of wind were calculated from the tower, radar, and lidar data. Spectra were calculated from the radar data by interpolating the data to a series of 32 grid points spaced 500 m apart. After the mean and trend were removed, Fourier analysis was done to resolve wavelengths between 1 and 16 km. Thirty-two spectra were averaged to give the spectra shown in Fig. 2.2.

Spectra from the lidar data were calculated in a similar way by interpolating data to a series of 32 grid points aligned along the flight path. Six spectra were averaged to yield the spectra shown in Fig. 2.3.

Spectra from the tower data were calculated assuming Taylor's hypothesis. A series of 32 grid points spaced at 500 m was aligned along the direction of the mean wind, and data were interpolated to the grid points by assuming that all of the data were advected with the mean wind at 444 m. Four spectra were averaged to give the spectra shown in Fig. 2.4.

2.3.3. Determination of Micrometeorological Parameters

The tower data collected enabled us to determine u_* the friction velocity, $Q_0 = (\overline{w'\theta_V'})$ the surface kinematic heat flux, and hence L the Obukhov length. Estimation of these parameters is necessary for comparing our observational results with numerical model results.

The surface kinematic heat flux Q_0 was estimated using a technique described by Sundara-Rajan *et al.*, (1984) for highly convective conditions. This technique (Appendix B) is based on the assumption that the normalized vertical velocity variance remains constant between the levels 0.2h and 0.6h where h is the height of the convective ABL -- an assumption adequately supported by observations of the convective ABL over horizontally homogeneous sites (Kaimal *et al.*, 1976). Sundara-Rajan *et al.*, (1984) found that this method gives reliable estimates of the average surface heat flux even over an

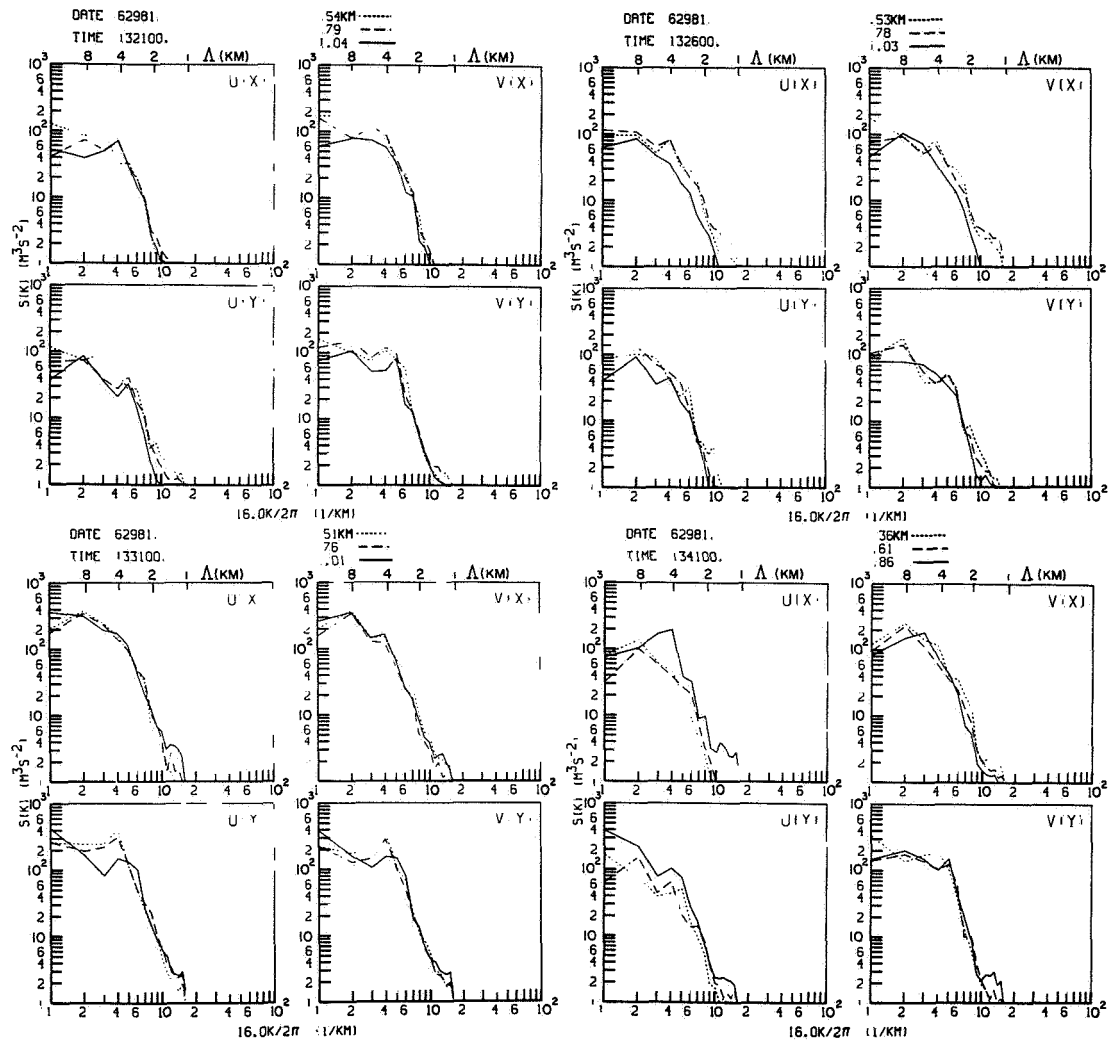


Figure 2.2 Spectra of horizontal wind velocity fluctuations from radar data.

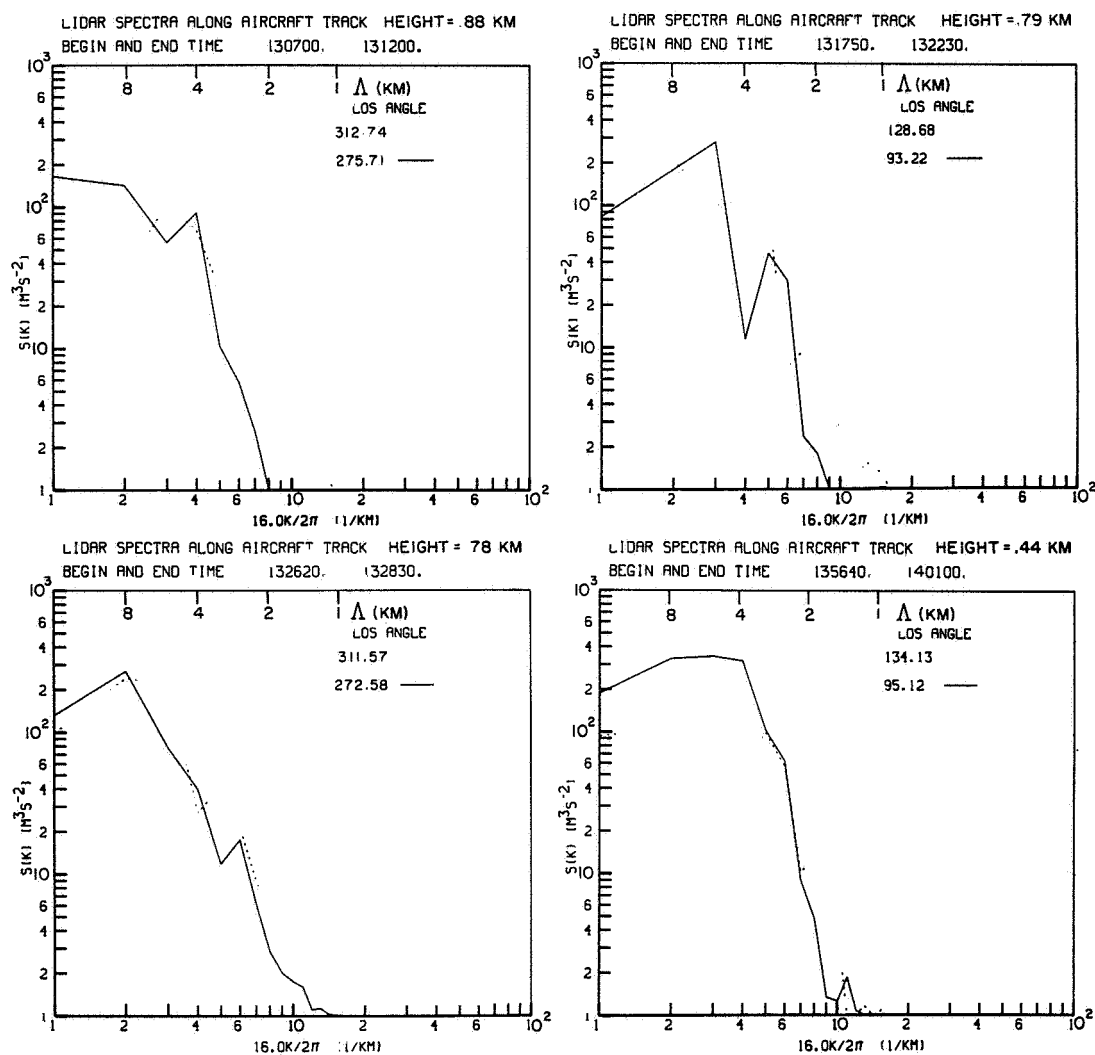


Figure 2.3 Spectra of horizontal wind velocity fluctuations from lidar data. LOS angle is the line-of-sight angle of the lidar beam. The two spectra represent data from the forward and aft looking beams.

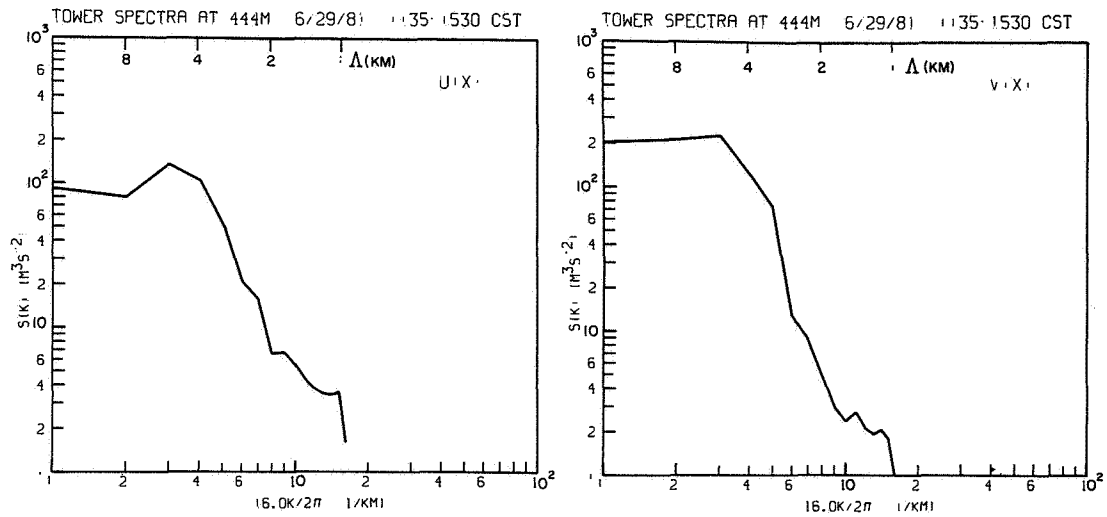


Figure 2.4 Spectra of horizontal wind velocity fluctuations from tower data.

inhomogeneous urban area like Oklahoma City. Thus, it is straightforward to compute Q_0 from the vertical velocity variance (w'^2) and the height (h) of the convective ABL using the assumption that

$$\frac{\overline{w'^2}}{w_*^2} = 0.39 \quad (2.1)$$

where w_* is the convective scaling velocity given by $w_* = (\beta h Q_0)^{1/3}$ where $\beta = g/\theta_0$ is the buoyancy parameter; g is the acceleration of gravity and θ_0 is the average virtual potential temperature of the surface layer. We had to resort to this indirect way of estimating Q_0 because the surface-layer temperature profile from the tower observations was not sufficiently accurate for the "profile" method (Appendix B).

The friction velocity u_* , used as a scaling parameter for our horizontal wind, was computed using an iterative technique assuming the following Businger-Dyer wind profile (Businger et al., 1971; Businger, 1973) for the convective surface layer:

$$\bar{u} = \frac{u_*}{k} [\ln(z/z_0) - \psi(\xi)] \quad (2.2)$$

where $\xi \equiv z/L$ and z_0 is the roughness scale. Eq. (2.2) was applied to the lowest levels (7 and 26 m) of the tower, yielding

$$\overline{u}_2 - \overline{u}_1 = \frac{u_*}{k} [\ln(z_2/z_1) + \psi(\xi_1) - \psi(\xi_2)] \quad (2.3)$$

where $\overline{u}_2 - \overline{u}_1$ are the mean wind speeds at the heights of z_2 and z_1 respectively. The function ψ is given by

$$\psi = 2 \ln [(1 + x)/2] + \ln [(1 + x^2)/2] - 2 \tan^{-1}(x) + \pi/2$$

where $x = (1 - 15\xi)^{1/4}$ and ξ_1 and ξ_2 are equal to z_1/L and z_2/L respectively. The von Karman constant k is assumed to be equal to 0.35 in accordance with Businger et al., (1971). Eq. (2.3) was used iteratively, starting with the assumption that $\psi(\xi_1)$ and $\psi(\xi_2) = 0$ (neutral stability). Approximately 10-15 iterations were needed for convergence. The Obukhov length $L = (-u_*^3/k\beta Q_0)$ was determined using the computed values of u_* and Q_0 .

The height h of the convective ABL was determined from the virtual potential temperature profile computed from the rawinsonde data (Fig. 2.5). For the two hours of data collection on June 29, 1981, the parameters were estimated to be:

$$Q_0 \approx 0.13 \text{ m s}^{-1}\text{K}, u_* \approx 0.42 \text{ m s}^{-1}, L \approx -70 \text{ m}, \text{ and } h \approx 1140 \text{ m}.$$

2.3.4. Estimation of Momentum Flux Profiles

From the observed wind and geostrophic wind profiles we can infer the profiles of momentum fluxes using the velocity defect equations:

$$f(V - V_g) = d \overline{u'w'} / dz \quad (2.4)$$

$$f(U_g - \overline{U}) = d \overline{v'w'} / dz \quad (2.5)$$

where f is the Coriolis frequency and U_g, V_g are the geostrophic wind components. These equations attribute the ageostrophic component of the wind to momentum flux gradients which are produced by turbulence in the ABL.

By integrating (2.4) and (2.5) with respect to z , using the boundary conditions $\overline{u'w'} = u_*^2$ and $\overline{v'w'} = 0$, at $z = 0$, we arrive at the equations for the momentum fluxes at height z

$$\overline{u'w'}(z) = \int_0^z f[V_g(z) - \overline{V}(z)]dz + u_*^2 \quad (2.6)$$

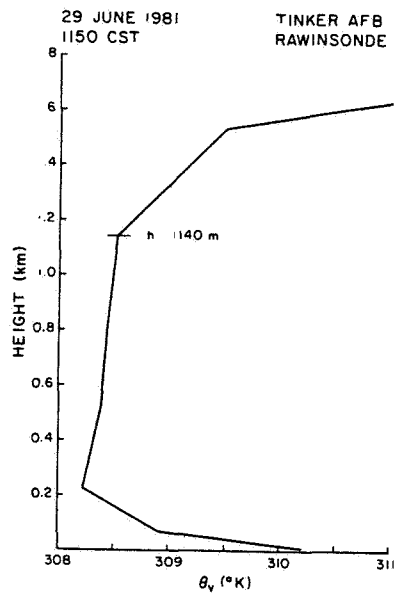


Figure 2.5 Virtual potential temperature profile from rawinsonde data showing the height of the capping inversion.

$$\overline{-v'w'}(z) = \int_0^z f[U(z) - U_g(z)]dz \quad (2.7)$$

Equations (2.6) and (2.7) were used to calculate the momentum fluxes at 100 m intervals through the ABL.

2.4. RESULTS

2.4.1. Vertically Averaged Winds

Using the observed wind profile, a vertical average over the whole ABL was computed for both components of wind. According to the hypothesis of Arya and Wyngaard (1975), the vertically averaged wind through the convective ABL can be regarded as independent of baroclinicity. To test this hypothesis, we also computed the vertically averaged wind components for the barotropic, convective ABL using the following relations for the similarity functions A_i and B_i given by Arya (1977) based on the results of some recent, sophisticated numerical models for the convective ABL.

$$A_i = \ln(-h/L) + \ln(fh/u_*) + 1.5 \quad (2.8)$$

$$B_i = k(fh/u_*)^{-1} = 1.8(fh/u_*) \exp(0.2h/L) \quad (2.9)$$

The similarity functions A_i and B_i are defined as:

$$A_i = \ln(h/z_o) - k \langle U_g \rangle / u_* \quad (2.10)$$

$$B_i = -k \langle V_g \rangle / u_* (\text{sign } f) \quad (2.11)$$

The values of A_i and B_i were first computed for the observed conditions of h/L , h/z_o , and fh/u_* were determined from equations (2.10) and (2.11). The vertically averaged wind components $\langle \bar{U} \rangle / u_*$ and $\langle \bar{V} \rangle / u_*$ were computed from the following relations for them derived from the velocity-defect equations (2.4) and (2.5):

$$\langle \bar{U} \rangle / u_* = \langle U_g \rangle / u_* \quad (2.12)$$

$$\langle \bar{V} \rangle / u_* = \langle V_g \rangle / u_* + u_*/fh \quad (2.13)$$

The vertically averaged wind components and their counterparts for the barotropic case are given in Table 2.1. The agreement between the two sets of values is good, supporting the hypothesis of Arya and Wyngaard (1975) that the vertically averaged winds over the convective ABL can be assumed to be independent of baroclinicity.

Unlike the vertically averaged winds, the vertical profile of wind is strongly affected by baroclinicity, as is evident from the numerical model results reported by Arya and Wyngaard (1975). Direct comparison of the observational results on the vertical wind profile with the results of Arya and Wyngaard (1975) could not be made because of the differences in the values of the baroclinicity parameters $M_{x_o} = \frac{h}{u_*} \left(\frac{\partial g}{\partial z} \right)_o$ and $M_{y_o} = \frac{h}{u_*} \left(\frac{\partial g}{\partial z} \right)_o$, and also the stability parameter h/L .

TABLE 2.1. Comparison of Vertically Averaged Winds

	$\frac{\langle U \rangle}{u_*}$	$\frac{\langle V \rangle}{u_*}$
Observed	18.2	-2.4
From similarity functions	18.0	0.0

2.4.2. Momentum Flux and Geostrophic Wind Profiles

For the estimation of momentum fluxes from equations (2.6) and (2.7), the geostrophic wind components at the surface and their variation with height should be known. The surface geostrophic wind was estimated from surface pressure gradients. The actual wind above the boundary layer at the highest level (2 km) measured by the radars was assumed to be equal to the geostrophic wind at that height; also the assumption of a linear variation of geostrophic wind with height was made. The computed momentum flux profiles are shown in Fig. 2.6. Also shown in the same figure are the momentum flux profiles computed from the higher order closure model of Wyngaard, *et al.* (1974) for a barotropic convective ABL. There is considerable disagreement between the two, and the momentum fluxes computed from the radar-detected winds (henceforth to be called "observed momentum fluxes") do not go to zero at the top of the boundary layer. This may well be due to the assumption of constant geostrophic shear as well as the difficulty of estimating correctly the surface geostrophic wind components from surface pressure gradients.

It can be seen from equation (2.7) that for $\overline{v'w'}$ to go to zero at the top of the boundary layer,

$$\langle U \rangle = \langle U_g \rangle \quad (2.13)$$

where the angle brackets denote the average over the whole boundary layer. Figure 2.6 shows clearly that this condition is not satisfied, indicating the possibility of inaccuracies in the computation of the geostrophic wind components.

Let us assume that the computed geostrophic wind components at the surface are accurate. It is not necessary to make any assumption regarding the

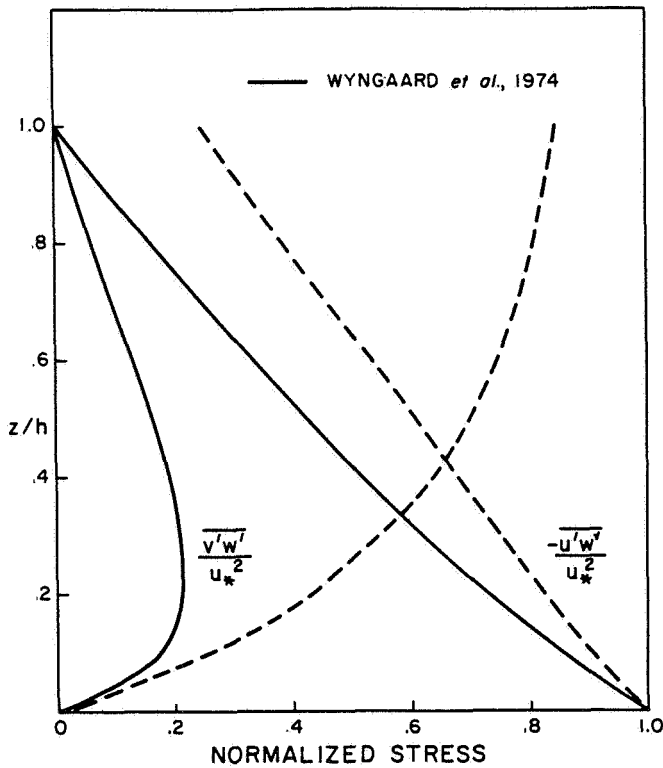


Figure 2.6 Momentum flux profiles (dashed lines) estimated from velocity defect equations using a geostrophic wind profile linear from the estimated surface geostrophic wind to the actual wind at 2 km. These flux profiles are compared to the numerical model results of Wyngaard, et al. (1974) for the barotropic, convective boundary layer.

geostrophic wind components above the top of the boundary layer if we make use of equation (2.3) and the following equation derived from equation (2.6):

$$\langle \bar{V} \rangle = \langle \bar{V}_g \rangle + u_*^2 / fh \quad (2.14)$$

for $\overline{u'w'}$ to be zero at the top of the boundary layer. But still the assumption of uniform geostrophic shear has to be made. As before, the momentum flux profiles could be computed from equations (2.6) and (2.7), and the results are shown in Figure 2.7. The agreement with the flux profiles reported by Wyngaard, et al. (1974) is better than that for Fig. 2.6. The observed momentum flux profiles show a shift to the right of the corresponding profiles for the barotropic case, as would be expected from the results of Arya and Wyngaard (1975) for the observed baroclinicity ($\partial U_g / \partial z = -6$ m/sec/km, $\partial V_g / \partial z = -4$ m/sec/km).

We can compute another set of momentum flux profiles without using the computed surface geostrophic wind components by assuming that the actual wind above the boundary layer at the highest level (2 km) detected by the radars equals the geostrophic wind at that height, together with the assumption of a linear variation of geostrophic wind with height. Figure 2.8 shows the computed momentum flux profiles based on these assumptions, and the agreement with the results of Wyngaard, et al. (1974) is much better, indicating that our assumption that the geostrophic wind equals the actual wind at the highest

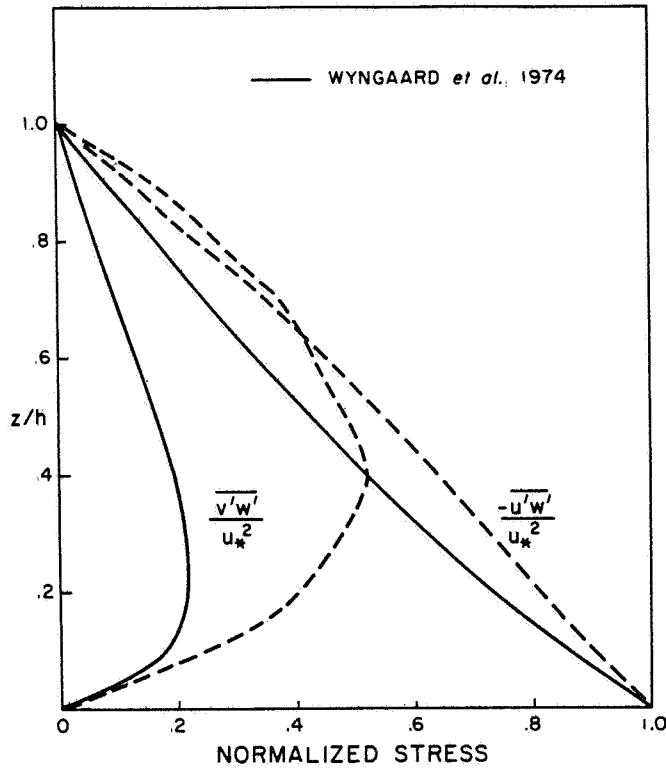


Figure 2.7 Momentum flux profiles computed using a geostrophic wind profile linear from the estimated surface geostrophic wind with the constraint that the momentum fluxes go to zero at $z = h$.

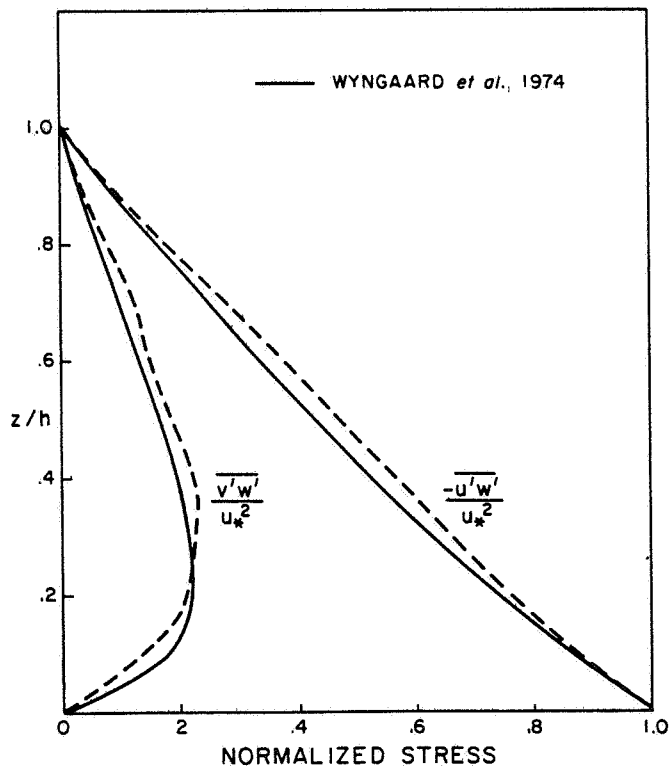


Figure 2.8 Flux profiles assuming a linear profile of geostrophic wind, for which the geostrophic wind equals wind at 2 km, and the constraint that the fluxes go to zero at $z = h$.

level measured by the radars may be fairly accurate. The slight shift of the observed momentum flux profiles to the right of the numerical model results is again in the correct sense for the observed baroclinicity.

2.4.3. Spectra of Horizontal Wind

Space and time averaged spectra from radar and tower (see Fig. 1.9 of Part I) compare very well both in magnitude and shape, as did the average spectra (averages of spectra along 6 lines 500 m apart) from radar and lidar-estimated wind fields (see Fig. 1.8 of Part I). A consistent peak, although weak, near 4 km wavelength can be noticed in Figures 2.2, 2.3, and 2.4. This peak was also noticed in horizontal wind spectra at different heights throughout the period of data collection, suggesting the prevalence of some time-consistent three-dimensional structure that is symmetrical in the horizontal directions with a horizontal wavelength of approximately 4 km. It is proposed that this three-dimensional structure is the result of symmetric cells that have a wavelength 4 times the boundary layer height ($h \approx 1140$ m during the period of this study), as shown by Kuettnner (1971) for the case of weak wind shear.

2.5. CONCLUDING REMARKS

The foregoing study of the structure of the convective ABL indicates that the vertically averaged winds over the boundary layer can be assumed to be independent of baroclinicity in accordance with the hypothesis of Arya and Wyngaard (1975). Our assumption that the geostrophic wind equals the actual wind measured above the top of the boundary layer along with a geostrophic wind profile that is linear throughout the boundary layer seems to yield momentum flux profiles which compare well with the numerical model prediction of Wyngaard, et al. (1974) and Arya and Wyngaard (1975). Likewise, this assumption yields surface geostrophic winds that are fairly consistent with those deduced from surface pressure gradients as can be seen in Fig. 2.1.

Spectra of the longitudinal and transverse components of the wind computed from lidar, radar and tower data compare well both in shape and magnitude. A consistent peak near the 4 km wavelength found in all the computed spectra is proposed to be caused by horizontally symmetric cells with horizontal wavelength 4 times the boundary layer height as shown by Kuettnner (1971).

This study has also demonstrated the feasibility of using the NASA airborne Doppler lidar system for observational studies of the structure of the clear air boundary layer.

PART III: DOPPLER LIDAR OBSERVATIONS IN
THUNDERSTORM ENVIRONMENTS

ABSTRACT

On 30 June 1981, the wind fields around a variety of convective clouds, ranging from large thunderstorm complexes to isolated cumulus congestus, were observed in some detail using an airborne Doppler lidar operated by the National Aeronautics and Space Administration (NASA). Despite the presence of errors caused by problems in sampling some of the aircraft attitude and motion parameters used in the data analysis, reasonably clear pictures of the main features of the flow fields near several clouds have been obtained.

Features of special interest seen in the lidar analyses are waves and vortices at the leading edge of a gust front marked by an arcus cloud formation, and secondary surges of outflow behind another gust front which was mostly free of clouds and rain at flight level. Observations from one of the NSSL mesonet stations overflown by the lidar aircraft in the vicinity of the arcus cloud serve to confirm the approximate location and character of the gust front at the surface depicted by the lidar analyses in that area. The storm system, which contained the gust front vortices, moved eastward, intensified and within one hour produced a damaging gust front tornado in Norman, OK.

Also seen by the lidar were clear air flows near the base and sides of an isolated cumulus congestus circumnavigated at two levels by the NASA aircraft. Prominent aspects of the observed flows near the isolated cumulus included 1 km-scale bands of enhanced convergence embedded in an overall pattern of convergence into the cloud region. These patterns were seen at both levels examined, 1100 m AGL (roughly at cloud base) and 2300 m AGL but must be regarded as suspect due to the presence of uncorrectable measurement errors associated with the navigation and aircraft motion sampling difficulties.

3.1. INTRODUCTION

The "Severe Storms Experiment" was designed specifically to study the clear air flows near convective clouds, especially those associated with severe thunderstorms, that might occur within range of one or both of the NSSL Doppler radars. Part III of this report concerns itself with the results of this experiment.

With the advent of Doppler radar systems, it first became possible to observe the internal wind flow patterns of convective storms in some detail (Lhermitte, 1970, Ray, *et al.*, 1975). However, in sampling air velocities at the edges of convective storms, the extremely small reflectivities in the "clear" air allow the much larger reflectivities of the adjacent storm, seen through the sidelobes, to contaminate Doppler measurements in the radar's resolution volume (Doviak and Zrnic', 1984), yielding radial velocity estimates which are biased toward storm-internal target motions. Furthermore, radial velocity estimates at low radar elevation angle and close range may also be biased (toward zero velocity) by ground clutter. At longer ranges, the sidelobe contamination and large radar resolution volume proportions can make it difficult to obtain adequately detailed pictures of the wind field near the edges of storms. In addition, storm features below cloud base are often shielded from the radar's view due to the earth's curvature when the storms are located beyond ranges of about 60 km (Doviak, *et al.*, 1979, Doviak and Zrnic', 1984).

Doppler lidars not only feature fine resolution with very compact sidelobes, but also can be designed such that range and Doppler velocity ambiguities will not be encountered in normal use. However, the infrared frequencies employed in many systems suffer significant attenuation during passage through moist air due to absorption by water vapor and carbon dioxide. Thus, Doppler lidars are well-suited to the task of detecting clear air winds outside of storm clouds, but can only probe short distances into the clouds, while Doppler radars perform best in the hydrometeor-rich environment within the clouds.

Although the wind field maps furnished by Doppler radars and radar arrays have been extremely helpful in revealing some aspects of the dynamics of severe storms, the limitations of such radars have prevented researchers from obtaining the definitive answers to many questions having to do with storm dynamics outside precipitation regions at cloud edge and cloud base.

For instance, better knowledge of the structure and interactions of thunderstorm inflow and outflow below cloud base and their implications with respect to production of damaging straight line winds, or of the amplification of vorticity during tornadogenesis, would be extremely useful to severe storm researchers and forecasters. While most severe storm investigators agree that the tilting and stretching of horizontal vorticity associated with vertical shear by differential rising motions and accelerations are of great importance in tornadic storms (Davies-Jones, 1982), there is still uncertainty regarding the impact on storm evolution of the many possible patterns of ambient vertical shear, buoyancy, and other parameters. Klemp and Wilhelmson (1978), using numerical simulation, have found storm evolution to be especially sensitive to the intensity and distribution of ambient vertical shear in the lower troposphere. Storms simulated by Weisman and Klemp (1982) exhibited behavior which appeared to be governed by the environmental value of a bulk Richardson Number relating buoyancy to vertical shear. Although direct verification of such simulations is accomplished using detailed observations, the results and conclusions drawn from them must be regarded as tentative.

With respect to more general questions regarding cumulus convection dynamics, a better understanding of the distribution of entrainment over the surfaces of convective clouds is eagerly sought by cumulus cloud modelers who continue to struggle with overly specific formulations which lack the desired general physical validity (Warner, 1970; Simpson *et al.*, 1982).

Although there has been little doubt of the existence of entrainment in cumulus clouds since the pioneering work of Stommel (1947), there has been considerable controversy over the relative importance of lateral versus cloud-top entrainment mechanisms. A number of authors (Morton, 1957, Turner, 1962; Squires and Turner, 1962) have presented theoretical models of cumulus updrafts which require lateral entrainment during the cloud's growing phase, and some workers (e.g., McCarthy, 1974) have found confirmation of the inverse-cloud-diameter dependence of the entrainment rate predicted by most of these models. However, others (Sloss, 1967) have been unable to verify this inverse relationship between cloud size and entrainment rate.

On the other hand, Squires (1958) and Fraser (1968) have proposed that a substantial proportion of total entrainment takes place through mixing at cloud top. Observational evidence in favor of their ideas has been obtained by Paluch (1979) and others. It seems likely that both lateral and cloud top

entrainment mechanisms work simultaneously on most convective clouds, though the relative importance of each as a function of cloud size, shape and stage of evolution remains an incompletely answered question.

Mounted aboard a Convair CV-990 jet aircraft, NASA's airborne Doppler lidar system (ADLS) not only offers good mobility but also fore-aft beam scanning during data collection so that differing views of wind features can be obtained. Retrieval of the full horizontal wind vector at a given point involves solution of two simultaneous equations, one from each of two different but well-defined line-of-sight views of the wind field at that point. As will be seen later, precise knowledge of aircraft attitude and motion is necessary in order to establish accurate estimates of the wind vectors.

It is the principal purpose of this study to see whether data collected by an airborne Doppler lidar system can provide useful insights into the wind flows near the edges and bases of a variety of convective clouds.

3.2. METEOROLOGICAL SETTING FOR THE EXPERIMENT

On 30 June, the second day of availability of the lidar, the morning meteorological situation in Central Oklahoma hinted at the possibility of strong thunderstorm activity late that day. A weak cold front had entered the northern part of the state the previous evening and had become quasi-stationary, lying roughly along an east-west line which meandered along the Kansas-Oklahoma border. McCaul (1985) gives a detailed description of the synoptic setting but we present here a few salient features.

The 1200 GMT (0600 CST) sounding from Oklahoma City (OKC) indicated unusually deep moisture with little or no capping inversion above the boundary layer. Winds were light and veered from south at the surface to northwest above the 50 KPA level, indicating a deep layer of weak warm advection. The sounding had not changed significantly by the 1855 GMT (1255 CST) launch time of a special rawinsonde from Tinker Air Force Base (TIK) where the lidar aircraft was stationed. Fig. 3.1 depicts the temperature, moisture and wind profile of the special TIK sounding. Of special interest in Fig. 3.1 is the presence of convective instability in lower layers; the lifted index of this atmosphere was about -3, and the convective available potential energy (CAPE) per unit mass for boundary layer parcels was about $1830 \text{ m}^2\text{s}^{-2}$. Precipitable water amounted to 5.08 cm. The convective temperature was estimated to be 29°C , which was just being reached at sounding time.

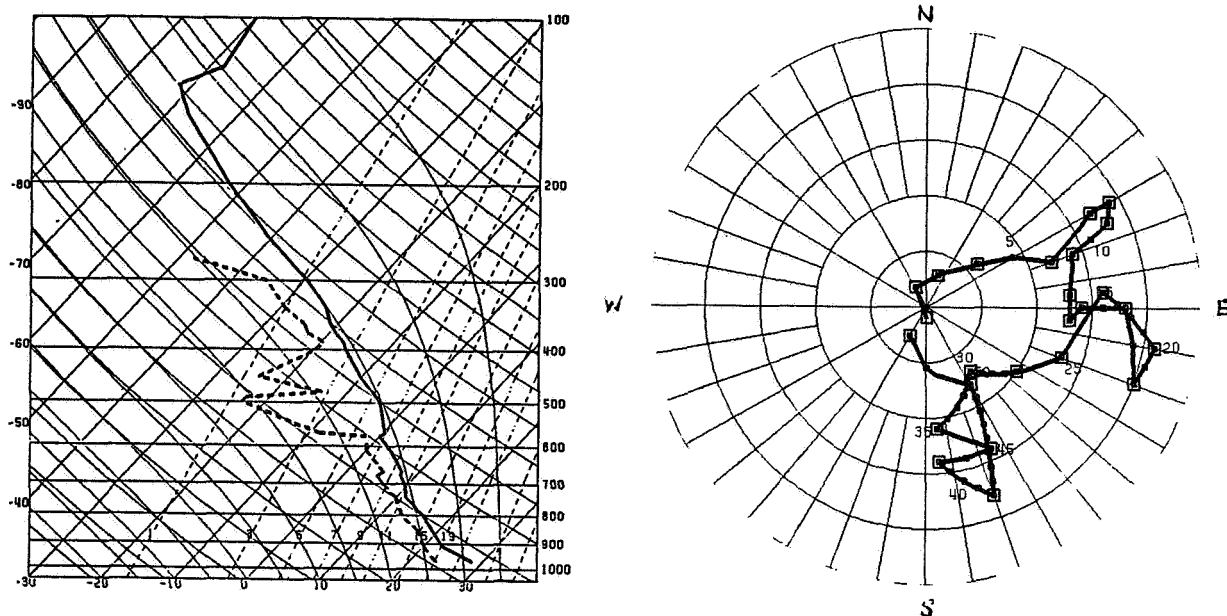


Figure 3.1 (a) Skew T-log p diagram; Tinker Air Force Base, 1855 GMT (1255 CST), 30 June 1981. (b) Hodograph of winds. Each circle represents 5 kt of windspeed and the numbers next to the curve give the altitude in thousands of feet above mean sea level.

The most striking feature of the wind profile is that at no point does the wind exceed 12 m s^{-1} (25 kt) in magnitude. There is a tendency for the shear vector, which always points parallel to the tangent to the hodograph itself, to rotate to the right with increasing altitude, at least in the lower half of the troposphere. Because of this shear vector rotation, tilting by updrafts of the horizontal vortex tubes, which lie everywhere perpendicular to the shear vectors, could in principle lead to production of the cyclonically rotating updrafts often seen in "supercell" storms (Browning, 1964; Barnes, 1968). In this case, however, the winds and shears were so weak that the production of rotating updrafts was likely to be inhibited by the inability of the shear to relieve the updrafts of sufficient amounts of condensed water load. Excessive water loading in storm updrafts is believed to be a major factor constraining the buoyancy and hence, presumably, also the persistence of storm updrafts (Lilly, 1979).

Around the time of the special TIK sounding, surface temperatures in many places in the state had risen above 30°C and deep convection was beginning west and southwest of Oklahoma City. At 2000 GMT (1400 CST) surface temperatures of 33°C were in southern Oklahoma at Ardmore, while a heavy thunder-shower was in progress at Ft. Sill (FSI) about 100 km to the southwest of

Norman, OK. Shortly before 2000 GMT it was apparent that the convection was becoming intense; thus, at about 2000 GMT the lidar aircraft departed TIK to collect data for the Severe Storms Experiment.

For the reasons mentioned earlier, the storms did not develop into classic supercells, but rather exhibited the characteristics of "multicell" storms (Byers and Braham, 1949). However, according to a report in STORM DATA for June 1981, one of the storms produced damaging winds and a brief gust-front tornado in Norman, OK, around 2120 GMT (1520 CST), and thus satisfied the National Weather Service (NWS) criteria for being "severe". According to OKC radar summaries, storm tops were observed to reach 60 kft (18.3 km), which seems consistent with the thermodynamic profile of Fig. 3.1 in view of the tropopause height of 47 kft (14.3 km).

3.3. DATA COLLECTION

The CV990 collected 15 runs of lidar data during its 30 June 1981 flight, which lasted from 1959 GMT (1359 CST) to 2244 GMT (1644 CST). Only runs 2 through 12 were used for this study because the other runs were taken before or between passes near convective activity. A map showing the flight track of the CV990 during the period when data runs 2 through 12 were being collected is given in Fig. 3.2.

Run 2 commenced at 2018 GMT (1418 CST) and run 12 ended at 2100 GMT (1500 CST). Thus, all the data used in this study were taken within a 42-minute period near the beginning of the flight.

The CV990 flew southwest toward the vicinity of Chickasha, OK, (CHK) immediately after takeoff, taking a preliminary run of data during ascent. By the time the aircraft started to approach Chickasha, several very strong thunderstorm cells had begun to develop in a loosely organized cluster just west and northwest of that City. Although the precipitation shafts were still distinct at this time, about 2015 GMT (1415 CST) outflow from the several cells was beginning to merge and move east-northeast behind a well-defined, nearly linear arcus cloud formation.

At about 2018 GMT (1418 CST) the CV990 veered toward the northwest to make a data-gathering run (run 2) along a flight track roughly parallel to this advancing quasi-linear outflow feature. The aircraft was flying at approximately 720 m above ground level (AGL) gathering data during run 2 which lasted more than 7 minutes. During this period the lidar scanned the arcus

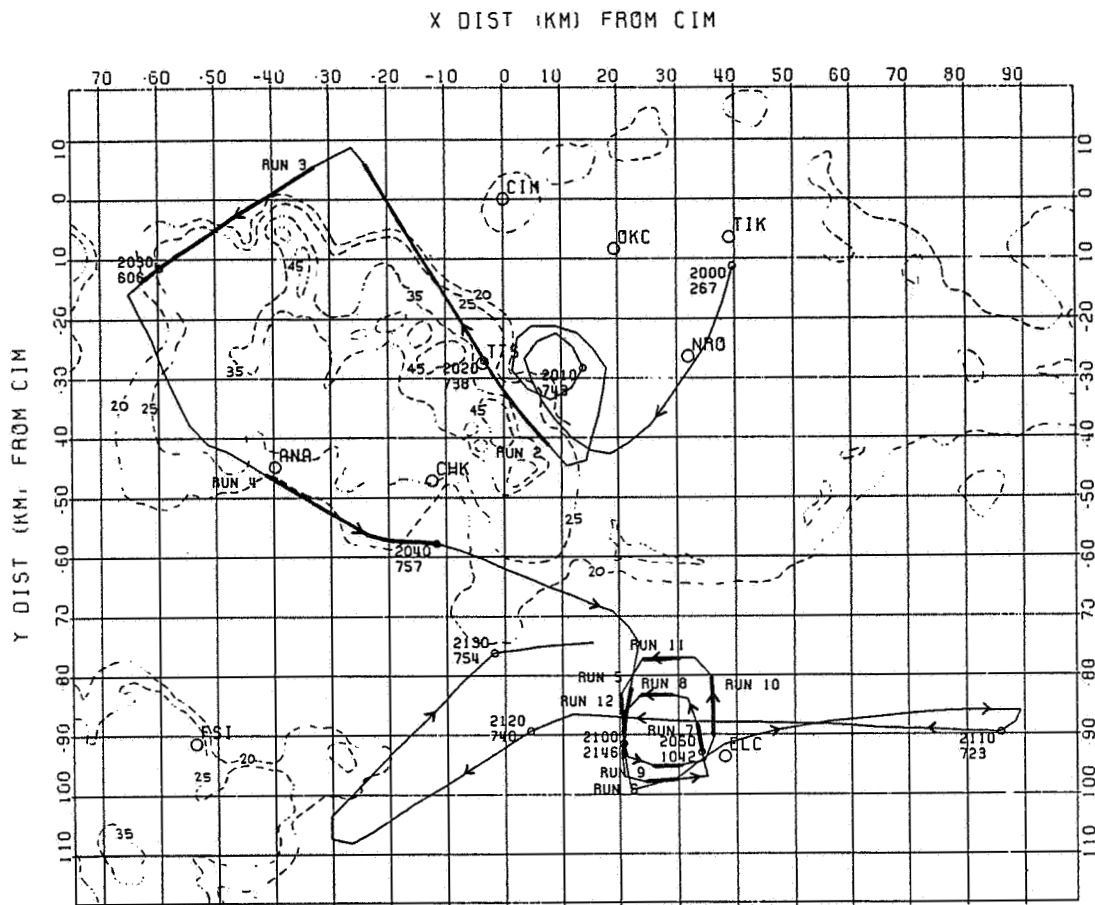


Figure 3.2 Flight track, NASA CV-990, 30 June 1981. Times (GMT) are shown every 20 min with aircraft altitude (AGL) printed just below the times. Radar reflectivities (dBZ) at 2037 GMT are shown in dashed contours.

cloud formation or the edges of heavy precipitation continuously, with laser frame duty cycles ranging anywhere from 1.25 s to 1.5 s.

Figure 3.3, one of a series of photographs (termed DF photos) taken by Dr. Dan Fitzjarrald on board the CV990 shows two things: (a) an isolated heavy thunderstorm rain core near Chickasha and (b) the arcus formation at the southern edge of another storm core to the northwest as viewed from the CV990 at about 2019 GMT (1419 CST).

Approximately 30 s after the time of Fig. 3.3, the CV990 came abreast of the arcus cloud formation surrounding the advancing edges of the northwestern storm. Judging from mission cloud photographs taken regularly from the aircraft at 1 s intervals and covering the lidar's scanning area, the base of the arcus cloud occasionally reached as low as an estimated 400 m above the ground. Although the mission cloud photos were useful in documenting the



Figure 3.3 Photo, looking southwest, ca. 201900 GMT (141900 CST), during run 2. Note rain core at center and arcus at right. Aircraft was moving toward the right.

cloud forms scanned by the lidar, they were unfortunately damaged somewhat during processing and thus were unsuitable for reproduction here. Nevertheless a DF photo taken just before 2020 GMT (1420 CST) and shown in Fig. 3.4 reveals the structure of the arcus formation as broadly lobed at a horizontal wavelength of about 300 m, with irregularities in the altitude of the cloud base. Other mission cloud photos show that the arcus cloud did not display an especially straight front edge, but rather meandered somewhat at scales of 3-5 km along its length.

At about 2020 GMT (1420 CST) the CV990 flew just southwest of Tuttle, OK, and within 1 km of one of NSSL's mesonet stations, Tuttle-South (TTS), which was operating at that time in support of the lidar experiments. Data from that station indicate the passage of a moderately strong gust front at about 2023 GMT (1423 CST), followed by heavy rain some 14 minutes later. These data are presented and discussed in Section 3.5.1.

By 2025 GMT (1425 CST) the CV990 had reached the northernmost edge of the developing convective complex, and thus commenced a 90° turn to the left to scan the northern edge of the storm. Run 3 of lidar data began at about 2026 GMT (1426 CST) and continued until just after 2030 GMT (1430 CST).



Figure 3.4 Photo, looking southwest, ca. 201930 GMT (141930 CST), during run 2. Note continuous, lobed arcus cloud in foreground, rain beyond it. Aircraft was moving toward the right.

Typical frame cycles in run 3 ranged from 1.22 to 1.50 s. At about 2027 GMT (1427 CST) the aircraft passed near the front edge of a bulging gust front which, judging from the orientation of the edge of the outflow as seen in the photographs and in the lidar analyses, was pushing toward the north and northeast. The aircraft, flying at an altitude of 550 m AGL, obtained a number of lidar velocity measurements at the edge of and just behind this gust front. In contrast to the well-defined arcus cloud previously seen on the east side of the storms and studied in run 2, this gust front was marked only by scud having a ragged, shredded appearance, often arranged in irregularly-shaped vertical filaments (Fig. 3.5).

The lidar aircraft began to pass out of the vicinity of the active convection just after 2030 GMT (1430 CST) as it continued toward the southwest. Consequently, at 2032 GMT (1432 CST) a left turn toward the southeast was made in order to fly along the back (or southwest) edge of the storm area.

Run 4 of lidar data was taken starting at 2036 GMT (1436 CST) and ending at about 2044 GMT (1444 CST) at altitudes ranging near 800 m and with frame cycles ranging from 1.12 to 1.40 s. Little or no outflow cloudiness was seen



Figure 3.5 Photo, looking south, ca. 202700 GMT (142700 CST), during run 3. Note presence of detached scud instead of arcus clouds. Aircraft was moving toward the right.

on the southwest side of the storms and only light rain was falling from an amorphous cloud base in that part of the complex. However, at 2039 GMT (1439 CST) the aircraft pulled away from this area of lingering light rain into an area of distinctly warmer air where cloud bases were noticeably better-defined, with bases at an estimated 1.5-2.0 km AGL. Sensors aboard the aircraft confirmed not only a 1°C ambient temperature increase, but also a significant 4°C rise in dew point. The location of this apparent boundary between rain-cooled and undisturbed air was about 12 km southwest of Chickasha. At this point, the CV990 turned briefly toward the east in order to obtain data closer to the retreating storms, then turned at 2040 GMT (1440 CST) back to the southeast to pass by the rear of another rain cell.

At about 2042 GMT (1442 CST) it was noticed that an isolated cumulus congestus was beginning to develop about 40 km to the southeast. Consequently, it was decided that several circumnavigations should be made of this new convective growth, which was centered about 10 km west of Elmore City, OK (ELC).

The CV990 approached the cumulus congestus from the north and began a square flight pattern at an altitude of about 1100 M AGL around the base of the cloud at 2046 GMT (1446 CST). Run 5 consisted of the data taken along the west side of the cloud as the aircraft headed south. Runs 6, 7 and 8 were taken on the other sides of the cloud after a succession of 90° left turns. Each run at the 1100 m level lasted an average of about 60 s.

Figure 3.6, a DF photo taken during run 7 while looking west toward the cumulus, reveals that the cloud tilted toward the south with height, suggesting the updraft was being subjected to a vertical shear which was northerly, at least through mid-height of the cloud.

At the conclusion of run 8 the CV990 was again at the northwest corner of the cloud, and the time was about 2052 GMT (1452 CST). The aircraft climbed as it headed south along the west side of the cloud in preparation for another circumnavigation at a higher level. An altitude of about 2300 m AGL had been attained when run 9 began at 2054 GMT (1454 CST) following a 90° left turn southwest of the cloud. Run 9 was taken as the aircraft headed east along the south side of the cloud, which could now be said to consist of a series of



Figure 3.6 Photo, looking west, ca. 205030 GMT (145030 CST), during run 7. Note towering cumulus being undercut and sheared off to south. Aircraft was moving toward the right.

contiguous towers oriented along a northeast-southwest line. Runs 10 through 12 were taken along the other edges of a square flight track around the cloud, each one lasting about 60 s average, as did runs 5-8. At the conclusion of run 12 the time was about 2100 GMT (1500 CST).

The towering cumulus did not develop into a thunderstorm; instead the uppermost parts of the turrets were observed to shear off toward the east and southeast before reaching the 10 km level, and no significant anvil cirrus formed.

3.4. DATA ANALYSIS

NASA furnished a data tape for the 30 June experiment which was to contain the following information:

- A. Header information regarding dates and times of each run,
- B. Position, attitude, groundspeed and heading information from the CV990 INS for each frame of each run,
- C. Aircraft altitude measured by down-looking radar during each frame,
- D. INS-derived wind vector at the aircraft for each frame of each run,
- E. Airspeed, ambient temperatures and dew points measured by the gust probe;
- F. Number of transmitted pulses per laser frame;
- G. COHO and VCO offset frequencies for each frame,
- H. Elevation angle of line-of-sight and positions of scanner wedges for each frame,
- I. Times and line-of-sight azimuths for each lidar frame,
- J. Raw Doppler velocities, echo intensities and spectral widths for each resolution volume along each frame,
- K. Edited and smoothed Doppler velocities and range-normalized intensities for each resolution volume of each frame;
- L. Smoothing coefficients used at each resolution volume of each frame. These were computed according to local data quality based on signal-to-noise considerations (Lee, 1981);
- M. Vorticity, divergence, stretching and shearing deformation of the flow at each resolution volume of each frame;

Upon inspection of the data from a number of runs, it was found that many of the data fields were either missing or erroneous, making it necessary to

ascertain whether or not the analysis of the data could be accomplished. The data that were missing, such as COHO and VCO frequencies, number of pulses per frame, pressure altitude, track angle and line of sight elevation, were either not critically important for the velocity analysis or were deducible from other given quantities. However, as discussed in Appendix A, the VCO frequency is an important parameter to record especially if the frequency is not tracking the Doppler shift associated with the measured air speed. The erroneous data, including such other important quantities as the corrected and smoothed lidar velocities and range-normalized lidar intensities, had to be recomputed anew from the raw data. Because the smoothing procedure (Lee, 1981) used by NASA was rather elaborate and would have been time-consuming to implement, a somewhat simpler approach to smoothing was ultimately taken, obviating the need to reconstruct the error-contaminated smoothing coefficient arrays furnished on tape.

Thus, it became necessary to perform a number of "check" computations of certain of the raw data fields in order to verify those given and obtain those missing. In the process of doing these computations, other errors in the data became apparent. In the following sections these errors and omissions and the techniques employed for correcting them are briefly mentioned. A complete discussion of the verification and correction techniques relevant to CV990 navigation data is given in Appendix C, while a similar discussion regarding verification and correction of the lidar moment data is given in Appendix D.

3.4.1 Navigation Data Review and Editing

Inertial navigation systems are subject to a variety of errors (Britting, 1971), one of which involves oscillations at the 84.4-minute Schuler period. INS velocity errors having amplitude of about 4 m s^{-1} and period near the Schuler period were discovered in the CV990 data and are described in Part I. Unfortunately, the approximately 30-minute long record of nadir photos which was available for the Severe Storms flight was too short to allow determination of whether or not Schuler periods were present in the INS errors which occurred in that flight.

Based on the amount of apparent variability in the INS errors and the timing of changes in direction of the errors seen during the flight, the most likely cause of the INS errors in the present data is faulty measurement of accelerations during sharp turns. A review of Fig. C.2 in Appendix C.3

reveals that aircraft position errors were about 1.6 km in magnitude during run 4; this is somewhat surprising since run 4 took place only about 40 min into the flight, and position errors are generally expected to be small during the early stages of a flight. Position errors of about 1.6 km were also noted as early as 20 min into the flight, which suggest that there was an initial position bias of 1.6 km (≈ 1 nautical mile); this initial bias might have been caused by a discrepancy of 1 arc min of latitude in the starting coordinates entered into the INS at take-off.

In reviewing the aircraft navigation data, the recorded values of aircraft latitude and longitude were found to contain errors which were the result of sampling the INS position output too infrequently. Thus, it was necessary to establish aircraft positions by forward-time integration of aircraft track and velocity data. Track angles had to be computed from drift angle and heading data, because track angle data were not furnished on the data tape.

Obvious errors were noted in certain of the data arrays furnished on the tape, apparently caused by use of incorrect conversion factors during the writing of the tape (Appendix C.1). These errors had to be diagnosed and corrected.

The times of the various lidar data frames were also subject to round-off errors, and had to be reconstructed by an interpolation process so that the actual distribution of lidar data points in space would be faithfully represented in the analyses. These corrections are described in Appendix C.2.

The corrected INS-derived aircraft positions were further tested against nadir-photography-derived positions for those portions of the flight where such photo data existed (Appendix C.3). Taking the smoothed sequences of photo-derived positions as true indicators of aircraft position, a variable southward position error of about 1.7 km average magnitude was noted (see Fig. C.2 of Appendix C.3); this position error could be described in terms of a constant bias in position plus superimposed time-dependent fluctuations in the position error. While a constant position bias would not corrupt wind field estimates, the time-dependent fluctuations suggested time-dependent errors in the ground velocity estimates which, in turn, can ruin wind estimates. Based on the behavior of the smoothed time-differentiated INS position errors, the ground velocity errors were found to be as large as 10 m s^{-1} or more during turns, and perhaps $2\text{--}4 \text{ m s}^{-1}$ during the several km of straight flight following turns.

Because the 10 s interval between nadir photos was too large to allow high-resolution study of the INS errors, and since other time-varying errors of nearly equal magnitude (about 2 m s^{-1}) were occurring along with the INS errors, only rough attempts at diagnosis and removal of these errors could be made. Such attempts were useful not so much for the marginal improvements in data quality which they produced, but rather to demonstrate quantitatively the magnitude of the harmful effects of the time-varying INS errors on the retrieved wind vector fields.

Although some success was obtained in defining the magnitude of the INS errors via the techniques outlined in Appendix C, the discussions there make it clear that it is not yet feasible to make precise corrections. Hence, in all figures of wind analyses to be presented in Section 3.5, the INS errors have not been removed except when specially noted. The principal benefit to accrue from the study of the INS errors described in Appendix C has been to give some rough idea of the magnitude of the errors, their time variability and of the level of confidence which can be assigned to the details of the analyzed wind fields.

3.4.2. Doppler Spectral Moment Data Review and Editing

Review and editing were needed not only for navigation data but also for Doppler moment data. After insuring self-consistency in all aircraft position and attitude data, the next step in the analysis involved examining fields of Doppler moment data and removing any errors and inconsistencies affecting these data. Modifications to data were needed in some cases to prepare it for subsequent processing and analysis.

The reflectivity estimates furnished by NASA showed evidence of being erroneous, so that these data had to be recomputed starting from the raw intensity data (Appendix D.1). The reflectivity estimation procedure employed in this study included correction for the inverse range-squared divergence experienced by backscattered photons as well as round-trip correction for absorption losses. The resulting normalized reflectivities were useful in identifying the positions of brightly reflective features such as cloud edges.

The Doppler velocity data supplied by NASA were also contaminated by errors and a full discussion of these and methods used to correct them are presented in Appendix D.2. It appears that significant errors in radial velocity estimates were caused by delays in reporting time varying INS measured parameters.

An optimal correction for these delays would have required an exhaustive investigation into the system electronics and data transfer queueing, a task which was beyond the scope of this study. However, the delays which most significantly affected the quality of the Doppler data were those involving the recording of drift angle (Appendix D.3) and ground velocity (Appendix D.4). The drift angle was observed to be a small but rapidly fluctuating quantity to which the radial velocities were quite sensitive, while the groundspeed was a large and relatively slowly varying quantity to which the radial velocities were somewhat less sensitive.

For rapidly varying quantities such as drift angle, the effect of the delays was to produce seemingly random errors (i.e. frame bias; Appendix D.3) in the measured range-averaged radial velocities, such errors could be effectively eliminated by simple filtering techniques. Although filtering was normally used to reduce the high-frequency errors caused by drift angle delays, tests of a delay correction algorithm were also routinely made; these tests met with limited success in some of the data runs.

For the more slowly varying quantities, cross-correlation techniques could theoretically be used to determine delays of various parameters with respect to the other related parameters (McCaul, 1985). However, this technique could not be applied to the present data in a straightforward manner due to simultaneous presence of several interacting errors, such as drift angle error and ground velocity error, each of which varied without well-defined periods. Even after attempts to remove ground velocity errors from the data, the cross-correlation technique failed because of the presence of lingering remnants of ground velocity error; techniques for elimination of the slowly varying ground velocity errors are not yet sophisticated enough to permit further analysis of those errors caused by delay of other slowly varying parameters.

Spectral width values furnished by the system were found to be somewhat more subject to noise than the Doppler velocities and intensities. Nevertheless, in many instances local maxima of spectral width were found to correlate well with positions of wind field boundaries or gradients.

3.4.3. Velocity Errors Due to Beam Pointing Errors

Velocity errors could be introduced through malfunctions of the wedge scanner which directs the beam onto a supposedly horizontal trajectory into the atmosphere.

Based on Lee's findings of beam pointing biases, some uncertainty initially surrounded the performance of the beam scanner. This uncertainty, caused by the failure of the scanner to compensate for aircraft roll, prompted a decision to delete all lidar data whenever the aircraft roll angle exceeded 1° in magnitude. However, based on results to be discussed in Appendix E, it appears that these deletions may have been unnecessary. However, the amount of data deleted by this roll angle criterion was quite small.

Doppler shifts recorded along radials which lie out of the horizontal plane can introduce considerable error in presence of vertical shear, as well as have contamination from any vertical velocity that might be present. Because data are collected only on a surface (hopefully a horizontal one), insufficient data are available for proper separation of the horizontal and vertical components of air motion, and thus data taken "out-of-plane" cannot strictly be corrected to be compatible with data from the horizontal plane.

Further problems related to beam elevation uncertainty arise because the lidar beam scanner is held fixed during the 0.4 s duration of each frame, allowing the sequence of pulses to sweep through a variety of elevation angles whenever the aircraft rolls in response to turbulence.

Velocity errors can also result from beam pointing errors because they can cause incorrect components of aircraft ground velocity to be included in the radial velocity data. The most reliable way of assessing beam pointing is through study of the variation of range of ground strikes versus the known variation in form of some topographic feature by which the aircraft passed during data collection. Although no beam strikes on mountainsides occurred during the Oklahoma flights, several beam ground strikes were observed during one aircraft left turn; the variation of range of these ground strikes versus the range expected based on aircraft altitude and roll angle provided an opportunity to make a limited assessment of the accuracy of the beam pointing. The results of these comparisons, discussed more fully in Appendix E, indicate that beam pointing errors were limited to less than 1-2 deg in the vertical. Using a technique outlined by McCaul (1985, Appendix F) involving comparison of derived wind vectors from regions where data from three or more lidar lines-of-sight were collected, it was possible to conclude that there were no apparent significant errors in horizontal beam pointing.

A conservative estimate of the windspeed error in these data caused by beam elevation errors is 0.5 m s^{-1} except above the gust fronts of runs 2 and

and along the cloud turrets of runs 9-12, where local errors could reach $2-3 \text{ s}^{-1}$. Clearly, the problems of laser misalignment and failure of the scanner to provide the proper beam elevation compensation during aircraft rolls should be corrected before the next series of experiments. In addition, it would be desirable if scanner positioning could be updated at least occasionally during each lidar frame so as to ensure horizontal beam trajectories for all pulses.

3.4.4. Preparation of Meteorological Data Fields

In order to synthesize meteorological data (i.e., reflectivity, wind, turbulence) fields from the edited moment data aligned along the laser beam and to present the results in a suitable form for display, it was convenient to interpolate moment data to a Cartesian grid whose origin was placed at the location of NSSL's Cimarron Doppler radar because intercomparison of Doppler and lidar wind fields were made (McCaul, 1985). Before the grid point values could be assigned, advection compensation had to be made.

i) Data Advection

The nonsimultaneity of the data collected by the lidar during each run, in some cases spanning about 500 s, required that attention be given to the problem of data advection. This was not so much a problem with respect to obtaining locally correct retrieval of wind or intensity patterns, which was governed by the maximum time delay (about 50 s) between fore and aft frame data used in analyzing fields at maximum ranges (about 10 km) from the aircraft, as it was a problem of obtaining a correct pattern over the larger scales.

In order to avoid distortion of the data patterns found near the storm outflow fronts, it was decided that advection proportional to the storm's velocity vector would be uniformly applied to all data in each run. Although this decision undoubtedly fails to account for some of the complexity of the three-dimensionality of outflows observed in the data, it is believed that the resulting fields are less error-prone than they would have been had local advection been used.

Tracking of the main storm cells on successive photographic images of NSSL's WSR-57 radar screen suggested a storm motion vector of 12.9 m s^{-1} from 256° . Due to rapid development and evolution of cells in this multicell complex as observed on the radar screen and in the field, this advection

vector must not be considered an absolutely accurate measure of how the cells moved or how the windfield patterns propagated.

Calculations of the mean wind from each data run used in the study of the main storm complex give values which differ substantially from the radar-derived motion vector. In fact, lidar run 4 showed an average wind vector of 11.5 m s^{-1} from 212° . This discrepancy may be taken as a rough indicator of the relative importance of propagation or differential motions in the wind fields studied here. In Appendix F, a model wind field, with a velocity (i.e., phase speed) of wind perturbations known but different than the mean wind in the layer, was sampled in exactly the same manner as the actual data. Wind vectors synthesized from radial velocity fields using the correct advection velocity and that equal to the mean wind in the layer show considerable differences.

ii) Data Interpolation and Wind Estimation

Interpolation to a Cartesian grid was done using the circularly symmetric distance weighting function (Cressman 1959) and details are discussed by McCaul (1985). To give maximum resolution to the features of interest, slightly different radii of influence were used for the interpolation velocity, intensity and spectral width data. The radius of influence for interpolation of velocity data was chosen to be 600 m in order to ensure that data from three or four different frames would be interpolated, but that data from only two or three resolution volumes along the beam would be used. This is important because of the tendency of the radial velocity data to show more variability from frame to frame (due to the drift-angle-related errors described earlier) than from range bin to range bin.

The radius of influence for the analysis of lidar echo intensity and spectral width was set at a smaller value, 400 m, in order to give maximum expression to the large gradients which occurred with these quantities in zones of strongest meteorological interest.

Although the interpolation procedure for the scalar fields followed standard procedures (see McCaul 1985), several additional steps were needed in the process of interpolating data for wind estimates. Because wind is a vector quantity derived from the scalar radial velocity data, the interpolation process had to be done four times: once for the forward frame velocity data, once the forward line-of-sight data (i.e., angular direction of the

beam), once for the aft frame velocity data, and finally, once for the aft line-of-sight data within the neighborhood of each grid point. The full horizontal wind vector is synthesized only after the two differently directed sets of radial velocity data and two differently directed lines of sight data had been separately interpolated to the Cartesian grid.

The geometric motivation behind the solution for the total vector is shown in Fig. 3.7. Solutions may be obtained in a variety of forms; the option used in this study retrieves the wind vector in terms of a magnitude "V" and an azimuth "AZ" according to

$$AZ = \text{ARCTAN} \left\{ \frac{VR1 \cdot \cos(AZLOS2) - VR2 \cdot \cos(AZLOS1)}{VR2 \cdot \sin(AZLOS1) - VR1 \cdot \sin(AZLOS2)} \right\} \quad (3.1a)$$

$$V = -VR2 / \cos(AZ - AZLOS2) = -VR1 / \cos(AZ - AZLOS1) \quad (3.1b)$$

where "AZLOS1" and "AZLOS2" are the fore and aft interpolated lines-of-sight and "VR1" and "VR2" are the fore and aft interpolated radial velocities valid at the grid point in question. In applying Eq. 3.1b, the solution for "V" is obtained using the form having the larger cosine value in the denominator. A

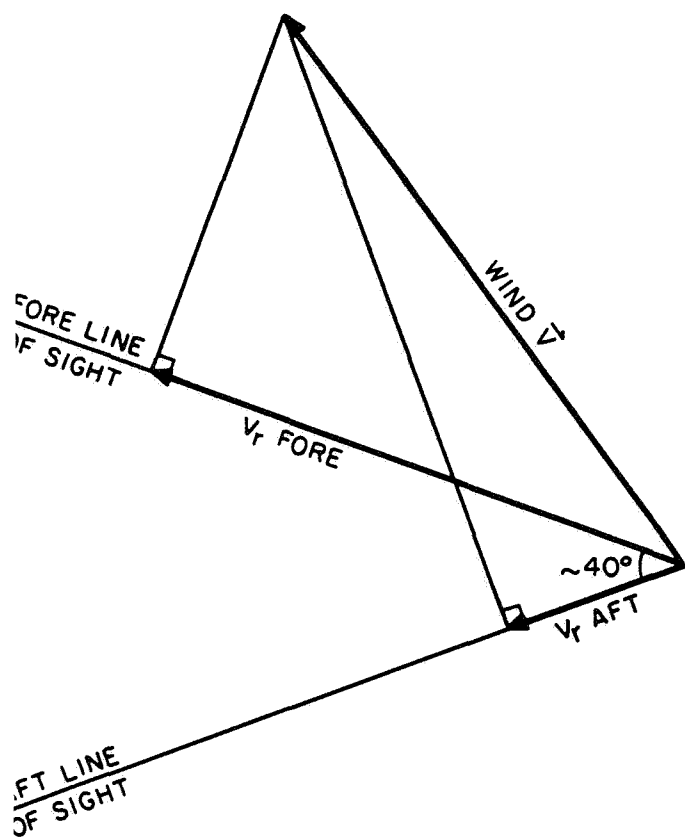


Figure 3.7 Construction of wind vector from fore and aft radial velocities. Intersection of perpendiculars from the tips of the components defines the wind vector

sample plot of wind vectors thus obtained from the raw data is shown in Fig. 3.8, along with the radial velocity data used in their calculation.

3.5. METEOROLOGICAL INTERPRETATION

In this section we present the results of the lidar data analysis in the vicinity of thunderstorm outflows and around an isolated cumulus congestus cloud.

3.5.1. Interpretation of Thunderstorm Outflow Data

In runs 2 and 3 of the lidar data, the horizontal structural features of several thunderstorm outflows were examined. Results from run 2 were obtained at an altitude of about 720 m AGL, while those from run 3 were obtained at about 510 m AGL.

In both cases lidar range was variable, with a minimum of 3 km near dense, low clouds and a maximum of 8 km in other areas. Strong attenuation was noted when the lidar beam entered arcus or scud, as in run 2, but less attenuation was observed in run 3 when the outflow was free of low clouds.

Run 2 was made on the northeast side of a complex of strong storm cells developing from Chickasha to El Reno, OK; the derived wind field is shown in Fig. 3.9 while the contoured fields of return intensity and spectral width are shown in Figs. 3.10 and 3.11. In Fig. 3.9, light southeast winds are evident in the area just east of the outflow front, and strong gusty southwesterly winds (sometimes 20 m s^{-1}) are seen at and behind the gust front. Fig. 3.9 shows a portion of the gust front which stretches from coordinates ($X = -5$, $Y = -33$) northwestward to coordinates ($X = -28$, $Y = 0$). Figs. 3.10 and 3.11 show a "wall" of high intensity returns and large spectral widths near the wind shift line seen in Fig. 3.9. As the evidence to be presented shortly will show, this "wall" of high intensity and spectral width was most likely due to the lidar signal impinging on the arcus cloud (Fig. 3.4) which occurred along much of the gust front in run 2.

In Fig. 3.11, the large spectral widths associated with the arcus cloud appear on the southwest edge of the data swath and should not be confused with the line of large spectral widths lying along the aircraft track on the northeast edge of the data swath. This line is an artifact of width values which are reported in the first range bin of each frame, and has no meteorological

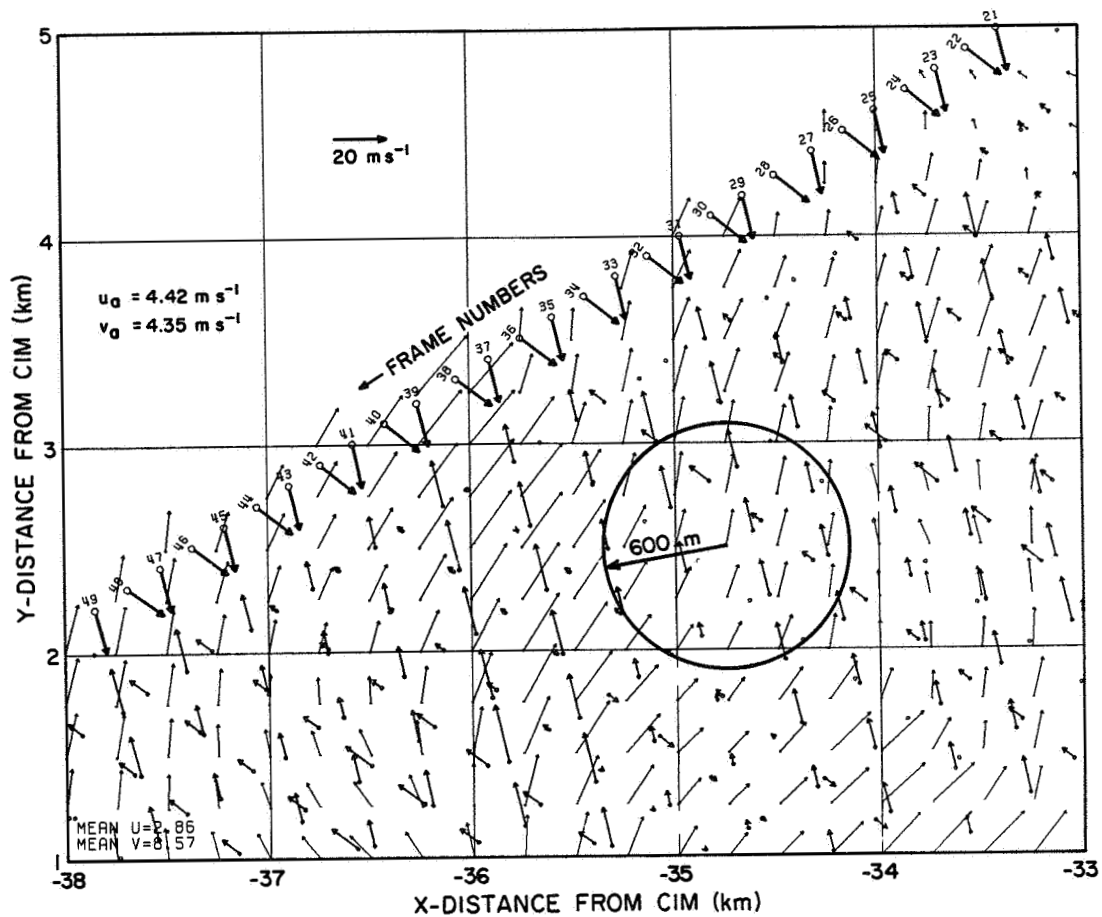


Figure 3.8 Sample field of radial velocity data and synthesized wind vectors. Run 3. Shown are the successive aircraft positions and the interpolation circle. A scaled velocity vector is on the upper left of the figure. The radial velocity vectors are those aligned along the fore and aft directions indicated by the vector attached to each frame number. The synthesized wind vectors are those located on the cartesian grid with 250 m spacings.

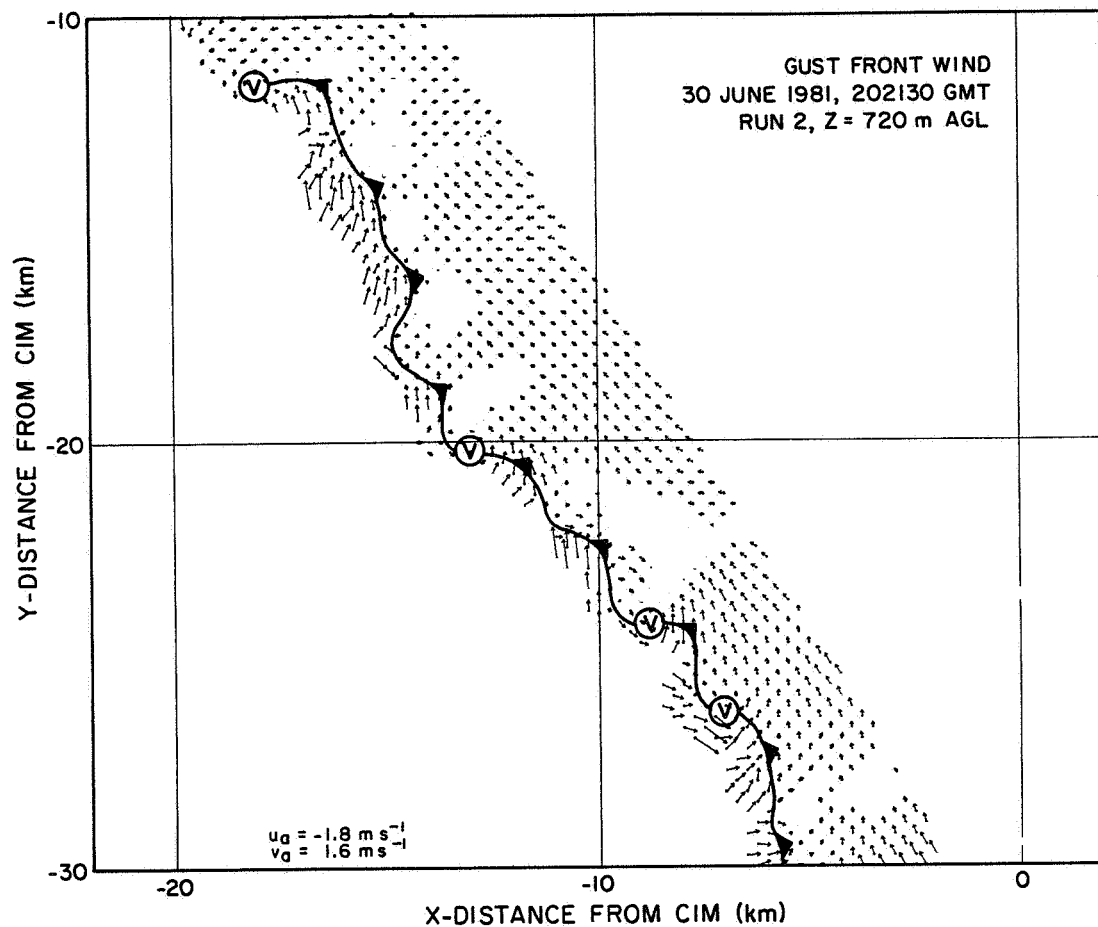


Figure 3.9 Vector plot of lidar-derived winds of storm outflow observed during run 2. Note stronger winds along the front of the outflow at left edge of the data swath, and the irregular form of its leading edge.

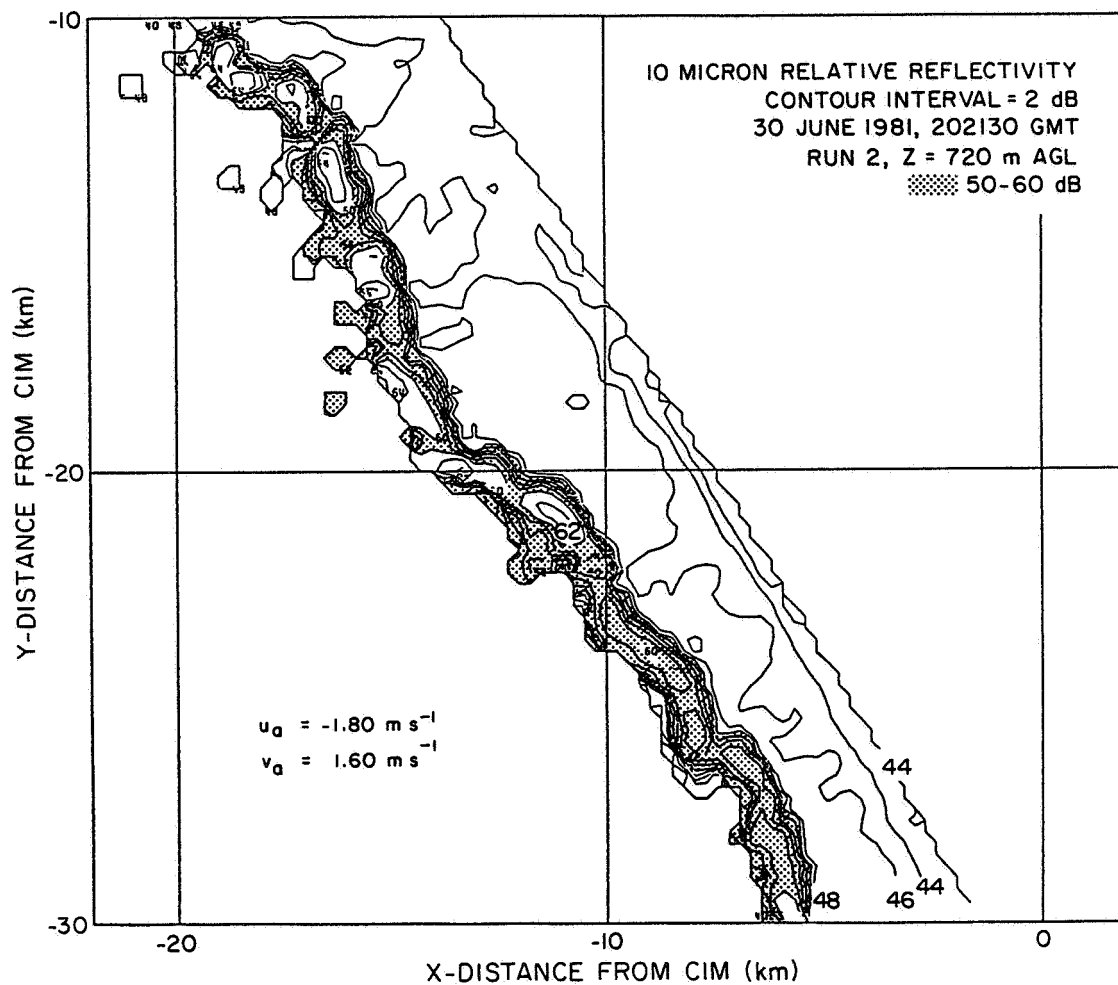


Figure 3.10 Contour plot of the normalized reflectivity along the front of an advancing storm outflow. Note correspondence of high intensity areas with the leading edge of the outflow seen in Fig. 3.9.

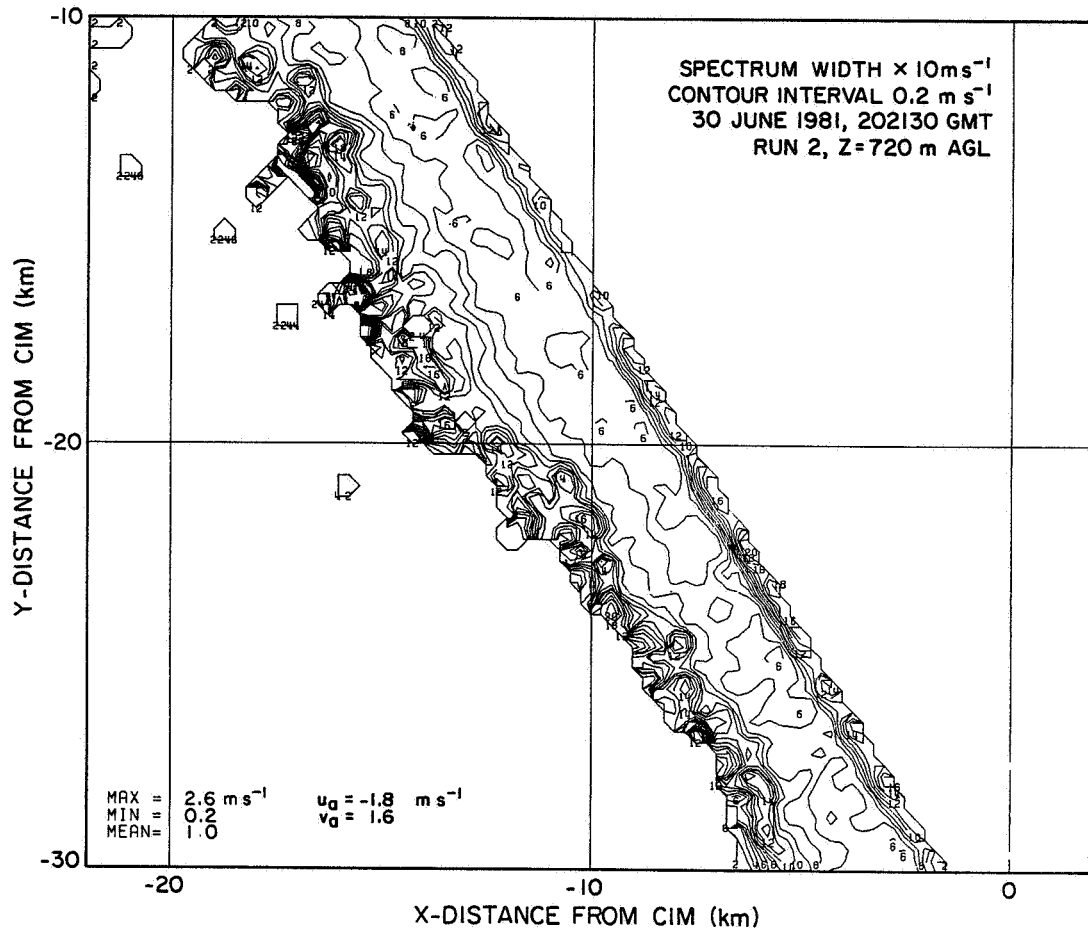


Figure 3.11 Contour plot of spectral widths (turbulence) in the vicinity of a thunderstorm outflow. Note correspondence of high spectral widths with the leading edge of the outflow.

significance. Such spurious patterns in spectral width may be seen in the first range bin in every data run. These large widths, as well as those seen at cloud boundaries, might have been caused by the large echo powers (from targets close to the lidar or from highly reflective cloud particles) that exceed the dynamic range of the receiver (≈ 54 dB for the 10 bit analog-to-digital converter) causing the echo signal peaks to be clipped. When echo signals are clipped, odd harmonics are generated that have alternately positive and negative frequencies about the mean Doppler shift of the echo and these harmonics can cause the spectral widths to be biased toward large values (Doviak and Zrnic', 1984, p. 158).

Particularly noteworthy in Fig. 3.9 are the vortex patterns which appear at irregular 3-7 km intervals along the gust front. The best examples are indicated by circled "Vee's". These patterns could be caused either by (a) the tilting of vertical-shear-induced roll vortices in the near-storm boundary layer by the lifting action of the cold outflow at the edge of the gust front, or (b) to the convergence of the vorticity associated with the strong horizontal shears found along the gust front.

Support for the former theory seems to be especially strong in the vicinity of the vortex located at ($X = -9$, $Y = -24$), where a surge of southeasterly wind is observed to extend from the aircraft's position back to the southwest into the vortex, producing a strong impression of a horizontal vortex tube seen in horizontal cross-section as it is tilted upward by the differential rising motion just ahead of the storm outflow. Analysis of this particular vortex pattern requires caution because spurious patterns can be produced by erroneous velocity data. Furthermore, no definite cloud pattern featuring a vortex in the arcus cloud could be seen in photographs (e.g., Fig. 3.4) taken at the time the lidar data were collected. The other vortices appear to be associated with notches or concavities seen both in the photographs (e.g., Fig. 3.4) and in the reflectivity patterns and thus appear to be genuine despite the relatively weak horizontal winds in the warm air ahead of the gust front.

Although lidar data were not collected at more than one level along this outflow (thus precluding a detailed three-dimensional diagnosis of the vertical shear distribution in the near-storm boundary layer), surface data from a NSSL mesonet station at Tuttle South (TTS) nearly under the aircraft flight track were available for comparison with the lidar-derived wind. Because the

aircraft apparently was closest to TTS (within 1 km) at 201955 GMT (141955 CST), the vertical shear at one point (TTS) could be estimated quite accurately by finding the difference between wind vectors obtained by the lidar and the surface station and dividing by aircraft altitude. Synthesis of the lidar data from bin 2 of frames 81 and 82 of the lidar data gave a wind of 4.3 m s^{-1} from 135° at the TTS location at 201955 GMT, while the surface station gave a 60-s average wind of 1.9 m s^{-1} from 134° at 202000 GMT. Using the aircraft altitude estimate of 722 m from the CV990's down-looking radar and ignoring the tiny difference in wind azimuths, we obtain a vertical shear of $3.3 \times 10^{-3} \text{ s}^{-1}$.

Thus, even though the winds were very light, there was vertical shear directed to the northwest in the immediate vicinity of the gust front that could have been tilted onto the vertical to produce the vorticity patterns seen in the run 2 data. To see whether the actual measured vorticities could be produced directly by the tilting mechanism, we examine the inviscid vorticity equation in height coordinates:

$$\partial \zeta / \partial t = -\vec{V} \cdot \vec{\nabla} (\zeta + f) - (\zeta + f) \delta - \hat{k} \cdot \vec{\nabla} W \partial \vec{V}_H / \partial z - \hat{k} \cdot \vec{\nabla} \alpha \vec{\nabla} P \quad (3.2)$$

where: ζ = vertical vorticity
 f = planetary vorticity
 δ = horizontal divergence
 \vec{V} = total three-dimensional wind vector
 \vec{V}_H = horizontal wind vector
 W = vertical wind component
 α = specific volume
 P = pressure
 \hat{k} = unit vector along Z-coordinate

If we neglect the small terms involving advection of planetary vorticity and horizontal pressure-density solenoidal effects, Eq. 3.2 may be rewritten in terms of the rate of change of parcel vertical vorticity following the motion as follows:

$$\frac{d\zeta}{dt} = -(\zeta + f) \delta - \hat{k} \cdot \vec{\nabla} W \partial \vec{V}_H / \partial z \quad (3.3)$$

where the first term on the right represents convergence of pre-existing and planetary vorticity and the second represents tilting of pre-existing vertical shear. Assuming that vertical vorticity is initially negligible, and using observed convergence rates of 10^{-2}s^{-1} and vertical shears of 10^{-3}s^{-1} along the gust front and an estimated gradient of rising motion of 10 m s^{-1} across 10 km , or 10^{-3}s^{-1} , we find a vorticity production rate of about 10^{-6}s^{-2} . Now assuming vorticity, vertical shear and gradients of rising motion are roughly independent quantities, it would take about 10^4 s to produce the observed vorticities of 10^{-2}s^{-1} , this time, which is approximately 3 hours, is too long to account for the observed vorticity development, which probably occurred in less than an hour.

However, we note from Eq. 3.3 that once vorticity reaches about 10^{-4}s^{-1} , it no longer can be neglected as a factor in the total vorticity production rate. Considering tilting only, a vorticity of 10^{-4}s^{-1} could be generated in only 100 s (about 2 min). Once such a vorticity exists, it will amplify exponentially in the presence of the strong convergence observed. Amplification by a factor of 100 gives the required observed vorticity; this can be achieved in an additional time "T" given by the natural logarithm of 100 divided by the observed convergence of 10^{-2}s^{-1} , or in only a time $T = 460\text{ s}$. Thus, we conclude that in the vicinity of the gust front observed in this storm, total vorticities of about 10^{-2}s^{-1} could be produced in about 560 s , or less than 10 min, due to tilting of initially horizontal vorticity and subsequent stretching by the strong frontal convergence field.

In the preceding argument we have based our calculations on pre-existing vertical shears estimated from surface data and lidar data at an altitude above 700 m AGL . Simpson (1982) has argued that the evolution of some meso-vortices may be the result of tilting of the much larger vertical shears found very near the surface. Assuming such mechanisms to be acting on our data, it is quite likely that tilting alone could explain the bulk of the vorticity observed.

If these vortices were indeed caused by the tilting of horizontal boundary layer vortex tubes by the lifting action of the outflow, then it is important to note that the relations between the boundary layer shear vector and the orientation of the lifting surface were almost ideal: the local shear vector was oriented from an azimuth of 135° , while the outflow was moving with

a vector almost perpendicular to the shear, providing maximum vorticity production all along the length of the front.

Vortices qualitatively similar in appearance to those observed here have been observed by Carbone (1982, 1983) along an intense winter-time cold front in California. In Carbone's data, peak vorticities and divergences were similar to those observed here, about 10^{-2}s^{-1} , but overall wind speeds were much higher (e.g., storm motions of 28 m s^{-1}), and the storm inflow was characterized by a strong jet parallel to the front. This jet was most intense at an altitude of 600 m AGL, and was hypothesized to be a storm-induced inflow feature.

The vortices observed by Carbone apparently had typical scales of about 13 km, somewhat larger than the 3-7 km observed here. Carbone attributed the vortices to Helmholtz instabilities in the regions of strong horizontal shear along the front. Barcilon and Drazin (1972) conclude, using standard linear stability analysis techniques, that shear zones which can be modeled as vertical vortex sheets are always unstable in the presence of superadiabatic lapse rates. Evidence for the presence of superadiabatic lapse rates near the outflow shown in these data is described below. Thus, it is possible that Helmholtz instabilities may have been responsible for the development of the vortical circulations observed in the lidar data discussed here. Vortices resembling Carbone's and those observed here have also been obtained along outflow shear zones in numerical simulations of convective clouds (Rotunno, 1984, private communication).

It is especially important to note that the vortices observed here are strong enough to appear in the plots of total measured wind vectors, rather than merely in the plots of perturbation vectors. The lingering presence of systematic errors in the lidar measurements was seen in places in the perturbation wind fields and in contour plots of certain kinematical quantities inferred from the lidar winds. One important conclusion to be made from this study is that while the winds derived from the lidar measurements are only subject to relatively minor errors (usually about 1 m s^{-1}), these errors are large enough to render suspicious many of the features seen in the perturbation wind fields.

Unfortunately, it was not possible to confirm the presence of these vortical patterns by an independent observation from Doppler radar due to the entry of the gust front into the region of ground clutter by the time the CIM

Doppler radar was turned on. Details of the gust front which lay outside of the ground clutter appeared noisy and were apparently subject to sidelobe contamination from storm reflectivity in adjacent beam radials. However, the strength of the winds in the outflow, about 20 m s^{-1} in spots, was observed to be similar to the CIM radial velocities reported in the core of the storm some 10 km southwest. As mentioned earlier, such velocities would probably be good estimates of the wind due to the approximate alignment of the mean winds in the outflow layer toward CIM.

Further confirmation of the strength of the outflow came when the front arrived at TTS. This station reported passage of the gust front at about 202230 GMT (142230 CST), with winds veering to southwest and increasing to maximum values of 12.5 m s^{-1} immediately after gust front passage. The surface winds at TTS at the time of gust front passage is shown in Fig. 3.12, along with other major meteorological parameters recorded. This figure, designed to depict the time series of TTS data in a space cross-section which might be seen across the outflow looking north-northwest, reveals not only a veering and surging of the wind associated with it, but also shows a sharp 9°C drop in temperature and a 1°C drop in a dew point behind the outflow. However, this temperature decline was evidently not directly associated with the onset of heavy rain which was delayed by about 14 minutes with respect to the time of passage of the gust front. The onset of heavy rain, which reached intensities of 120 mm/hr briefly, was also evidently accompanied by a second surge of strong wind, with a peak gust of 18.3 m s^{-1} from the west-southwest. This lag between the first wind surge and the onset of heavy rain provides strong evidence that the "wall" of high intensity returns seen by the lidar in the vicinity of the gust front was associated only with the arcus cloud and not with heavy precipitation.

Additional information about the structure of this outflow may be gleaned from the data using appropriate assumptions about frontal motion. If the speed of propagation of the front is taken, following Goff (1975), to be about 0.67 times the peak surface gust value at the leading edge, then it is possible to deduce a frontal propagation speed of about $0.67 \times 12.5 = 8.3 \text{ m s}^{-1}$. Using the speed and the observed delay (about 150 s) between 2020 GMT and the time of frontal passage at TTS, it appears that the surface front was roughly $150 \times 8.3 = 1250 \text{ m}$ west-southwest of TTS at 2020 GMT. The lidar raw data taken from forward frame 82 at 201955 GMT indicate the frontal position at 722 m

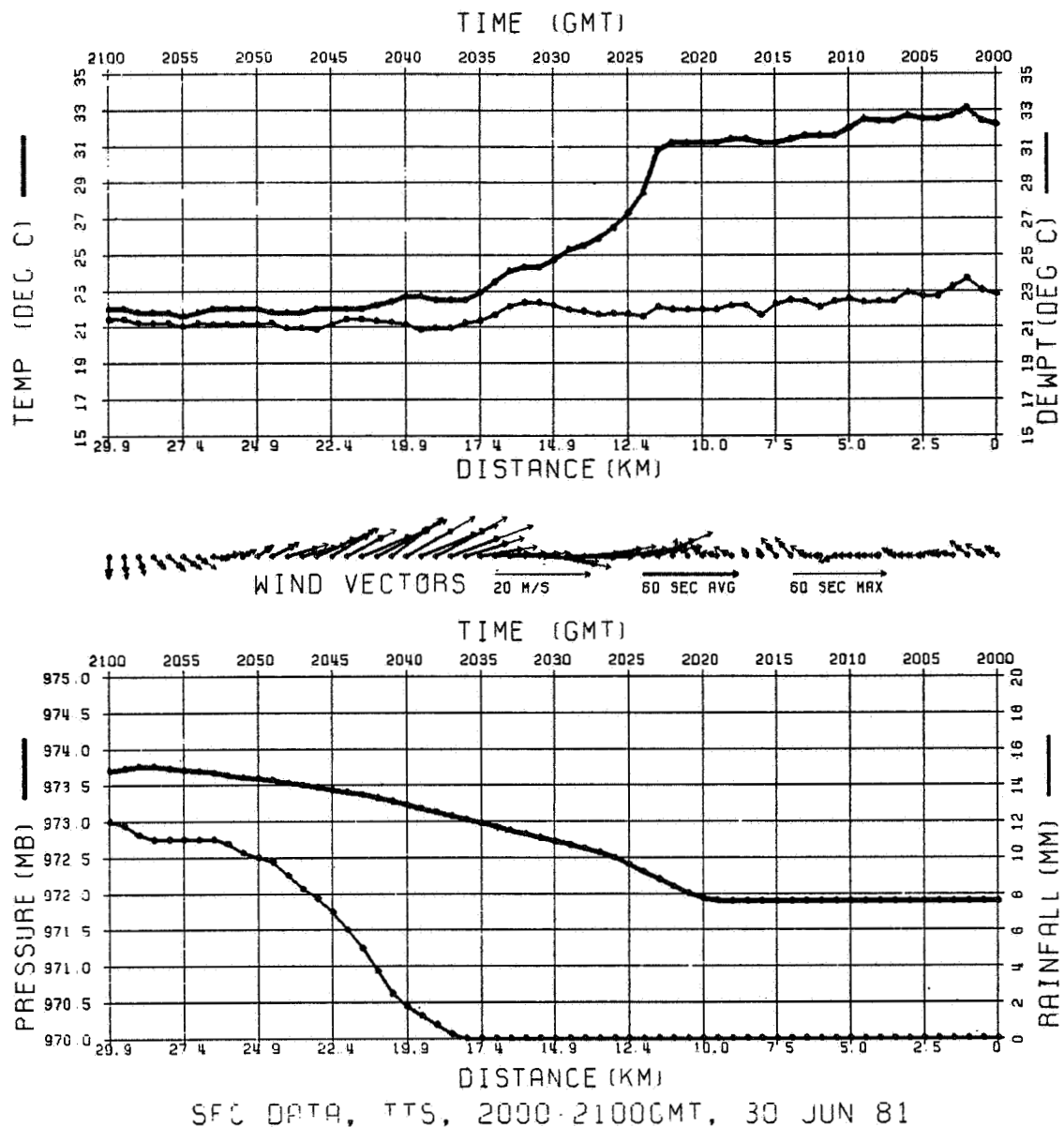


Figure 3.12 Plot of meteorological observations at TTS (Tuttle South), 2000-2100 GMT, 30 June 1981. Note passage of the outflow at 2023 GMT (three min after the CV 990 over flight) and delayed onset of heavy rain. The vector labeled 20 m s^{-1} scales the wind vectors; the bold arrows are 60 sec. averaged winds whereas the thin superimposed arrows are the peak winds in each 60 sec. period. Wind direction is referenced to North which is toward the page top.

altitude to be in resolution volume 12, at a distance of $192 + 11 \times 320 = 3712$ m. Even if we account for as much as 1 km error in aircraft position with respect to the front, it is still reasonable to conclude that the front sloped back to the west-southwest at a slope of about $722 / (3200 - 1250) = 0.37$. While the front almost surely did not maintain a simple wedge shape at its leading edge, we can at least deduce that much of the lidar data collected in run 2 was collected just above the leading several km of a sloping storm outflow airmass. Unfortunately, the relative positions of the surface front and the lidar observed front cannot be given along the entire length of the front because the appropriate surface data were not available.

Comparison of surface temperature data with temperature data taken by the aircraft reveals the likely presence of a slightly superadiabatic lapse rate of 10.6°C per km of altitude at TTS location at 2020 GMT, just two and one-half minutes before the arrival of the outflow.

Additional outflow data were taken during run 3 along the northern edge of the storms. Plots of the derived winds are shown in Fig. 3.13. Note the presence of wavelike patterns in the wind field intensity and also the sinuous shape of the leading edge of the outflow as observed earlier along run 2. These features may be manifestations of the cellular character of the convection or may be related to the vortical perturbations seen further southeast in run 2. Indeed there appears to be some continuity to the form of the outflows in the northeast corner (beginning) of run 3 and the northwest corner (ending) of run 2, both showing strong southerly or south-southwesterly flow at about 20 ms^{-1} . However, at least some of the perturbations observed during run 3, especially those behind the leading edge of the outflow, are probably artifacts of lidar and INS system instrumental or coordination errors which were not completely or adequately handled by the filtering methods employed in these analyses.

A feature of significance seen in Fig. 3.13 is the sharply defined change in velocity located just southwest of the gust front by a distance of about 3 km and oriented northwest-southeast. This is evidently caused by an especially blatant case of the lidar system error mentioned earlier, because it is seen to align itself quite closely with the direction of aft-pointing lidar lines of sight in run 3. This particular lidar error may be associated with the "shock" experienced by the aircraft when it actually penetrated a portion of the gust front at coordinates ($X = -36$, $Y = 4$). INS measured wind and drift angle data from this run confirm the impact the gusty outflow had on

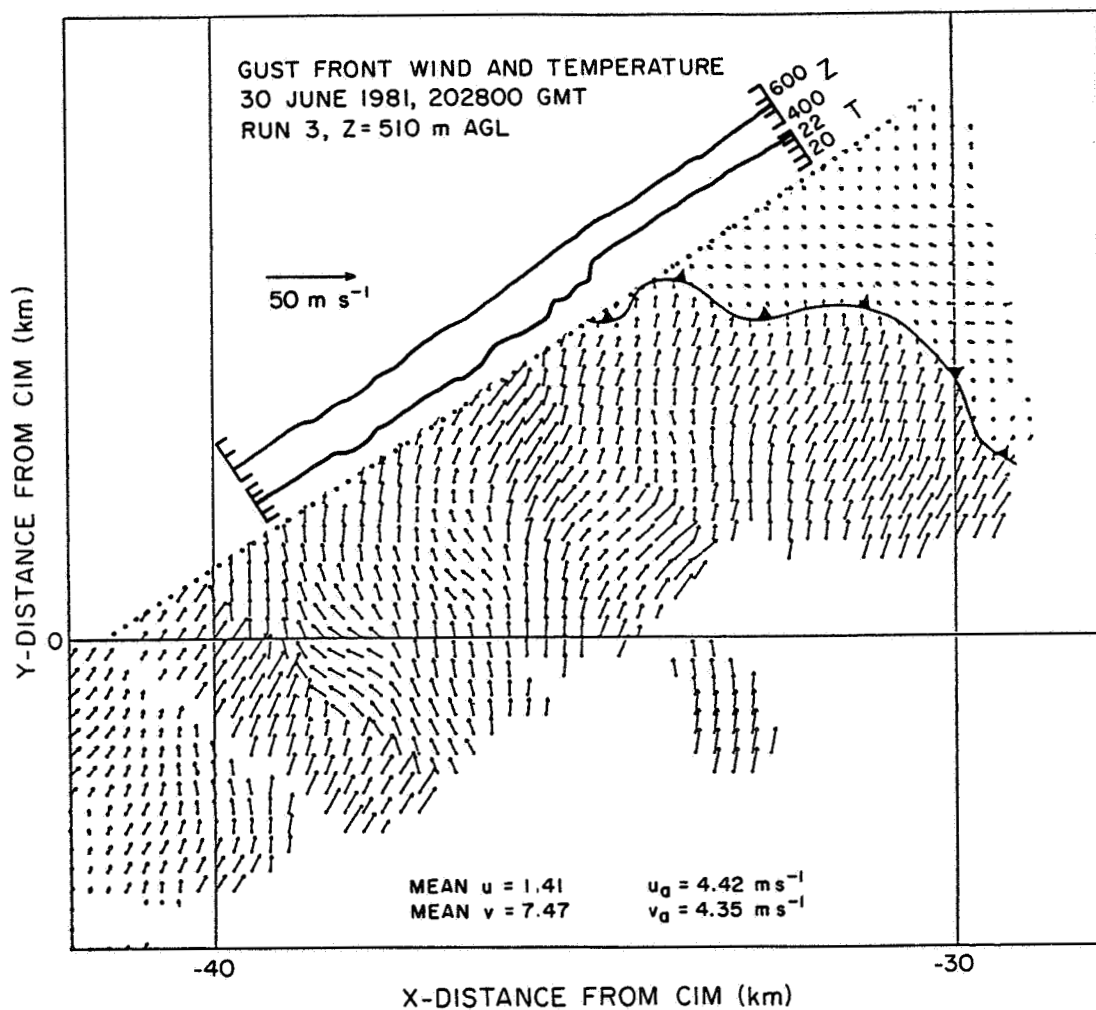


Figure 3.13 Vector plot of lidar-derived winds observed during run 3.

the aircraft: INS measured winds fluctuated by as much as $6 \text{ m}\cdot\text{s}^{-1}$ in magnitude, and drift angles changed by more than 2° between successive lidar frames during the gust front penetration. Plots of aircraft-measured temperature and altitude are also provided (Fig. 3.13) to demonstrate the penetration of the outflow by the aircraft and to suggest that the temperature changes measured at the aircraft were likely to be due to more than just the slight altitude change it experienced.

Clearly the results obtained by the lidar during the period while it was being buffeted strongly must be viewed with extreme skepticism. Thus, some of the larger wind shifts seen southwest of the gust front's leading edge are probably erroneous. Only the lidar data collected prior to penetration of the gust front seem fully credible; fortunately the orientation of the front was such that a relatively good view of the frontal wind structure was obtained while the aircraft was still in smooth air.

Fig. 3.14 shows the field of reflectivity. The only significant features in the intensity field are noted near and just south of the outflow's leading edge. This small band of high intensity returns may be due to precipitation or to scud filaments which were observed along this portion of the storm (e.g., Fig. 3.5). No organized arcus cloud was observed during run 3.

In Fig. 3.15 the spectral width is seen to have a well defined maximum at coordinates ($X = -32$, $Y = 4$), which correspond closely to the position of a portion of the leading edge of the outflow where it is strongly curved and apparently characterized by convergence and cyclonic vorticity. Also evident in Fig. 3.15 are the noisy widths, whose origins were explained earlier, in the nearest range bin to the aircraft.

Based on the observations made in run 3 and confirmation from similar studies of the results from other runs, it is possible to make several general statements about the systematic errors found in the lidar data and their impact on the results of this study. First, wind shifts which show a preferential orientation along either the fore or aft lidar lines-of-sight - in run 3 (either 170° and 130°) must be considered suspect. Second, the presence and the intensity of the system errors seem to be quite sensitive to the relative motion of the aircraft and the ambient wind, with the worst errors noted when the aircraft was subject to a crosswind. Third, kinematical parameters, such as divergence, vorticity, and stretching and shearing deformation, are quite sensitive to the presence of these errors.

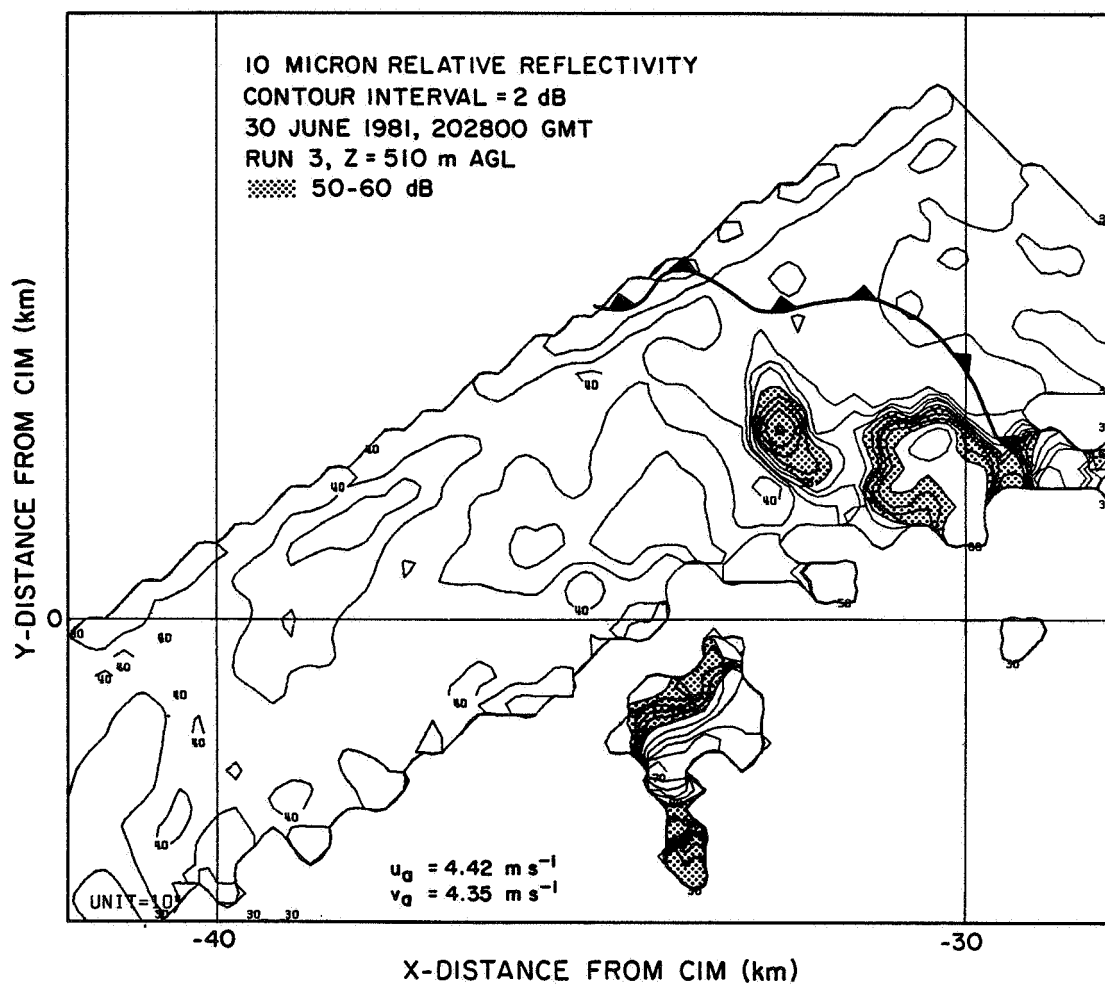


Figure 3.14 Contour plot of normalized reflectivity observed during run 3. Note relative lack of strong intensity areas near the gust front, due to the absence of the arcus cloud formation.

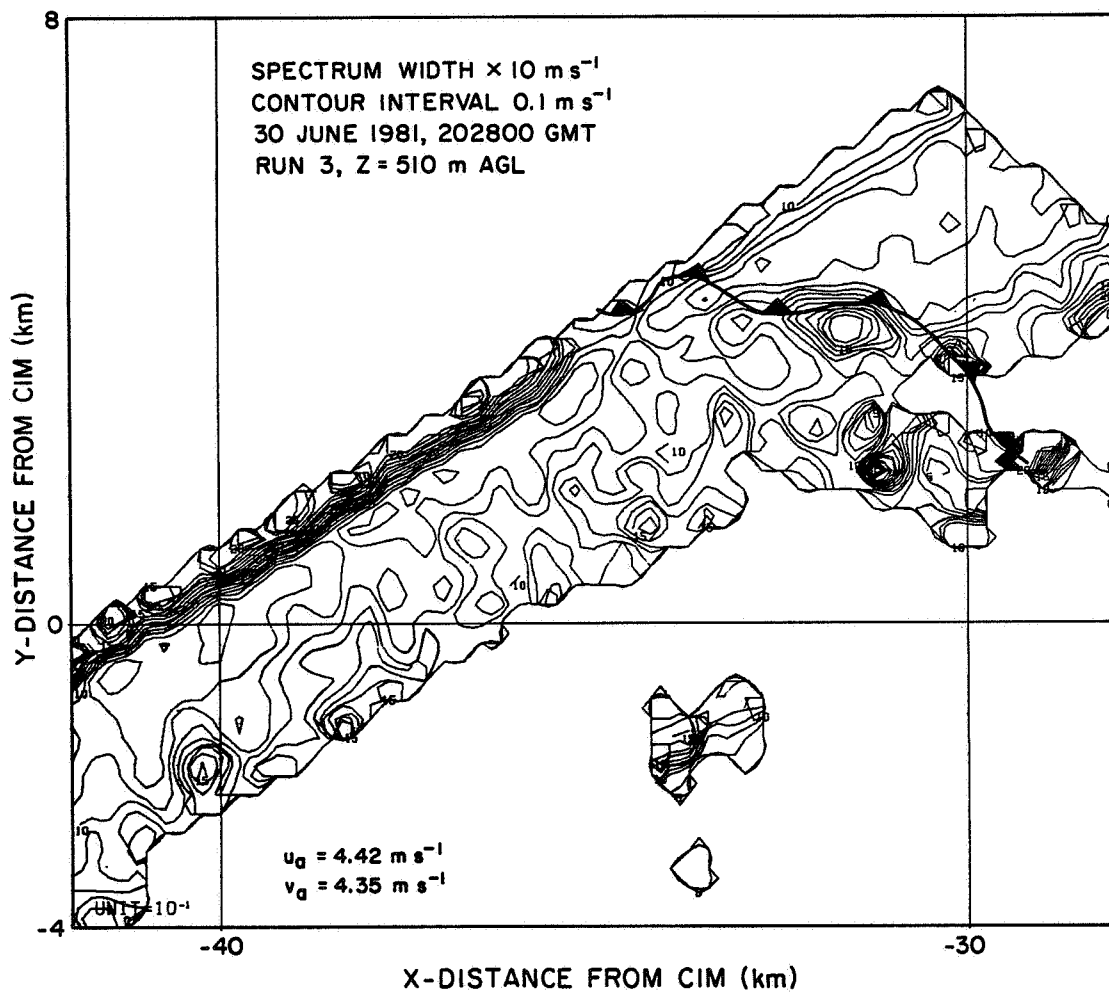


Figure 3.15 Contour plot of spectral widths (turbulence) observed during run 3.

3.5.2. Interpretation of Data at the Edge of an Isolated Cumulus Congestus

During runs 5 through 12, lidar observations were made of an isolated cumulus congestus near Elmore City (ELC), OK (Fig. 3.2). Observations were made at 1100 m AGL and at 2300 m AGL, the former being close to cloud base and the latter well above cloud base. Fields of velocity vectors, reflectivity, and spectral width were generated using an advection vector given by the mean of the four run-averaged wind vectors used in each circumnavigation. Thus, the advection vector for the lower level was not the same as that used for the upper level. Time differences between observations at each level were less than 350 s, but were as much as 750 s between levels, rendering the use of one common advection vector and objective analysis time inappropriate in view of the obvious convective growth which was taking place in the region of interest.

The lidar range was about 6-8 km during the lower altitude passes and increased to more than 12 km during the higher altitude passes. This increase in range was, of course, probably attributable to the decrease in ambient water vapor with altitude.

Figs. 3.16 and 3.17 show the lidar-derived wind vectors computed by combining forward and aft lidar data from within single runs only, one run at a time for altitudes of 1.1 and 2.3 km respectively. However, for small scale circumnavigation studies such as those involving runs 5-8 and 9-12, further information about the wind field, especially in the corner regions not well covered in the standard analysis (i.e., combining fore and aft data only in each run), can be obtained by combining lidar data from pairs of different but adjacent runs. In such analyses, for instance, wind vectors were computed using lidar data from forward frames in run 5 and aft frames in run 6; similar analyses were made for forward and aft data from runs 6 and 7, 7 and 8, and 8 and 5 respectively (Fig. 3.18) .

It should be noted that several forward and aft frames were deleted at the beginning of run 11 (at about $X = 29$, $Y = -77$) due to excessive roll by the aircraft. These deletions have produced a gap in the analysis shaped like an inverted "V" (Fig. 3.17).

Note that in plots 3.16, 3.17 and 3.18 the superimposition of vectors computed from the various combinations of runs offered an opportunity to examine the lidar analyses for consistency and time continuity. In Fig. 3.16, agreement of vectors in areas of overlap between data collected in the four

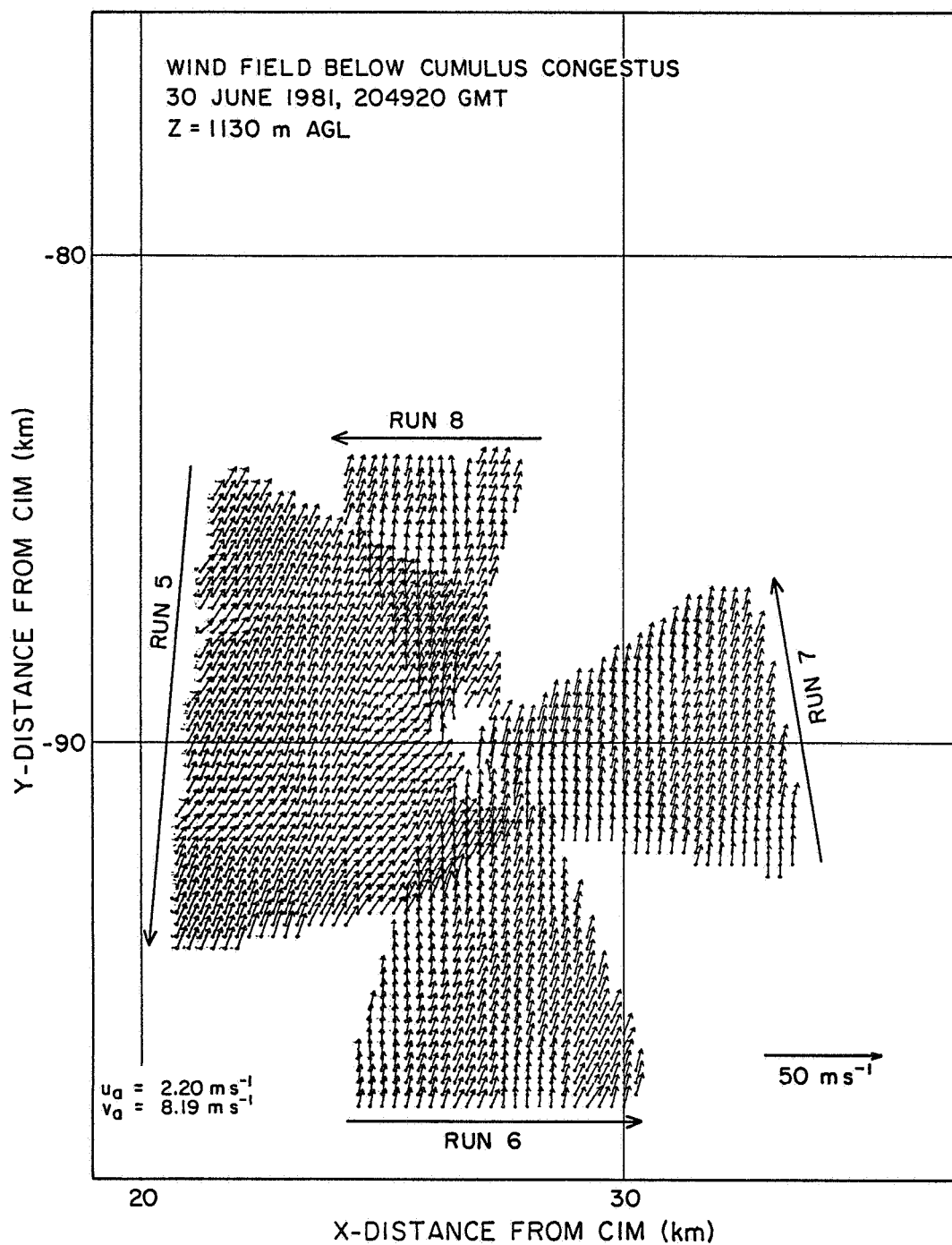


Figure 3.16 Vector plot of lidar-derived winds observed during runs 5-8 (each run taken singly). The data were taken just below and around a towering cumulus at 1130 m AGL.

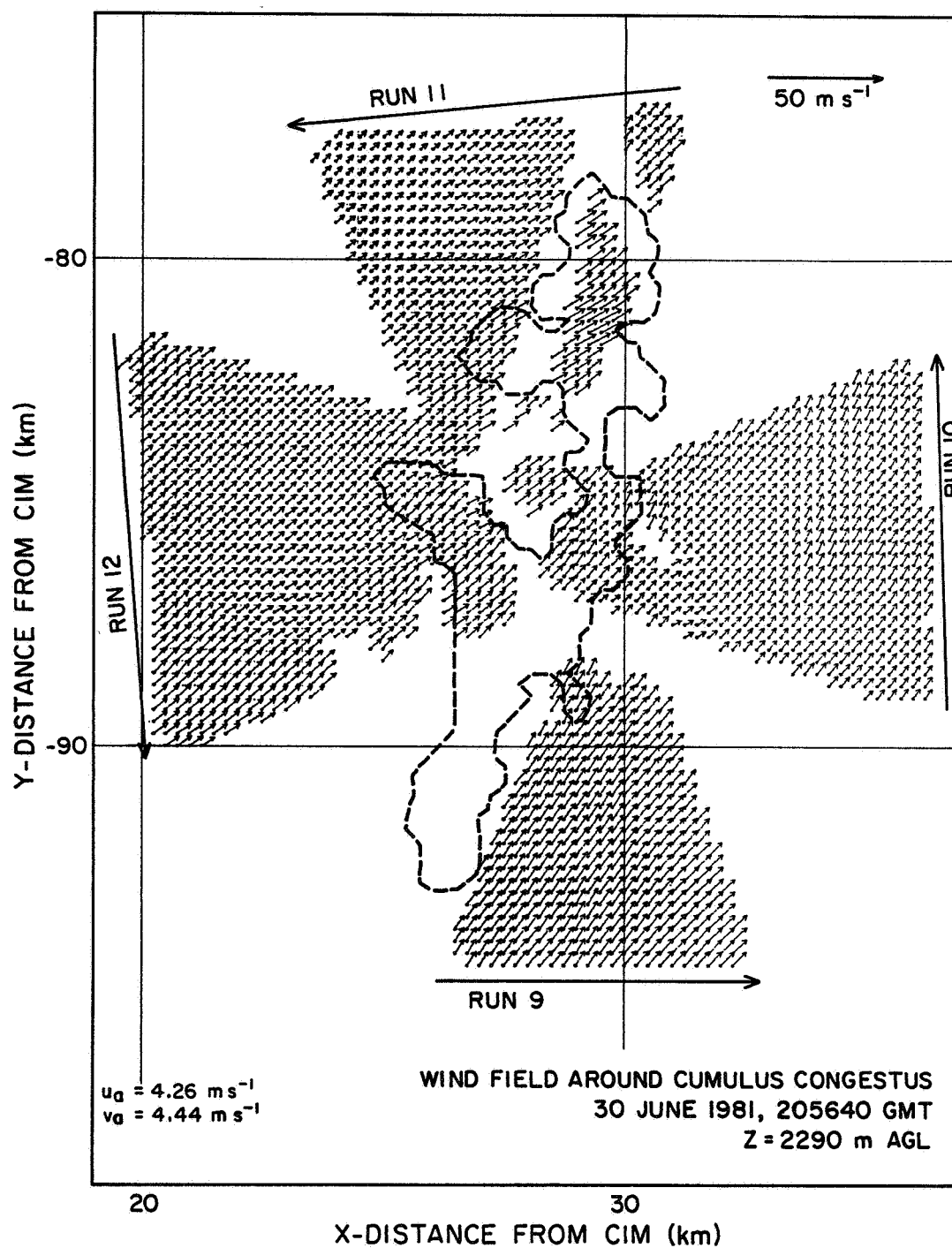


Figure 3.17 Vector plot of lidar-derived winds observed during runs 9-12 (each run taken singly). The data were taken at mid-levels at an altitude of 2290 m AGL. The dashed line is the outline of high reflectivity regions shown on Fig. 3.21.

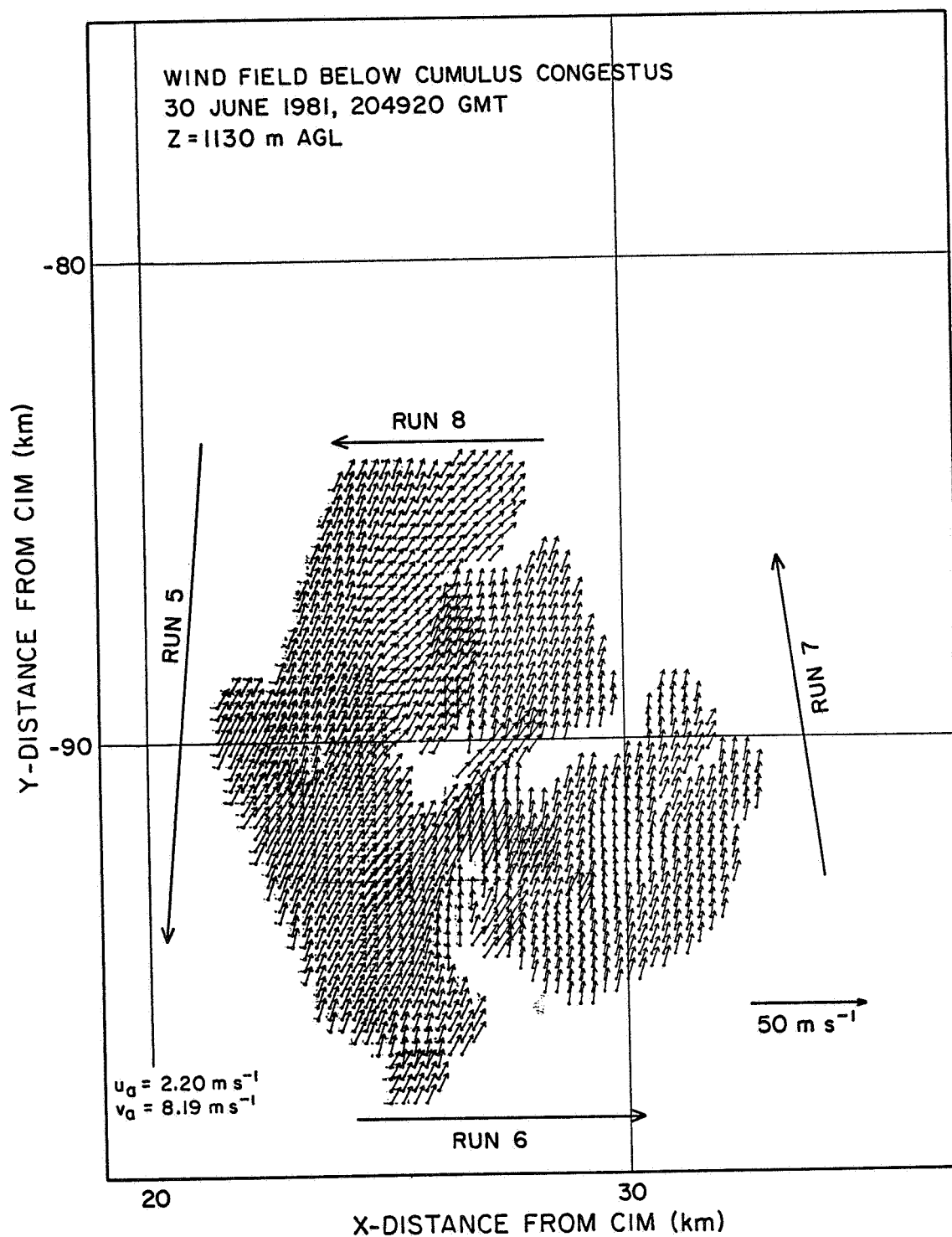


Figure 3.18 Vector plot of lidar-derived winds observed during runs 5-8 (using pairs of adjacent runs' data in the wind synthesis).

runs is variable, but consider the fact that the flow under examination is at the base of an active towering cumulus and that the time difference between observations used to construct the wind vector is as large as 90 s. Vector agreement ranges from near collinearity at coordinates ($X = 27$, $Y = -88$) to 40° azimuth discrepancy at ($X = 27$, $Y = -92$). These differences are highlighted in Fig. 3.19, which shows the perturbation vectors calculated relative to the assumed advection vector (see "UA" and "VA" in the plot label) used for runs 5-8. The reasons for this and other disagreements are not known, but the actual time evolution of the features may be responsible. Another possibility is systematic instrument error in the lidar system, which as we have seen, has the capability to interfere significantly with the proper retrieval of the perturbation windfield.

Accurate estimates of cloud-scale deformation, divergence, and vorticity can be made with an accuracy better than 10^{-3}s^{-1} on a 250 m grid only if the velocities are obtained to within 0.25 m s^{-1} accuracy. For these data, excursions, and presumably errors in drift angle measurements were on the order of 0.2° , leading to uncertainties of about 0.5 m s^{-1} in the retrieved wind data; for larger drift angle errors, large errors in retrieved winds are unavoidable. Hence, many of the computed fields of divergence and vorticity obtained from the lidar data tend to be dominated by the presence of these systematic errors.

Despite the differences in time and altitude, the two circumnavigations reveal the presence of several cloud-scale zones of convergence. Although there was considerable variation in the local pattern (Figs. 3.19 and 3.20), the general character of the environment near the towering cumulus was seen to be one of convergence at both levels. This would tend to confirm the observations of Byers and Braham (1949), who found convergence in active thunderstorms often extended upward from above the low-level outflow up to beyond the mid-troposphere. This represents a substantially different type of cumulus cloud than that observed by Raymond and Wilkening (1982) in the New Mexico mountains, who found convergence below cloud base and divergence above it up to at least 6 km above mean sea level and inferred the presence of strong cloud-top mixing as the dominant entrainment mechanism at work. It should be noted that although our data show considerable evidence in support of the presence of lateral entrainment, the additional presence of cloud-top entrainment cannot be ruled out.

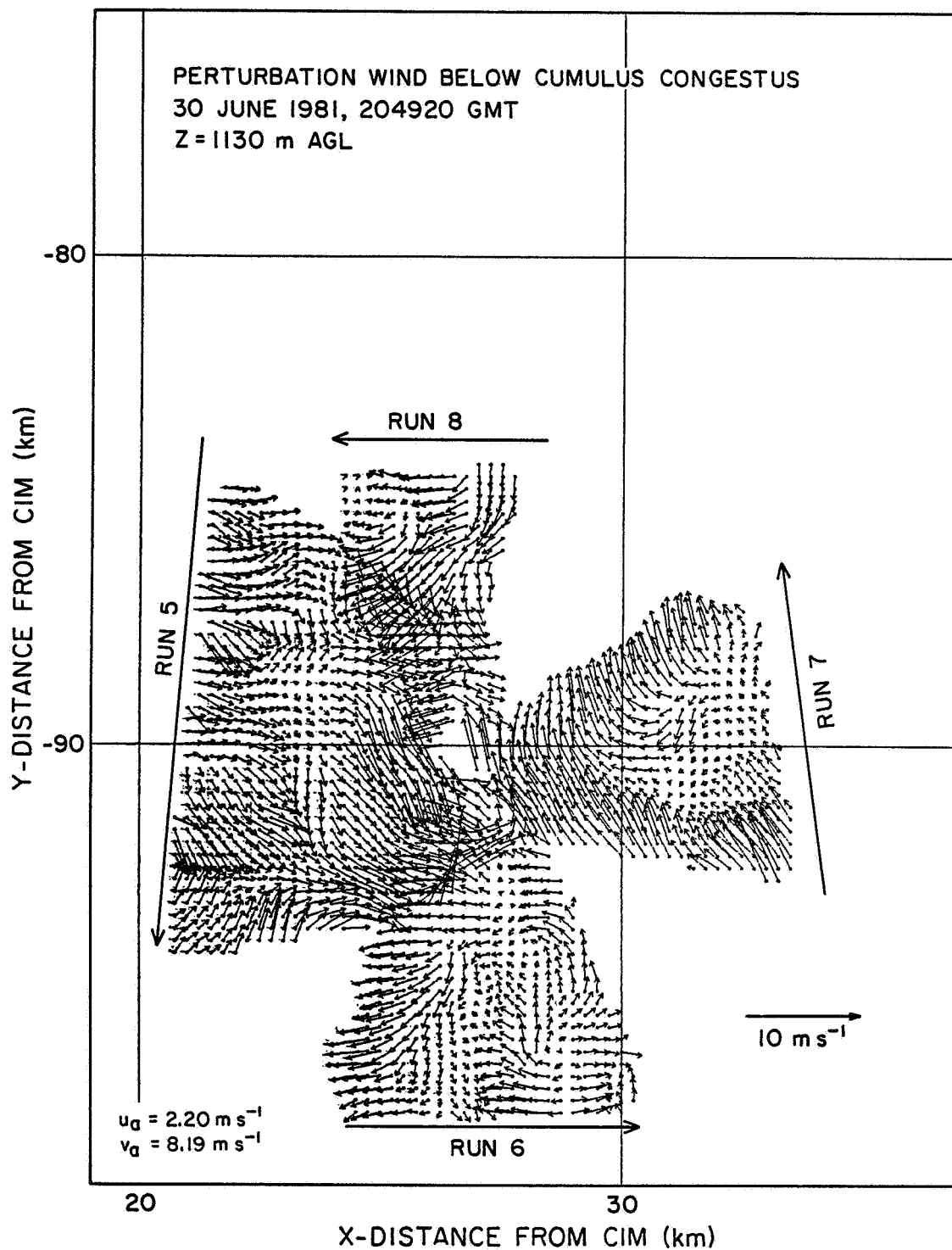


Figure 3.19 Vector plot of perturbation winds at 1130 m AGL

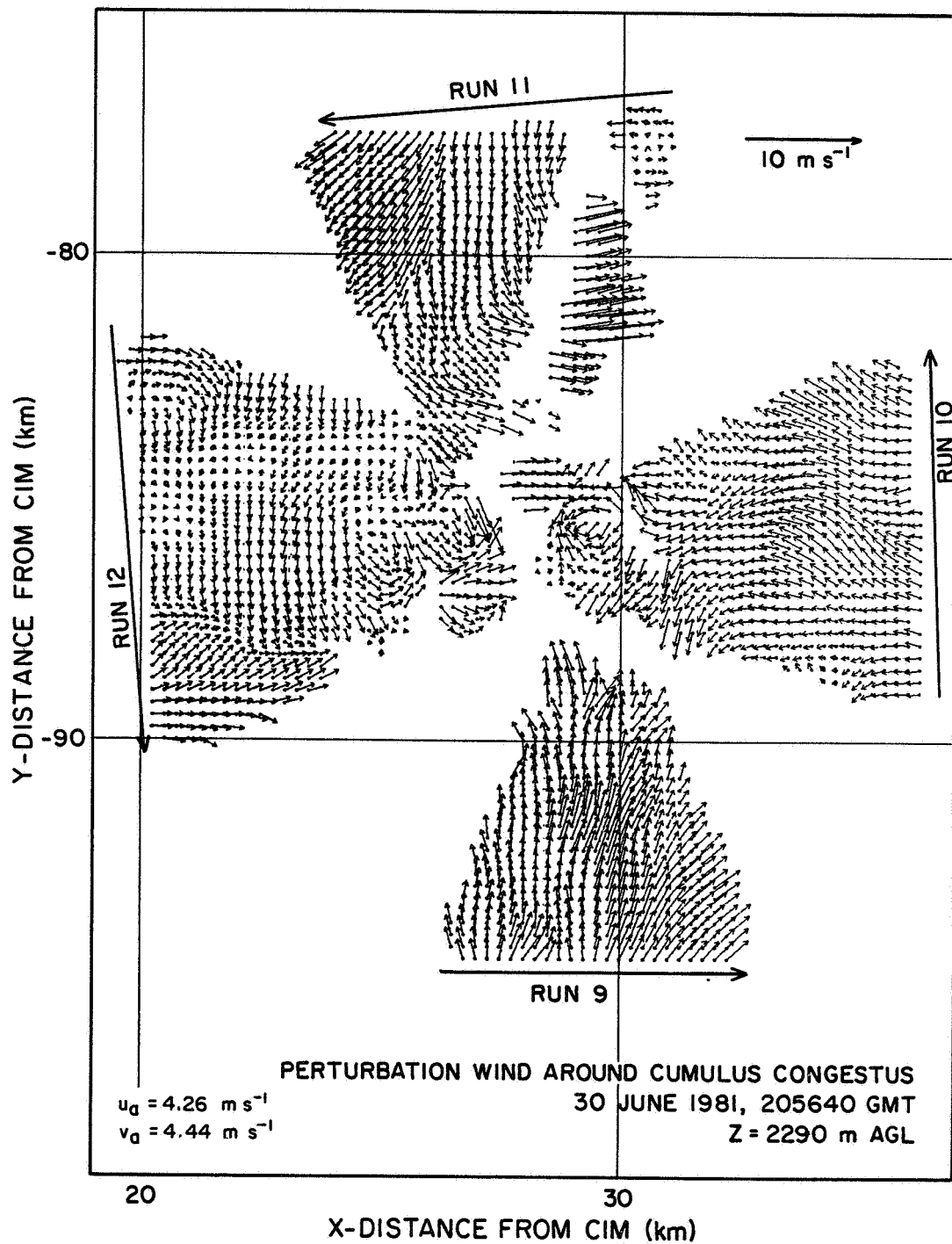


Figure 3.20 Vector plot of perturbation winds at 2290 AGL

This particular towering cumulus cloud failed to grow into an active thunderstorm; tops of the cloud were observed to tilt toward the east and southeast before reaching a level where an anvil could be produced or significant precipitation generated. Such behavior is inconsistent with the observed wind hodographs taken at OKC and TIK earlier in the day, which showed weak winds and weak shear at all levels. Entrainment, which quite likely prevailed at cloud edge based on the prevailing convergence observed at both levels examined, surely played a role in reducing the buoyancy of the updrafts.

The approximate location of the edge of the cumulus may be deduced from an inspection of Fig. 3.21 which shows the pattern of reflectivity from the lidar data taken during runs 9-12. This pattern of reflectivity should be compared with that shown on Fig. 3.22 which is for data below cloud base and which does not show any high reflectivity boundaries. Although some data voids are present in Fig. 3.21, the edge of the cloud may be estimated to follow the dashed line which encloses all the anomalously high intensities. At this point it may be worthwhile comparing Fig. 3.21 with the photo of the cloud shown on Fig. 3.6, taken during run 7. Both figures show that the cloud is ragged, suggesting that the cloud is being eroded, probably by the entrainment of drier air above the mixed layer. This entrainment is consistent with the general pattern of convergence observed (Figs. 3.13 and 3.14). Also important is the fact that, from comparison of Figs. 3.16 and 3.17, the velocities at the higher altitude are slightly smaller than those at the lower altitude and suggest veering with height. Thus the shear vector averaged over the area was from the northeast, which may account for the northeast alignment of the cloud.

Questions still remain as to why the larger thunderstorms were not subject to the unfavorable mechanisms which prevented the observed cumulus cloud from growing into a thunderstorm. Although they were closer to the main frontal boundary, it seems hard to support the view that 40 km of distance from such a weak boundary could make such a large difference in the fate of the convective elements. Such increased distances from the front did not prevent Ft. Sill, in southwestern Oklahoma, from experiencing a heavy thundershower early on the afternoon of 30 June. Further observations with both lidar and radar, including more time continuity studies, along with temperature and pressure measurements and numerical simulation studies of convective clouds in specified environments will be needed to resolve the questions related to the success or failure of individual cumulus clouds to mature into thunderstorms,

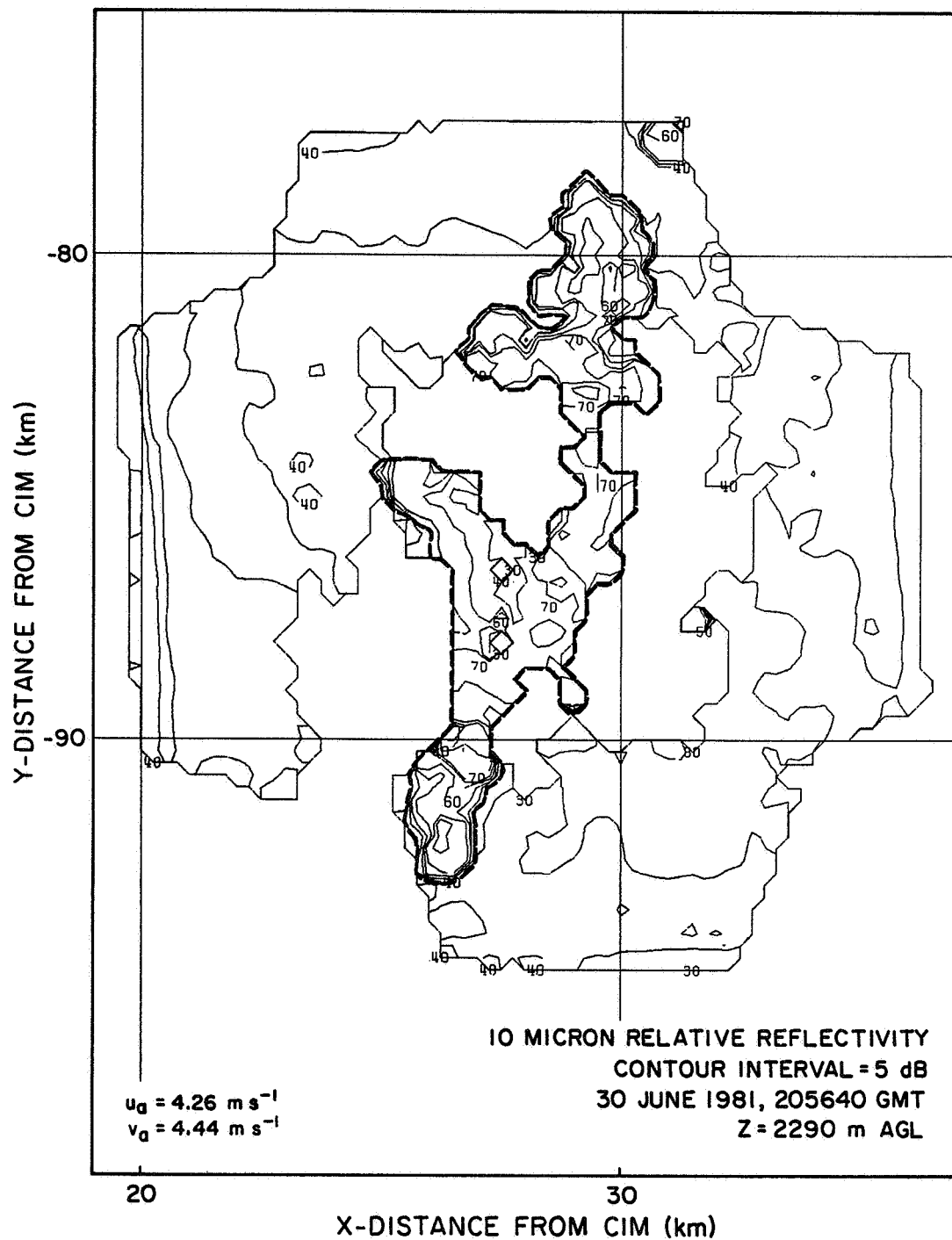


Figure 3.21 Contour plot of normalized reflectivity at 2290 m AGL. Note strong reflectivity gradients at cloud edges (dashed line).

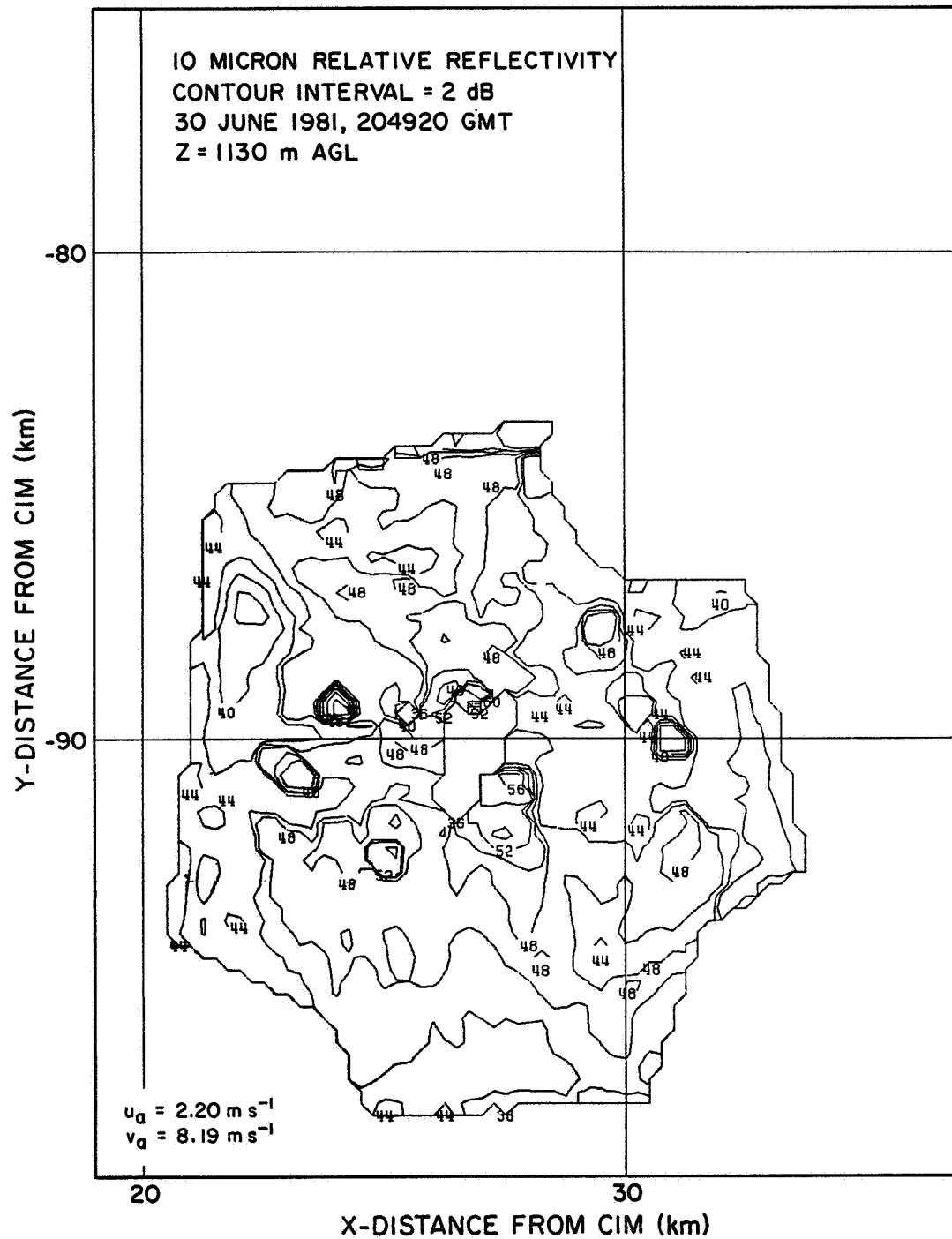


Figure 3.22 Contour plot of normalized reflectivity 1129 m AGL.

and to resolve the questions regarding the evolution of ordinary thunderstorm into severe thunderstorms.

3.6. CONCLUSIONS AND RECOMMENDATIONS

By the use of airborne Doppler lidar it has been shown that significant information not readily available from any other source can be obtained about the flow field in the storm environment. Details of the low-level outflow were mapped for a large multicell thunderstorm system which occurred in Oklahoma on 30 June 1981. In addition, ambient wind flow at cloud base and aloft was studied for an isolated cumulus congestus which occurred that same day.

In the case of the outflow study, waves and vortices were noted along the leading edge of the flow, especially where the outflow air propagated perpendicular to the ambient low-level shear vector. The vortices appeared to be due to tilting of vertical-shear-related horizontal vortex sheets by the differential rising motions ahead of the outflow, to convergence of horizontal shear at the frontal boundary, and possibly to Helmholtz instability of the sheared interface between the warm air and the cool outflow.

The flows around the cumulus congestus were generally characterized by cloud-scale convergence at cloud base and at mid-levels, with a number of confluence lines outside the cloud and divergent flow patterns of a variety of scales at both levels. Flows at mid levels near the cloud edge appeared to be a reflection of the expansion or contraction of active cloud turrets.

An intercomparison with single Doppler radar was attempted for that portion of the lidar data most suitable for such a study, but noisiness and poor resolution in the radar data prevented any definite conclusions from being drawn other than that the instruments agreed to within $1 \text{ m}\cdot\text{s}^{-1}$ on the average velocities retrieved.

Most of the meteorological data fields produced by the Doppler lidar measurements seemed consistent and believable, but there remained evidence, even after intensive data editing, of some systematic errors in the data. These errors were apparently related in a complex way to poorly understood and inadequately measured fluctuations in the aircraft attitude during data collection. Although the basic wind vectors derived from the Doppler lidar data seemed to give a satisfactory and often revealing view of near-cloud flow patterns, systematic errors often prevented clear-cut views of the smaller perturbations in the windfield.

To take full advantage of the airborne Doppler lidar's spatial resolving capability, Doppler velocities must be obtained with a 0.50 m s^{-1} accuracy in order to estimate cumulus-scale (i.e., 500m) divergence and vorticity, which frequently have magnitudes of 10^{-3} s^{-1} . For these data, even the quantization errors in the drift angle measurement on the order of 0.2 deg generated uncertainties of about 0.5 m s^{-1} in the retrieved wind data; because larger drift angle errors also occurred, larger errors in retrieved winds, sometimes on the order of $3\text{--}4 \text{ m s}^{-1}$, were observed. Hence many of the fields of divergence and vorticity obtained from the lidar data tend to be dominated by the presence of these systematic errors.

One explanation for the reason the calculated kinematical parameters proved to be so sensitive to lidar errors has to do with the objective analysis scheme used in the interpolation of raw data to a regular grid. The Cressman weighting function used in the objective analyses of these lidar data was circularly symmetric. Such a weighting function is best suited for use in data fields which are rather evenly distributed. Although in general the lidar data network satisfied this requirement for evenness of distribution, there were notable instances where lidar data along certain noise-contaminated frames had to be deleted. These missing frames tended to occur, of course, in just those parts of the flight characterized by significant velocity fluctuation. The absence of data along these frame radials caused the distribution of raw data points within the circular Cressman regions of influence around some grid points to be quite uneven. The uneven distributions of data within the circles of influence, along with the exaggerated error characteristics of the raw data obtained during turbulent flight, combined to produce especially biased estimates of gridded quantities near the "missing" radials. Application of finite differencing to pairs of gridded estimates which happened to be biased in opposite ways was one way in which the analysis technique used here might have amplified existing errors.

In future work with this sort of data, an interpolation scheme which can deal effectively with asymmetric data distributions in the vicinity of gradients should be used. The interpolation scheme will not be urgently needed if steps are taken to reduce the laser's susceptibility to "moding" during turbulent flight, and if the roll angle compensation in the lidar optics is operating properly.

Whenever the aircraft is experiencing large drift angle perturbations, systematic velocity errors (frame bias) may also enter the data even after applying the algorithm designed to remove frame biases if: (a) the duration of the lidar frame is long with respect to the period of drift angle perturbation, (b) the drift angle perturbation is of a form which allows significant variations in aircraft groundspeed to enter the actual lidar radial velocities, and (c) the values of drift angle and groundspeed assigned to the lidar frame do not correspond to the properly weighted values needed for an accurate removal of the aircraft groundspeed component. In run 3, a possible instance of this problem occurred when the aircraft penetrated the outflow which came from the storm under surveillance. Differences of 2° were noted between successive measurements of drift angle along with 6 m s^{-1} changes in lidar-derived radial velocity between successive like-directed lidar frames. These sharp changes could be associated with significant systematic error in the lidar-derived velocities, which were obtained at each range by averaging the returns from some 50 pulses fired during a 0.5 s period. This problem might be present to a lesser extent whenever the aircraft is flying through air containing milder turbulence.

In order to eliminate this problem, it would be necessary to remove the aircraft's time-varying ground-relative component of Doppler shift in the echo of each transmitted pulse prior to the averaging which provides the estimate of radial velocities along a frame. If this proposed method of eliminating the problem is too burdensome to be compatible with real-time hard-wired data processing, then an alternative approach would be to record more frequently the drift angle, heading, and groundspeed. Further study of this potential source of error seems warranted to determine its importance for future work with this type of data.

Another potentially significant source of error that could affect the computation of lidar-derived wind vectors is that related to possible differences in altitude of the fore and aft data used in solving for the wind vectors. Due to the beam pointing errors which the lidar system experienced as a result of the scanner's roll and pitch compensation problems, there was a $1\text{-}2^\circ$ uncertainty in the beam elevation angles. Obviously, fluctuations in lidar beam elevation angle will have their most injurious effect on retrieval of wind vectors at large ranges from the aircraft and in situations characterized by strong vertical shear. In fact, for a range of 10 km from the aircraft, the use of two different lidar frames having elevation angles differing

by 2° implies use of radial wind data from levels separated by about 350 m. When vertical shear is strong (e.g., 10^{-2} s^{-1}) this difference can produce errors comparable to the errors produced by the drift angle delay.

A conservative estimate of the wind speed error caused by beam elevation errors is 0.5 m s^{-1} except above the outflow on runs 2 and 3 and along the cloud turrets of runs 9-12, where local errors appeared to reach $2\text{-}3 \text{ m s}^{-1}$. Clearly, the problems of laser misalignment and failure of the scanner to provide the proper beam elevation compensation during aircraft rolls should be corrected before the next series of experiments. In addition, it would be desirable if scanner positioning could be updated at least occasionally during each lidar frame so as to ensure horizontal beam trajectories for all pulses.

Another source of error contaminating the lidar data is that associated with uncertainty of aircraft groundspeed. If delays are present in the reporting of data during periods when the aircraft is neither accelerating nor decelerating, analysis shows that ground velocity uncertainty contributes only about 0.3 m s^{-1} to radial velocity errors in the lidar wind data. However, if the aircraft is accelerating or decelerating, then ground velocity errors can be as large as the product of the acceleration and the delay. This can be a significant source of error during reconstruction of the wind fields.

Several other problems were encountered during the data analysis with respect to improper sampling or recording of various aircraft motion and attitude parameters. Improved accuracy and detail in the recording of latitudes, longitudes, velocities, angles and times will be helpful in future work with the data from the NASA's airborne Doppler lidar. In view of the magnitudes of some of the velocity errors found in some parts of the flight, special care should be taken to insure that a detailed record of the INS performance is maintained. It is especially important that all portions of data collection flights be documented with nadir photography, so that the aircraft positions computed by the INS can be compared with the actual positions obtained from detailed maps. The timing of the photographs should be perhaps slightly faster on short flight legs (such as those found in cloud circumnavigations) in order to get a sufficiently large number of photos per run.

One possible alternative to the use of nadir photography in determining whether or not the INS is furnishing erroneous data involves a scheme in which ground strike data are obtained after every fore/aft frame pair and the mea-

sured Doppler velocity of the ground compared with its expected value of zero. While this idea shows considerable promise for providing a direct way of measuring the INS errors, the nadir photography should not be dispensed with until the merits of any newly proposed technique have been established experimentally.

With respect to the determination of the delays which tend to occur in the data recording process, one possible way of studying this problem would be to fly a specially designed test track at both the beginning and the end of each day's data collection effort. The track would consist of level flight, first at a constant but slow ground speed of say 120 m s^{-1} for a period of about 30 s; this would be followed by a 30 s period of steady acceleration to a ground speed of 150 m s^{-1} , then followed by 30 s of flight at that high velocity; finally another 30 s period of steady deceleration back to 120 m s^{-1} would ensue. After another 30 s of straight flight at 120 m s^{-1} , a final 60-s leg featuring shallow weaving and banking maneuvers to the left and the right would be made, with banking in each direction lasting 10 s or so. Nadir photographs would be taken every 3-5 s to provide adequate coverage of each leg of the test run, and the lidar would operate in its normal data collection mode. Inspection of the wind field analyses from such test runs would be undoubtedly helpful in showing whether any errors or inconsistencies are affecting the data.

In summary, the lidar thus far has demonstrated considerable promise in portraying the details of the clear air flows near an assortment of convective clouds. Not only can the wind fields be obtained in the clear air near cloud edges, but the probable locations of those cloud edges can be determined from inspection of the echo intensities. Doppler spectral widths often are useful in locating wind field shifts and perturbations. Revisions to the lidar system which are currently underway will probably correct most of the problems noted above, and result in even more detailed and revealing insights of the flows near convective clouds.

APPENDIX A

DESCRIPTION OF INSTRUMENTATION

A.1 Doppler Lidar

A description of the lidar system has been given in Bilbro, **et al.** (1984), nevertheless, certain features of the system merit discussion due to the novelty of the instrument's use in this type of experiment and the ways in which system performance can affect data quality. Fig. A.1 depicts in block diagram form the system's main components and their interrelationships.

The NASA lidar employs an 8 W continuous-wave CO₂ laser which emits infrared radiation at a wavelength of 10.6 μm . This laser, which acts as the master oscillator in a master-oscillator power amplifier system, sends its output to a beam splitter, which transmits most of the infrared beam along a pathway toward the atmosphere, and diverts the small remaining portion for use as a reference frequency during detection of the Doppler shifted echoes.

That portion of the beam which is bound for the atmosphere is first sent to an electro-optic modulator where it is converted from a vertically polarized continuous wave into a train of horizontally polarized 2.0 μs pulses at a rate of f_p of 100 Hz. The electro-optic modulator consists of a mercury cadmium telluride crystal flanked by polarizing filters of vertical and horizontal orientation at its input and output sides respectively. The actual conversion of the CW radiation into a pulse train with new polarization occurs because the crystal, under the influence of a transverse electric field (applied for the specified pulse duration at the specified pulse repetition rate), becomes birefringent and causes the vertically polarized radiation from the input filter to acquire horizontal polarization during passage through the crystal, thus permitting unobstructed passage through the output filter only during those time intervals designated for pulse transmission. The pulses produced by the electro-optic modulator then pass through a Faraday optical isolator which prevents scattered radiation from re-entering the master laser and causing any frequency shifts ("pulling") in that Laser's output.

Next the pulses enter a beam expander and a series of amplifiers where they experience some 36 dB of gain, giving them typical energies of about 15 mJ per pulse. The pulses then pass through a Brewster window aligned to

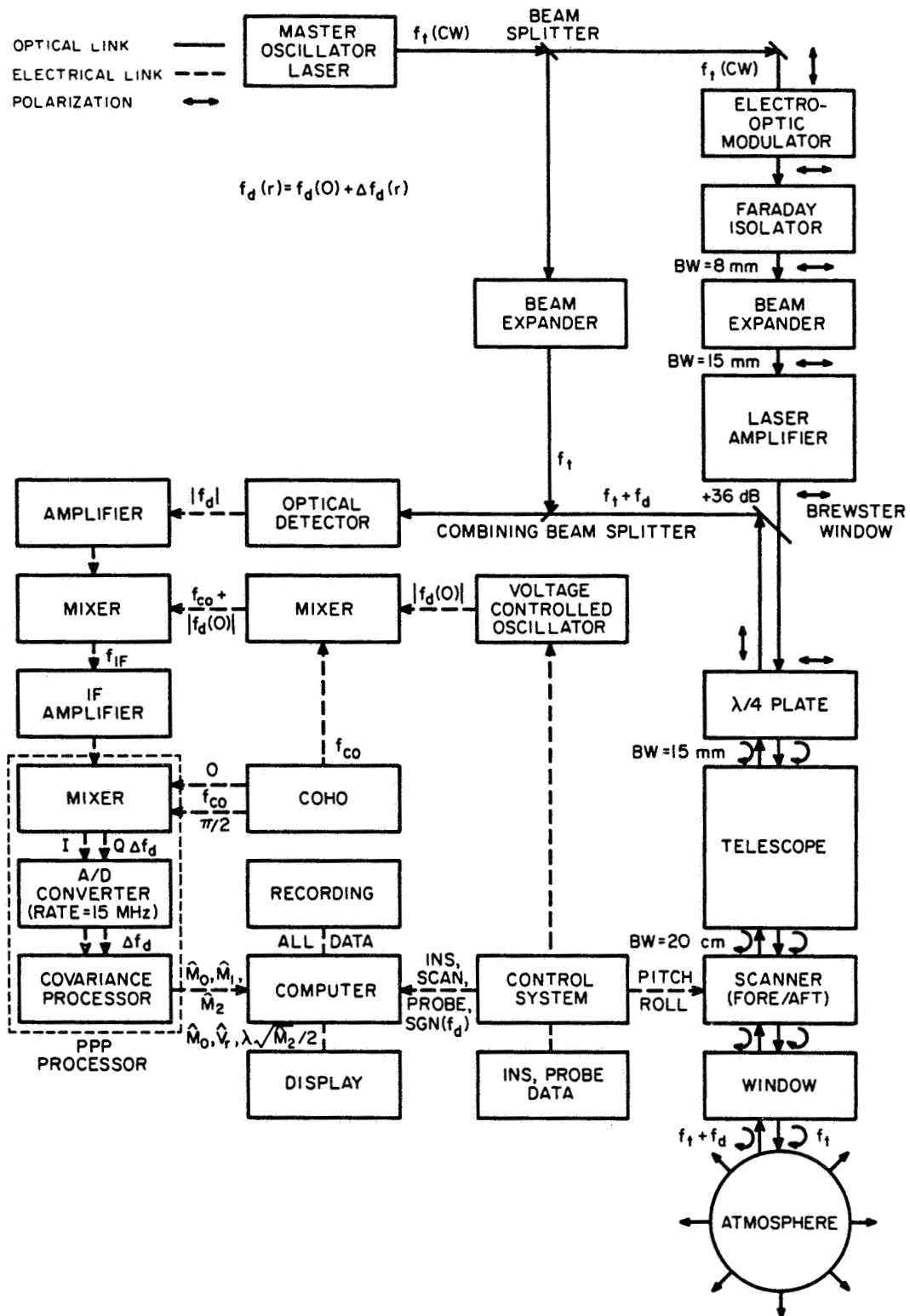


Figure A.1 Block diagram of NASA's Airborne CO₂ Doppler Lidar System (ADLS). BW is the width of the beam. Symbols are defined in the text.

pass only horizontally polarized radiation. Next the pulses pass through a quarter-wave plate made of transparent material having an index of refraction which is a function of the polarization orientation. The quarter-wave plate is oriented so that the mutually perpendicular axes for which indices of refraction are minimal and maximal are both 45° from the horizontally oriented axis of polarization of the outbound laser radiation. Thus, after traversing the quarter-wave plate, one component of the initially horizontally polarized radiation lags its normal component by 90° of phase, and the resulting net radiation transmitted by the plate is circularly polarized.

After passing through the quarter-wave plate the pulsed beam is expanded and collimated by an all-aluminum folded parabolic off-axis telescope and directed through a scanner which deflects the beam out an exit window on the left side of the aircraft and onto a specified path through the atmosphere. Because of the series of expansions the laser beam undergoes while on its way through the system optics, the width of the beam increases from about 8.5 mm at the master oscillator to about 20 cm at the point of entry into the atmosphere, as measured between the $(1/e^2)$ points of a Gaussian function which approximates the power distribution across the beam.

The scanner consists of a pair of separately rotatable germanium wedges, the angular orientations of which determine the beam's trajectory within a cone having a 19.6° half-angle and axis normal to the left side of the aircraft. For this experiment the system was programmed so that the scanner wedges would, for any value of aircraft pitch and for all values of aircraft roll smaller than 9° , direct the beam in a true horizontal plane at the maximum possible forward and aft deviations from the centerline of the cone, which itself always points normal to the left side of the aircraft. For roll angles greater than 9° , the wedges were programmed simply to direct the beams out the aircraft at the angle (relative to the aircraft) that would be chosen if the aircraft were assumed to be in roll-free flight. Thus, in the absence of significant aircraft roll, the pulses were to be horizontally directed approximately 20° fore or aft of a line extending from the left side of the aircraft and having an orientation normal to the aircraft heading vector (Fig. 1.1).

Lee (1982) found evidence from some lidar data taken in California in 1981 that the scanner was directing the lidar beam slightly out of the horizontal plane during quasi-roll-free flight. He measured elevation biases of about -0.4° for aft shots and $+1.0$ or more for fore shots. Because such beam

elevation biases can lead to significant differences in the altitudes of the various resolution volumes of data used in the objective analyses, attempts were made in this study to confirm whether or not the scanner was operating according to specification. The technique used to assess scanner performance and the results and implications of that assessment are discussed in Appendix E.

Typical operation of the data sampling cycle in this experiment involved the transmission of about 50 pulses, requiring about 0.5 s in the forward direction, followed by a time gap of at least 0.6 s for the reorientation of the wedges, followed by the transmission of about 50 pulses in the aft direction, and again reorientation of the wedges. This pattern was repeated more or less continuously for the several minutes of each of the many data runs. For the purposes of subsequent discussion, each distinct sequence of 50 similarly directed transmitted pulses is denoted by the term "frame". The wedges remain locked in position during the interval in which the pulses of each frame are transmitted. In this experiment, the period between frames varied from 1.1 to 1.5 s. Although generally each frame was followed by a counter-directed frame, exceptions to this rule were occasionally noted.

The sense of rotation of the polarization vector of the backscattered radiation, viewed along the direction of propagation, is reversed by spherically symmetric scatterers (Newell *et al.*, 1955). Thus, the radiation which was originally right-circularly polarized prior to being scattered becomes left-circularly polarized after being scattered (see Fig. A.1). This returned radiation is also characterized by a Doppler shift in frequency given by $f_d = -2V_r/\lambda$, where λ is the wavelength of the transmitted radiation and V_r is the target's radial velocity (positive when motion is away from the lidar) relative to the aircraft. The received signal (quasi-continuous in time if aerosols are quasi-uniformly distributed in space) when sampled at any range-time delay (i.e., time interval following the transmission of the pulse) gives a sample amplitude proportional to the sum of the incoherent echoes from all scatterers within the resolution volume associated with that particular sample (Doviak and Zrnic', Chapter 4, 1984).

After returning to the telescope, the Doppler-shifted "echoes" travel back through the quarter-wave plate where they have their polarization converted from circular to planar (Fig. A.1). During this final change of polarization, the lagging component of the circularly polarized backscattered

wave experiences a further retardation of phase by 90° , causing the received signals to acquire vertical polarization instead of the horizontal polarization they originally possessed prior to traversing the quarter-wave plate on the outbound portion of their excursion into the atmosphere. The Brewster window which the returns encounter next thus reflects them toward a beam splitter which combines them with the original master oscillator signal and directs both to the surface of a cryogenically cooled mercury cadmium telluride detector.

The detector takes the resulting time-varying interference patterns and converts them into an output signal having a modulation frequency equal to that of the Doppler shift f_d of the echo signals. Fig. A.2a shows a pair of transmitted pulses and (b) the interference pattern, at the detector input, caused by mixing the Doppler shifted echo signals (assumed to be returned from a uniform distribution of targets all having the same 10 m s^{-1} velocity) with the master oscillator signal. The repetition time (PRT) of the pulses and the corresponding spatial separation are indicated on the figure as well as the approximate pulse shape, but the schematic exaggerates the period f_t^{-1} of the radiation. The Doppler shift $f_d(r)$ associated with the echoes from the various resolution volumes is due to the aerosol target speed added to the aircraft airspeed along the lidar line-of-sight (L.O.S.). An aircraft airspeed of 150 m s^{-1} causes about a $\pm 10 \text{ MHz}$ shift for the fore- or aft-directed beams.

Although the optical detector cannot distinguish positive from negative Doppler shifts (that is the reason for absolute signs around f_d in Fig. A.1), ambiguities in the sign of $f_d(r)$ are avoided because of the dominance of the Doppler shift due to aircraft airspeed along the lidar L.O.S., a shift whose sign can always be determined from a knowledge of the direction of the lidar scan. Now $f_d(r)$ may be expressed in terms of the Doppler shift due to the aircraft airspeed along the L.O.S., namely $f_d(0)$, and some superimposed range-dependent deviations $\Delta f_d(r)$ from $f_d(0)$ due to the L.O.S. speed of aerosols relative to the L.O.S. speed of air at the aircraft.

Following extraction of the Doppler-shifted signal by the detector, an amplified version of the detector's output is mixed with a signal having a frequency given by the sum of $f_{co} = 60 \text{ MHz}$ and $|f_d(0)|$, the latter being near 10 MHz , to produce a difference frequency at an intermediate frequency f_{IF} near 60 MHz but shifted slightly from it by the amount $\pm \Delta f_d(r)$ for the aft or

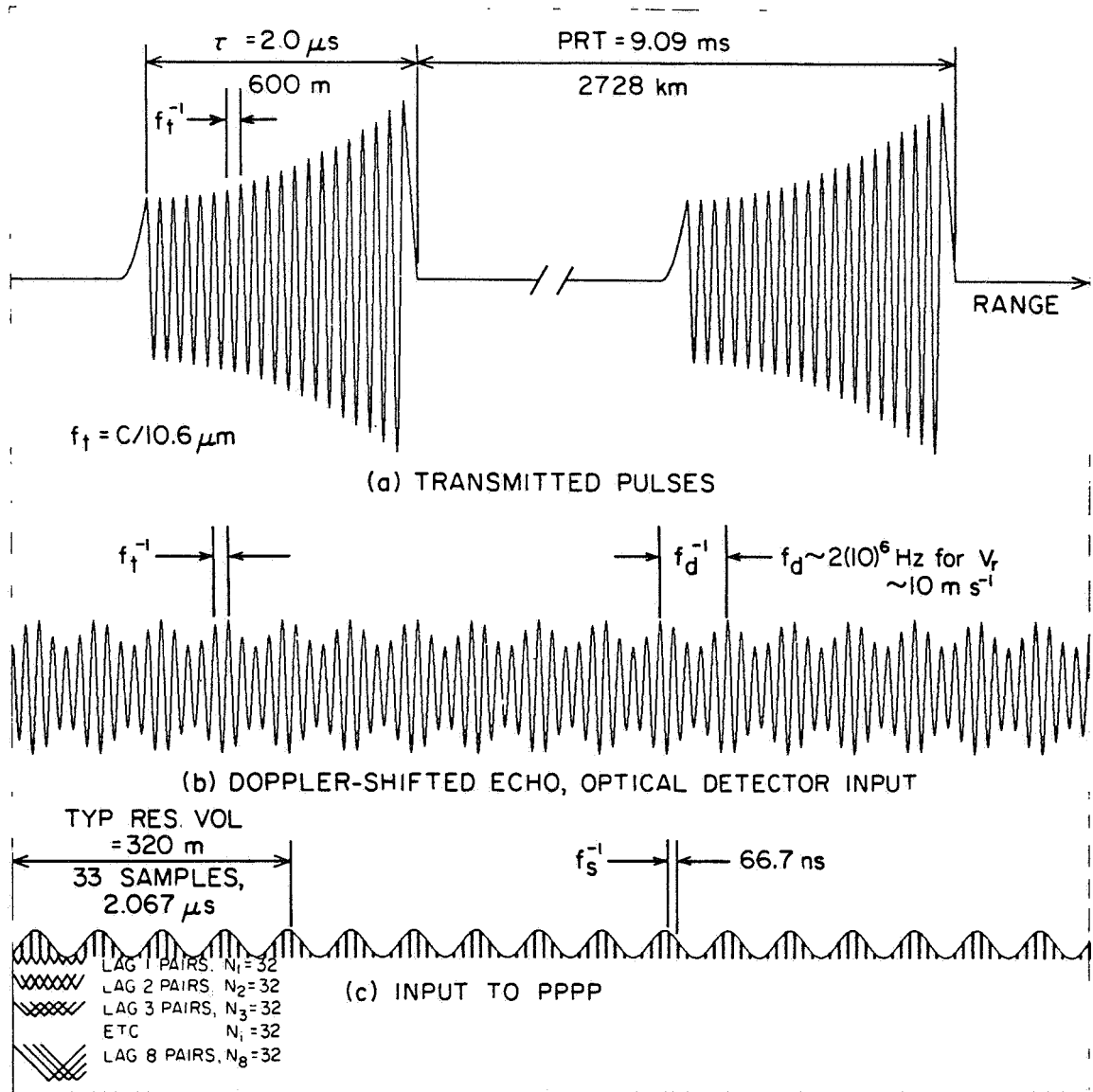


Figure A.2 Transmitted pulses (a) and the interference pattern (b) at the input to the optical detector assuming airspeed is zero and aerosols are uniformly distributed and all move at a radial velocity of 10 m s^{-1} . (c) The inphase (or quadrature phase) signal input to the poly pulse pair processor's (PPPP) analog to digital (A/D) converter. The bold vertical lines indicate the spacings of signal samples digitized by the A/D Converter.

fore beams respectively. The 60 MHz signal is supplied by a coherent oscillator (COHO), while the signal having frequency $|f_d(0)|$ is supplied by a voltage-controlled oscillator (VCO) tuned to the most recent value of the aircraft airspeed component along the lidar line-of-sight. The signal $|f_d(0)|$ is added to f_{co} in the mixing process in order to keep the mixer's output near 60 MHz, and to obviate the need for estimating directly the inconveniently large Doppler shift $f_d(r)$. The aircraft's airspeed is measured by a probe and monitored by the Central Timing and Control System (CTCS) which provides commands to the VCO.

The signal, now at f_{IF} , is next sent to a poly-pulse-pair processor (PPPP) where it is mixed with inphase (0) and quadrature phase ($\pi/2$) components of the COHO voltage in order to generate the complex video (I and Q) version of the range-dependent Doppler shift $\Delta f_d(r)$, the sign of which is determined by the relative phase of I and Q. Figure A.2c shows the I or Q signal at the input of the PPPP or, if airspeed is zero, at the output of the optical detector. In the PPPP, the complex video, usually having a frequency of not more than several MHz, is converted from an analog signal to a digital sample at a 15 MHz rate and then subjected to the autocovariance and spectral processing which produces the estimates of the signal's first three moments: intensity (zeroth moment M_0), mean frequency (first moment M_1) and spectral width (the square root of the second moment M_2).

The poly-pulse-pair processor represents a natural extension of the familiar pulse-pair processor (PPP) employed in most Doppler weather radar systems. In the PPP, the mean frequency shift of the returns from a resolution volume is estimated from the argument of the first lag of the autocovariance function (acvf) of the digitized complex video signal. However, because of the smallness of the phase shifts that occur during the timespans of the pulse durations typically used by Doppler radar, the autocovariance estimation technique for such systems usually involves formation of lagged products of echo signal samples associated with sequentially transmitted pulses. In contrast, because of the larger Doppler phase shifts associated with the use of the lidar's higher transmitted frequencies, the calculations of autocovariance made by the lidar's poly-pulse pair processor is accomplished using echo samples associated with individual transmitted pulse. Furthermore, because the lidar has a wavelength much shorter than the radar, echos from successive transmitted pulses are uncorrelated for the PRTs used. However, for each resolution volume the PPPP averages 32 lagged products at

each lag of the acvf examined in order to reduce the statistical fluctuations of the estimated acvf. Although 32 contiguous samples (spaced $\tau_s = 66.7$ ns apart) for each lag product (Fig. A.2c) are averaged to reduce the statistical uncertainty in the covariance estimates, the equivalent number of independent samples effective in reducing variance is significantly less than 32 for large signal to noise ratios (SNR) because the contiguous lag product samples, when spaced within the time span of the transmitted pulse, are highly correlated (Doviak and Zrnic', 1984). However, for low SNR samples of signal plus noise are not highly correlated and hence a large number of nearly independent estimates are obtained to reduce variance in the estimate of the acvf.

The PPP uses only the zeroth and first lag of the acvf to estimate the mean frequency M_1 and width $\sqrt{M_2}$ of the Doppler spectrum, whereas the PPPP estimates the first 8 lag (i.e. $1\tau_s \leq n \tau_s \leq 8\tau_s$) products of the acvf in order to improve the accuracy of these spectral moment estimates. The acvf is then Fourier transformed after setting to zero those values of the acvf that are not estimated at longer lags (i.e., $1024\tau_s > n\tau_s > 9\tau_s$). This zero weighted extension of the lag domain increases the density of lines in the spectral domain so that the peak of the Doppler spectrum is better resolved. In NASA's PPPP the 8 lag acvf is unweighted before the Fourier transformation is performed but it has been shown (Lee and Lee, 1980) that an optimum weighting is obtained when each lag product is multiplied by the magnitude of the acvf at its respective lag before the Fourier transformation. The first moment estimate \hat{M}_1 (the caret symbol is used to signify an estimate) is then the Doppler shift of the line which has the largest power. The intensity \hat{M}_0 of this line is also recorded in order to estimate echo power given the estimate \hat{M}_2 and noise power, as well as the assumption of a Gaussian shaped Doppler spectrum. However, no attempt was made to incorporate the second moment estimate \hat{M}_2 in the computation of echo power. The truncation of the acvf at $8\tau_s$ generates a spectral window that is usually much broader than the width of the Doppler spectrum associated with turbulent velocities inside the resolution volume. In this case, the intensity of the peak spectral line is proportional to the signal plus noise power. Although the zeroth lag product is not computed, errors in power estimates are usually small (i.e., <1dB) when the Doppler spectral width is small compared to the width of the spectral window. The second moment M_2 is estimated by least-squares fitting the measured autocovariance magnitude to the assumed Gaussian function. The noise power may be estimated by examining the behavior of the peak line intensity as

a function of range where targets are not detected and may be removed from each intensity estimate via an algorithm described in Appendix D.1. The actual estimates of intensity, velocity and width assigned to a given resolution volume are the average values in the appropriate "range bin" (range interval corresponding to the resolution volume, numbered and ordered with respect to distance from the aircraft) obtained from processing echo samples from each of the 50 transmitted pulses that comprise each frame of moment data.

After calculating the spectral moments in all resolution volumes of a given data frame, the PPPP sends the results to an on-board minicomputer which computes the target's Doppler velocity relative to ground using the aircraft ground velocity and airspeed estimates derived from the Inertial Navigation System (INS). Fig. A.3 depicts the relation between the various components of aircraft-measured velocities and the PPPP estimate \hat{M}_1 . This figure is drawn for the hypothetical case in which the lidar is measuring wind at zero range (i.e., at the aircraft itself). In the case depicted, the true airspeed vector equals the sum of the ground velocity and wind vectors, but the drawing is equally valid if the wind vector is measured at nonzero range, however, in this latter case the sum of the ground velocity and wind vectors does not equal the true airspeed vector. Sensors measure the airspeed along the heading direction but the true airspeed vector is the vector sum of the measured airspeed and the speed of air perpendicular to the heading ("sideslip"). Although sideslip is not measured by the aircraft sensors, the accuracy of the lidar-derived radial wind data is not compromised, since any sideslip velocity components are automatically included in the lidar's radial velocity estimates. However, the INS estimates of wind at the aircraft will be in error if the sideslip is nonzero.

For accurate retrieval of the Doppler velocities, the VCO (Fig. A.1) must accurately track the measured airspeed such that $f_d(0)$ always equals:

$$|f_d(0)| = 2 (\text{REF } V_r) / \lambda \quad (\text{A.1})$$

for the fore and aft radial components of measured airspeed which establish reference Doppler velocities "REF V_r ". However, it is not critical that the VCO frequency satisfy Eq. (A.1) exactly, since the L.O.S. airspeed component REF V_r removed from the raw Doppler signal during generation of f_{IF} is restored intact during subsequent calculations (see Eq. (A.2) below) in which account is taken of the L.O.S. components of aircraft airspeed and ground

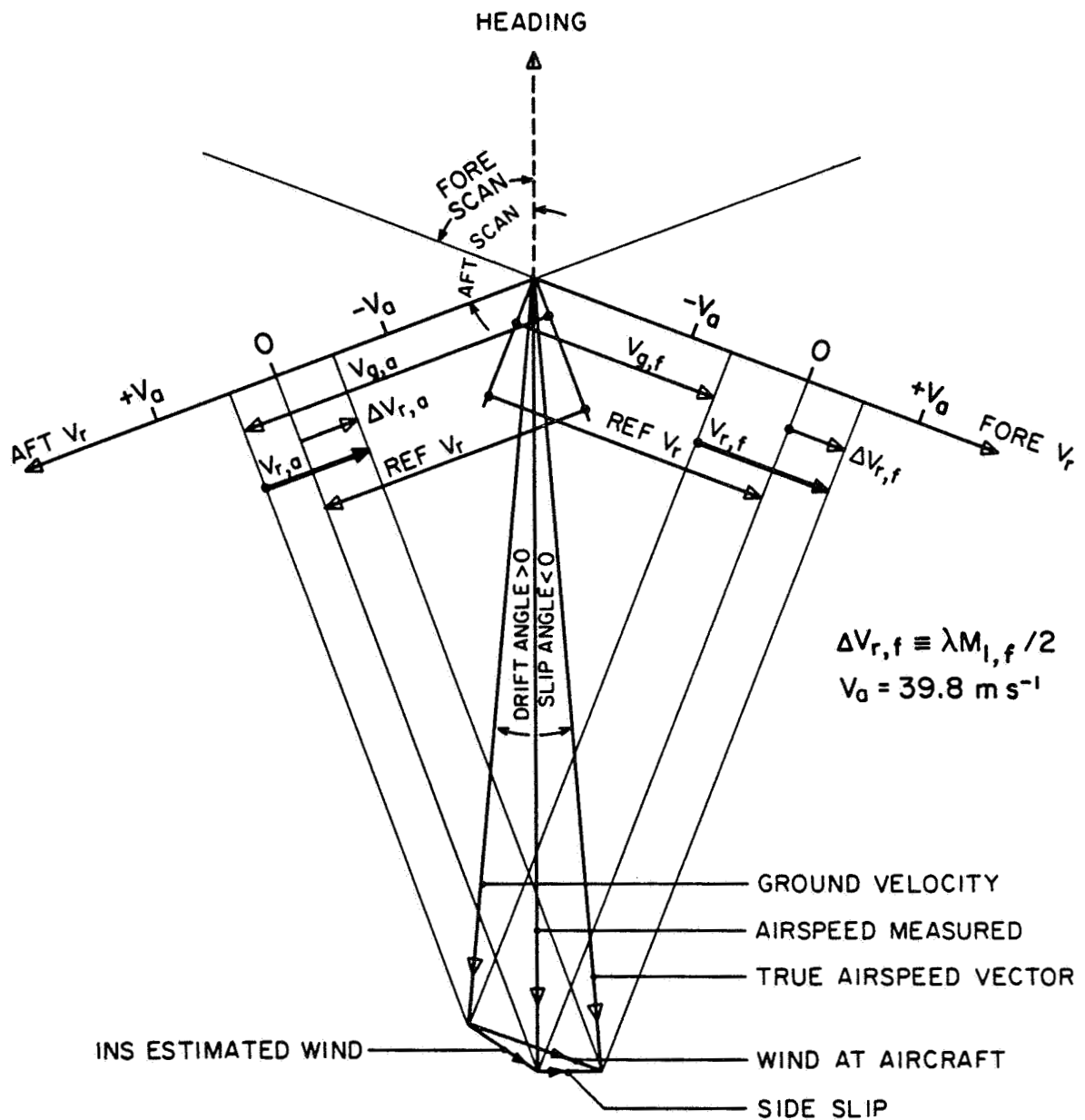


Figure A.3 The various velocity components used to derive the horizontal wind vector from lidar measurements. This schematic assumes the measurement of wind is made at $r=0$ (i.e., at the aircraft) where the sum of aircraft's ground velocity and wind equals the true airspeed vector.

velocity. As mentioned earlier the REF V_r is used in order to place the observed Doppler shifts into the bandwidth of the PPPP, which has a Nyquist velocity V_a of 39.8 m s^{-1} . Because the fore and aft data are not acquired simultaneously the fore and aft REF V_r are generally not equal to each other as they are in Fig. A.3.

The quantity ΔV_r is the velocity to be estimated by the PPPP (i.e., $\Delta V_r = \lambda M_1/2$). Using Fig. A.3 it is easy to deduce the relations between the fore and aft radial components of the wind and those measured quantities $\hat{\Delta V}_r$, INS-estimated ground velocity, and REF V_r . The equations deduced from this figure are.

$$V_{r,a} = \Delta V_{r,a} - (\text{REF } V_r - V_{g,a}) \quad (\text{A.2a})$$

$$V_{r,f} = \Delta V_{r,f} + (\text{REF } V_r - V_{g,f}) \quad (\text{A.2b})$$

where $V_{r,a}$ and $V_{r,f}$ are the L.O.S. components of the wind vector along the aft and fore directions respectively, and $V_{g,a}$ and $V_{g,f}$ are the L.O.S. components of the aircraft ground velocity in those respective directions. These equations are equally valid for measurements of wind far from the aircraft where the sum of ground velocity and wind does not equal the true airspeed vector.

The digital sampling rate, 15 MHz, used in the PPPP is such that the highest Doppler frequency unambiguous to the processor, 7.5 MHz, corresponds to a Doppler velocity of 39.8 m s^{-1} relative to the measured aircraft airspeed REF V_r along the lidar line-of-sight (see Fig. A.3). Signals having Doppler frequencies larger than 7.5 MHz relative to $f_d(0)$ are filtered at the input side of the PPPP's digital converter. Nevertheless, ground-relative radial wind velocities of magnitude greater than 39.8 m s^{-1} can be measured by the system if V_g differs from REF V_r such that ΔV_r remains within the Nyquist interval $(-V_a, +V_a)$. However, if the wind vector produces a L.O.S. velocity ΔV_r larger than 39.8 m s^{-1} an accurate estimate of ΔV_r will not be made because the signal with the Doppler frequency implied by such a large deviation will be filtered at the input to the PPPP and then only noise will remain to be analyzed by the processor. This has implications for the strategies which will be needed if the ADLS is to be used successfully to study such intense phenomena as tornadoes and tropical cyclones, where the variations of radial velocity along certain lines-of-sight could exceed 39.8 m s^{-1} . On the other hand, it also indicates the importance of tracking REF V_r with the VCO

in order that the Doppler-shifted echoes do not fall outside the Nyquist interval.

A diagram showing the typical arrangement of resolution volumes in a data frame and of lines of sight associated with successive frames is given in Fig. A.4. Networks of fore- and aft-directed data are generated by the pulsed lidar beam as it scans the area to the left side of the aircraft. Both networks are presumed to lie in the same horizontal plane in the data analyses described in the main body of this report. Because many of the lidar lines of sight deviated slightly from true horizontal due to aircraft roll and surveyor error, some of the fore and aft resolution volumes which appear to overlap when viewed in plan actually differ in altitude by amounts which increase with range. This point receives further discussion in Section 3.4.3. A tabular listing of all important parameters governing the operation and performance of the Doppler lidar system is given in Table A.1.

A.2 DOPPLER RADAR

The National Severe Storms Laboratory (NSSL) operates two 10 cm Doppler radars, one located in Norman (NRO) and the other at Page Airport (CIM, formerly Cimarron airport) 40 km northwest of NRO (Fig. 3.2). Parameters from these Doppler radars are compared with parameters of the lidar system in Table A.1. The obvious advantage of the lidar system is that it has excellent angular resolution and low power requirements. However, its range is limited and because of strong atmospheric attenuation, increases in transmitted power do not increase range in direct proportion to the increase of transmitted power.

The Doppler radar operation principles and methods have been described elsewhere in detail; see for example Doviak and Zrnic' (1984), or Doviak et al., (1979).

A.3 OTHER INSTRUMENTS ON BOARD THE AIRCRAFT

In addition to the lidar itself, a number of additional instruments on board the CV-990 took measurements which were important to the success of the experiments. For the sake of completeness, those instruments which furnished data mentioned (excluding cameras), are briefly described here. Where available, information regarding the resolution and probable accuracy of the various system components is included, for further details see Bilbro (1982) and Ames Research Center (1981).

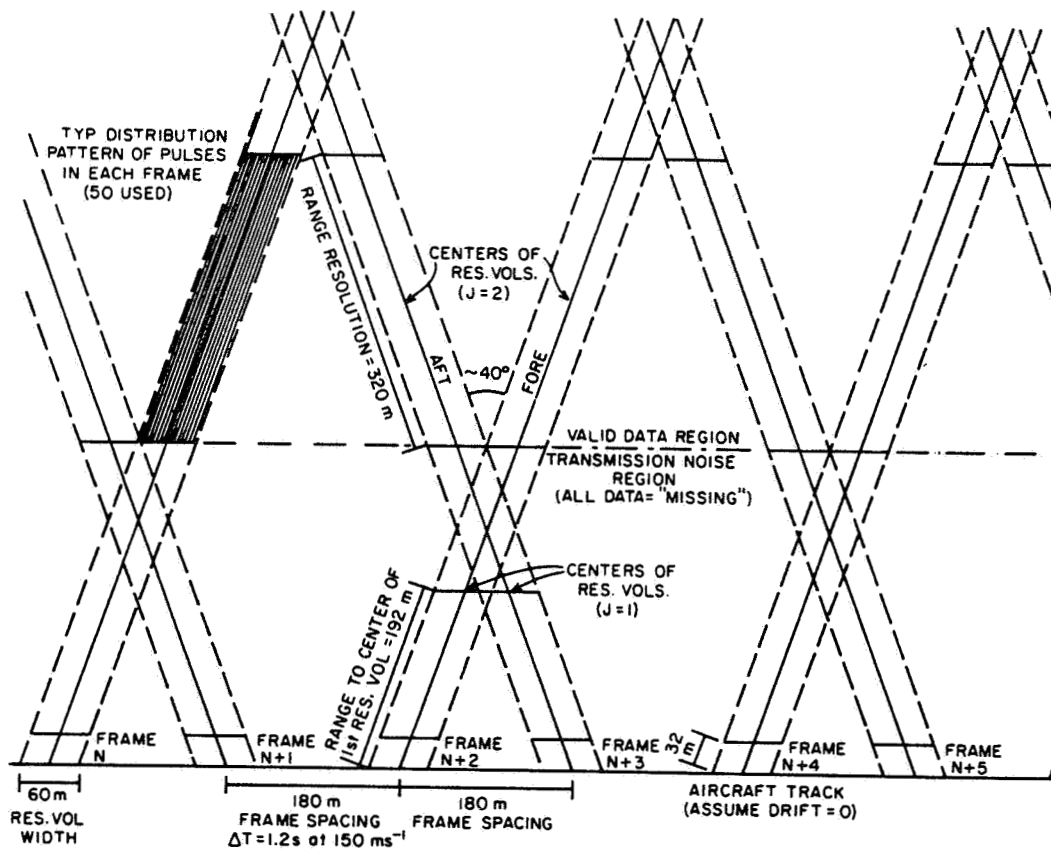


Figure A.4 Typical arrangement of data samples in space. Raw data values (i.e., M_0 , M_1 , M_2) for each resolution volume are the result of Poly Pulse-Pair Processing echos from 50 transmitted pulses.

TABLE A.1
Doppler Radar and Lidar Parameters

<u>Parameter</u>	<u>NRO</u>	<u>CIM</u>	<u>Lidar</u>
Beamwidth (3 dB width)	0.81°	0.85°	20 cm
Resolution Volume Range Length	150 or 450 m	150 or 450 m	320 m
Peak Transmitted Power	750 kW	600 kW	6 kW
# of Transmitted Pulses for a Velocity Estimate	64	64	50
Pulse Width	1 or 3 μ s	1 or 3 μ s	2 μ s
Unambiguous Range	115 or 345 km	115 or 345 km	1364 km
Nyquist Velocity	34.3 or 11.4 m s ⁻¹	35.4 or 11.8 m s ⁻¹	39.8 m s ⁻¹
Wavelength	10.5 cm	10.9 cm	10.6 μ m
Maximum Range of Detected Targets (clear air)	≈80 km	≈80 km	≈10 km
Maximum Range Sampled	all	all	28.8 km

a. INERTIAL NAVIGATION SYSTEM (INS)

Two Litton LTN-51 units were used. These gyro-stabilized, four-gimbal, all-attitude units employ two degree-of-freedom gyros with gas bearings. The data furnished to the data acquisition system are:

- position (latitude, longitude, resolution 0.1 min);
- true heading (resolution 0.1 deg, accuracy 0.4 deg),
- track angle (resolution 0.1 deg, accuracy 0.5 deg);
- drift angle (resolution 0.1 deg, accuracy 0.5 deg);
- pitch angle (resolution 0.044 deg, accuracy 0.5 deg),
- roll angle (resolution 0.044 deg, accuracy 0.5 deg);
- groundspeed (resolution 0.51 m s⁻¹, accuracy 0.51 m s⁻¹),

wind speed (resolution 0.51 m s^{-1});

wind azimuth (resolution 1.0 deg),

b. TOTAL AIR TEMPERATURE PROBE

The Rosemount 102 AH2AG probe furnishes total air temperature and static air temperature data (resolution 0.1 deg) to an on-board computer which calculates airspeed (resolution 0.51 m s^{-1}) in the heading direction, the airspeed data are furnished to the INS computer be used in calculating the INS windspeed and azimuth at the aircraft (see Fig. A.3).

c. DEW-FROST POINT HYGROMETER

General Eastern 1011 thermoelectric hygrometer (response $1\text{-}3 \text{ deg per second}$).

d. RADAR ALTIMETER

Stewart-Warner APN-159, resolution 0.61 m ; accuracy 1 percent.

A.4 STATIONARY AUTOMATED MESONET INSTRUMENTATION

Although the lidar experiments were not within the time period of the major portion of the data collection effort by NSSL for 1981, four automated mesonet stations were operating. Below is a brief summary of the instrumentation used to collect meteorological data near the surface (see Doviak (1981) for further details):

a. WIND SPEED

Specially calibrated NWS F-420-C rotating cup DC generator-type anemometer (resolution 0.4 m s^{-1})

b. WIND DIRECTION

NWS F-420-C splayed-tail wind vane with modified direction transmitter (resolution 1.4 deg).

c. DRY-BULB/WET-BULB TEMPERATURE

Linearized Yellow Spring Model 44202 Thermistors, with self-wetting wet bulb, housed in standard NWS Stevenson screen (resolution 0.2 K).

d. STATION PRESSURE

Texas Electronics Aneroid/LVDT Unit (resolution 0.5 mb);

e. RAINFALL

Belfort Model 5-780 weighing bucket raingage with weight-sensing load cell (resolution 0.6 mm).

Dew point temperatures were computed from the dry-bulb and wet-bulb temperature data by integration of the Clausius-Clapeyron equation, assuming latent heat of vaporization to be constant.

APPENDIX B

ESTIMATION OF THE AVERAGE SURFACE HEAT FLUX OVER AN INHOMOGENEOUS TERRAIN FROM THE VERTICAL VELOCITY VARIANCE

B.1 INTRODUCTION

It is straightforward to compute the surface fluxes of heat and momentum for the horizontally homogeneous atmospheric boundary layer (ABL) from the surface-layer profiles of wind and potential temperature by the profile method which uses the integrated form of the flux-profile relationships (Paulson, 1970); it is also possible to compute both the friction velocity and surface heat flux from the surface-layer wind profiles alone, using the method suggested by Klug (1967). For the convective ABL, the surface heat flux can also be computed from just the surface-layer potential temperature profiles using the free convection formula, and this approach seems to give a heat flux estimate that is better than Klug's method and is as good as the profile method (Sundara-Rajan and Macklin, 1976).

But it is not that easy to get a reliable estimate of the surface fluxes of heat and momentum if we don't have surface-layer profile data. This paper describes a method of determining the surface heat flux from the observations of the vertical wind velocity variance ($\overline{w'^2}$) at the lower mid-levels of the convective ABL. This method is based on the assumption that the vertical wind velocity variance remains constant between the levels 0.2h and 0.6h where h is the height of the convective ABL - an assumption adequately supported by observations of the convective ABL over horizontally homogeneous sites (Kaimal et al., 1976). The heat flux estimates obtained with this method were surprisingly good, considering the fact that this method was used over a terrain which was far from being homogeneous.

B.2 THE METHOD USED AND RESULTS

Convective ABL observations over horizontally homogeneous sites (Kaimal et al., 1976) indicate, between levels 0.2h and 0.6h,

$$\frac{\overline{w'^2}}{w_*^2} \approx 0.39 \quad (B.1)$$

where w_* is the convective scaling velocity; $w_* = (\beta h Q_0)^{1/3}$ where Q_0 is the kinematic heat flux at the surface, and $\beta = (g/\theta_0)$ is the buoyancy parameter. We assumed the above relationship for w_*^2 and computed the values for Q_0 from the observed values of the vertical velocity variance at mid-levels of the ABL, and the height (h) of the ABL.

The data we used were from the NSSL-KTVY tower located about 10 km north-northeast of Oklahoma City on a rolling, generally undeveloped terrain that is bounded on the south by developed urban terrain. A detailed description of the terrain and tower is given by Sanders and Weber (1970) and Lee and Stokes (1978). The highest level of measurement was at 444 m, and this restricted us to use the data collected during the early morning hours when the height of the ABL was still below 444 m. The height of the ABL was determined from the vertical profiles of virtual potential temperature, and only those runs for which the ABL height could be accurately determined were included in the analysis.

The vertical velocity measurements were made at six levels (26, 45, 89, 177, 266, 444 m) with R.M. Young Model 27103 Propeller anemometers at a sampling rate of 10 seconds. The somewhat slow response of the propeller anemometer can lead to an underestimation of vertical velocity variance in the surface-layer (Kaimal, 1975), but the lowest level of measurement used for the analysis reported here was 89 m. Also, since the free convection similarity implied in relation (1) holds good for highly convective conditions, only data for which $h/L > -10$ were used. The Obukhov length $L (= -u_*^3/k\beta Q_0)$ for each run was computed from the values of Q_0 and the friction velocity (u_*) determined from the mean wind speed values at 26 m and 45 m using the flux-profile relationships reported by Businger, *et al.* (1971) for the surface-layer. Although the u_* estimates from the mean wind speed values at heights above the surface-layer should be considered relatively crude, they are sufficient for the computation of the values of the stability parameter h/L which are used here only for the selection of runs. The values of z , z/h , h/L , and Q_0 are given in Table B.1.

We wish we had independent measurements of surface heat flux to test the accuracy of the Q_0 estimates using this method. We did not have any, but we estimated the surface heat flux indirectly from the observed boundary layer heating rate. The heating rate equation is given by (Tennekes, 1973):

$$\left(\frac{\partial \bar{\theta}}{\partial t}\right)_{b1} = \frac{Q_o}{h} - \frac{Q_i}{h} \quad (\text{B.2})$$

TABLE B.1. Surface kinematic heat flux estimates from the vertical velocity variance and the boundary layer heating rate.

DATE	Time (LST)	z (m)	z/h	-h/L	Q _o (m s ⁻¹ K)	
					Variance method	Heating rate method
7-7-77	8:15	89	0.34	10.4	0.104	0.093
7-10-77	8:15	89	0.36	17.63	0.080	0.089
7-10-77	8:45	89	0.34	33.5	0.084	0.122
7-14-77	8:45	89	0.34	24.5	0.073	0.082
7-15-77	8:45	177	0.40	54.8	0.093	0.102
7-18-77	8:15	89	0.34	11.5	0.132	0.119
7-18-77	8:45	177	0.40	10.2	0.152	0.183
7-19-77	8:15	89	0.36	49.1	0.104	0.112
7-19-77	8:45	89	0.29	62.3	0.080	0.084
7-25-77	9:15	177	0.40	23.4	0.184	0.163
7-28-77	9:15	177	0.50	47.3	0.121	0.147
7-30-77	8:45	89	0.44	61.3	0.149	0.100
8-26-77	8:45	89	0.20	44.9	0.260	0.305
9-3-77	8:15	89	0.58	12.23	0.118	0.148
9-3-77	8:45	89	0.39	21.0	0.118	0.120
5-11-79	7:15	89	0.37	80.3	0.119	0.097
5-17-79	8:15	177	0.50	16.2	0.154	0.149
5-19-79	8:15	177	0.42	10.6	0.149	0.141
6-3-79	10:15	177	0.43	577.5	0.332	0.274
6-4-79	7:15	89	0.60	12.6	0.073	0.077
6-4-79	7:45	89	0.49	54.8	0.094	0.087
6-4-79	8:15	89	0.34	11.2	0.113	0.126
6-9-79	10:15	177	0.44	10.4	0.275	0.296
6-10-79	7:45	89	0.27	36.5	0.106	0.123
6-10-79	8:15	89	0.27	10.2	0.127	0.144

It was found that for all the runs included here, the strength of inversion was negligible, and hence the downward kinematic heat flux Q_i at the inversion base could be neglected.

The Q_0 values computed using the variance method and the boundary layer heating rate method are compared in Fig. B.1. The agreement between the two sets of values is very good, the standard error being $0.024 \text{ m s}^{-1}\text{K}$ which is almost the same order as that for the profile method (Sundara-Rajan and Macklin, 1976).

B.3 CONCLUDING REMARKS

It seems that this method of computing the surface kinematic heat flux from the vertical velocity variance gives a fairly reliable estimate of the average surface heat flux values over an inhomogeneous terrain. Unfortunately, independent and direct estimates of surface heat flux were not available to test rigorously the validity of this method. What was done was a comparison with the surface heat flux estimates from the boundary layer heating rates, and the results are encouraging. Further documentation from other inhomogeneous sites is required to confirm the results of this study.

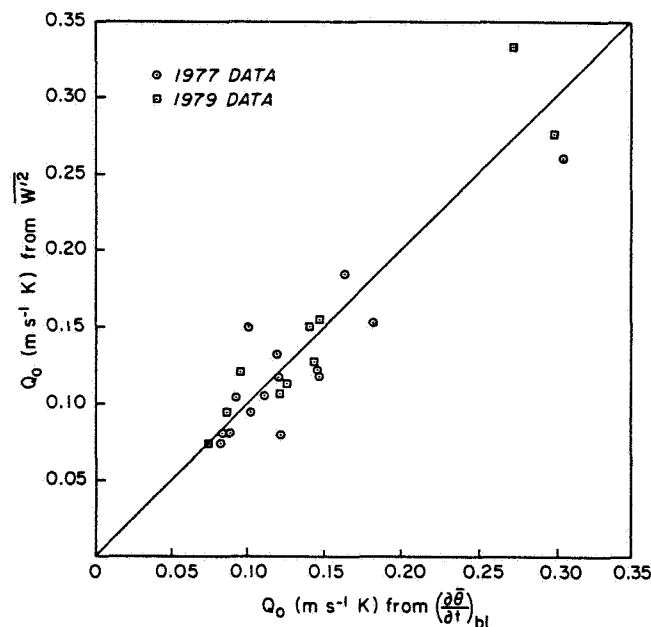


Figure B.1 Comparison of surface heat flux estimates from the variance method and the heating rate method.

APPENDIX C

INSPECTION AND VERIFICATION OF CV990 INS DATA

In this Appendix the process of verifying the aircraft position and attitude data, and correcting any errors found in those data is described. The aircraft position was defined in terms of latitude and longitude recorded at the time of each frame in each run. However, inspection of the raw data indicated that these latitude and longitude measurements were either not being updated frequently enough or were subject to some sort of round-off error, as the values tended to remain constant for periods as long as 6-8 s at a time. Although it was clear that many of the specific positions suggested by these latitude and longitude values were in error, it was also evident that if the latitude and longitude measurements were averaged with a "running mean" filter extending about 10 data points either side of each given datum in the respective series of latitudes and longitudes, the resulting set of aircraft positions seemed to give a good representation of the aircraft flight path.

This was verified by comparing the smoothed INS-derived positions with those obtained from nadir photographs taken at about 10 s intervals during several of the lidar data runs.

Although the INS-derived attitude and velocity data contained significant error, they showed sufficient internal self-consistency that they could be used to generate a first guess of aircraft positions, which would later be compared with photo-derived positions to yield estimates of the larger-scale INS biases in the lidar velocities. Thus it was deemed satisfactory for the overall analysis to obtain the aircraft latitudes and longitudes by integration forward in time using the starting positions of the aircraft at the beginning of each run as reference points and the INS-measured groundspeeds and directions as the velocity. This procedure would also permit a verification to be made of the interrelationships (Fig. C.1) among the airspeeds, groundspeeds, heading angles and drift angles reported on tape. It was especially important to verify these data since they would have to be used to compute the track angle which was not furnished on the data tape. In addition, verification of drift angle values was crucially important due to the sensitivity of the lidar-derived wind vectors to drift angle fluctuations.

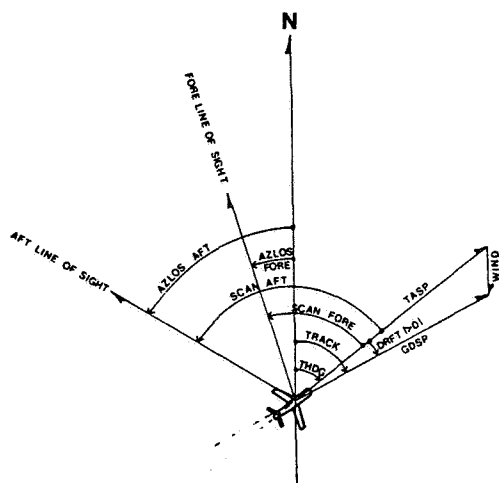


Figure C.1 Aircraft flight parameters relevant to data analysis.

C.1 ERRORS IN CONVERSION FACTORS

Prior to discussing this verification process, one obvious error in the INS derived wind azimuth data (INS derived wind azimuth describes the azimuth of the wind vector estimated by the aircraft INS and is recorded at the time of each lidar frame) had to be corrected before beginning the verifications. Examination of the INS derived wind azimuth values showed some angles larger than 360° , which was easily traced to the use of an incorrect conversion factor during the creation of the data tape. Multiplication by a suitable ratio of factors remedied this problem and gave believable INS wind direction values.

In the first step of checking the aircraft attitude and position data, it became apparent that forward integration of the aircraft velocity vector, as defined by the groundspeed and track angle ($=$ true heading $+$ drift angle), yielded discrepancies in aircraft position which increased steadily with time. Since the INS wind azimuths were previously found to be in error by a factor given by the ratio of two conversion factors, it was suspected that a similar problem might be contaminating the drift angle values. Several test solutions of the vector triangle relating aircraft ground-relative motion, air-relative motion and INS-measured winds quickly confirmed this hypothesis. Although the INS wind azimuths had been found to be in error,

confidence in the INS wind speeds was warranted because of their agreement with the magnitudes suggested from the soundings taken on the day of the experiment. This impression was confirmed during subsequent analysis of the radar and lidar wind data (see section 1.6). In fact, it was ultimately ascertained that the errors in INS wind azimuth and drift angle were complementary: the conversion factors for each quantity had been inadvertently switched during the writing of the tape data. It was thus a simple matter to recompute the correct values of the aircraft drift angles by multiplying them by the ratio of the correct conversion factor to the incorrect one, as had been done for the INS wind directions.

Late in the analysis stage a similar conversion factor problem was detected in the recorded values of roll angle, which were all too small by a factor of 2.27. Evidence of the roll angle errors came from a sequence of 13 ground returns observed in run 4 during a left turn in which lidar data were collected; confirmation of the errors was obtained by comparison of the roll angle values recorded on the lidar data tape with those recorded independently by the aircraft INS system. Because of the lateness of the discovery of the roll angle error and because the roll angle errors had no impact on the calculations of aircraft position, no correction was applied to erroneous roll angle values.

C.2 CORRECTION TO THE RECORDED INS DERIVED POSITION DATA

After modifying values of aircraft drift angle to reflect use of the proper conversion factor, it was possible to compute consistent track angles and to carry out the time integration of the ground-relative velocity vector in order to establish a consistent set of latitudes and longitudes. The actual integration was performed in a local x-y coordinate system having an origin at the starting point of each run. The calculations were made using double precision arithmetic, as the use of single precision arithmetic was found to cause position biases large enough to interfere with accurate assessment of the INS position errors. The revised computed aircraft x and y position coordinates were then transformed back to latitudes and longitudes by means of:

$$\text{LAT}(I) = \text{LAT}(I-1) + A*(X(I) - X(I-1)) \quad (\text{C.1a})$$

$$\text{LON}(I) = \text{LON}(I-1) + A*(X(I) - X(I-1))/(\text{COS}(\text{LAT}(I))) \quad (\text{C.1b})$$

where "A" is a factor which converts distance to degrees.

Latitude-longitude values obtained in this manner followed quite closely the track suggested by the smoothed version of the data given on the tape, and since these computed positions were obtained in a deterministic manner, they were deemed appropriate for use in all subsequent calculations.

A sample of the uncorrected tape data from the first 62 frames of run 2 dealing with aircraft position and attitude is given in Table C.1. The position problems discussed above are evident in the latitudes ("LAT") and longitudes ("LON") as well as the calculated x and y coordinates of the aircraft relative to the start of the run ("XCV990" and "YCV990"). Note in Table C.1 the tendency of all of these quantities to remain constant for periods of time lasting up to 4-5 s. A typical example is seen in the sequence of XCV990 values from frames 36 through 39. An even more disturbing sequence is seen in frames 59-61, where both the XCV990 and YCV990 values, as well as LAT and LON, remain constant, suggesting that the aircraft remained stationary for several seconds! It should be noted that although the drift angle data (DRANGL) appear to be reasonable, they still contain the conversion factor error described above, and are too small by more than a factor of two.

Another portion of the output of tape data is given in Table C.2; this table again deals with the first 62 frames from lidar run 2. Of particular interest are the values of INS wind azimuth (WINDAZ), some of which (frames 1-3 for example) are seen to exceed 360°.

The effect of the corrections made during the data review stage of the analysis can be gauged by examining Tables C.3 and C.4, which are revised versions of Tables C.1 and C.2, with some format changes in the case of Table C.4 to accommodate some new calculated parameters. Note the increased smoothness of rate of change of the LAT, LON, XCV990 (renamed "C1X990" in Tables C.3-C.4) and YCV990 (renamed "C1Y990") arrays in Table C.3, and the conversion of the erroneous WINDAZ values in Table C.2 to credible values of "AZINS" in Table C.4. Note also that in Table C.4 the values labelled "VINS" represent INS-derived wind magnitudes in meters per second obtained by converting the "WINDSP" values in Table C.2 from knots. In Table C.3 values of drift angle can also be seen to have increased; some hint of problems to be discussed later is seen in the fact that the drift angles are not resolved to a precision beyond 0.1 deg. Note also that a number of other parameters have been revised as well; the reasons for these changes and the method of making the changes will be discussed below.

FRAME	TIME	LAT	LON	ZPRES	ZRADR	XCV990	YCV990	TRUEHEAD	DRANGLE
1	201810.	35.113	-97.737	0.	2424.	0.	0.	310.999	0.703
2	201811.	35.113	-97.737	0.	2404.	0.	0.	311.202	0.571
3	201812.	35.115	-97.740	0.	2410.	-280.	180.	311.262	0.571
4	201815.	35.117	-97.740	0.	2470.	-280.	360.	312.185	0.439
5	201817.	35.118	-97.745	0.	2394.	-740.	560.	313.503	0.044
6	201818.	35.118	-97.747	0.	2378.	-900.	560.	313.767	0.044
7	201819.	35.122	-97.748	0.	2390.	-1040.	920.	313.767	0.132
8	201821.	35.122	-97.748	0.	2424.	-1040.	920.	314.690	0.396
9	201822.	35.123	-97.748	0.	2402.	-1040.	1100.	314.690	0.308
10	201824.	35.123	-97.752	0.	2386.	-1340.	1100.	315.569	0.308
11	201825.	35.127	-97.755	0.	2414.	-1640.	1480.	316.272	0.308
12	201827.	35.120	-97.757	0.	2398.	-1800.	1660.	316.799	0.439
13	201828.	35.132	-97.758	0.	2400.	-1960.	2040.	316.799	0.439
14	201830.	35.132	-97.758	0.	2424.	-1960.	2040.	317.371	0.396
15	201831.	35.132	-97.758	0.	2456.	-1960.	2040.	317.678	0.483
16	201833.	35.133	-97.762	0.	2394.	-2260.	2220.	317.986	0.571
17	201834.	35.135	-97.762	0.	2372.	-2260.	2400.	318.381	0.571
18	201836.	35.137	-97.767	0.	2338.	-2720.	2580.	318.689	0.527
19	201837.	35.138	-97.768	0.	2348.	-2860.	2780.	318.689	0.527
20	201839.	35.138	-97.768	0.	2334.	-2860.	2780.	318.689	0.439
21	201840.	35.138	-97.768	0.	2354.	-2860.	2780.	319.568	0.220
22	201842.	35.143	-97.772	0.	2398.	-3160.	3320.	319.568	0.220
23	201843.	35.145	-97.772	0.	2402.	-3160.	3520.	319.568	0.220
24	201845.	35.145	-97.775	0.	2374.	-3480.	3520.	319.568	0.264
25	201846.	35.148	-97.778	0.	2352.	-3780.	3980.	319.963	0.352
26	201847.	35.148	-97.778	0.	2362.	-3780.	3880.	320.403	0.0
27	201849.	35.148	-97.780	0.	2322.	-3920.	3880.	320.403	0.0
28	201850.	35.148	-97.780	0.	2338.	-3920.	3880.	320.403	0.0
29	201851.	35.152	-97.782	0.	2352.	-4080.	4260.	320.403	0.132
30	201852.	35.152	-97.782	0.	2376.	-4080.	4260.	320.491	0.132
31	201854.	35.157	-97.783	0.	2356.	-4220.	4800.	320.579	0.176
32	201855.	35.157	-97.783	0.	2372.	-4220.	4800.	320.579	0.176
33	201856.	35.158	-97.785	0.	2368.	-4380.	5000.	320.579	0.088
34	201858.	35.158	-97.785	0.	2392.	-4380.	5000.	320.579	0.088
35	201859.	35.158	-97.785	0.	2452.	-4380.	5000.	320.798	0.088
36	201900.	35.162	-97.792	0.	2426.	-4980.	5360.	320.798	0.264
37	201901.	35.162	-97.792	0.	2444.	-4980.	5360.	321.194	0.264
38	201903.	35.163	-97.792	0.	2390.	-4980.	5540.	321.194	0.308
39	201904.	35.163	-97.792	0.	2382.	-4980.	5540.	321.370	0.220
40	201905.	35.167	-97.795	0.	2372.	-5300.	5920.	321.501	0.132
41	201906.	35.168	-97.795	0.	2370.	-5300.	6100.	321.501	0.132
42	201908.	35.168	-97.795	0.	2378.	-5300.	6100.	321.501	0.044
43	201909.	35.170	-97.798	0.	2364.	-5600.	6280.	321.501	0.176
44	201910.	35.172	-97.798	0.	2384.	-5600.	6480.	321.677	0.132
45	201912.	35.172	-97.802	0.	2376.	-5900.	6480.	321.677	0.132
46	201913.	35.172	-97.802	0.	2378.	-5900.	6480.	321.677	0.176
47	201914.	35.172	-97.802	0.	2404.	-5900.	6480.	322.600	0.176
48	201915.	35.178	-97.805	0.	2418.	-6200.	7220.	322.600	0.176
49	201917.	35.178	-97.805	0.	2492.	-6200.	7220.	323.391	0.176
50	201918.	35.180	-97.807	0.	2482.	-6360.	7400.	323.391	-0.264
51	201919.	35.182	-97.808	0.	2454.	-6500.	7580.	323.171	0.132
52	201921.	35.183	-97.812	0.	2462.	-6800.	7760.	323.171	0.132
53	201922.	35.183	-97.812	0.	2412.	-6800.	7760.	323.875	-0.088
54	201923.	35.185	-97.813	0.	2404.	-6960.	7960.	323.567	0.0
55	201924.	35.185	-97.813	0.	2422.	-6960.	7960.	323.567	0.0
56	201926.	35.185	-97.813	0.	2438.	-6960.	7960.	323.875	0.088
57	201927.	35.190	-97.813	0.	2480.	-6960.	8500.	324.182	0.088
58	201928.	35.192	-97.817	0.	2446.	-7260.	8700.	324.490	-0.088
59	201930.	35.193	-97.818	0.	2430.	-7420.	8880.	324.490	-0.088
60	201931.	35.193	-97.818	0.	2422.	-7420.	8880.	324.490	-0.088
61	201932.	35.193	-97.818	0.	2436.	-7420.	8880.	324.402	0.132
62	201933.	35.197	-97.823	0.	2416.	-7880.	9240.	324.402	0.132

Table C.1 Sample of raw position data NASA CV 990.
See text for definition of terms.

WINDSP	WINDAZ	TTOTC	TSTAT	DEWPT	TSRFC	TSENS	TIMPOS	FREOLD	OFFSET
11.00	375.50	33.90	23.90	18.90	31.90	0.10	0.0	0.0	0.0
11.00	375.50	33.90	23.90	19.10	31.20	0.10	0.0	0.0	0.0
11.00	375.50	33.90	23.90	18.60	32.00	0.10	0.0	0.0	0.0
10.00	318.60	33.60	23.60	20.00	29.70	0.10	0.0	0.0	0.0
10.00	318.60	33.70	23.60	18.80	29.90	0.10	0.0	0.0	0.0
10.00	355.00	33.60	23.80	19.40	30.40	0.10	0.0	0.0	0.0
10.00	355.00	33.70	23.70	20.30	30.40	0.10	0.0	0.0	0.0
10.00	355.00	33.70	23.70	19.40	30.10	0.10	0.0	0.0	0.0
13.00	357.30	33.70	23.70	19.50	30.70	0.10	0.0	0.0	0.0
13.00	373.20	33.60	23.50	19.80	31.80	0.10	0.0	0.0	0.0
14.00	361.80	33.70	23.50	19.30	31.70	0.10	0.0	0.0	0.0
13.00	366.40	33.60	23.50	19.20	31.00	0.10	0.0	0.0	0.0
14.00	357.30	33.80	23.50	20.50	31.30	0.10	0.0	0.0	0.0
14.00	357.30	33.80	23.70	19.30	30.50	0.10	0.0	0.0	0.0
14.00	368.60	33.90	23.70	18.80	29.50	0.10	0.0	0.0	0.0
14.00	368.60	33.90	23.70	19.60	30.40	0.10	0.0	0.0	0.0
15.00	366.40	33.90	23.70	19.00	29.90	0.10	0.0	0.0	0.0
14.00	368.60	34.00	23.60	19.90	30.70	0.10	0.0	0.0	0.0
14.00	368.60	34.00	23.60	19.50	30.40	0.10	0.0	0.0	0.0
14.00	368.60	34.10	23.60	19.80	31.10	0.10	0.0	0.0	0.0
11.00	339.10	34.10	23.70	20.90	30.50	0.10	0.0	0.0	0.0
11.00	339.10	34.20	23.60	18.80	29.90	0.10	0.0	0.0	0.0
11.00	366.40	34.20	23.60	19.50	30.50	0.10	0.0	0.0	0.0
10.00	355.00	34.00	23.70	19.00	30.50	0.10	0.0	0.0	0.0
11.00	316.30	34.00	23.60	20.60	29.40	0.10	0.0	0.0	0.0
11.00	316.30	33.90	23.50	19.70	30.40	0.10	0.0	0.0	0.0
12.00	316.30	33.90	23.60	20.90	30.40	0.10	0.0	0.0	0.0
12.00	325.40	33.90	23.60	19.80	31.00	0.10	0.0	0.0	0.0
13.00	343.60	33.90	23.70	19.80	29.90	0.10	0.0	0.0	0.0
13.00	343.60	33.80	23.70	20.10	29.80	0.10	0.0	0.0	0.0
14.00	343.60	33.80	23.50	19.50	30.70	0.10	0.0	0.0	0.0
14.00	343.60	33.60	23.60	20.10	30.80	0.10	0.0	0.0	0.0
14.00	332.20	33.80	23.60	21.20	30.60	0.10	0.0	0.0	0.0
14.00	341.30	33.90	23.60	19.90	29.80	0.10	0.0	0.0	0.0
14.00	350.40	33.90	23.60	20.00	29.20	0.10	0.0	0.0	0.0
14.00	350.40	33.90	23.70	21.50	29.20	0.10	0.0	0.0	0.0
14.00	350.40	34.00	23.60	19.60	29.90	0.10	0.0	0.0	0.0
14.00	352.70	34.00	23.60	19.70	29.80	0.10	0.0	0.0	0.0
14.00	352.70	34.00	23.70	18.50	30.00	0.10	0.0	0.0	0.0
13.00	334.50	34.00	23.70	18.80	30.00	0.10	0.0	0.0	0.0
13.00	334.50	34.00	23.70	20.30	30.80	0.10	0.0	0.0	0.0
13.00	334.50	33.90	23.50	19.50	29.20	0.10	0.0	0.0	0.0
13.00	334.50	34.10	23.50	19.40	29.10	0.10	0.0	0.0	0.0
12.00	345.90	34.00	23.50	20.80	29.90	0.10	0.0	0.0	0.0
12.00	345.90	34.10	23.60	18.80	30.90	0.10	0.0	0.0	0.0
12.00	345.90	34.10	23.50	19.80	30.20	0.10	0.0	0.0	0.0
13.00	304.90	34.10	23.70	21.10	31.00	0.10	0.0	0.0	0.0
13.00	304.90	34.00	23.60	19.50	31.20	0.10	0.0	0.0	0.0
13.00	304.90	34.30	23.50	20.20	29.40	0.10	0.0	0.0	0.0
13.00	304.90	34.30	23.70	19.90	29.90	0.10	0.0	0.0	0.0
12.00	336.80	34.40	23.50	19.00	29.80	0.10	0.0	0.0	0.0
10.00	316.30	34.60	23.40	19.80	30.80	0.10	0.0	0.0	0.0
10.00	316.30	34.60	23.60	19.30	31.10	0.10	0.0	0.0	0.0
8.00	336.80	34.70	23.50	19.80	31.30	0.10	0.0	0.0	0.0
8.00	336.80	34.60	23.50	20.40	30.90	0.10	0.0	0.0	0.0
8.00	336.80	34.50	23.50	20.50	30.40	0.10	0.0	0.0	0.0
8.00	336.80	34.40	23.30	20.40	29.10	0.10	0.0	0.0	0.0
8.00	289.00	34.30	23.10	20.80	29.40	0.10	0.0	0.0	0.0
8.00	289.00	34.40	23.20	20.60	30.20	0.10	0.0	0.0	0.0
8.00	289.00	34.20	23.10	19.50	32.40	0.10	0.0	0.0	0.0
9.00	345.90	34.30	23.20	20.20	34.10	0.10	0.0	0.0	0.0
9.00	319.60	34.30	23.30	20.50	34.00	0.10	0.0	0.0	0.0

Table C 2. Sample of raw meteorological data, NASA CV 990.
See text for definition of terms.

ORIGINAL PAGE IS
OF POOR QUALITY

FRAME	TIME	TSEC	CLAT	CLON	ZHADR	C1X990	C1Y990	TRUEAD	DRANGLE
-1	201810.0	0.0	35.113	-97.737	739.	-146.	135.	310.999	1.600
2	201811.4	1.40	35.115	-97.738	733.	-293.	269.	311.262	1.300
3	201812.7	2.80	35.116	-97.740	735.	-584.	540.	311.262	1.300
4	201815.6	5.60	35.118	-97.743	753.	-729.	676.	312.185	1.000
-5	201817.0	7.00	35.119	-97.745	730.	-873.	814.	313.503	0.100
6	201818.4	8.40	35.121	-97.746	725.	-1017.	953.	313.767	0.100
7	201819.7	9.80	35.122	-97.748	728.	-1159.	1094.	313.767	0.200
8	201821.2	11.20	35.123	-97.749	739.	-1299.	1237.	314.690	0.200
-9	201822.6	12.60	35.124	-97.751	732.	-1439.	1381.	314.690	0.700
10	201823.9	14.00	35.126	-97.752	727.	-1578.	1528.	315.569	0.700
11	201825.4	15.40	35.127	-97.754	736.	-1734.	1698.	316.272	0.700
12	201827.0	17.00	35.129	-97.756	731.	-1880.	1858.	316.799	1.000
-13	201828.5	18.50	35.130	-97.757	732.	-2025.	2019.	317.371	0.900
14	201830.0	20.00	35.131	-97.759	739.	-2169.	2182.	317.673	1.100
15	201831.5	21.50	35.133	-97.760	749.	-2312.	2347.	317.986	1.300
16	201833.0	23.00	35.134	-97.762	740.	-2454.	2513.	318.381	1.300
-17	201834.5	24.50	35.136	-97.764	723.	-2595.	2680.	318.689	1.200
18	201836.0	26.00	35.137	-97.765	713.	-2736.	2848.	318.689	1.200
19	201837.5	27.50	35.139	-97.767	716.	-2878.	3015.	318.639	1.000
20	201839.0	29.00	35.140	-97.768	711.	-3019.	3183.	319.568	0.500
-21	201840.5	30.50	35.142	-97.770	718.	-3160.	3351.	319.568	0.500
22	201842.0	32.00	35.143	-97.771	731.	-3300.	3519.	319.568	0.500
23	201843.5	33.50	35.145	-97.773	732.	-3454.	3703.	319.568	0.600
24	201845.1	35.14	35.146	-97.774	724.	-3574.	3848.	319.568	0.800
-25	201846.6	36.43	35.148	-97.776	717.	-3693.	3993.	320.403	0.0
26	201847.7	37.71	35.149	-97.777	720.	-3813.	4138.	320.403	0.0
27	201849.0	39.00	35.150	-97.778	708.	-3933.	4283.	320.403	0.0
28	201850.2	40.29	35.152	-97.780	713.	-4052.	4428.	320.403	0.300
-29	201851.6	41.57	35.153	-97.781	717.	-4172.	4574.	320.491	0.300
30	201852.8	42.86	35.154	-97.782	724.	-4291.	4721.	320.579	0.400
31	201854.1	44.14	35.156	-97.784	718.	-4409.	4867.	320.579	0.400
32	201855.4	45.43	35.157	-97.785	723.	-4528.	5013.	320.579	0.200
-33	201856.7	46.71	35.158	-97.786	722.	-4648.	5160.	320.579	0.200
34	201857.9	48.00	35.160	-97.788	729.	-4767.	5306.	320.798	0.200
35	201859.2	49.29	35.161	-97.789	747.	-4885.	5454.	320.798	0.600
36	201900.6	50.57	35.162	-97.790	739.	-5003.	5602.	321.194	0.600
-37	201901.7	51.86	35.163	-97.791	745.	-5107.	5734.	321.194	0.700
38	201902.9	53.00	35.165	-97.793	728.	-5224.	5883.	321.370	0.500
39	201904.2	54.29	35.166	-97.794	726.	-5340.	6032.	321.501	0.300
40	201905.5	55.57	35.167	-97.795	723.	-5457.	6180.	321.501	0.300
-41	201906.7	56.86	35.169	-97.796	722.	-5575.	6329.	321.501	0.100
42	201908.1	58.14	35.170	-97.798	725.	-5692.	6477.	321.501	0.400
43	201909.3	59.43	35.171	-97.799	721.	-5809.	6626.	321.677	0.300
44	201910.6	60.71	35.173	-97.800	727.	-5925.	6775.	321.677	0.300
-45	201911.9	62.00	35.174	-97.801	724.	-6041.	6925.	321.677	0.400
46	201913.2	63.29	35.175	-97.803	725.	-6157.	7075.	322.600	0.400
47	201914.5	64.57	35.177	-97.804	731.	-6270.	7226.	322.600	0.400
48	201915.7	65.86	35.178	-97.805	737.	-6383.	7378.	323.391	0.400
-49	201917.1	67.14	35.179	-97.806	760.	-6497.	7530.	323.391	0.600
50	201918.3	68.43	35.181	-97.808	757.	-6611.	7682.	323.171	0.300
51	201919.6	69.71	35.182	-97.809	748.	-6724.	7835.	323.171	0.300
52	201920.9	71.00	35.183	-97.810	750.	-6837.	7988.	323.875	0.200
-53	201922.2	72.29	35.185	-97.811	735.	-6950.	8141.	323.567	0.0
54	201923.5	73.57	35.186	-97.813	733.	-7063.	8294.	323.567	0.0
55	201924.7	74.86	35.188	-97.814	738.	-7175.	8448.	323.875	0.200
56	201926.1	76.14	35.189	-97.815	743.	-7287.	8603.	324.182	0.200
57	201927.3	77.43	35.190	-97.816	756.	-7398.	8758.	324.490	0.200
58	201928.6	78.71	35.192	-97.818	746.	-7510.	8914.	324.490	0.200
59	201929.9	80.00	35.193	-97.819	741.	-7622.	9069.	324.490	0.200
60	201931.2	81.29	35.194	-97.820	738.	-7733.	9225.	324.492	0.300
-61	201932.5	82.57	35.196	-97.821	743.	-7844.	9382.	324.492	0.300
62	201933.7	83.86	35.197	-97.822	736.				

Table C 3. Sample of corrected position data NASA CV-990.
See text for definition of terms.

AZ990	RAN990	EFS990	IFCRE	7ZLCS	VINS	AZINS	VRINS	TTOT	SATM	TCEW	TSFC
170.2	40755.	0.851	1	240.80	5.7	165.0	-5.6	33.9	23.9	18.9	31.9
170.3	40599.	0.846	-1	242.10	5.7	165.0	-5.6	33.9	23.9	19.1	31.2
170.5	40442.	0.848	1	241.10	5.7	165.0	-5.6	33.9	23.9	18.6	32.0
170.5	40130.	0.882	1	242.00	5.1	140.0	-4.4	33.6	23.6	20.0	29.7
171.0	39973.	0.862	-1	244.30	5.1	140.0	-4.4	33.7	23.6	18.8	29.5
171.2	39816.	0.863	1	243.60	5.1	156.0	-5.0	33.6	23.8	19.4	30.4
171.4	39659.	0.865	-1	244.60	5.1	156.0	-5.0	33.7	23.7	20.3	30.4
171.5	39499.	0.888	1	244.50	5.1	156.0	-5.0	33.7	23.7	19.4	30.1
171.7	39338.	0.885	-1	245.50	6.7	157.0	-6.5	33.7	23.7	19.5	30.7
171.9	39177.	0.881	1	245.40	6.7	164.0	-6.6	33.6	23.5	19.8	31.8
172.1	39014.	0.905	-1	247.10	7.2	159.0	-7.0	33.7	23.5	19.3	31.7
172.3	38825.	0.902	1	246.60	6.7	161.0	-6.6	33.6	23.5	19.2	31.0
172.4	38648.	0.911	-1	247.70	7.2	157.0	-6.9	33.6	23.5	20.5	31.3
172.6	38470.	0.919	1	247.20	7.2	157.0	-6.9	33.6	23.7	19.3	30.5
172.8	38292.	0.945	-1	248.50	7.2	162.0	-7.1	33.9	23.7	18.8	29.5
173.0	38112.	0.918	1	247.80	7.2	162.0	-7.1	33.9	23.7	19.6	30.4
173.2	37932.	0.909	-1	245.20	7.7	161.0	-7.5	33.9	23.7	19.0	29.9
173.3	37750.	0.900	1	248.50	7.2	162.0	-7.1	34.0	23.6	19.9	30.7
173.5	37570.	0.908	-1	245.50	7.2	162.0	-7.1	34.0	23.6	19.5	30.4
173.7	37389.	0.917	1	248.50	7.2	162.0	-7.1	34.1	23.6	19.8	31.1
173.9	37209.	0.932	-1	210.40	5.7	149.0	-5.1	34.1	23.7	20.9	30.5
174.1	37028.	0.960	1	246.40	5.7	145.0	-5.1	34.2	23.6	18.8	29.9
174.3	36847.	0.957	-1	210.40	5.7	161.0	-5.5	34.2	23.6	19.5	30.5
174.5	36650.	0.968	1	249.40	5.1	156.0	-4.9	34.0	23.7	19.0	30.5
174.7	36495.	0.949	-1	210.60	5.7	139.0	-4.6	34.0	23.6	20.6	29.4
174.8	36341.	0.964	1	250.20	5.7	139.0	-4.6	33.9	23.5	19.7	30.4
175.0	36167.	0.946	-1	211.20	6.2	139.0	-5.0	33.9	23.6	20.9	30.4
175.2	36034.	0.961	1	250.20	6.2	143.0	-5.2	33.9	23.6	19.8	31.0
175.3	35880.	0.969	-1	211.20	6.7	151.0	-6.1	33.9	23.7	19.8	29.9
175.5	35726.	0.991	1	250.30	6.7	151.0	-6.1	33.8	23.7	20.1	29.8
175.7	35572.	0.993	-1	211.40	7.2	151.0	-6.5	33.8	23.5	19.5	30.7
175.8	35418.	0.987	1	250.40	7.2	151.0	-6.5	33.8	23.6	20.1	30.8
176.0	35264.	0.996	-1	211.40	7.2	146.0	-6.2	33.6	23.6	21.2	30.6
176.2	35111.	1.012	1	250.40	7.2	150.0	-6.5	33.9	23.6	19.9	29.8
176.4	34958.	1.063	-1	211.60	7.2	154.0	-6.7	33.9	23.6	20.0	29.2
176.6	34805.	1.051	1	250.60	7.2	154.0	-6.6	33.9	23.7	21.5	29.2
176.7	34652.	1.061	-1	212.00	7.2	154.0	-6.6	34.0	23.6	19.6	29.9
176.9	34516.	1.039	1	251.00	7.2	155.0	-6.7	34.0	23.6	19.7	29.6
177.1	34362.	1.041	-1	212.20	7.2	155.0	-6.7	34.0	23.7	18.5	30.0
177.3	34210.	1.036	1	251.30	6.7	147.0	-5.8	34.0	23.7	18.8	30.0
177.4	34057.	1.046	-1	212.30	6.7	147.0	-5.8	34.0	23.7	20.3	30.6
177.6	33905.	1.062	1	251.30	6.7	147.0	-5.8	33.9	23.5	19.5	29.2
177.8	33753.	1.065	-1	212.30	6.7	147.0	-5.7	34.1	23.5	19.4	29.1
178.0	33602.	1.074	1	251.50	6.2	152.0	-5.5	34.0	23.5	20.8	29.9
178.2	33451.	1.076	-1	212.50	6.2	152.0	-5.5	34.1	23.6	18.8	30.9
178.4	33300.	1.094	1	251.50	6.2	152.0	-5.5	34.1	23.5	19.6	30.2
178.6	33148.	1.104	-1	213.40	6.7	134.0	-4.8	34.1	23.7	21.1	31.0
178.8	32995.	1.122	1	252.40	6.7	134.0	-4.7	34.0	23.6	19.5	31.2
179.0	32842.	1.164	-1	214.20	6.7	134.0	-4.7	34.3	23.5	20.2	29.4
179.1	32689.	1.167	1	253.20	6.7	134.0	-4.7	34.3	23.7	19.9	29.9
179.3	32537.	1.162	-1	214.00	6.2	142.0	-5.2	34.4	23.5	19.0	29.8
179.5	32386.	1.181	1	252.60	5.1	135.0	-3.9	34.6	23.4	19.6	30.6
179.7	32232.	1.150	-1	214.70	5.1	135.0	-3.9	34.6	23.6	19.3	31.1
179.9	32080.	1.153	1	253.40	4.1	148.0	-3.5	34.7	23.5	19.8	31.3
180.1	31928.	1.172	-1	214.40	4.1	148.0	-3.5	34.6	23.5	20.4	30.9
180.3	31776.	1.184	1	253.70	4.1	146.0	-3.5	34.5	23.5	20.5	30.4
180.5	31622.	1.212	-1	215.00	4.1	148.0	-3.5	34.4	23.3	20.4	29.1
180.8	31470.	1.207	1	254.30	4.1	127.0	-2.4	34.3	23.1	20.8	29.4
181.0	31317.	1.201	-1	215.30	4.1	127.0	-2.4	34.4	23.2	20.6	30.2
181.2	31165.	1.204	1	254.30	4.1	127.0	-2.4	34.2	23.3	19.5	32.4
181.4	31012.	1.233	-1	215.20	4.6	152.0	-4.0	34.3	23.2	20.2	34.1
181.6	30859.	1.228	1	254.20	4.6	140.0	-3.5	34.3	23.3	20.5	34.0
181.8	30723.	1.230	-1	215.60	4.6	146.0	-3.8	34.3	23.5	19.6	33.0

Table C.4. Sample of corrected meteorological data, NASA CV-990.
See text for definition of terms.

In examining the times of each of the frames as reported on tape, it was found that although the average spacing of frames in time was just slightly over 1 s, the resolution of the time measurements was limited to whole seconds. This problem is seen in Table C.1 in the column marked "TIME", although no digits of time beyond the decimal were printed in this particular table, such digits of the raw time data were examined and always found to be zero. This "time quantization" was capable of introducing a highly patterned error into the aircraft positions during the time integrations, for instance, aircraft positions would be in error by amounts ranging up to 120 m every fifth frame if frames were taken every 1.2 s and the aircraft were flying at 150 m s^{-1} , because the reported times would be in error by as much as 0.8 s. As a consequence of these time errors, it was possible for velocity errors as large as 1 m s^{-1} to be generated by the objective analysis scheme if a frame of data were missing in an area having significant velocity gradients; such a situation was actually observed to occur occasionally in the data collected near gust fronts (see Section 3.5.1). Thus, it was deemed necessary to construct a special algorithm which could produce more accurate estimates of the time at which each data frame was collected.

The design of this time correction algorithm was nontrivial in that the lidar duty cycle between frames was not constant for more than about 20 or 30 seconds at a time on average, and often much less. This made it necessary for the algorithm to scan backward and forward locally through the data in each run until best straight line fits could be made locally to the recorded time values. The ultimate aim of the algorithm was to establish corrected times spaced as evenly (locally) as possible which, when truncated by dropping the fractional parts of each second, would yield the original recorded times. A sample of the raw recorded time data and the corrected time data output by the algorithm is shown in Table C.5, which consists of a "before corrections" and an "after corrections" section, again for the first 62 frames of run 2. The quantity "TSEC" is the relative time measured in seconds from the beginning of the run, and is calculated in the "before" section by merely comparing the values of the "TIME" array with the initial value of "TIME". In the "after" section, however, TSEC is the basic quantity; it has been computed in the time correction algorithm and then used to create a corrected version of the TIME array. Note the significant improvement in time resolution with much smoother rates of change of the time parameters. The small discrepancies between the digits to the right of the decimal in the final TSEC and TIME arrays is a

ORIGINAL PAGE IS
OF POOR QUALITY

FRAME	TSEC	TIME	FRAME	TSEC	TIME
1	0.0	2018110.000	1	0.0	2018110.000
2	1.000	2018111.000	2	1.400	2018111.375
3	2.000	2018112.000	3	2.800	2018112.750
4	5.000	2018115.000	4	5.600	2018115.562
5	7.000	2018117.000	5	7.000	2018117.000
6	8.000	2018118.000	6	8.400	2018118.375
7	9.000	2018119.000	7	9.800	2018119.750
8	11.000	2018221.000	8	11.200	2018221.187
9	12.000	2018222.000	9	12.600	2018222.562
10	14.000	2018224.000	10	14.000	2018223.937
11	15.000	2018225.000	11	15.400	2018225.375
12	17.000	2018227.000	12	17.000	2018227.000
13	18.000	2018228.000	13	18.500	2018228.500
14	20.000	2018330.000	14	20.000	2018330.000
15	21.000	2018331.000	15	21.500	2018331.500
16	23.000	2018333.000	16	23.000	2018333.000
17	24.000	2018334.000	17	24.500	2018334.500
18	25.000	2018336.000	18	26.000	2018336.000
19	27.000	2018337.000	19	27.500	2018337.500
20	29.000	2018339.000	20	29.000	2018339.000
21	30.000	2018440.000	21	30.500	2018440.500
22	32.000	2018442.000	22	32.000	2018442.000
23	33.000	2018443.000	23	33.500	2018443.500
24	35.000	2018445.000	24	35.143	2018445.125
25	36.000	2018446.000	25	36.429	2018446.375
26	37.000	2018447.000	26	37.714	2018447.687
27	39.000	2018449.000	27	39.000	2018449.000
28	40.000	2018550.000	28	40.286	2018550.250
29	41.000	2018551.000	29	41.571	2018551.562
30	42.000	2018552.000	30	42.857	2018552.812
31	44.000	2018554.000	31	44.143	2018554.125
32	45.000	2018555.000	32	45.429	2018555.375
33	46.000	2018556.000	33	46.714	2018556.687
34	48.000	2018558.000	34	48.000	2018557.937
35	49.000	2018559.000	35	49.286	2018559.250
36	50.000	2019000.000	36	50.571	2019000.562
37	51.000	2019001.000	37	51.857	2019001.750
38	53.000	2019003.000	38	53.000	2019002.937
39	54.000	2019004.000	39	54.286	2019004.187
40	55.000	2019005.000	40	55.571	2019005.500
41	56.000	2019006.000	41	56.857	2019006.750
42	58.000	2019008.000	42	58.143	2019008.062
43	59.000	2019009.000	43	59.429	2019009.312
44	60.000	201910.000	44	60.714	201910.625
45	62.000	201912.000	45	62.000	201911.875
46	63.000	201913.000	46	63.286	201913.187
47	64.000	201914.000	47	64.571	201914.500
48	65.000	201915.000	48	65.857	201915.750
49	67.000	201917.000	49	67.143	201917.062
50	68.000	201918.000	50	68.429	201918.312
51	69.000	201919.000	51	69.714	201919.625
52	71.000	201922.000	52	71.000	201920.875
53	72.000	201922.000	53	72.286	201922.187
54	73.000	201923.000	54	73.571	201923.500
55	74.000	201924.000	55	74.857	201924.750
56	76.000	201926.000	56	76.143	201926.062
57	77.000	201927.000	57	77.429	201927.312
58	78.000	201928.000	58	78.714	201928.625
59	80.000	201930.000	59	80.000	201929.875
60	81.000	201931.000	60	81.286	201931.187
61	82.000	201932.000	61	82.571	201932.500
62	83.000	201933.000	62	83.857	201933.750

Table C.5. Sample of raw and corrected time data. See text for further details.

consequence of single-precision arithmetic round-off of the TIME values. This round-off error has no effect on any other computations, since only the TSEC arrays were used in estimating relative times in the analyses.

APPENDIX C.3 INS GENERATED ERRORS IN AIRCRAFT POSITION AND GROUND VELOCITY

Low-frequency frame biases (i.e., changes in average radial velocity error from frame to frame) enter the lidar data as a result of time-varying errors in the output from the aircraft INS. These errors cause incorrect components of aircraft ground velocity to be removed from the raw radial velocity estimates during the operation of referencing the Doppler velocity to ground-relative coordinates (Appendix A.1). Components of the ground velocity errors along the lidar lines-of-sight then contaminate the PPPP estimated radial air velocities and, after synthesis of the wind field, ultimately show up as any of a variety of vector error patterns superimposed on the true wind field. The problem may be either minor or serious depending on both the amplitude of the INS errors and on their time rate of change; the INS error amplitude is found to influence the amplitude of the error introduced into the calculated wind field, while the time rate of change of the INS error is found to influence the spatial scale of the error patterns produced.

Nadir photographs taken at 10 s intervals during portions of the Severe Storms flight could be used to establish reasonably accurate aircraft positions during selected time intervals, allowing at least rough estimation of the magnitude and direction of the INS position and velocity errors for portions of the flight. Although at first glance it might seem that the nadir photographs would resolve conclusively any controversy about the aircraft's exact position, it was found that sufficient uncertainty existed in the photographically derived positions to render their interpretation difficult. These uncertainties (caused by the relative absence of landmarks easily identified in the photos), the relatively coarse scale of the U.S. Geological Survey 7.5 Minute Topographic Quadrangle maps which were compared to the photos, the relatively long time period between photos, and the sensitivity of camera orientation to aircraft pitch and roll perturbations, produced random uncertainties of about 30 m (standard deviation) in the photographically derived positions. These uncertainties imply lateral aircraft velocity uncertainties of about 30 m each 10 s, or about 3 m s^{-1} from photo to photo, far too large to be of help in studying any short-time-scale INS errors in aircraft velocity.

Nevertheless, the nadir photo-derived positions were useful in studying the INS velocity errors over larger spatial scales (i.e., over many frames). Such studies were made for those runs where the photos were available, runs 2-4, and the results indicated the INS-derived ground velocity errors were often as large as 2 m s^{-1} when averaged over each run.

The technique employed to estimate the INS-derived aircraft position and ground velocity errors was made complicated by the differing sampling rates of the photos and the INS reports on aircraft positions, the variability of the position sampling rate, and the inherent non-straightness of many of the flight track segments. There are two ways to define the INS-derived position error in these data: one involves interpolating the INS positions at the times of lidar frames to the much wider spaced times of the nadir photos, then subtracting the x and y coordinates of the two sets of positions to obtain position error estimates at the nadir photo times; the other involves interpolating the nadir photo positions to the much closer spaced times of the lidar frames, followed again by subtraction of coordinates to obtain position error estimates at the lidar frame times.

Attempts to use either technique to determine the best estimates of position error required smoothing of the photo derived positions. After some experimentation with various smoothing techniques, a method based on detrending followed by Fourier filtering was finally developed which seemed to give satisfactory results. In this method, the position errors at the times of the lidar frames are detrended such that the remaining time series of "residual" position error are forced to be periodic within the data sequence; these residual values are then Fourier analyzed, then subsequently Fourier synthesized using only harmonics 0, 1 and 2. Addition of the originally diagnosed trend back to these smoothed residual position error data produced the smoothed sequence of INS position errors (Fig. C.2). These smoothed position errors were then finite-differenced with respect to the time intervals between lidar frames in order to produce estimates of the aircraft's ground velocity error occurring in each frame. Additional Fourier filtering of the velocity error results was needed because of new noise introduced during the differencing process as a result of the non-constancy of the time intervals between lidar frames.

Although a number of simplifying assumptions were made in these INS error analyses, the results of the technique seem to show good fidelity to the

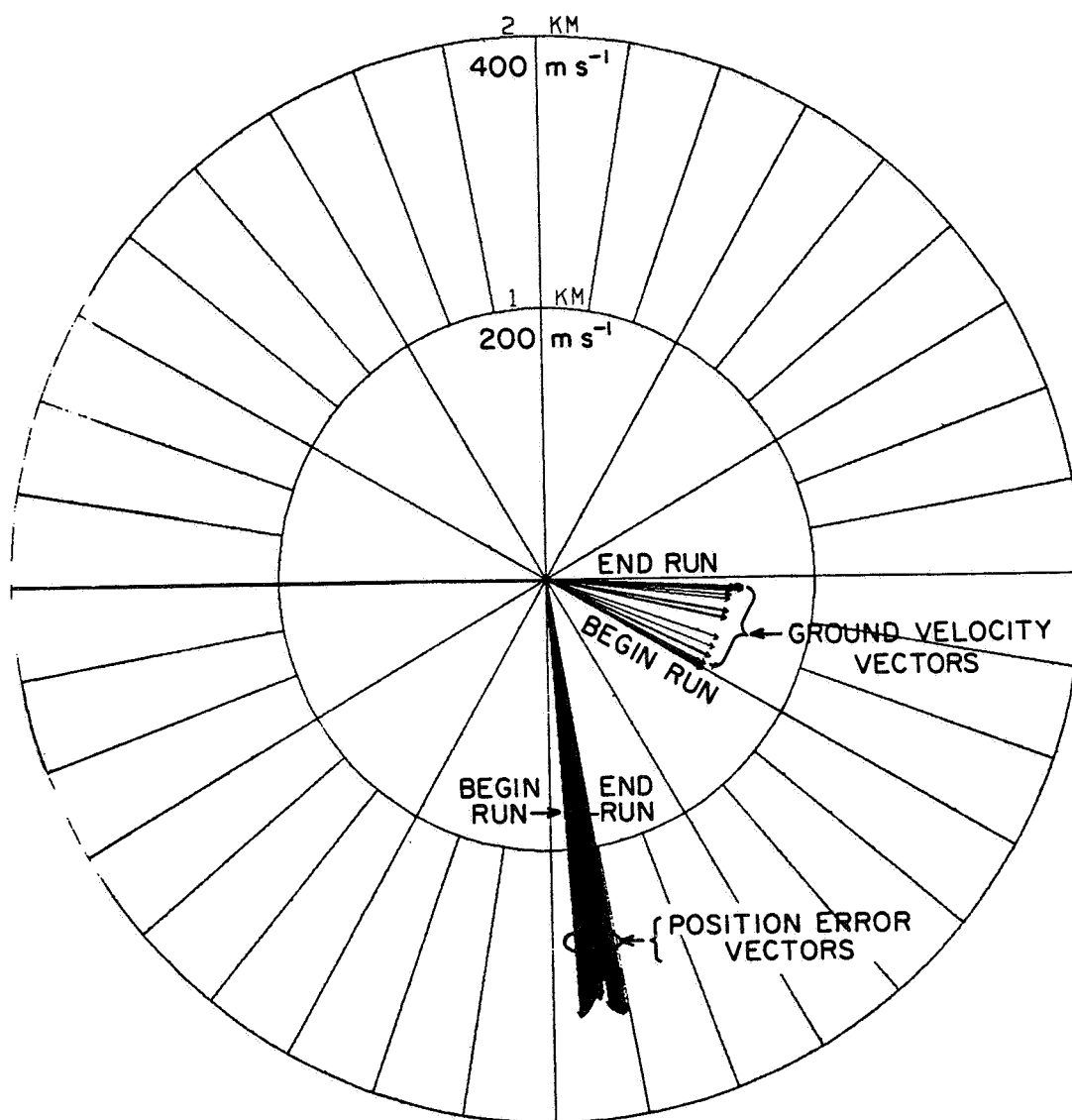


Figure C.2 INS derived position error vectors for run 4. Also shown are the aircraft's ground velocity errors throughout the run.

original photo-derived position error data. The vector error in INS position is seen in Fig. C.2 to average about 1.6 km south-southeast of the "true" (photo-derived) position, with variations of about 200-300 m around this average. However, it is just the time rates of change of these position error variations which are of interest, because they define the INS-derived ground velocity errors. As noted at the bottom of the figure, the position error vector shifted, from its initial coordinates, toward the east-northeast (81.4 deg) by some 171 m during the course of the 255.1 s-long data run, implying an average INS velocity error of 0.67 m s^{-1} from a direction of 261.4 deg during the run. The fact that the aircraft made a nearly 30 deg left turn during the run is shown by the ground velocity vectors which have been added to the diagram; the effects of this turn on the quality of the INS data will be shown to be quite dramatic.

In order to analyze the ground velocity errors in more detail, the x- and y-components of the position and velocity errors were computed and studied separately. In Figs. C.3 and C.4 are depicted the x- and y-position errors at the times of lidar frames.

The Fourier-filtering was performed separately over the three main parts of the time series of position data for run 4 (Fig. 3.2): (a) the initial straight flight leg prior to the left turn; (b) the left turn (as identified from the time series of aircraft roll angles); and (c) the final straight flight leg following the left turn. Following reconstruction of the Fourier-filtered position time series, additional smoothing using a simple three-point filter was applied to remove cusps which occurred at the junction points between the three parts of the run 4 data.

The final filtered sequences of x- and y-position errors used to compute the ground velocity errors in run 4 are given in Figs. C.5, C.6. Note the removal of the high-frequency noise and the retention of the basic pattern that had been evident in the unfiltered data. In Figs. C.7 and C.8 are given the ground velocity estimates which were deduced from the time variations of the data in Figs. C.5, C.6. Fourier-filtering techniques similar to those applied to the position data have been used. Note that it is apparent both from the velocity curves and also from the position curves that the ground velocity errors may exceed 2 m s^{-1} during straight flight, 10 m s^{-1} during turns, and may vary with time. The time variability of these errors has par-

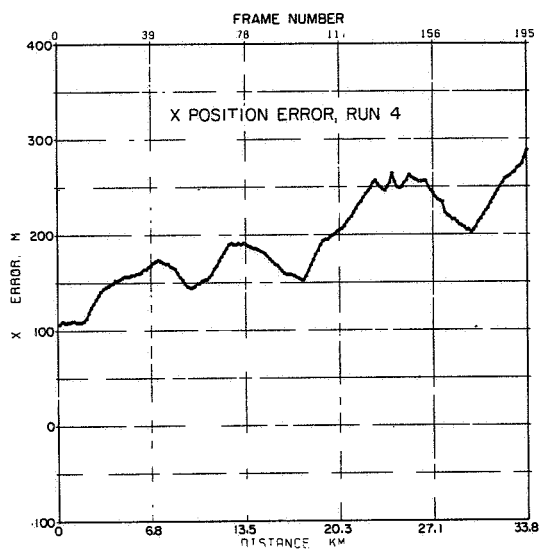
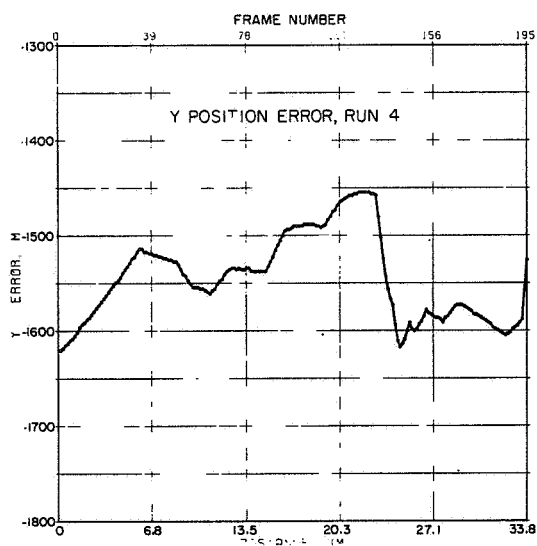


Figure C.3 The x-position errors at frame times for run 4. Mean error is 193 m.

Figure C.4 The y-position errors at frame times for run 4. Mean error is -1545 m.



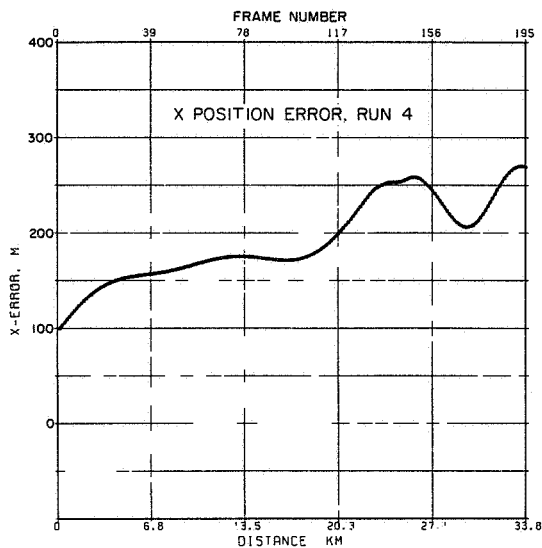
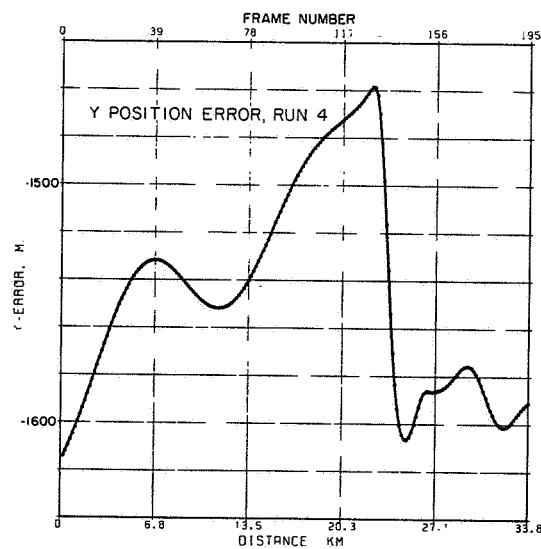


Figure C.5 Fourier-filtered version of x position error data in Fig. C.3. Only harmonics 0, 1 and 2 plus the observed trend were used to create these position data.

Figure C.6 The same as Fig. C.5 except for the y position errors.



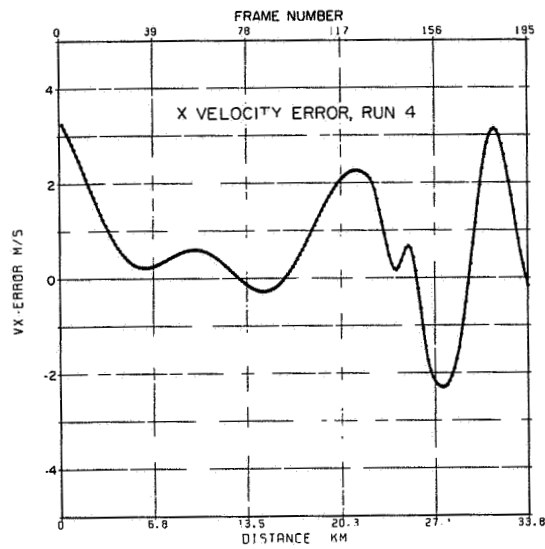


Figure C.7 The x component of ground velocity errors estimated using data in Fig. C.5. After differentiation with respect to the uneven frame time intervals, further Fourier filtering was used. Mean error = 0.70 m s^{-1} .

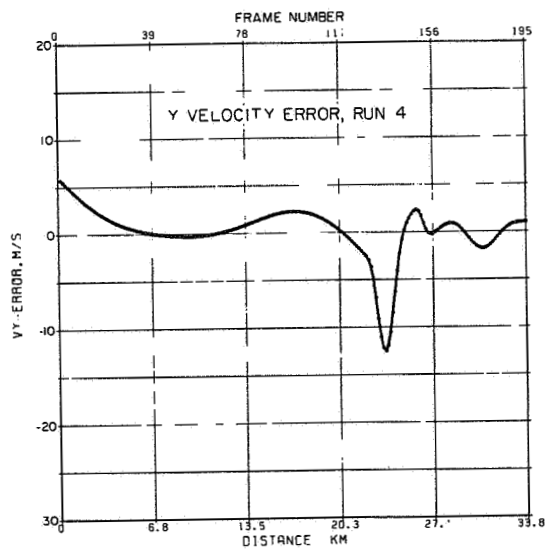


Figure C.8 The same as Fig. C.7 except this is y component of ground velocity errors estimated using data in Fig. C.6.

ticularly important consequences for the credibility of the lidar-measured winds as is discussed in Section C.4.

Note also the appearance of large ground velocity errors at the beginning of the run; this pattern could be the result of the method of detrending the raw position errors, which did not employ any least-squares straight-line fitting. The detrending technique used in this study, while insuring pure periodicity of the residual data within the data domain, is vulnerable to the effects of large random data errors at the end point. However, close examination of the raw data associated with the beginning of run 4 failed to reveal any noteworthy irregularities in the photo position estimates that might account for the large ground velocity estimates obtained there, rather it appeared that these errors came directly from a large-scale error trend which was clearly apparent in the raw data. In summary, some skepticism is warranted for the values of ground velocity error obtained near the endpoints of data sequences, although for the data shown here evidence also exists which tends to support the values calculated.

The estimated ground velocity errors are well outside the manufacturer's specifications of a 3-sigma velocity error of 0.5 m s^{-1} , and are capable of introducing significant bias into the lidar radial velocity measurements with respect to the ground. Substantial further investigation, including additional field measurements, will be needed in order to obtain more definite information regarding the magnitudes and variability of the ground velocity errors on time scales that affect the wind estimates. The effect of these time-dependent errors on the wind vectors retrieved by the lidar system are demonstrated in Section C.4.

C.4 EFFECTS OF NAVIGATION ERRORS ON DOPPLER LIDAR DERIVED WIND FIELDS

Important to the wind field estimate accuracy is the velocity error associated with the time rate of change of the position error. Samples of estimates of the two components of the velocity error were presented in Figs. C.7 and C.8. The most conspicuous feature of these two plots was the large but relatively brief y-velocity error which occurred between frames 132 and 153, during a left turn made by the aircraft. This velocity error attained a magnitude of more than 10 m s^{-1} for a portion of the turn, a magnitude which was roughly confirmed by inspection of the behavior of the y-position error in Fig. C.6. Most of the velocity error was confined to the y-direction during

the turn, and since the aircraft track was nearly eastward at the time, it appeared that most of the ground velocity was due to inaccurate measurement of lateral accelerations. It is clear that INS errors are especially likely to occur in the vicinity of aircraft turns. This suggests strongly that biases might be present in the lidar-measured winds from the towering cumulus circumnavigations (runs 5-12), which featured numerous sharply banked turns. Unfortunately nadir photo documentation of the aircraft's movement was not available during the cumulus circumnavigations due to a temporary malfunction of the camera; therefore the performance of the INS during these contorted maneuvers could not be assessed.

The exact manner in which these large errors are introduced into the INS output is not yet known, although it is possible that internal filtering processes employed in the INS computation sequence might be capable of producing large transient errors during turns and accelerations. Further investigation will be needed in order to isolate the true cause or causes of the errors.

In order to establish what sort of wind vector errors might be introduced into the lidar analyses as a result of neglect of or incorrect compensation for the INS errors, artificial data or "measurements" consisting only of the components of estimated ground velocity errors along the lidar lines-of-sight, were synthesized to generate wind vectors. Hence the raw velocity data used in these analyses consisted of "data" which were strictly independent of range for each lidar frame. The results, a sample of which is shown in Fig. C.9 for run 4 data, reveal the presence of a number of vortical and divergent "flows" generated by patterns in the time-varying ground velocity error interacting with the overlapping of fore and aft lines-of-sight at various ranges. Some of these error vectors have magnitudes of $3-4 \text{ m s}^{-1}$, quite significant in view of the fact that the actual wind field itself was only about 10 m s^{-1} in strength for much of the data examined.

It is most important to realize that the magnitudes of the wind field errors caused by these time-varying errors in radial velocity are not limited to the actual magnitudes of the ground velocity errors which caused the radial velocity errors. Rather, the components of the ground velocity errors along the lidar lines-of-sight are "distributed" throughout the data collection area as the aircraft continues along its flight track, only to be combined with other erroneous radial velocity components resulting from later or earlier

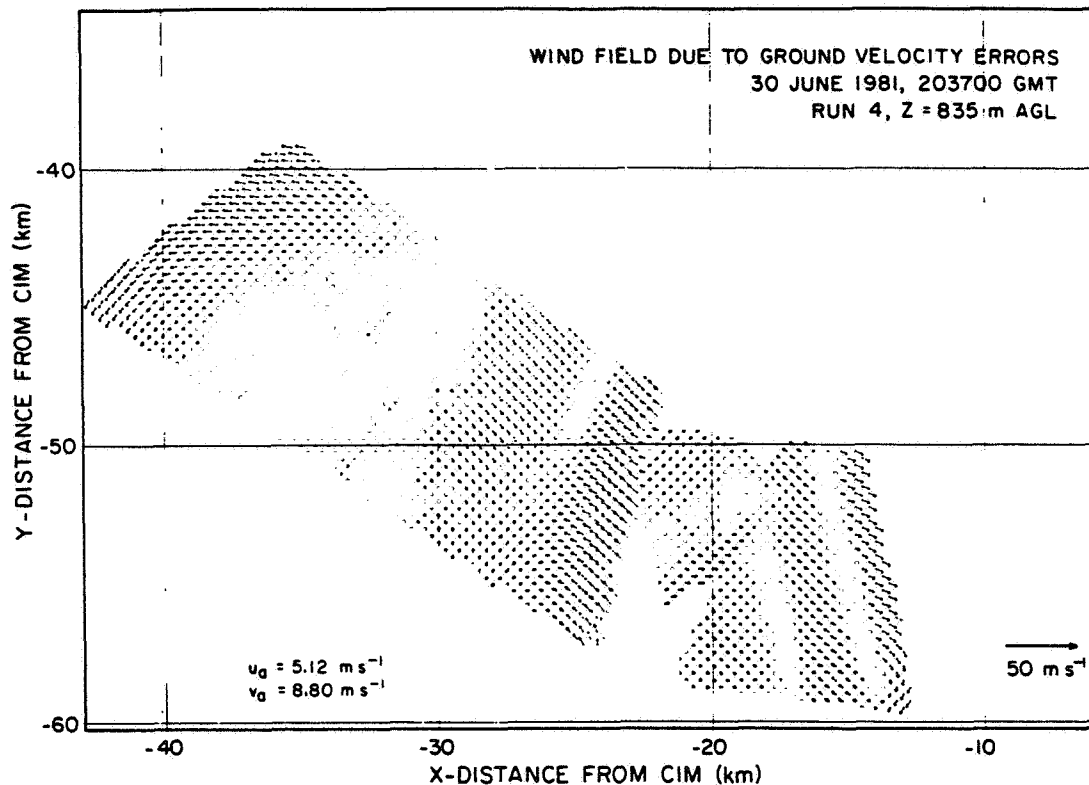


Figure C.9 Wind field corresponding to INS velocity errors from Figs. C.7 and C.8. Note the presence of vortical and divergent patterns resulting from the time-varying INS errors.

errors. If the error vectors should happen to lie outbound along a fore line-of-sight at one moment, to be followed a moment later by an error of the same magnitude lying inbound along an aft line-of-sight, the error in the wind field vector estimate obtained from combining these two radial velocity errors would be almost three times as large in magnitude as either of the original ground velocity errors.

Although the error in wind vectors of Fig. C.9 was obtained using estimates of ground velocity error which varied relatively smoothly with time, it is clear that any time-varying errors introduced into the radial velocity data have the potential to generate wind error. Generally, the vector error patterns will have a spatial scale which corresponds with the time scale of the radial velocity errors, and will have magnitudes which correspond roughly to the magnitudes of the radial velocity errors. Lingering errors caused by incorrect estimation of drift angle biases could, for instance, produce small-scale, weak vortical and divergent patterns in the wind field analyses; at the same time, ground velocity errors which are larger in magnitude but more

slowly varying in time could produce a superimposed pattern of larger scale vorticities and divergences.

Thus it would appear that any wind perturbations having magnitude of $3-4 \text{ m s}^{-1}$ or less obtained from the Doppler data analysis must be viewed with caution and skepticism, as perturbations of that magnitude could have been caused solely by any of the various forms of bias errors in the radial velocity measurements. Fortunately, many of the gust front observations made during the Severe Storms Experiment contained such strong wind field features that even large errors of the type discussed here could not obscure the real flow pattern.

APPENDIX D

INSPECTION AND VERIFICATION OF DOPPLER SPECTRAL MOMENT DATA

Inspection of listings of the data fields from the tape furnished by NASA showed that the NASA-corrected velocities and intensities contained occasional inconsistencies that were suggestive of data processing errors. The raw data fields, however, seemed to be unaffected by these errors.

Table D.1 shows a sample of the raw tape contents from the first frame of run 2, featuring the corrected data supplied by NASA as well as the raw data. The columns marked "XBEAM" and "YBEAM" give the X and Y coordinates of each resolution volume center relative to the start of the run. The raw lidar velocities are given under "RAWVEL", while the corrected and smoothed lidar velocities furnished by NASA are given under "CORVEL". All velocities are given in $\text{m}\cdot\text{s}^{-1}$. Raw lidar intensities are given in units of dB above noise. Spectral widths are given in logarithmic coded form under "WIDTH". Conversion of width values to $\text{m}\cdot\text{s}^{-1}$ format is described below.

Of particular note in Table D.1 is the susceptibility of CORVEL to large errors; see resolution volumes ("BINS") 12 to 14 and 16 for examples. In these same resolution volumes the parameter RAWVEL is seen to be much better behaved; of the first 18 resolution volumes only the first contained noisy data, and this was expected based on the fact that the transmission of the signal was still in progress during the time the first resolution volume was being sampled.

Values of CORAMP seem fairly reasonable, except that the steady decrease seen from resolution volumes 2 to 14 suggests that a range-squared correction may not have been incorporated. The coded values of width appeared to be quite consistent and credible; note the near constancy of width through resolution volume 13, followed by a sudden degeneration to large noisy values at larger ranges. Note also the fact that the RAWVEL array retains consistency out to larger ranges than width; this is a consequence of the way in which spectral width is estimated in the poly-pulse-pair processor (PPPP) (Lee, 1980) and is not sufficient reason to consider the velocities lying in the region of large width to be suspect. Furthermore it was ascertained that the values of XBEAM and YBEAM (Table D.1) were not consistent with ranges to the resolution volumes (bins) deduced from the measured time positions of the sampling gates in the PPPP (McCaul, 1985).

ORIGINAL PAGE IS
OF POOR QUALITY

BIN CATALOG, FRAME 1, 45 ENTRIES

BIN	XBEAM	YBEAM	RAWAMP	RAWVEL	WIDTH	CORAMP	CORVEL	ERROR
1	0.	0.	150.0	-37.0	7.	0.0	0.0	23.55
2	-280.	-160.	145.7	3.1	4.	0.0	0.0	-11.06
3	-560.	-300.	147.0	3.6	5.	23.3	0.7	20.38
4	-840.	-460.	146.8	4.2	5.	23.4	3.4	4.57
5	-1120.	-620.	145.1	4.7	5.	22.3	4.6	6.09
6	-1400.	-780.	143.4	4.0	5.	21.0	3.9	0.17
7	-1680.	-940.	140.6	3.5	6.	18.6	3.4	0.30
8	-1960.	-1080.	139.3	3.3	5.	17.8	3.2	0.42
9	-2240.	-1240.	138.2	2.1	5.	17.1	2.0	0.57
10	-2520.	-1400.	135.2	1.8	6.	14.6	1.6	-31.81
11	-2800.	-1560.	134.4	1.8	5.	14.3	1.8	0.64
12	-3080.	-1720.	131.6	2.1	7.	11.8	-196.6	3.75
13	-3360.	-1860.	131.2	2.3	7.	12.0	-121.9	14.91
14	-3640.	-2020.	129.4	2.6	14.	12.0	-121.9	14.91
15	-3920.	-2180.	127.5	3.3	15.	9.0	3.2	-32.44
16	-4200.	-2340.	127.1	2.6	15.	9.0	174.9	-6.82
17	-4480.	-2500.	124.3	2.7	15.	0.0	2.6	-32.44
18	-4760.	-2640.	126.2	1.6	15.	8.8	1.5	-32.44
19	-5040.	-2800.	124.1	22.0	15.	0.0	-49.4	-9.42
20	-5320.	-2960.	125.1	21.8	15.	8.3	-339.9	3.54
21	-5600.	-3120.	124.9	21.8	15.	8.4	-337.7	-21.35
22	-5880.	-3280.	123.7	21.7	14.	0.0	-358.5	-21.89
23	-6160.	-3440.	123.9	22.2	15.	0.0	-297.1	8.96
24	-6440.	-3580.	126.9	-1.8	14.	11.4	-98.8	3.59
25	-6720.	-3740.	128.8	-2.7	13.	13.7	-2.8	-32.44
26	-7000.	-3900.	125.8	-3.4	13.	10.9	-3.5	-32.44
27	-7280.	-4060.	123.4	21.7	14.	10.9	-3.5	-32.44
28	-7560.	-4220.	124.3	21.1	14.	0.0	21.0	-32.44
29	-7820.	-4360.	124.1	21.4	15.	0.0	21.4	-32.44
30	-8100.	-4520.	124.1	21.8	14.	0.0	21.8	-32.44
31	-8380.	-4680.	123.6	21.9	14.	0.0	21.8	-32.44
32	-8660.	-4840.	123.7	21.8	15.	0.0	21.7	-32.44
33	-8940.	-5000.	124.9	21.8	13.	0.0	21.7	-32.44
34	-9220.	-5140.	123.7	21.6	15.	0.0	21.5	-32.44
35	-9500.	-5300.	124.1	21.8	14.	0.0	21.7	-32.44
36	-9780.	-5460.	124.9	21.9	12.	12.4	21.8	-32.44
37	-10060.	-5620.	123.9	22.0	14.	0.0	21.9	-32.44
38	-10340.	-5780.	124.9	21.7	14.	0.0	21.2	-32.44
39	-10620.	-5920.	122.8	21.3	15.	0.0	21.2	-32.44
40	-10900.	-6080.	123.6	22.2	14.	0.0	22.1	-32.44
41	-11180.	-6240.	124.7	21.9	13.	13.3	21.8	-32.44
42	-11460.	-6400.	123.2	22.0	13.	0.0	21.9	-32.44
43	-11740.	-6560.	124.1	21.5	14.	0.0	21.4	-32.44
44	-12020.	-6700.	124.1	21.8	14.	0.0	21.7	-32.44
45	-12300.	-6860.	123.2	21.3	15.	0.0	21.2	-32.44

Table D.1. Sample of raw lidar moment data from frame 1 of run 2. See text for further details.

Inspection of data such as that shown in Table D.1 made it clear that all data preparation for meteorological interpretation would have to be accomplished starting with the raw data and that resolution volume coordinates would have to be recomputed. Furthermore, raw data also made it clear that much raw data at longer ranges from the aircraft were noisy and should be ignored when creating disk files of raw data to be used in later analyses. The range beyond which data degenerated to noise was found to depend on aircraft altitude, and hence probably was controlled by levels of ambient moisture. For runs 2 through 8, only the first 28 range bins out of 45 available were retained for subsequent analysis; for the higher altitude runs 9 through 12, the first 40 range bins were retained.

In order to prepare the data for meteorological interpretation, it was necessary to range-normalize the raw intensity data to produce estimates of reflectivity, convert the width data to $\text{m}\cdot\text{s}^{-1}$ format, and remove any "frame bias" from the measured Doppler (radial) velocity data. This frame bias consisted of velocity errors which were approximately constant within each frame of data and were associated with incomplete or erroneous documentation of small scale variations in aircraft attitude and motion. The removal of frame bias from the velocities in each frame is done only after point editing, and is discussed in Section D.3.

D.1 PREPARATION OF REFLECTIVITY FIELDS

Range normalization of the raw intensity furnished by NASA was accomplished using a two-step algorithm and is fully discussed by McCaul (1985). Therefore, only an outline is given here. The first step was to determine for each frame the background noise level of the intensity field. This noise level was found by averaging the intensity from the most distant 20 resolution volumes, with any intensity features rising more than 3 dB above the minimum of all resolution volumes excluded from the averaging. In cases where the minimum intensity in any frame occurred at a range closer than the outermost 20 resolution volumes, the bin number of that minimum value was used as the inner range bin limit in the search through maximum range for values to be used in computing the noise level for that frame. The exclusion of any high intensity features from the noise level calculations was made necessary by the occasional occurrence of highly reflective cloud edges in the most distant 20 resolution volumes. The noise level was determined for each frame because small random changes of 1-2 dB were noted in the background noise values during the course of the typical data run.

The second step in the range normalization was to subtract the noise level from all recorded values of intensity and to multiply the result by the sum of the squares of the resolution volume range and of a "Rayleigh Range" factor related to laser beam divergence (Murty and Bilbro, 1978). An exponential range-dependent attenuation function is included in the Murty and Bilbro formulation.

It was appropriate to estimate the attenuation constant k by linearly fitting the range-dependent decibel variations in intensity. Although the actual intensity attenuates exponentially with range if k is constant and independent of range, the intensity, expressed in decibel units, will decrease linearly with range.

Only relative intensities were computed because the information regarding emitted laser power was not available for each frame. An example of estimated relative reflectivity fields computed from raw intensity data using the above described method is shown on Figure D.2 whereas Fig. D.1 shows the raw intensity data. The raw intensity profile from frame 12 of run 9 (Fig. D.1) is seen to settle down to a noise-level value beyond a range of 5 km from the aircraft, after showing a large jump at a cloud edge which was located at a range of about 4 km. The cloud-strike reflectivities (Fig. D.2) are seen to stand out clearly from the reflectivities in the cloud free air at near ranges. The cloud attenuates the lidar pulse so that no echoes are received beyond 4.8 km range although cloud may be present there.

The results of all the revisions documented above are visible in Table D.2, which represents the corrected version of Table D.1, with the decoded versions of Doppler spectral width (McCaul 1985) listed under the "WIDTH" column. Note that not only are spectral widths converted to $\text{m}\cdot\text{s}^{-1}$ format and reflectivities estimated, but also the positions of the lidar resolution volumes with respect to the aircraft have been modified so as to be consistent with resolution volume positions deduced from timing measurements.

D.2. THRESHOLDING AND EDITING OF DOPPLER MOMENT DATA

The next stage in preparing the data for analysis involved "point-editing", or removal of noisy data point-by-point based on detailed inspection of the data. Point editing was performed on velocity, intensity, and width fields separately. The first step was to apply a "thresholding" algorithm which could set to "missing" the large numbers of obviously useless values

BIN CATALOG, FRAME 1, 28 ENTRIES

BIN	XBEAM	YBEAM	RAWAMP	RAWVEL	RWIDTH	CORAMP	CCRVEL	ERROR
1	-168.	-94.	150.0	-37.0	1.03	44.8	-37.0	0.07
2	-447.	-250.	145.7	3.1	0.51	42.1	3.0	0.12
3	-726.	-406.	147.0	2.6	0.65	45.1	1.9	11.45
4	-1006.	-562.	146.8	4.2	0.65	46.6	2.4	30.58
5	-1285.	-718.	145.1	4.7	0.65	46.6	2.4	7.43
6	-1564.	-874.	143.4	4.0	0.65	46.5	3.6	2.33
7	-1844.	-1030.	140.6	3.5	0.82	45.9	7.0	8.79
8	-2123.	-1186.	139.3	3.3	0.65	46.5	3.2	0.42
9	-2402.	-1343.	138.2	2.1	0.65	47.3	2.0	0.57
10	-2682.	-1499.	135.2	1.8	0.82	46.0	1.1	0.20
11	-2961.	-1655.	134.4	1.8	0.65	47.1	1.7	0.25
12	-3240.	-1811.	131.6	2.1	1.03	45.7	2.0	0.91
13	-3520.	-1967.	131.2	2.3	1.03	47.2	83.8	5.86
14	-3799.	-2123.	129.4	2.6	5.14	46.5	-531.0	32.27
15	-4078.	-2279.	127.5	3.3	6.48	45.1	-206.2	-6.55
16	-4358.	-2435.	127.1	2.6	6.48	46.2	2.6	-32.44
17	-4637.	-2592.	124.3	2.7	6.48	0.0	2.6	-32.44
18	-4916.	-2748.	126.2	1.6	6.48	0.0	-239.9	23.65
19	-5196.	-2904.	124.1	22.0	6.48	0.0	21.9	-32.44
20	-5475.	-3060.	125.1	21.8	6.48	0.0	-208.2	23.12
21	-5754.	-3216.	124.9	21.8	6.48	0.0	-334.5	-5.84
22	-6034.	-3372.	123.7	21.7	5.14	0.0	-409.0	-1.41
23	-6313.	-3528.	123.9	22.2	6.48	0.0	-275.8	31.52
24	-6592.	-3684.	126.9	-1.8	5.14	60.4	308.3	17.10
25	-6872.	-3840.	128.8	-2.7	4.09	65.5	-2.8	-32.44
26	-7151.	-3997.	125.8	-3.4	4.09	0.0	-3.5	-32.44
27	-7430.	-4153.	123.4	21.7	5.14	0.0	21.6	-32.44
28	-7710.	-4309.	124.3	21.1	5.14	0.0	-124.1	15.20

Table D.2. Sample of corrected lidar wind, intensity and width data for data in Table D.1. See text for further details.

ORIGINAL PAGE IS
OF POOR QUALITY

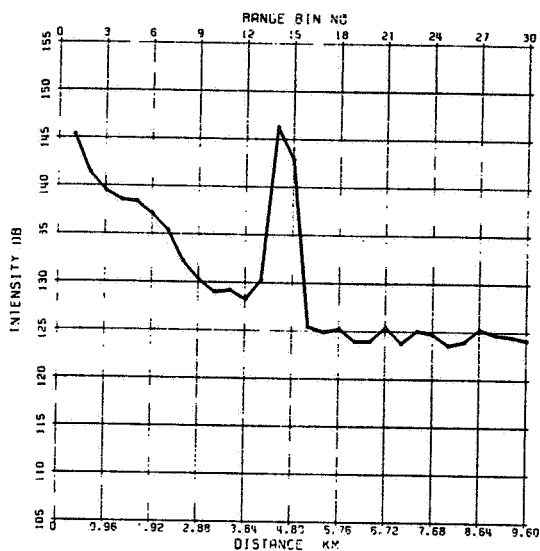


Figure D.1 Typical raw intensity profile for a lidar frame containing a cloud strike (frame 12 of run 9).

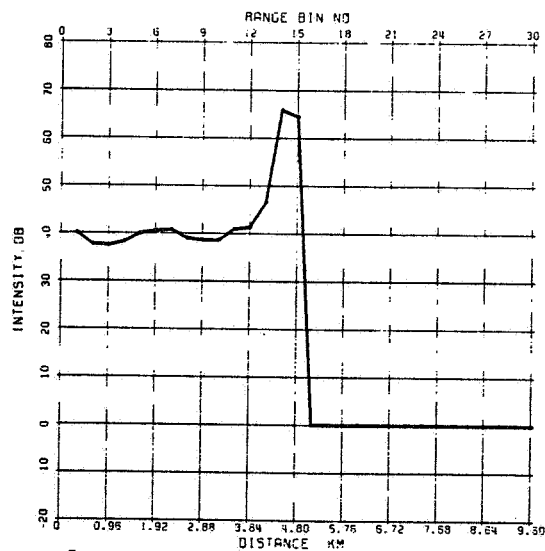


Figure D.2 The profile of relative reflectivity estimated from data in Fig. D.1. Note that reflectivity is uniform in range until the lidar pulse strikes the cloud at 4 km.

encountered at ranges beyond the lidar's functional limits. The editing of width and intensity data required no special threshold routine because all valid (i.e., non-spurious) reflectivity estimates were found to fall between the fixed thresholds of 20 and 80 dB above noise and all valid Doppler spectral widths were found to fall between 0 and $6.0 \text{ m}\cdot\text{s}^{-1}$. The velocity threshold limits had to be established individually for each data run; for a list of the values used, consult Table D.3. The spurious velocities which were removed via the thresholding method were easily identified in listings of raw data because of their relatively large magnitudes; examples are visible in Table D.1 under the RAWVEL (Raw Velocity) column, beginning at resolution volume (BIN) 19.

Further editing was often needed to remove spurious point values. To simplify this sometimes tedious process, a graphical routine was designed which displayed each of the fields to be edited in a way which would facilitate finding spurious data quickly. Samples of the graphical output are shown in Figs. D.3-D.6, for data from run 10 of the Severe Storms experiment.

In Fig. D.3 the raw radial velocities in each fore and aft frame are depicted in approximately their true relative positions in space; the "vectors" representing the radial velocities are drawn at an angle with respect to the line-of-sight of each lidar frame for clarity and ease of pattern observation.

Fig. D.4 shows both the lidar intensity and spectral width for the data of run 10. The circles which represent the locations of the data points in space have diameters proportional to relative reflectivity, while the line-weight with which each circle is rendered is roughly proportional to spectral width. The band of large circles seen at mid-range in Fig. D.4 thus represents a highly reflective target, in this case the edge of a cumulus congestus cloud. The lightweight line with which the large circles are drawn indicates small measured spectral widths, and presumably, good definition of mean Doppler velocity.

Figures D.5 and D.6 depict the observed distributions of observed radial velocities for each fore (Fig. D.5) and aft (Fig. D.6) lidar frame. The velocity scale used in these figures runs from $-20 \text{ m}\cdot\text{s}^{-1}$ at the bottom of the plot to $+20 \text{ m}\cdot\text{s}^{-1}$ at the top. In both figures valid meteorological data appear as swaths of loosely distributed points near the centers of the plots, with spurious returns arranged in swaths at the edges of the plots. In Fig. D.6

Table D.3

Summary of Characteristics of Lidar Data Runs

RUN	NFRAME	VMIN	VMAX	UADV	VADV	TSTART	TSTOP	OATIME
2	282	-10.0	11.8	-1.80	1.60	201810	202529	202130
3	210	-8.0	18.3	4.42	4.35	202547	203021	202800
4A	195	-14.2	-7.3	5.12	8.80	203549	204005	203700
5	71	-9.0	9.0	4.14	7.57	204614	204739	204920
6	33	-20.0	7.0	2.09	8.40	204832	204910	204920
7	33	-9.0	18.0	1.96	9.63	205006	205044	204920
8	24	-9.0	13.0	1.59	7.16	205128	205156	204920
9	33	-10.0	0.0	4.83	6.35	205401	205438	205640
10	35	-2.0	10.0	3.09	4.46	205537	205619	205640
11	39	-2.0	0.0	4.17	2.88	205715	205801	205640
12	48	-10.0	0.0	4.53	3.82	205849	205945	205640

NFRAME = Total number of lidar frames taken in the run

VMIN = Minimum radial velocity used in thresholding

VMAX = Maximum radial velocity used in thresholding

UADV = Zonal motion component used in data advection

VADV = Meridional motion component used in advection

TSTART = Time (GMT) data collection began in the run

TSTOP = Time (GMT) data collection ended in the run

OATIME = Time (GMT) of objective analysis of the run

ORIGINAL PAGE IS
OF POOR QUALITY

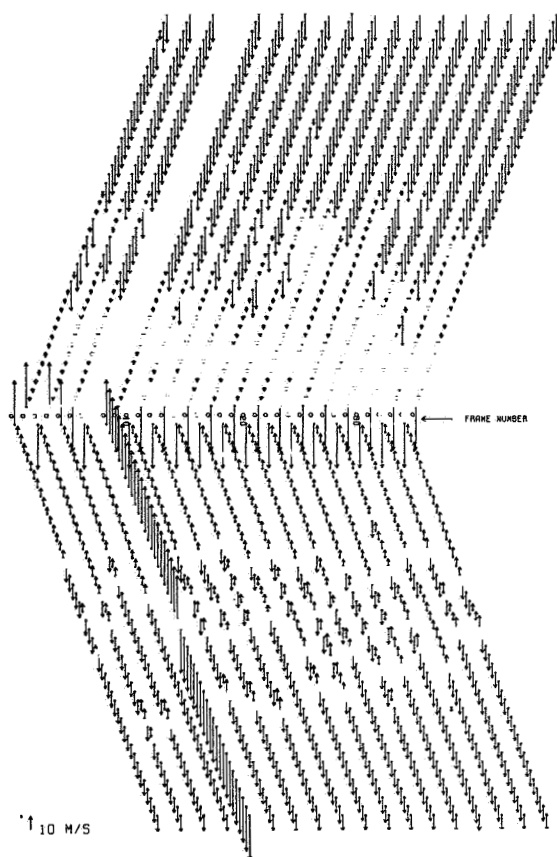


Figure D.3 Graphical output for editing data: raw lidar radial winds from run 10. Wind data from fore frames are shown above; aft data shown below. Along-track distance scale is expanded for clarity.

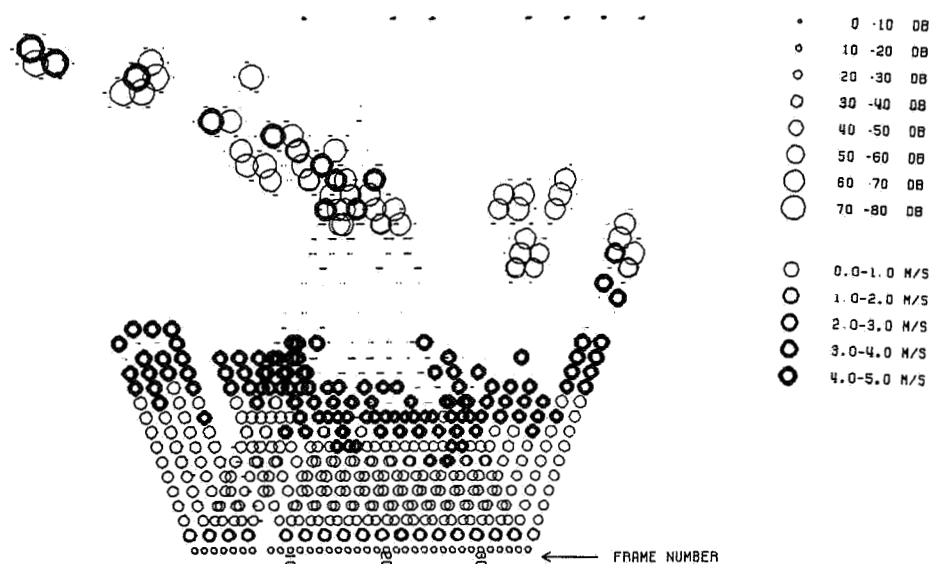


Figure D.4 Graphical output (run 10) for editing data: relative reflectivity is proportional to circle diameter, and spectrum width values are scaled in proportion to line weight. Small dashes indicate low-intensity, large-width returns.

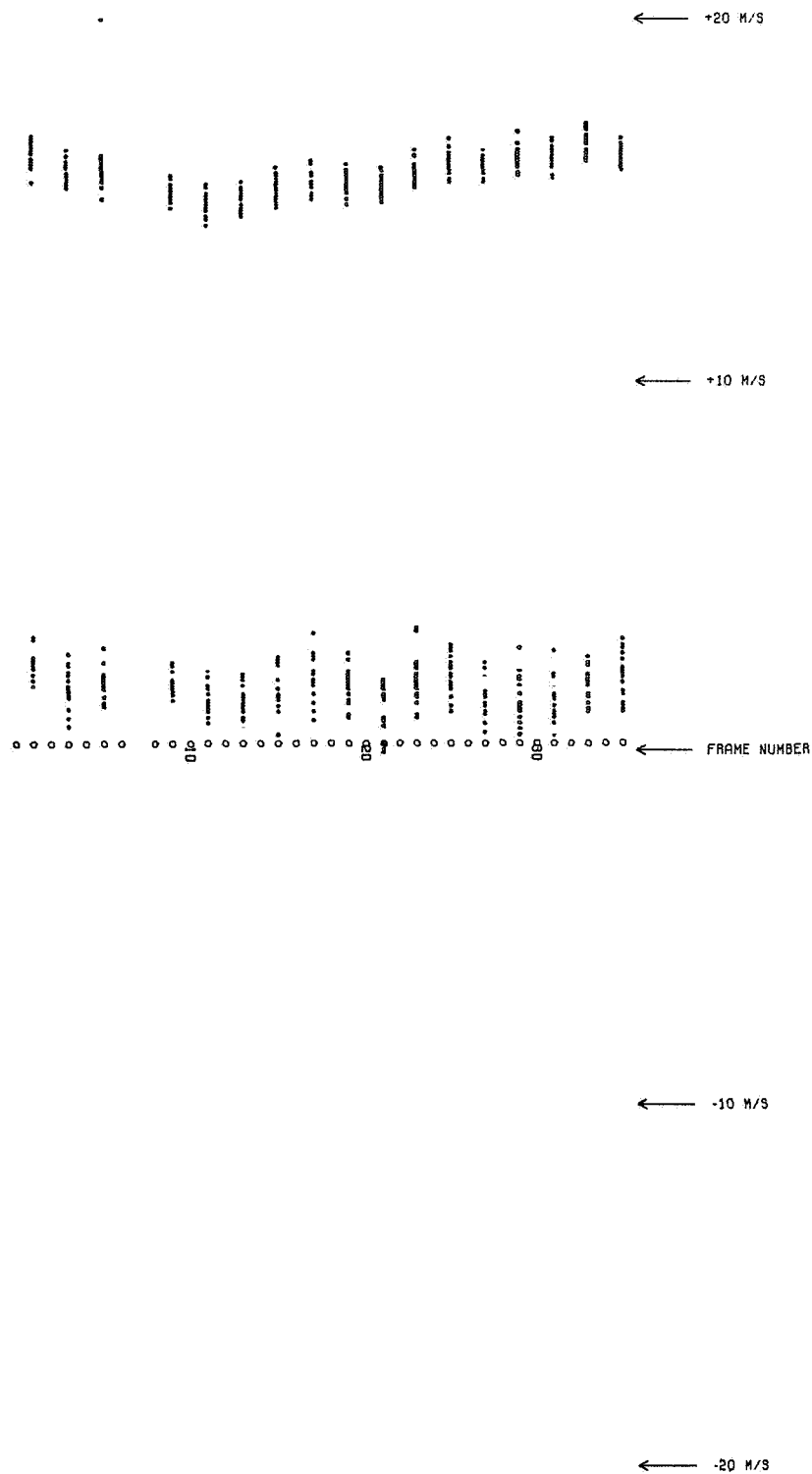


Figure D.5 Graphical output for editing velocity data: velocity distribution is for the same fore frame data presented in Fig. D.3. Data points near top or bottom margins are due to moding in the lidar transmitter.

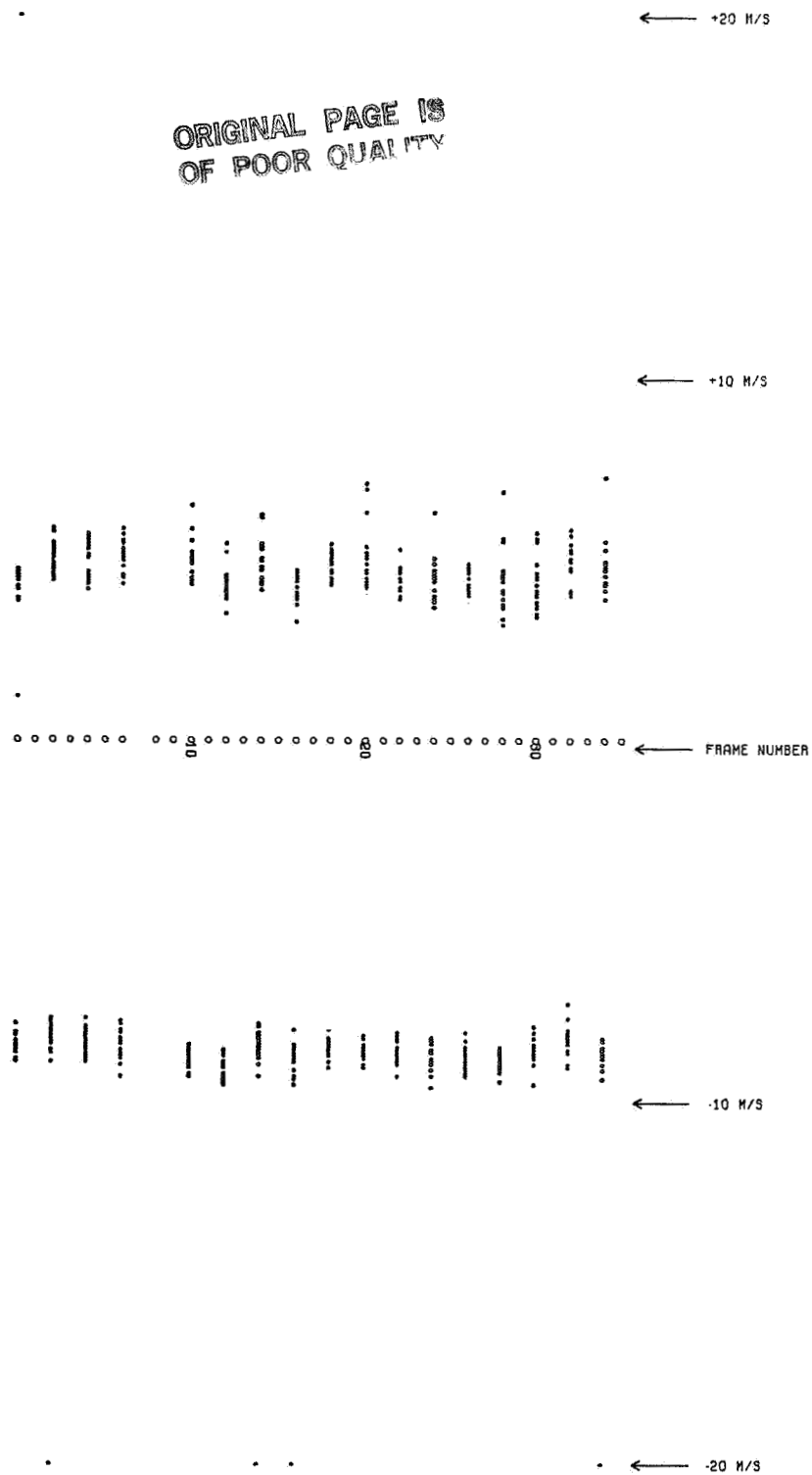


Figure D.6 Same as Fig. D.5 except for the aft frame data.

the meteorologically useful data is the swath of positive velocities whereas the swath of negative velocities is associated with resolution volumes at unusably long ranges (Fig. D.3) as is the data swath near $+17 \text{ m s}^{-1}$ in Fig. D.5. Velocity estimates at long ranges, where echo intensity is less than noise, should be uniformly distributed across the Nyquist interval. These coherent velocity swaths in echo free regions might be caused by leakage of coherent signals into the PPPP.

Thus, with the help of graphical displays, it was possible to examine the data from each resolution volume of each lidar frame and to determine quickly which data points were consistent with neighboring data points. Such a visual examination was made for every data point in every run, and if an inconsistent data value was found, it was included in a list of "bad" points contained directly in the text of a point edit subroutine whose function was to replace such data points with a "missing" data parameter value, usually -999.99. On some occasions it was necessary to delete entire frames from the data set due to noise contamination.

D.3. DIAGNOSIS AND REMOVAL OF RADIAL VELOCITY BIASES

The next step in preparing the data for meteorological interpretation involved deletion of velocity biases which contaminated radial velocity data in each frame. Correction of the measured radial velocities for this "frame bias" was a difficult and troublesome task. Lee (1982), McCaul (1985), and other investigators using the NASA data have described various approaches taken.

Lidar frame bias manifests itself in the tendency for the variability of the measured velocities to be much larger from frame to frame at a given range than from resolution volume to resolution volume within a given frame. The underlying physical cause of the bias is not completely understood, but apparently is related to inadequate measurement of changes in aircraft attitude and relative airspeed, especially those associated with quasi-periodic fugoid motions and cyclic feedback effects in the aircraft flight control system, and to larger-than-expected delays in recording certain INS-derived data such as drift angle (Lee, 1982).

Lee (1982) found evidence in a detailed study of lidar data taken in 1981 in California that the frame biases were most likely due to delays in reporting INS-measured drift angle values to the data recording system. Lee

(1982) examined various possible delays in drift angle and found a remarkable correlation between the excursions of the range-averaged radial velocities and the excursions of the lag-2 differences in measured drift angles. An attempt was made in this study to duplicate Lee's findings by means similar to those he employed. However, for the runs examined in the 30 June data, no clear cut relation between velocity excursions and drift differences emerged.

In general, the large variability of the true wind speed in the convective situation found on this day prevented the discovery of the specific physical mechanisms responsible for the biases. However, examination of the behavior of the velocity in all the data runs suggested that the magnitude of the problem was sensitive to the local turbulence of the flow near the aircraft and to the relative orientation of the airspeed and ambient wind vectors.

Based on a drift angle study conducted by McCaul (1985), and the absence of any clear-cut evidence as to the physical mechanism responsible for the frame bias, it was decided to handle the problem by means of filtering only.

Two important additional causes of low-frequency velocity errors (i.e., frame bias) were found in the present data: ground velocity bias associated with data recording delays, and ground velocity errors produced by the INS (appendix C.4). Both of these error sources were found to be capable of causing radial velocity errors of 2 m s^{-1} or more, and are thus comparable in importance to the high-frequency drift angle delay errors already discussed. Unfortunately, neither the errors due to delays in recording ground velocity (discussed in the next paragraph) nor errors generated by the INS could be eliminated by using simple filtering techniques because their spectral content was too similar to that of the true wind field. These low-frequency frame biases therefore had to be estimated using independent means.

A portion of the radial velocity errors (frame biases) were found to result from delays of recording INS-derived ground velocity during periods of aircraft acceleration or deceleration. The transmission of the ground velocity errors "EGS" through the data collection chain for an assumed calm wind field and accelerating aircraft is depicted in Fig. D.7. From the figure it is clear that an erroneous wind vector equal in magnitude and direction to the ground velocity error vector EGS is "measured" by the lidar system as long as the aircraft acceleration is maintained constant. Addition of a constant nonzero wind field to this hypothetical situation will not alter the error.

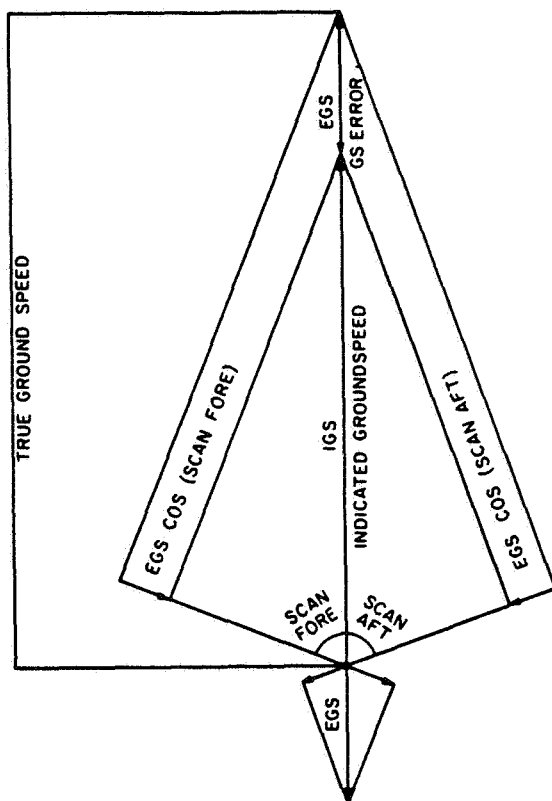


Figure D.7 Geometrical explanation of the effects of ground velocity errors (due to delays in recording data) on the radial velocity computation.

However, depending on the relative magnitudes of the ambient wind vector and the error EGS, and on the orientation of the ambient wind vector with respect to the aircraft track, an apparent rotation of the lidar-derived wind vectors from their true orientation will be observed. Thus for an ambient wind blowing from right to left across the aircraft track and a situation where the aircraft is accelerating, the data synthesis will produce wind vectors whose tips are rotated rearward of their true orientation with respect to the aircraft; for a decelerating aircraft subject to the same wind, the synthesized wind vectors will be rotated forward of their true aircraft-relative orientation. Some complication of the pattern will occur at the endpoints of the aircraft acceleration, where the fore and aft lidar beams are unequally affected by delays in reporting the ground velocity.

Although the delays in reporting the aircraft's ground velocity could not be estimated in detail, it is believed that they contribute significantly to the error budget of the lidar system for the data reported here.

APPENDIX E

ASSESSMENT OF SCANNER PERFORMANCE

A series of 13 consecutive lidar beam ground strikes was observed during a left turn executed by the aircraft at about 2039 GMT (1439 CST) during run 4 data collection. Through study of this sequence of ground strikes, it was possible to obtain some insight into how well the scanner system was operating. Figure E.1 shows plots of the sequences of corrected (see Appendix C.1) roll angles (curve in top plot) and range bins in which ground strikes, identified by peaks in lidar intensity, were observed (boxes in bottom plot). It is apparent from a comparison of the variations of roll angle and observed ground strike ranges that the measured values of roll angle corresponding to the various lidar frames were being recorded approximately one frame, or about 1.33 s, too late. When roll angle and ground strike range data are appropriately paired (for instance, roll angle from frame 139 with ground strike range from frame 138), a rough quantitative assessment of two aspects of beam pointing performance can be made.

First it can be seen that, in accord with design specifications, no ground returns were observed for roll angles more negative than -9° ; the roll angle of -8.4° reported in frame 134 might have been expected to produce a ground return in range bin 20 of frame 133 (accounting for the 1-frame delay in reporting of roll) if the scanner were not compensating properly for roll angles between $+9^\circ$ and -9° , but because no ground return was found in frame 133 there was no evidence that the beam scanner was failing to compensate for roll angles. This of course does not conclusively rule out possible beam pointing errors in near-zero roll situations, where the scanner operates in a different manner in its attempts to maintain horizontal beam trajectories. Although a range of 20 bins is considerable, it is not too far for the reception of signals from highly reflective targets.

Additionally, it is possible to predict from a knowledge of the roll and scan angles and aircraft altitude the range bin in which a ground strike should occur, assuming flat terrain and operation of the scanner according to specifications (i.e., return the beam to point along a line perpendicular to the aircraft heading and in the plane of the wings) at roll angles greater in magnitude than 9° . By comparing the predicted ground return range with the

ORIGINAL PAGE IS
OF POOR QUALITY

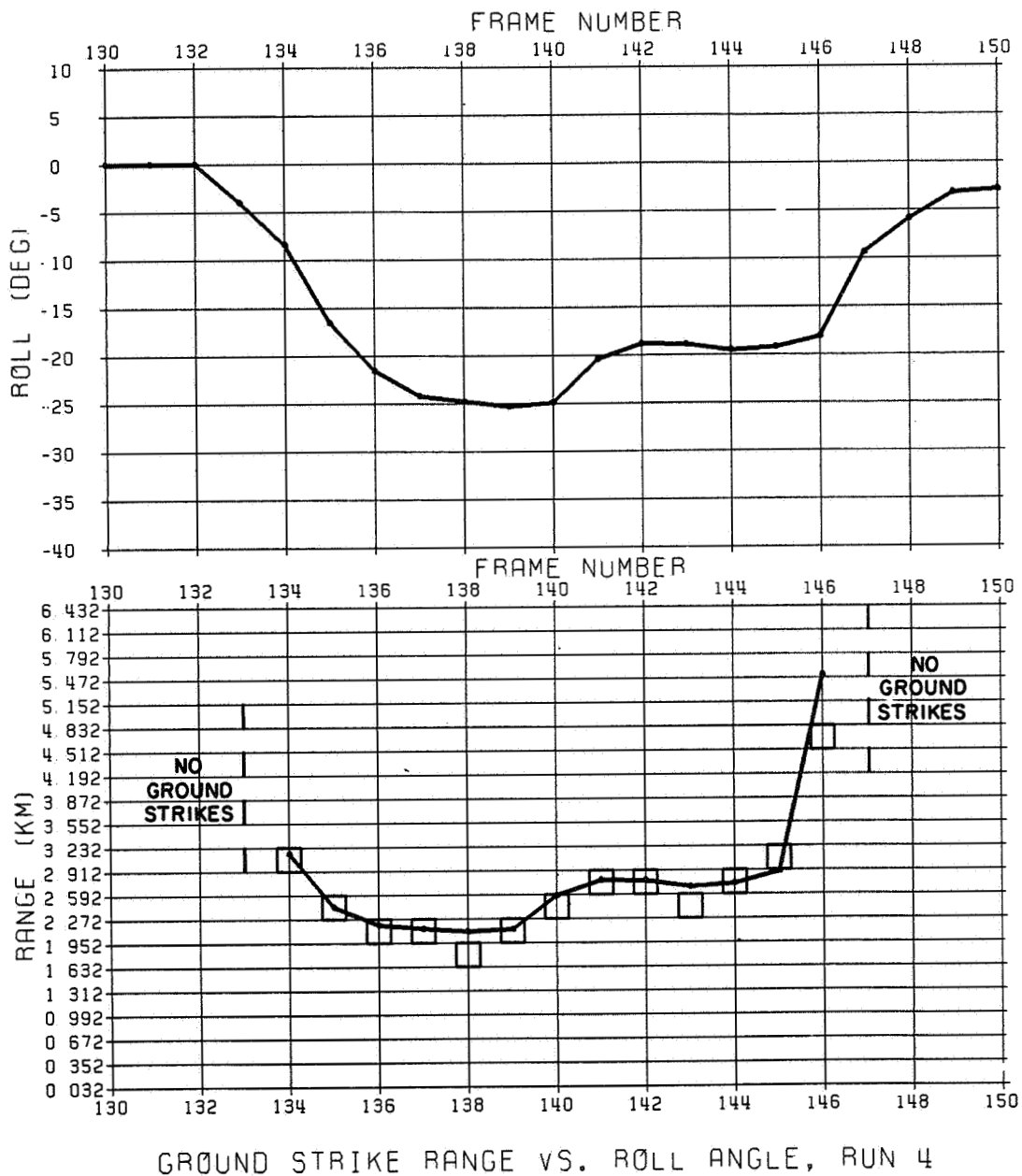


Figure E.1 Ground strike ranges and aircraft roll angles as a function of frame number. Top curve depicts aircraft roll angle; bottom depicts predicted (line) and observed (boxes) range of ground returns.

observed value, limits can be placed on the magnitude of the beam pointing biases reported by Lee (1982), assuming the biases are always present in the scanner performance regardless of the roll angle.

Such a comparison is made in the lower plot of Fig. E.1, where the solid curve superimposed on the observed values of ground strike range represents the values of predicted ground strike range, taking the 1-frame delay in roll angle properly into account. An averaged aircraft altitude of 847 m was used in all calculations of ground strike range in order to remove the influence of topographical variations, observed to be about 10-20 m in magnitude, from the computed range values. In general, the agreement between the predicted and observed ground strike ranges is excellent, with all but three frames showing exact agreement. Of the three frames not showing exact agreement, two are in "error" by only one range bin, and the other lies at the edge of the data sequence, where the roll angle magnitude was decreasing rapidly and the ground strike range was growing even more rapidly in response.

For the ground strike ranges shown in Fig. E.1, typically 2-3 km, and the aircraft altitudes associated with those ground strikes, 850 m, the appearance of a ground strike in a given range bin defines the beam elevation angle (measured relative to the horizon) only to within about a degree. Although the range to ground targets is quite sensitive to errors in beam elevation angle, the nearness of some for the ground strikes to the aircraft, the large range extent of the range bins and the relative sparseness of sampling in time prevent a more definitive bracketing of the elevation errors.

In conclusion, it appears that if the elevation errors of the scanner at small roll angles are similar to the errors seen at larger roll angles, then those errors are apparently limited to about $1.5\text{--}2.0^\circ$ for both fore and aft shots. The biases found by Lee (1982) fall well within these limits. Although the elevation error for both fore and aft shots could be zero, it is likely that some nonzero elevation error, probably of the same order as that observed by Lee, was present in the lidar data. Such elevation angle errors, of the order of 1° , could introduce significant errors in wind estimates in zones of strong vertical wind shear.

APPENDIX F

TESTS USING MODEL WIND FIELD

It was also found desirable to test the wind retrieval algorithms on a simulated monochromatic wind field designed to have properties which would be easy to identify on plotter output. To perform this test, starting position information from runs 9 through 12 were used to initialize the aircraft location at the times given for the beginning of those runs. Then, using actually measured aircraft airspeed data from each of the runs and the model wind field specified by:

$$U(X,Y,T) = 10 + 2*\text{COS}[(2\pi/5000)*(X + Y - 5T)] \quad (\text{F.1})$$

$$V(X,Y,T) = 10 + 3*\text{COS}[(2\pi/5000)*(X + Y - 5T)] \quad (\text{F.2})$$

the aircraft was forced to fly through the simulated atmosphere along a track obtained by solving the vector triangle of airspeed/heading, ground velocity/track and the model windspeed/direction for each frame in each of the four runs using INS-derived headings and initial positions for each run. The solution involved computation of the magnitude and direction of the ground velocity vector, because the other two quantities were assumed to be known.

As the aircraft progressed through the model wind field, sample lidar frames were acquired at times specified to be identical to those given in the actual real data runs, and "observations" of the appropriate radial component of the true wind in the various resolution volumes were taken based on the behavior of the model wind field as a function of space and time. The simulated observed radial velocities and line of sight angles were then subjected to the analysis algorithms described in section 3.4.4.

For the analyses it was necessary to estimate the phase speed at which the analytical wind field features are being "advected". Because the "true" phase speed was specified in the form of the model wind field itself (see the coefficients of time T in the sinusoids of Eqs. F.1 and F.2, i.e., $C_x = C_y = 5.0 \text{ m s}^{-1}$, the phase lines propagated to the northeast at 3.53 m s^{-1} and it was possible to study the impact of an incorrect guess of the advection speed on the analyzed wind vectors.

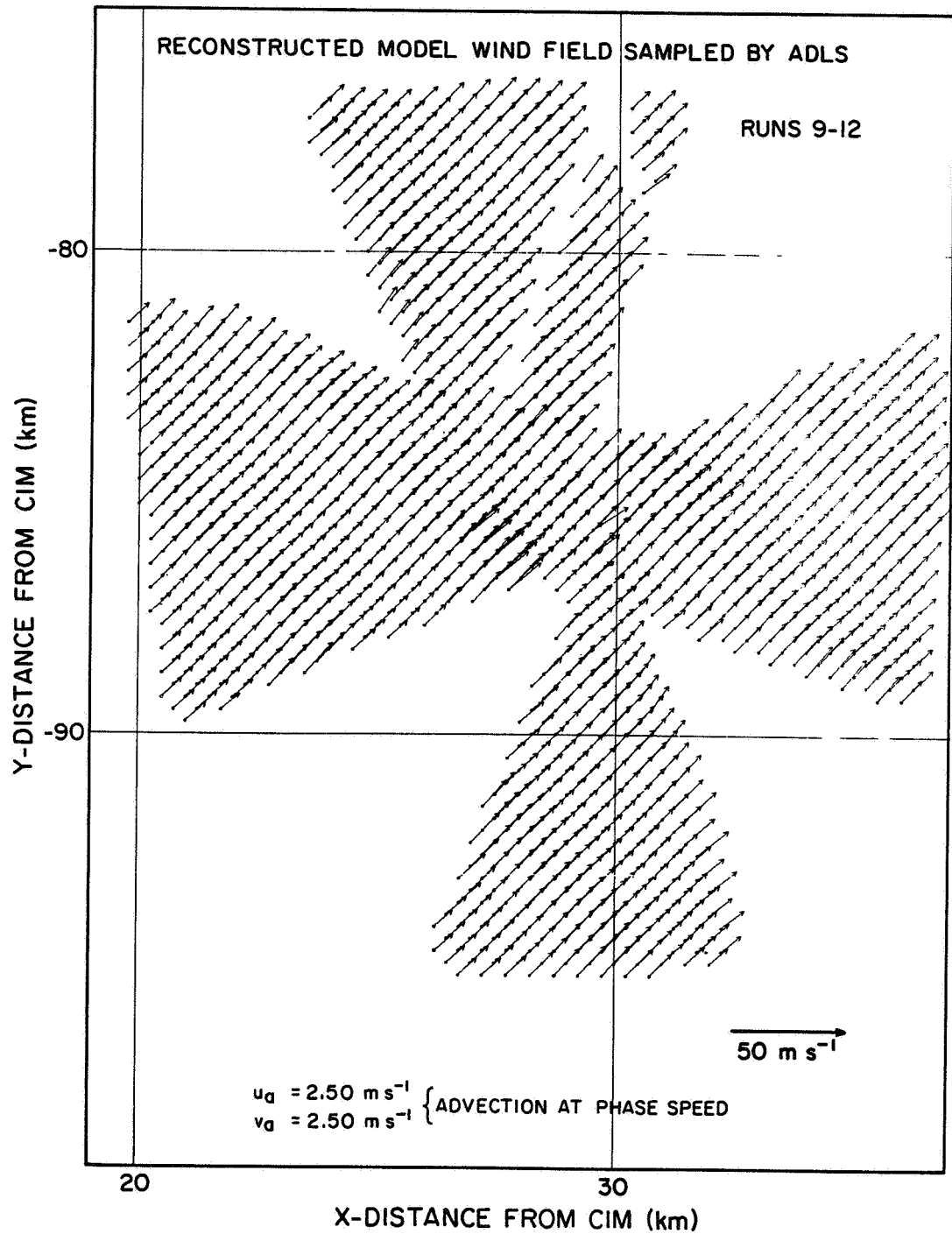


Figure F.1 Wind field synthesized from simulated lidar observations of a modeled wind field. Data are advected using an advection velocity equal to the true one (i.e., $U_a = V_a = 2.5 \text{ m s}^{-1}$).

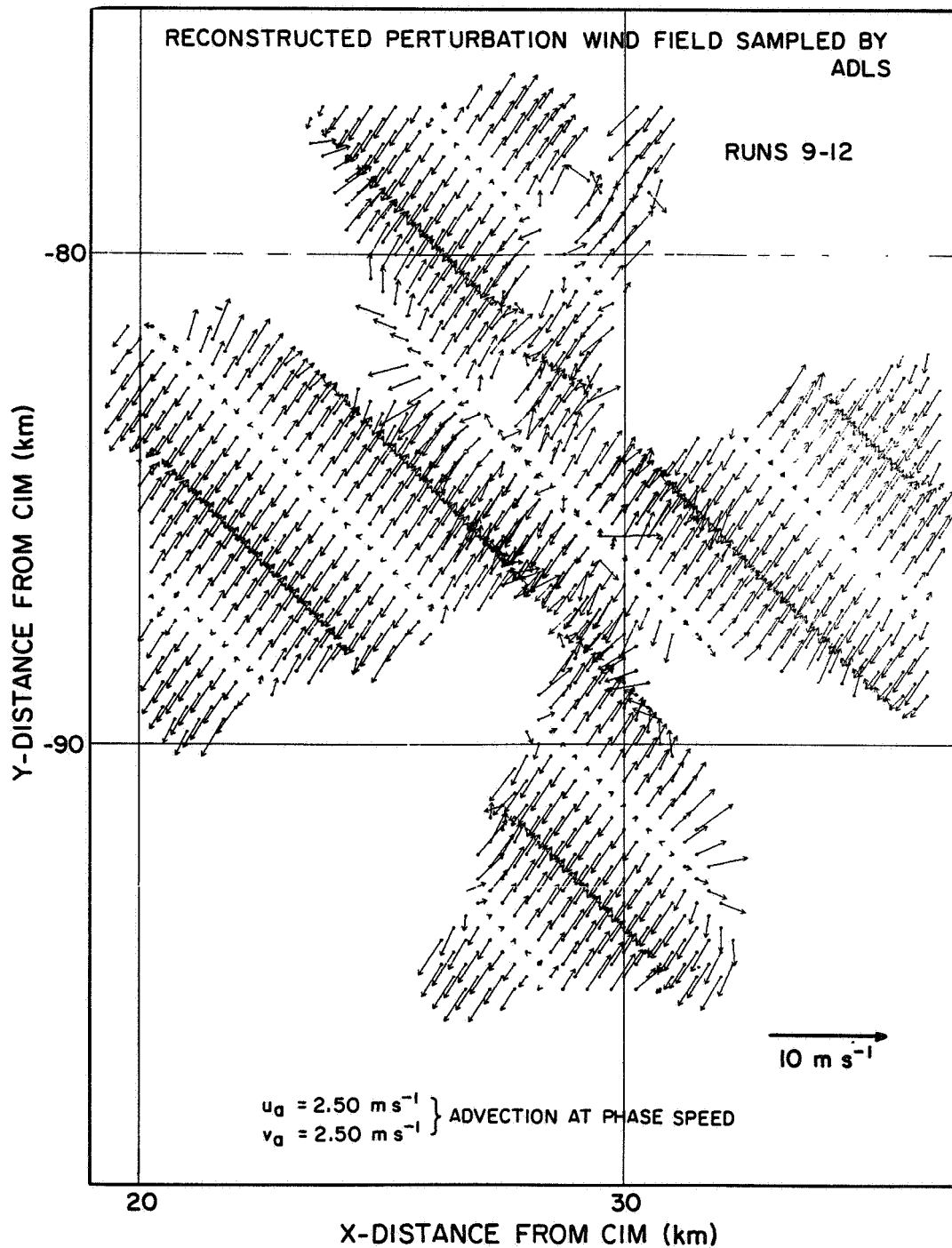


Figure F.2 Perturbation wind field of Fig. F.1 (mean of wind shown on Fig. F.1 subtracted).

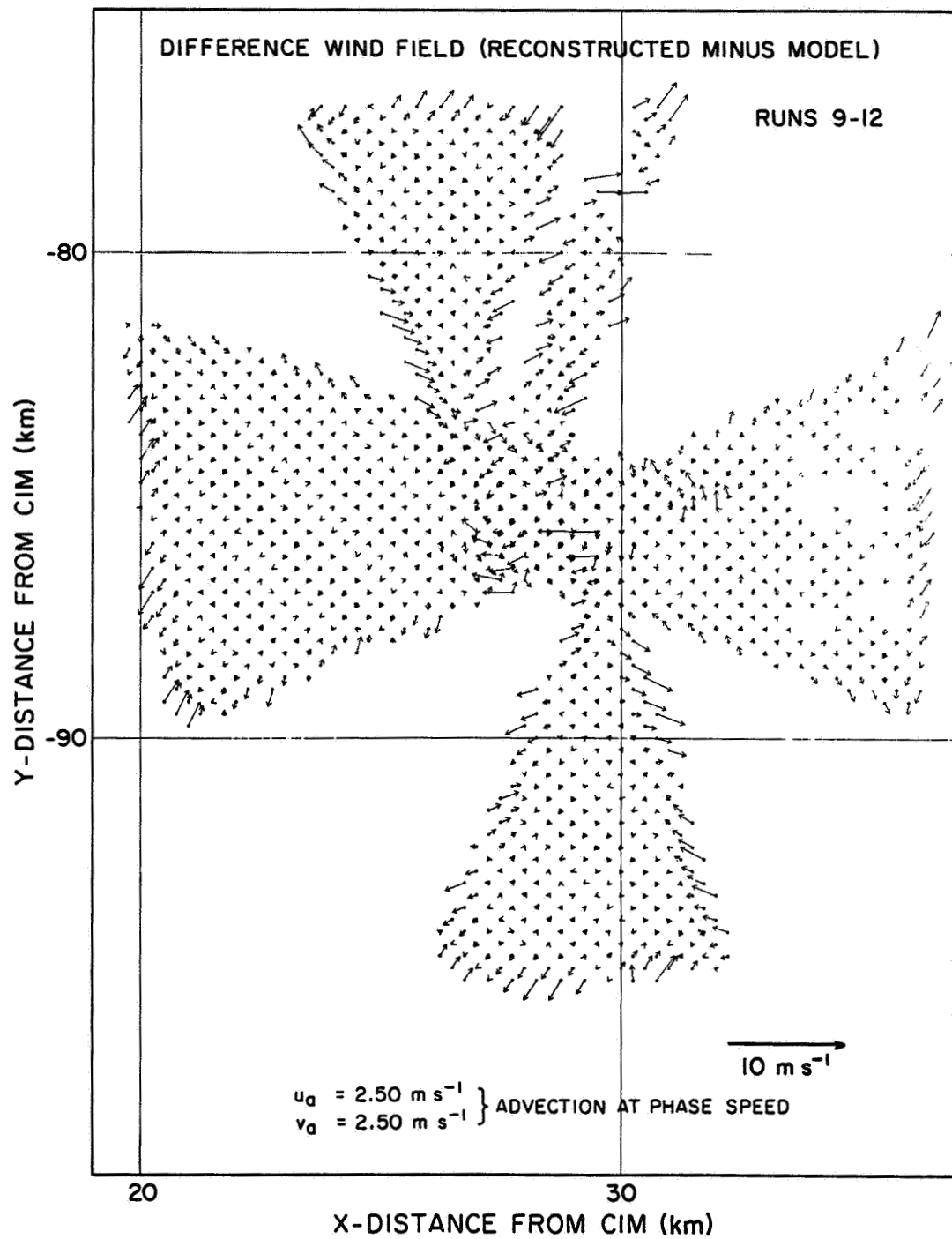


Figure F.3 Velocity vector differences between the true perturbation wind field and that synthesized from the simulated observation.

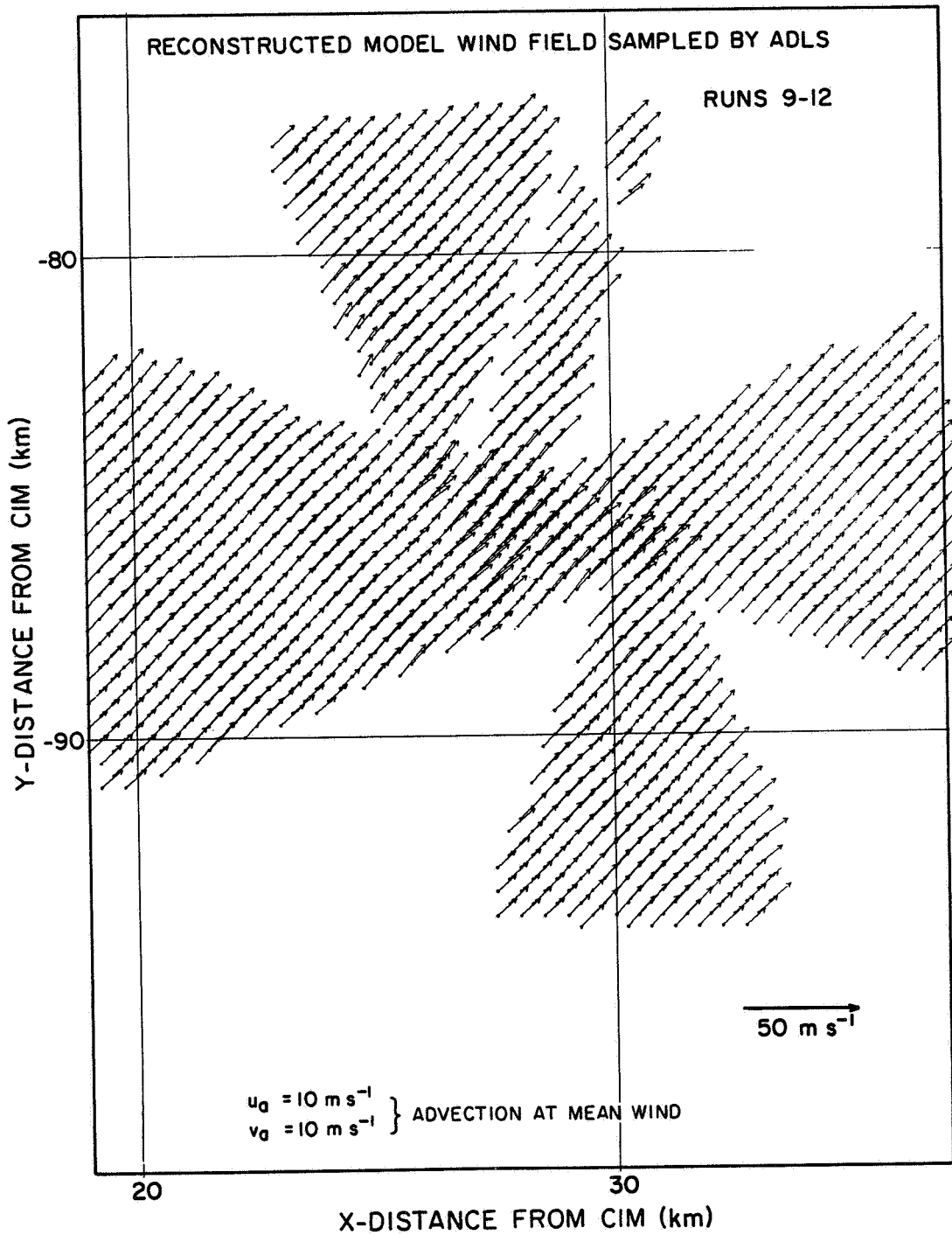


Figure F.4 Same as Fig. F.1 except $U_a = V_a = 10 \text{ m s}^{-1}$.

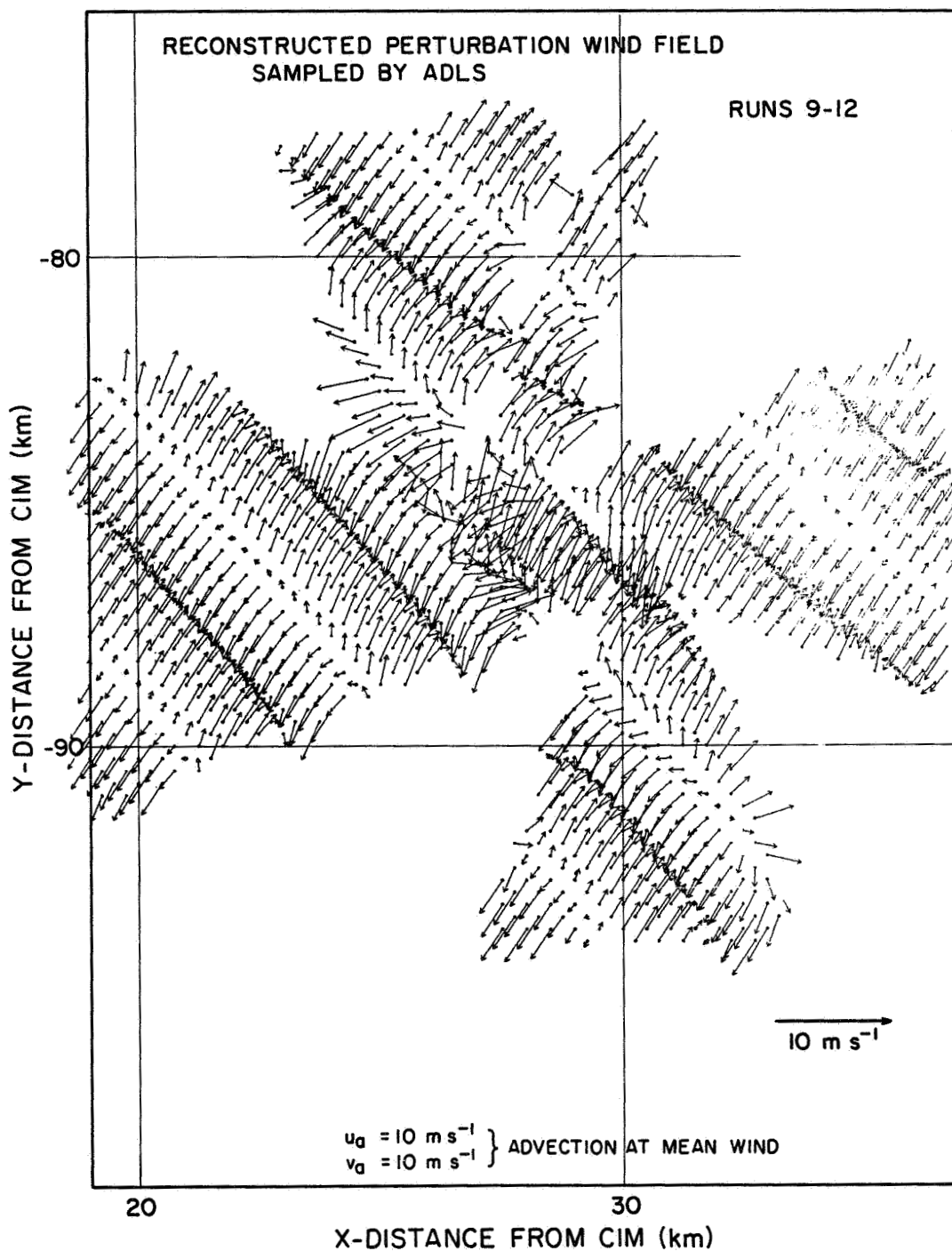


Figure F.5 Same as Fig. F.2 except $U_a = V_a = 10 \text{ m s}^{-1}$.

ORIGINAL PAGE IS
OF POOR QUALITY

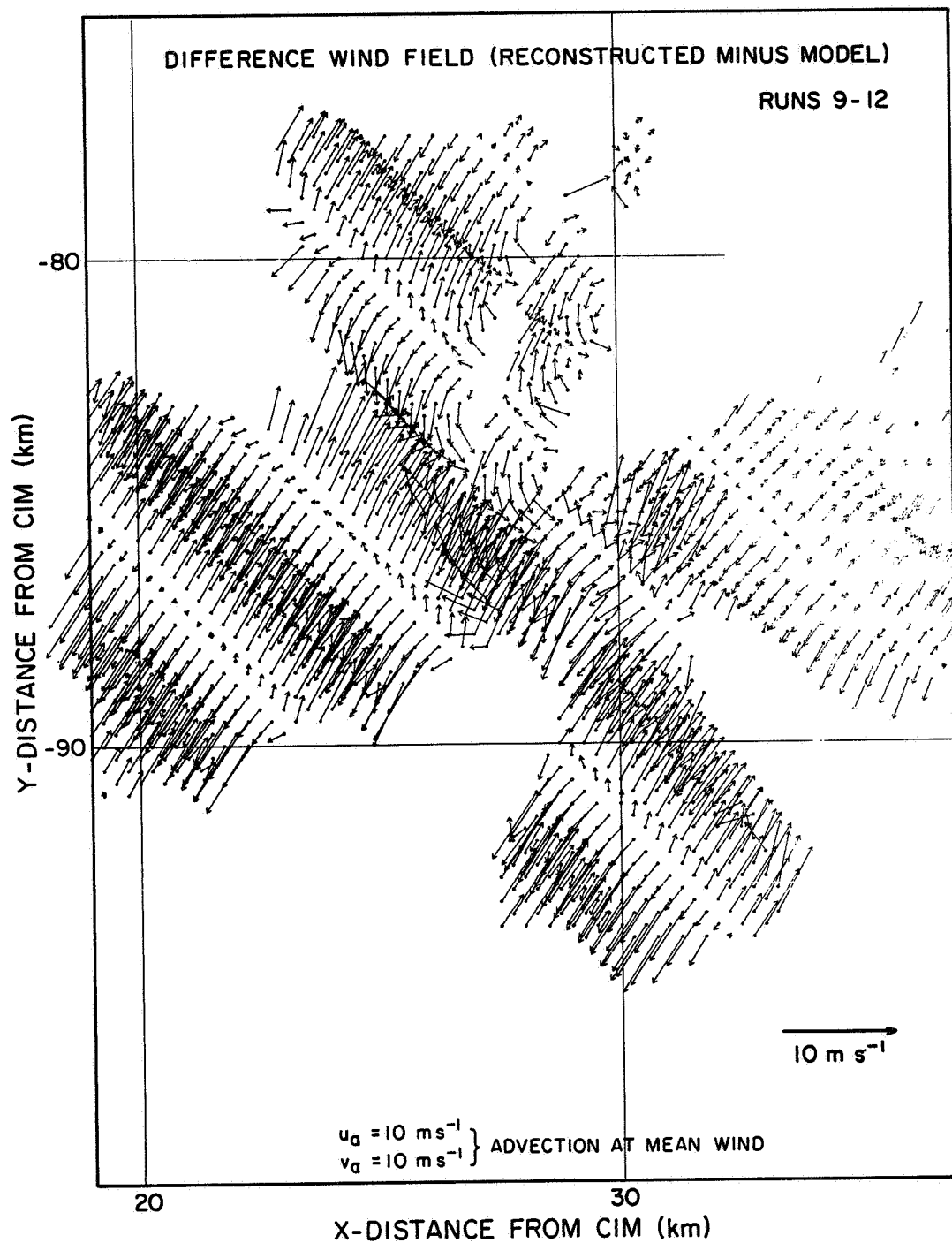


Figure F.6 Same as Fig. F.3 except $U_a = V_a 10 \text{ m s}^{-1}$.

The results of the analysis for an assumed advection which matched the true "advection" (i.e., $U_a = V_a = 2.5 \text{ m s}^{-1}$) are given in Fig. F.1. It is clear that the true wind field pattern is quite well depicted, although there are some errors near the edges of the analysis area which can be easily seen in the perturbation wind field pattern shown in Fig. F.2. Note that the errors are largest along the edges of the field as can be seen in Fig. F.3 which shows the differences in the true perturbation wind field and that synthesized wind from simulated observations. These errors are due to the inadequacies of the Cressman interpolation scheme when data are not uniformly distributed over the interpolation volume. Note also the smooth blending of the retrieved vectors in areas where two runs of data overlap in space.

When the estimated advection vector is set equal to the mean wind ($U_a = V_a = 10 \text{ m s}^{-1}$) in the layer, the results, shown in Figs. F.4-F.6 are significantly different. The basic pattern of the wind vectors is still quite accurately represented, but some inconsistencies arise in areas of overlap between two data runs. Note the displacement of data areas by comparing Figs. F.1 and F.4. In Fig. F.5, displacements are noted between the convergence lines retrieved from the synthesis of data from the different runs. The difference fields shown in Fig. F.6 are considerably larger than in the case when the correct advection velocity is used. These inconsistencies are clearly the result of the improper shift of the data points in space caused by the advection correction algorithm having to use an erroneous advection velocity.

BIBLIOGRAPHY

- Ames Research Center, 1981: CV-990 flight summary report, Severe Storms Program (flights 1-9), June 12-July 3, 1981. NASA Ames Research Center, CA.
- Arya, S.P.S., and J.C. Wyngaard, 1975: "Effect of Baroclinicity on Wind Profiles and the Geostrophic Drag Law for the Convective Planetary Boundary Layer", *J. Atmos. Sci.*, **32**, 767-778.
- Barcilon, A., and P. Drazin, 1972: Dust devil formation. *Geophys. Fluid Dyn.*, **4**, pp. 147-158.
- Barnes, S., 1968: On the source of thunderstorm rotation. *Essa Tech. Memo. NSSL-38*, Norman, OK, 28 pp.
- Bilbro, J., G. Fichtl, D. Fitzjarrald, M. Krause, and R. Lee, 1984: Airborne Doppler lidar wind field measurements. *Bull. Amer. Meteor. Soc.*, **65**, pp. 348-359.
- Bilbro, J., 1982: Engineering documentation for the 1981 Severe Storms Doppler lidar flight program. NASA Marshall Space Flight Center, AL, 176 pp.
- Britting, K., 1971: *Inertial Navigation System Analysis*. Wiley-Interscience, New York.
- Browning, K., 1964: Airflow and precipitation trajectories within severe local storms which travel to the right of the winds. *J. Atmos. Sci.*, **21**, pp. 634-639.
- Businger, J.A., 1973: "Turbulent Transfer in the Atmospheric Surface Layer", *Workshop in Micrometeorology*, American Meteorological Society, Boston, 67-100.
- Businger, J.A., J.A. Wyngaard, Y. Izumi, and E.F. Bradley, 1971: Flux-profile relationships in the atmospheric surface layer. *J. Atmos. Sci.*, **28**, 181-189.
- Byers, H., and R. Braham, 1949: *The Thunderstorm*. Govt. Print. Off., Washington, 287 pp.
- Carbone, R., 1982: A severe frontal rainband. Part I: Stormwide hydrodynamic structure. *J. Atmos. Sci.*, **39**, pp. 258-279.
- Carbone, R., 1983: A severe frontal rainband. Part II: Tornado parent vortex circulation. *J. Atmos. Sci.*, **40**, pp. 2639-2654.

- Clarke, R.H., A.J. Dyer, R.A. Brook, D.G. Reid, and A.J. Troup, 1971: **The Wangara Experiment: Boundary Layer Data.** Tech. Paper No. 19, CSIRO, Div. Meteor. Phys., 362 pp.
- Cressman, G.P., 1959: "An operational objective analysis system". **Mon. Wea. Rev.**, No. 10, pp. 367-374.
- Davies-Jones, R., 1982: Observational and theoretical aspects of tornadogenesis. **Topics in Atmospheric and Oceanic Sciences, Intense Atmospheric Vortices.** Springer-Verlag, New York, pp. 175-189.
- Deardorff, J.W., 1972: "Numerical Investigation of Neutral and Unstable Planetary Boundary Layers", **J. Atmos. Sci.**, **29**, 91-115.
- Doviak, R.J., P.S. Ray, R.G. Strauch, and L.J. Miller, 1976: "Error estimation in wind fields derived from dual-Doppler radar measurement". **J. Appl. Meteor.**, **15**, pp. 868-878.
- Doviak, R.J., and C.T. Jobson, 1979: "Dual Doppler radar observations of clear wind perturbations in the planetary boundary layer". **J. Geophysics Res.**, **84**, pp. 697-702.
- Doviak, R.J., and M.I. Berger, 1980: "Turbulence and waves in the optically clear planetary boundary layer resolved by dual-Doppler radars". **Radio Science**, **15**, pp. 297-317.
- Doviak, R.J., and D.S. Zrnic', 1984: **Doppler Radar and Weather Observation**, Academic Press, New York.
- Eilts, M.D., 1983: **The structure of the Convective Boundary Layer as Seen by Lidar and Doppler Radars**, M.S. Thesis, University of Oklahoma, Norman, OK.
- Fraser, A., 1968: The white Box: The mean mechanics of the cumulus cycle. **Quart J. Roy. Meteor. Soc.**, **94**, pp. 71-87.
- Frye, W.E., 1958: "Inertial guidance and navigation". **Advances in Astronautical Sciences**, **2**, Plenum Press, N.Y., pp. 9-1 to 9-12.
- Goff, R., 1975: Thunderstorm outflow kinematics and dynamics. **NOAA Tech. Memo. ERL NSSL-75**, Norman, OK, 63 pp.
- Izumi, Y. and S.J. Caughey, 1976: Minnesota 1973 Atmospheric Boundary Layer Experiment Data Report. AFCRL Res. Report, AFCRL, Bedford, Mass.
- Kaimal, J.C., 1975: Sensors and techniques for direct measurement of turbulent fluxes and profiles in the atmospheric surface layer. **Atmospheric Technology**, **7**, 7-14.
- Kaimal, J.C., J.C. Wyngaard, D.A. Haugen, O.R. Cote, Y. Izumi, S.J. Caughey, and C.J. Readings, 1976: Turbulence structure in the convective boundary layer. **J. Atmos. Sci.**, **33**, 2152-2169.
- Klemp, J., and R. Wilhelmson, 1978: Simulations of right and left moving storms produced through storm splitting. **J. Atmos. Sci.**, **35**, pp. 1097-1110.

- Klug, W., 1967: Determination of turbulent fluxes of heat and momentum from the wind profile. **Quart. J. Roy. Meteor. Soc.**, **93**, 101-104.
- Kuettner, J.P., 1971: "Cloud bands in the earth's atmosphere". **Tellus**, **23**, pp. 404-425.
- Lee, J.T., and J. Stokes, 1978: Tall tower and aircraft instrumentation: Quality control procedures--development and application. **Preprints of Fourth Symposium on Meteorological Observations and Instrumentation**, Apr. 10-14, 1978, Denver, Colorado, Amer. Meteor. Soc., 18-24.
- Lee, R., and K. Lee, 1980: A poly-pulse-pair signal processor for coherent Doppler lidar. **Proceedings**, Topical meeting on coherent laser radar for atmospheric sensing, Aspen, CO.
- Lee, R., 1981: Processing of two-dimensional lidar-derived windfields. **Proceedings**, 20th Conference on Radar Meteorology, Boston, pp. 601-605.
- Lee, R., 1982: NASA airborne Doppler lidar program: Data characteristics of 1981 wind field measurements. **Tech. Rept. No. 1**, Lassen Research, Manton, CA.
- Lee, R.W., 1980: "Windfield retrieval from Doppler lidar observations". In **First scientific working group meeting of airborne Doppler lidar wind velocity measurement program**. Edited by J.W. Kaufman, pp. D-1 to D-20, NASA Conference Publication, CP-2161.
- Lhermitte, R., 1970: Dual Doppler radar observations of convective storm circulation. **Proceedings**, 14th Conference on Radar Meteorology, Boston, pp. 153-156.
- Lilly, D., 1979: The dynamical structure and evolution of thunderstorms and squall lines. **Ann. Rev. Earth Planet. Sci.**, **7**, pp. 117-161.
- Mason, P.J., and R.I. Sykes, 1980: "A two dimensional numerical study of horizontal roll vortices in the neutral atmospheric boundary layer". **Quart. J. Royal Meteor. Soc.**, **106**, pp. 351-356.
- McCarthy, J., 1974: Field verification of the relationship between entrainment rate and cumulus cloud diameter. **J. Atmos. Sci.**, **31**, pp. 1028-1039.
- McCaul, E.W. 1985: Observations of Oklahoma convection using airborne Doppler lidar and ground-based Doppler radar. **M.S. Thesis**, University of Oklahoma, Norman, OK.
- Morton, B., 1957: Buoyant plumes in a moist atmosphere. **J. Fluid Mech.**, **2**, pp. 127-144.
- Murty, S., and J. Bilbro, 1978: **Atmospheric Effects on CO2 Laser Propagation**. NASA TP-1357, Marshall Space Flight Center, Huntsville, AL.
- NASA, 1979: **CV-990 Airborne Laboratory Experimenters Handbook**. Ames Research Center, Moffet Field, California, p. 3-2.

- Newell, R., S. Geotis, M. Stone, and a. Fleisher, 1955: How round are raindrops? **Proceedings**, Fifth Weather Radar Conf., Asbury Park, NJ.
- Paulson, C.A., 1970: The mathematical representation of wind speed and temperature profiles in the unstable atmospheric surface layer. **J. Appl. Meteor.**, **9**, 857-861.
- Paluch, I., 1979: The entrainment mechanism in Colorado cumuli. **J. Atmos. Sci.**, **36**, pp. 2467-2478.
- Ray, P., R. Doviak, G. Walker, D. Sirmans, J. Carter, B. Bumgarner, 1975: Dual Doppler observations of a tornadic storm. **J. Appl. Meteor.**, **14**, pp. 1521-1530.
- Raymond, D., and M. Wilkening, 1982: Flow and mixing in New Mexico mountain cumuli. **J. Atmos. Sci.**, **39**, pp. 2211-2228.
- Raytheon Company, 1983: **Specification for Airborne Pulsed Doppler Lidar Operational Control System**. Wayland, Mass., 85 pp.
- Rotunno, R., 1984: Private communication.
- Sanders, L.D., and A.H. Weber, 1970: Evaluation of roughness lengths at the NSSL-WKY meteorological tower. **ESSA Tech. Memo.**, ERLTM-NSSL 47, 24 pp.
- Simpson, J., 1982: Cumulus rotation: Model and observations of a waterspout-bearing cloud system. **Topics in Atmospheric and Oceanic Sciences, Intense Atmospheric Vortices**. Springer-Verlag, New York, pp. 161-173.
- Simpson, J., G. Van Helvoirt, and M. McCumber, 1982: Three-dimensional simulations of cumulus congestus clouds on gate day 261. **J. Atmos. Sci.**, **39**, pp. 126-145.
- Sloss, P., 1967: An empirical examination of cumulus entrainment. **J. Appl. Meteor.**, **6**, pp. 878-881.
- Squires, P., 1958: Penetrative downdrafts in cumuli. **Tellus**, **10**, pp. 381-389.
- Squires, P. and J. Turner, 1962: An entraining jet model for cumulonimbus updraughts. **Tellus**, **14**, pp. 422-434.
- Stommel, H., 1947: Entrainment of air into a cumulus cloud. **J. Meteor.**, **4**, pp. 91-94.
- Sundara-Rajan, A., and S.A. Macklin, 1976: Comments on the heat flux and friction velocity in free convection near the ground. **J. Atmos. Sci.**, **33**, 715-718.
- Sundara-Rajan, A., M.D. Eilts, and R.J. Evans, 1984: "Estimation of the Average Surface Heat Flux Over an Inhomogeneous Terrain from the Vertical Velocity Variance", accepted for publication in **Boundary Layer Meteor.**
- Turner, J., 1962: The "starting plume" in neutral surrounding. **J. Fluid Mech.**, **13**, pp. 356-368.

- Waldteufel, P., 1976: An analysis of weather spectra variance in a tornadic storm. NOAA Technical Memo. ERL NSSL-76. The National Severe Storms Laboratory, Norman, Okla. 73069.
- Warner, J., 1970: On steady-state models of cumulus convection. **J. Atmos. Sci.**, **27**, pp. 246-255.
- Weisman, M., and J. Klemp, 1982: The dependence of numerically simulated convective storms on vertical wind shear and buoyancy. **Mon. Wea. Rev.**, **110**, pp. 504-520.
- Wyngaard, J.C., Q.R. Cote, and K.S. Rao, 1974: "Modelling of the Atmospheric Boundary Layer", **Advances in Geophysics**, **18A**, 193-211.

1. REPORT NO. NASA CR-3960		2. GOVERNMENT ACCESSION NO.		3. RECIPIENT'S CATALOG NO.	
4. TITLE AND SUBTITLE Analysis of Airborne Doppler Lidar, Doppler Radar, and Tall Tower Measurements of Atmospheric Flows in Quiescent and Stormy Weather				5. REPORT DATE February 1986	
				6. PERFORMING ORGANIZATION CODE	
7. AUTHOR(S) H. B. Bluestein, R. J. Doviak, M. D. Eilts, E. W. McCaul, R. Rabin, A. Sundara-Rajan, and D. S. Zrnic'				8. PERFORMING ORGANIZATION REPORT #	
9. PERFORMING ORGANIZATION NAME AND ADDRESS University of Oklahoma National Severe Storms Laboratory, and Cooperative Institute for Mesoscale Meteorological Studies Norman, Oklahoma 73069				10. WORK UNIT NO. M-511	
				11. CONTRACT OR GRANT NO. NAS8-34749	
12. SPONSORING AGENCY NAME AND ADDRESS National Aeronautics and Space Administration Washington, D.C. 20546				13. TYPE OF REPORT & PERIOD COVERED Contractor Report April 27, 1982 - July 31, 1985	
				14. SPONSORING AGENCY CODE	
15. SUPPLEMENTARY NOTES H. B. Bluestein and E. W. McCaul: University of Oklahoma, Norman, Oklahoma. R. J. Doviak, M. D. Eilts, R. Rabin, and D. S. Zrnic': National Severe Storms Laboratory, Norman, Oklahoma. A. Sundara-Rajan: Cooperative Institute for Mesoscale Meteorological Studies, Norman, Oklahoma. Technical Monitors: Daniel E. Fitzjarrald and Margaret B. Alexander. Prepared for the Atmospheric Sciences Division, Systems Dynamics Laboratory, Marshall Space Flight Center, Alabama 35812					
16. ABSTRACT The first experiment to combine airborne Doppler Lidar and ground-based dual Doppler Radar measurements of wind to detail the lower tropospheric flows in quiescent and stormy weather was conducted in Central Oklahoma during four days in June-July 1981. Data from these unique remote sensing instruments, coupled with data from conventional in-situ facilities, i.e., 500-m meteorological tower, rawinsonde, and surface based sensors, were analyzed to enhance understanding of wind, waves and turbulence. The purposes of the study were to (1) compare winds mapped by ground-based dual Doppler radars, airborne Doppler lidar, and anemometers on a tower; (2) compare measured atmospheric boundary layer flow with flows predicted by theoretical models; (3) investigate the kinematic structure of air mass boundaries that precede the development of severe storms; and (4) study the kinematic structure of thunderstorm phenomena (down-drafts, gust fronts, etc.) that produce wind shear and turbulence hazardous to aircraft operations. The report consists of three parts: Part I, "Intercomparison of Wind Data from Airborne Lidar, Ground-Based Radars and Instrumented 444 m Tower." Part II, "The Structure of the Convective Atmospheric Boundary Layer as Revealed by Lidar and Doppler Radars." Part III, "Doppler Lidar Observations in Thunderstorm Environments."					
17. KEY WORDS Atmospheric Boundary Layer Remote Sensing Circulation (Wind) Turbulence Wind Shear			18. DISTRIBUTION STATEMENT Unclassified - Unlimited Star Category: 47		
19. SECURITY CLASSIF. (of this report) Unclassified		20. SECURITY CLASSIF. (of this page) Unclassified		21. NO. OF PAGES 176	
				22. PRICE A09	